FLUID-INCLUSION AND GEOCHEMICAL STUDIES AT THE EMPEROR GOLD MINE, FIJI.

by

Masood Ahmad

Submitted in partial fulfilment of the requirements
for the degree of Doctor of Philosophy
at the University of Tasmania.

HOBART

August
1979

This thesis contains no material which has been accepted for the award of any other degree or diploma in any University and, to the best of my knowledge and belief, contains no copy or paraphrase of material previously published or written by another person, except where due reference is made in the text of this thesis.

Masood Ahmad
August, 1979.

CONTENTS

LIST OF PLATES

List of Plates cont.

LIST OF FIGURES

List of Figures cont.

List of Figures cont.

List of Figures cont.

LIST OF TABLES

ABSTRACT

The gold-silver telluride deposits of the Emperor mine (Vatukoula, Fiji) are fairly typical of the epithermal deposits found in association with Tertiary volcanic activity in the circum-Pacific belt. The mine produces about 60,000 troy ounces of gold per annum, together with silver and tellurium. It lies on the western margin of a Pliocene caldera (the Tavua caldera or Tavua basin) and the host rocks for the mineralization are olivine basalt flows and andesite dykes. The olivine basalt sequence is about 2000 m thick and is probably underlain by mid-Tertiary calcareous sedimentary rocks approximately 1500 m thick. The sedimentary rocks are probably underlain by early Tertiary andesitic rocks.

Five phases of volcanic (and associated intrusive) activity have been recognised in the Tavua cauldron. The K-Ar dating indicates two major periods of igneous activity, which commenced at about 10 m.y. with widespread eruptions of olivine basalt (phase I) and continued to about 7.5 m.y. A period of quiescence followed. The later phases of volcanic activity (phases II to V) date between 5 and 4.3 m.y. Phase II volcanism is represented by minor eruptions of trachybasalt, phase III by augite trachyandesite, phase IV by biotite trachyandesite and phase V by monzonite and trachyte. The later phases (phases III to V) are essentially intrusive in nature and are represented by cone sheets, dykes and small plugs, and generally occur within the limits of the caldera. Te^{130}-Xe^{130} dating on a telluride sample gave an age of 7.2 m.y. indicating that the bulk of the mineralization was probably associated with the first period of igneous activity (10 to 7.5 m.y.).

Initial hydrothermal activity resulted in widespread propylitization and carbonatization of basalt, and this was followed by limited K-silicate alteration and mineralization. The lodes are essentially fracture fillings with well-developed crustification textures and vugs. Ore-mineral, sulphide and carbonate precipitation appears to have been intermittent, whereas quartz precipitation was essentially uninterrupted, and continued after the cessation of ore-mineral precipitation. The ore-minerals are native gold, native tellurium and gold-silver tellurides. Paragenetic studies suggest ten stages of ore and gangue mineral precipitation, viz. stage IA: widespread propylitic alteration with the development of carbonate, chlorite, actinolite, epidote etc.; stage IB: fringe K-silicate alteration which includes K-feldspar, sericite, dolomite and sulphides; stage IIA: barren vein quartz deposition; stage IIB: vein quartz, dolomite, K-feldspar, sericite, roscoelite, native tellurium and gold-rich tellurides; stage IIIA: barren vein-quartz deposition; stage IIIB: vein quartz, dolomite, K-feldspar, sericite, roscoelite, native gold and silver-rich tellurides; stage IVA: white barren vein quartz; stage IVB: amber barren vein quartz; stage IVC: white barren quartz; and stage V: calcite deposition. The bulk of mineralization (stage IIB tellurides) is restricted to 12 level and above while stage IIIB tellurides and native gold are distributed throughout.

Fluid-inclusion studies on quartz indicate a temperature range from 205 to 317^{o}C during stage IIA and from 170 to 230^{o}C during stage IIIA. Temperatures during stage IVA, IVB and IVC ranged from 160 to 240^{o}C and peaked around 180^{o}C. Fluid inclusions in stage V calcite are rare and very small, and generally lack a visible vapour phase; no temperature determinations were possible. Temperatures during stage IIA show an apparent increase with depth but no such changes are

apparent during other stages. A number of inclusions from near the top of the mine show evidence that the fluids were boiling and it is possible to reconstruct dramatic variations in the water table during the vein formation which apparently overlapped caldera formation.

Freezing temperatures of fluid inclusions indicate about 5.5 wt.% eq. NaCl and there is no apparent variation in salinity with time. Leaching studies of fluid inclusions indicate that the fluid averaged 0.1 molal K, 0.35 molal Na, 0.26 molal Ca and 0.005 molal Mg.

The δD values of fluid-inclusion water from vein quartz (stages IIA to IVC) range from -26 to -58 per mil and there is no apparent variation in these values with time. The $\delta^{18}O$ values of water (stages IIA to IVC) calculated from the oxygen isotopic composition of quartz range from +3 to +9 per mil and it appears that the solutions were progressively depleted in the lighter isotope with time. The $\delta^{18}O$ values of fresh rocks range from +5.5 to +7 per mil. The ^{18}O values of propylitized rocks range from +9 to +12.5 per mil and K-silicate rocks range from +15.5 to +17 per mil. The $\delta^{18}O$ values of vein quartz (stages IIA to IVC) range from +16 to +21 per mil. It is suggested that the hydrothermal fluids were largely meteoric waters which underwent extensive oxygen-isotope exchange with the country rocks. The δD values of inclusion water in stage V calcite range from -60 to -80 per mil suggesting a magmatic source at this stage.

The $\delta^{13}C$ values of carbonates in the propylitic rocks range from -1.1 to -1.4 per mil. The $\delta^{13}C$ values of early vein carbonates (stages IIB and IIIB) range from +0.3 to -1 per mil. The $\delta^{13}C$ values of calcite in the supposedly underlying sedimentary rocks range from -0.8 to -4 per mil. It is suggested that the hydrothermal carbon (stages IA to IIIB) was derived from the underlying sedimentary rocks. The $\delta^{13}C$ values of stage V calcite range from -4 to -8.6 per mil

suggesting a magmatic parentage. It is suggested that intrusion of minor plugs and dykes during the second period of igneous activity (5 to 4.3 m.y.) probably resulted in the formation of shallow convection cells and the stage V carbon was either directly derived from these intrusions or was leached from the surrounding volcanic rocks.

The $\delta^{34}S$ values of pyrite (stages IA to IIIB) range from -5.5 to -15.3 per mil. When considered in conjunction with f_{O_2}-T-pH conditions these values are compatible with a magmatic source.

Chemical analyses of fresh and altered rocks indicate that SiO_2 was depleted from the propylitic rocks but was added to the K-silicate rocks. MgO, CaO, Al_2O_3, Na_2O and TiO_2 show progressive depletion with the intensity of alteration.

Physicochemical conditions of ore deposition have been approximated from mineral stability and other data. They are: T = 200 to 250°C; pH = 5.5 ± 0.5; $m_{Cl} = 1$; I = 1; $m_{\Sigma S} = 10^{-3}$; $m_{\Sigma C} = 10^{-2}$; $m_{\Sigma S_r}/m_{\Sigma S_o} = 1$ and $f_{O_2} = 10^{-35}$ to 10^{-40}. Metal solubility calculations suggest that under these conditions the solutions may carry 10 to 1 ppm Zn, 100 to 10 ppm Fe, 0.05 to 0.02 ppm Au and 0.1 to 0.01 ppm Pb, Ag and Cu each.

Stability fields of several tellurides have been constructed and the existing thermodynamic data indicate that the tellurium concentrations as low as 10^{-11} molal will result in stabilising a number of tellurides. Apparently the thermodynamic data on the aqueous tellurium species need revision.

A fluid convection model is proposed in which meteoric water circulated for most of the history of the system through basalt and the underlying sediments. The probable cauldron geometry requires only one major discharge zone for the convective system. Though this limits the

potential for further deposits related to the Tavua caldera it emphasises the ore potential of other similar structures in Fiji. It is estimated from the settling properties of pyrite grains that the fluid velocity in the vein was about 4 cm/sec. This with other assumptions regarding metal solubility and the length and width of the feeder channel suggest that deposits of the size of Emperor could form in about 10^3 years.

A model is envisaged in which the circulating meteoric waters reacted with the underlying calcareous sediments and volcanics and picked up sedimentary carbon and heavy oxygen. The ore and gangue mineral constituents were also probably leached from these rocks. These solutions were channeled upwards through existing fractures and boiled at the site of deposition. A decrease in temperature together with a drop in $m_{\Sigma S}$ and increase in pH due to boiling were probably the main causes of ore and gangue mineral precipitation.

Chapter 1

INTRODUCTION

1.1 GENERAL

The lodes at the Emperor gold mine are typical of gold-silver telluride deposits found in the Tertiary volcanic belt surrounding the Pacific Ocean. The mine is located about 8 km inland from the northern coast of Viti Levu, the largest island of Fiji (Fig. 1.1). The mining township (population 6,425) is known as Vatukoula, the Fijian equivalent of "gold rock", and the nearest shopping town, Tavua, is about 8 km north of the mine. The nearest international airport, Nandi (or Nadi), on the Sydney to San Francisco route, is about 70 km southwest of the mine.

Viti Levu covers an area of about 10,345 sq km and extends from longitude 177°15'E to 178°45'E and latitude 17°15'S to 18°15'S. A circum-insular road connects all the major towns, from which secondary roads strike off towards the centre of the island. No road has yet been made across the rugged interior.

The Vatukoula area is geomorphologically young and differential erosion of predominantly pyroclastic rocks exposed within the boundary of a Mio-Pliocene caldera (also known as Tavua caldera) has produced a circular topographic depression, about 6 km in diameter. This is sometime referred to as the Tavua or Vatukoula basin. The basin is ringed to the south, east and west by hills that rise to between 600 and 1100 m, but the northern side is open to the sea and is the drainage outlet of the basin (Plate 1.1). Nasivi River, the main drainage channel, flows in a northerly direction.

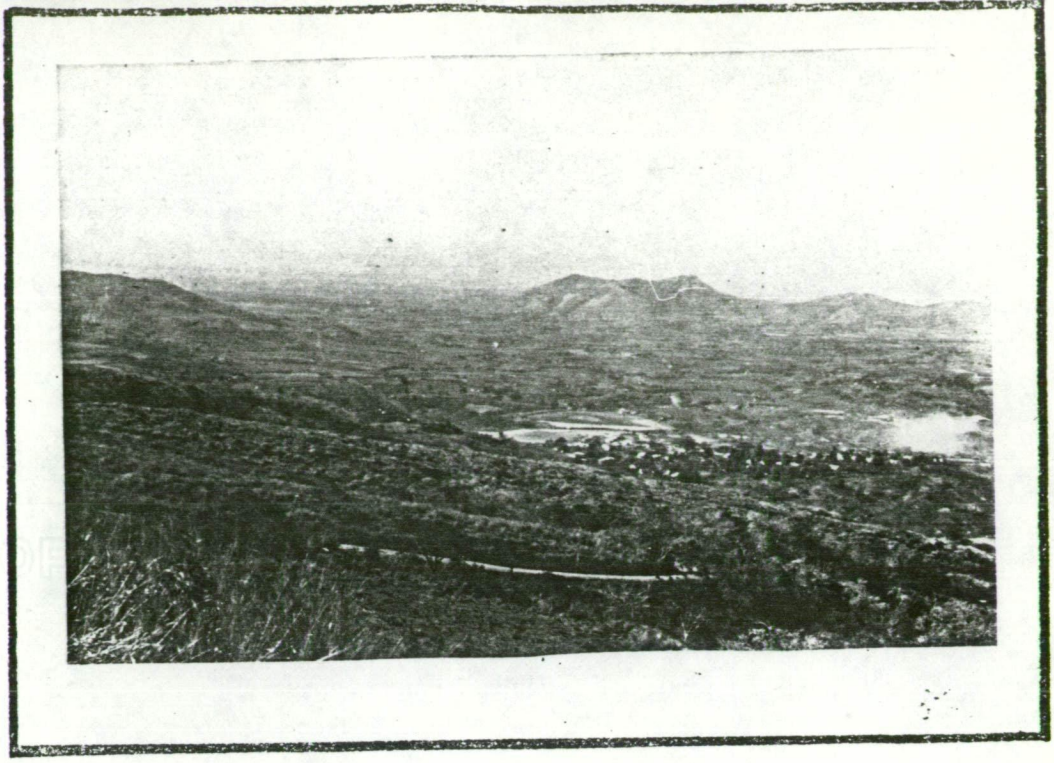

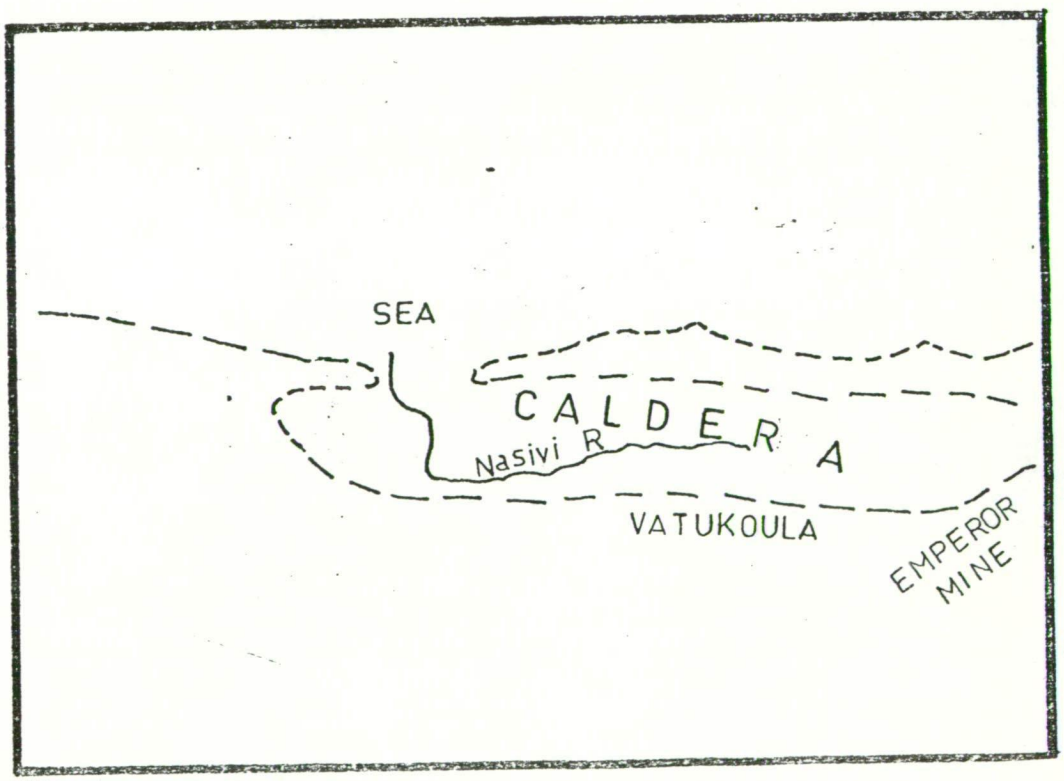

Plate 1.1 A view of the Tavua caldera looking north-east from the Emperor mine guest house.

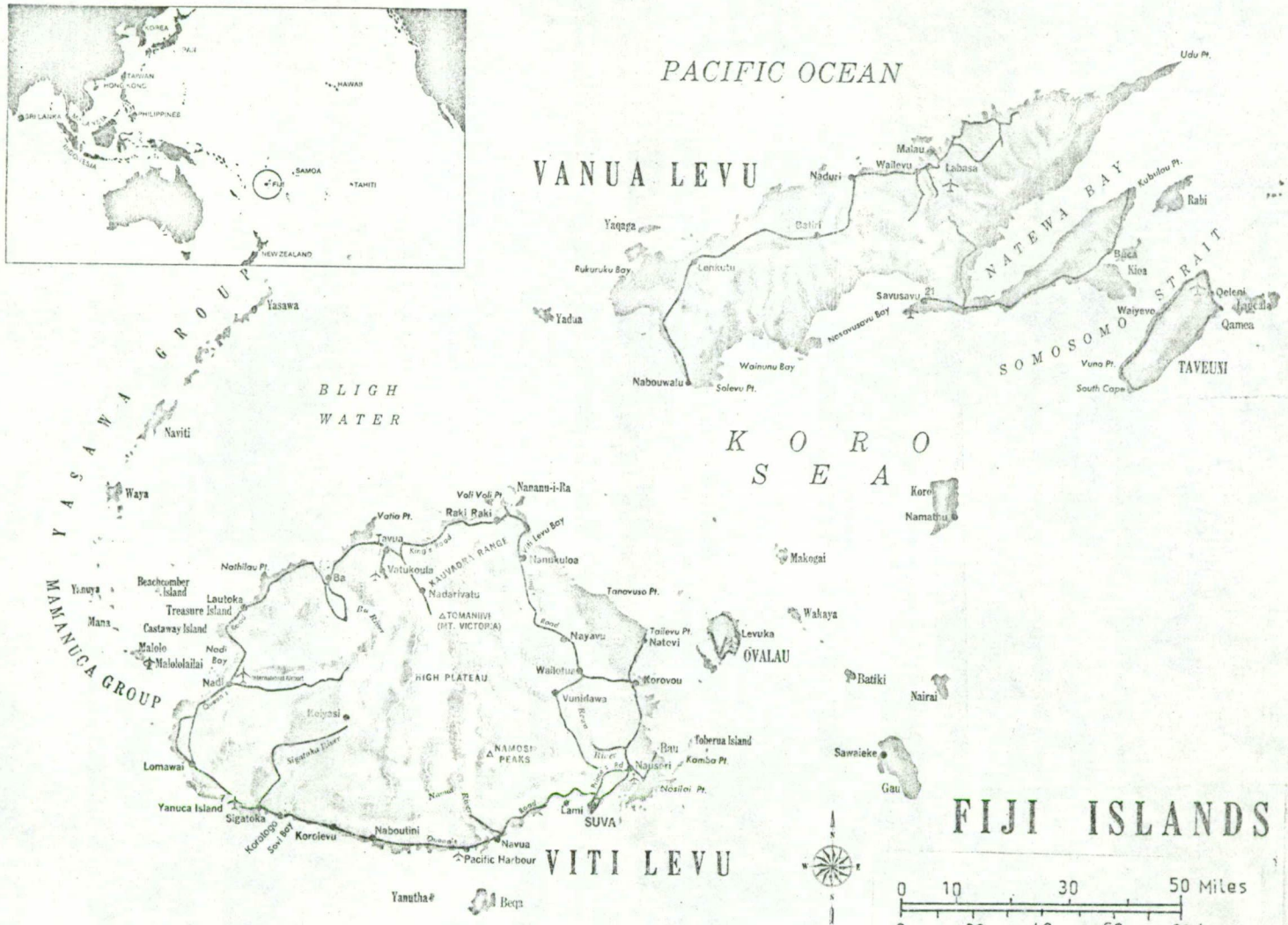

Fig. 1.1 Location map of Fiji Islands

The Vatukoula area receives about 200 cm of rain from November to April and about 50 cm during the rest of the year.

1.2 SCOPE OF THE STUDY

This thesis deals with mineralogical, fluid-inclusion, stable-isotope and thermochemical studies designed to reconstruct the physico-chemical conditions of lode formation in the Emperor deposit.

The project was suggested by Dr. M. Solomon, who visited the mine in 1970 and 1975 and collected nine samples from the mineralized lodes for preliminary studies. All of these samples showed useful fluid-inclusions in vein quartz.

The follow-up field work was completed in two field trips of three weeks each in August, 1975 and September, 1977. On each occasion Dr. Solomon guided the field work for a period about one week.

At the time of our field work the mining activity concentrated mainly on the 166, 1010 and Prince of Wales (P.O.W.) lodes. The lower levels of the mine were inaccessible, and samples from these levels were obtained from Forsythe's (1967) collection at the University of Melbourne. These samples have provided a great deal of valuable information.

The stable-isotope analyses were done at the Institute of Nuclear Sciences, Wellington, New Zealand, under the supervision of Dr. P. Blattner and Dr. B.W. Robinson. A total of seven weeks were spent by the writer at this Institute in November-December, 1976. Most of the analyses were completed during this period except for three carbon-isotope and three sulphur-isotope determinations which were carried out by Dr. Blattner in October, 1978.

1.3 ACKNOWLEDGEMENTS

Grateful thanks are due to Dr. M. Solomon for suggesting this project and for his constant supervision throughout the study,

I am also indebted to the Emperor Gold Mining Company Ltd. for permission to carry out this project. My special thanks are due to Chief Geologists Messrs. R. Horn and J.R. Ekstrom, and other members of the geological staff for useful discussions, and assistance in the field, especially Mr. M. Antonio and Mr. J. Martino.

I am grateful to Mr. P. Rodda of the Geological Survey of Fiji for many useful discussions.

I am grateful to Dr. T.A. Rafter, Director of the Institute of Nuclear Sciences, Wellington, New Zealand, for allowing me to use the facilities for the stable isotope analyses. Supervision and assistance of Drs. P. Blattner and B.W. Robinson during the stable-isotope analyses is gratefully acknowledged. Discussions with Dr. M. Stewart and Dr. J. R. Hulston during my work at the above-mentioned Institute have been of great help. I am also indebted to Mrs. M. Cox for stable isotope determinations on fluid-inclusion and present day meteoric waters.

I am indebted to the members of the staff at the University of Tasmania, especially to Dr. R. Varne and Mr. R. Ford, for their suggestions and comments. My special thanks are due to Dr. J.L. Walshe who introduced me to the thermodynamics of hydrothermal systems and helped in formulating the computer programme for generating the various phase diagrams presented in this study.

I am grateful to my fellow post-graduate students at the University of Tasmania especially Messrs. A. Bush, A. Khwaja, C. Eastoe, J. Foden, B. Griffin, G. Green, P. Collins and D. Patterson for their suggestions and comments.

My special thanks are due to P. Robinson, analyst, for assistance with chemical analyses.

I am also indebted to Mr. D. Nath and his family for their kind hospitality during my visits to Fiji.

The project was financed by a post-graduate scholarship awarded by the University of Tasmania and University research funds. The Emperor Gold Mining Company Ltd. provided accommodation during my stay at Vatukoula and paid the cost of transportation of samples to Hobart.

Finally, for her support, encouragement and patience I am indebted to Munawwar, my wife.

1.4 HISTORY AND PRODUCTION

Gold was discovered near Vatukoula in 1932 by W. Borthwick. This discovery led to intensive prospecting in the following years. A number of prospects were located in virtually the whole of Viti Levu, but only those near Vatukoula proved to be economical. Three companies (The Emperor Gold Mining Company Ltd., Loloma (Fiji) Gold Mines Ltd. and Dolphin Mines Ltd.) started production in 1934 from the lodes exposed near Vatukoula. The latter two companies relinquished their holdings in 1956, leaving the Emporer Gold Mining Company Ltd. as the sole operator.

Until 1942, the mining activity concentrated on the near-surface ore bodies by open cutting. This was followed by underground development. The present mine workings extend to a depth of about 700 m and three shafts, namely Wallace Smith Shaft, Borthwick Shaft and Cayzer Shaft are presently in operation (Fig. 5.1).

Since production started in 1934, the Vatukoula area has produced about 3.6 million troy ounces of gold and about 1.3 million troy ounces of silver (computed from the yearly production of gold and silver from Fiji given in Mineral Year Book, 1950-1978 and from data given in Blatchford, 1953). The present production from the lodes in this area is about 60,000 troy ounces of gold per annum and about about 30,000 troy

ounces of silver per annum. Since 1975 approximately 8000 lbs of tellurium have been extracted each year. The average grade of lodes is about 5 dwt Au per ton, though in the past some lodes gave average grades as high as 33 dwt Au per ton.

1.5 MINING TERMINOLOGY

Lodes are described as steep lode or flatmake depending on whether the average dip exceeds or is less than 45^{o} respectively. Sheeted zones of flatmakes are locally termed "shatter ore-bodies".

Drives generally follow the strike direction of the lodes. Workings parallel to the dip of the lodes are called rises.

Lodes are generally given names such as Crown, Prince of Wales or are referred to by mine co-ordinates, i.e. 2000 North flatmake, 166 flatmake.

The Emperor mine co-ordinate system has its point of origin at the Karoere triangulation station (Fig. 5.1) and has a true north base line. Reduced levels are measured upward from an arbitrary datum. Mine levels are measured downward from the surface. The level interval is approximately 30 m down to No. 6 level, and approximately 40 m to No. 18, the lowermost level.

Chapter 2

A REVIEW OF THE WORLD'S GOLD DEPOSITS

2.1 GENERAL

Production of gold in the non-communist countries in 1977 totalled about 966 tons (Glynn,1978). The principal producing countries were South Africa (70.9%), Canada (5.2%), U.S.A. (3.2%) and New Guinea (2%). The world gold production for 1977 is given in Fig. 2.1.

Gold occurs in many and varied geological environments. Several attempts have been made to classify gold deposits (e.g. Emmons, 1937; Lindgren, 1933; Bateman, 1959; Simons & Printz, 1973; Casadevall, 1976). The classification adopted here is given below:

1. Sedimentary deposits
2. Porphyry-copper deposits
3. Epithermal vein-type deposits, subdivided into
    (a) Au-Ag-Pb-Zn-Cu association
    (b) Au-Ag-Te association
4. Au-quartz deposits.

2.2 SEDIMENTARY DEPOSITS

About 75% of the world gold production comes from sedimentary deposits (Fig. 2.2; Casadevall, 1976). These deposits include placers, palaeoplacers and chemically or biochemically precipitated ores. The largest known deposits are in South Africa. The geology of these deposits has been described by Pretorious (1974, 1976), Saager & Easler (1969) and Koppal & Saager (1973). Other ore deposits of similar type but of less economic importance are the Jacobina mine, Brazil (Bateman,

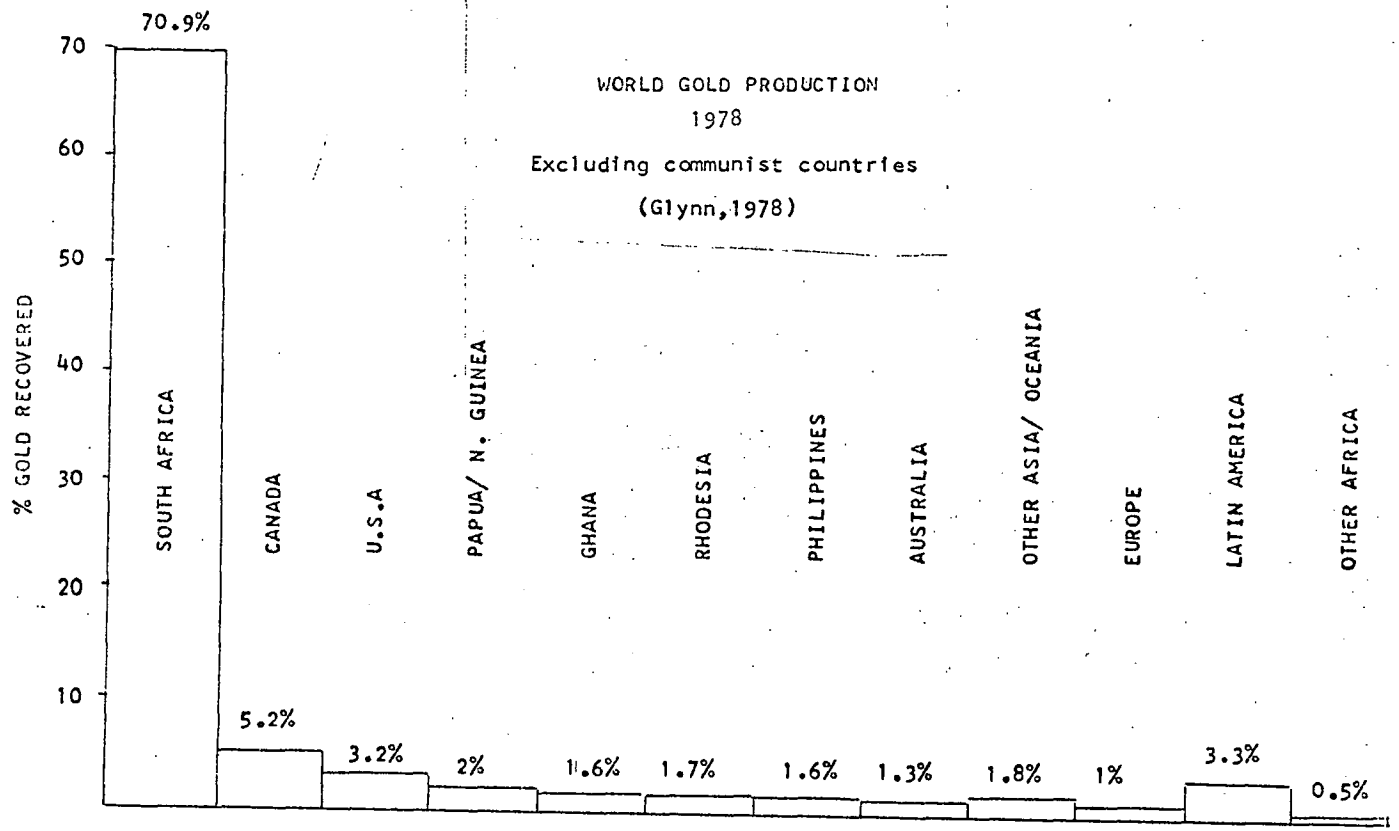

Fig.2.1 World gold production.

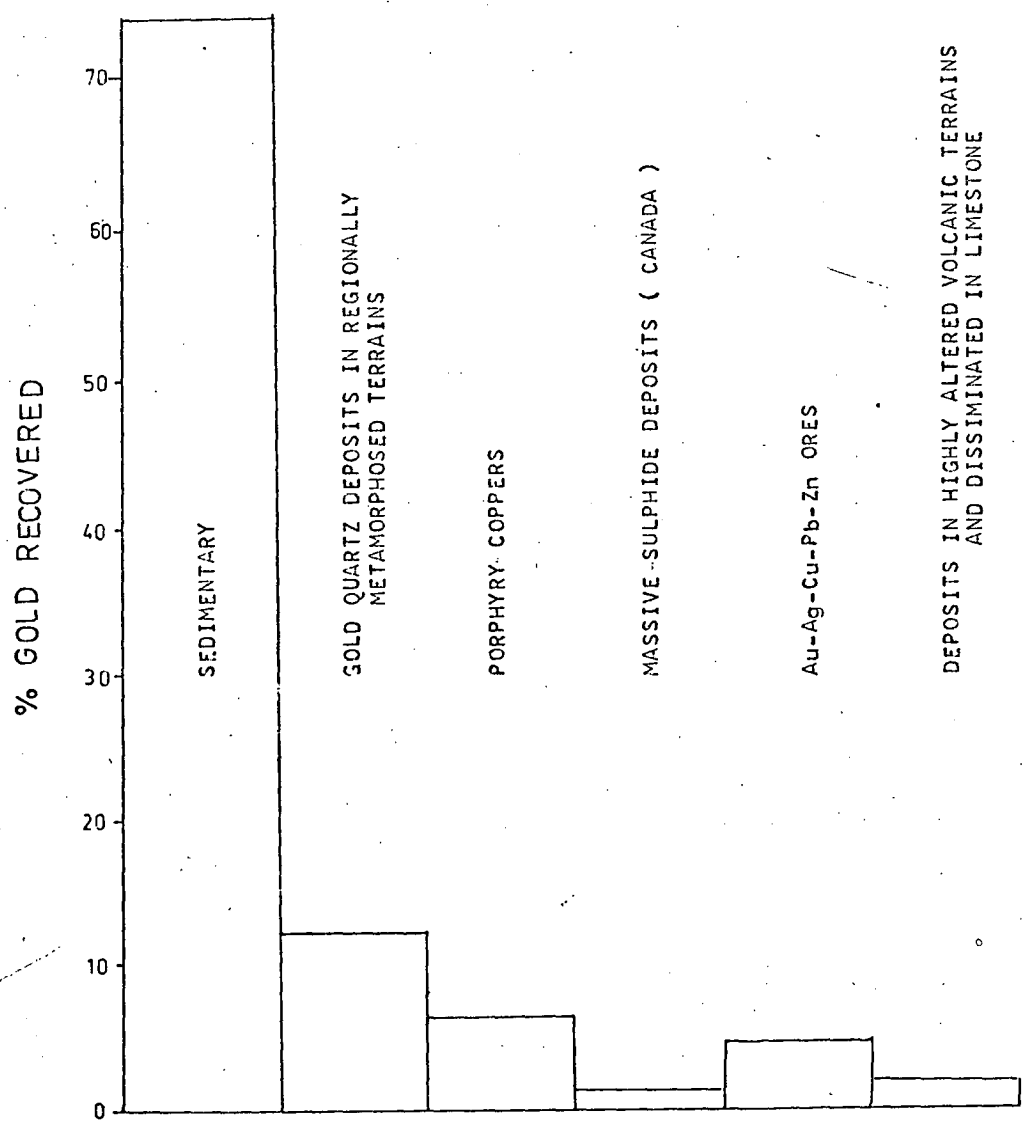

Fig.2.2 Gold production from different types of deposits, after Casadevall (1976).

1958; Cox, 1967; Gross, 1968) and the Tipuani mine, Bolivia (Stoll, 1961). Considerable tonnage has been recovered from placer deposits in the area surrounding the mother lode system of California and the Antioquic area, Colombia (Emmons, 1937).

In the South African deposits gold occurs predominantly in native form in Proterozoic rocks which include conglomerate, quartzite, shale, silty dolomite, dolomitic argillite and algal mats. Gold was probably derived from the mafic and ultramafic volcanics of greenstone belts, transported by rivers and deposited along with the sediments in fluvial fans (Pretorious, 1974, 1976).

2.3 PORPHYRY-COPPER DEPOSITS

The gold associated with porphyry-copper deposits occurs with primary copper sulphides disseminated in granodiorite to monzonite intrusions. In most cases the recovery of gold alone would be uneconomical. The mineralogy of gold in these deposits is not well documented. At Panguna, native gold or electrum is known but most of the gold is probably in solid solutions with copper sulphides (Eastoe, 1979). Since gold is intimately associated with copper ores, it can be assumed that fluids responsible for copper sulphide ores were also responsible for the deposition of gold.

The temperature and salinity of the solutions associated with porphyry-copper deposits have been described in a number of studies. The fluids were generally of high temperatures (300 to 700^{o}C) and had salinity up to 75 wt. % eq. NaCl (Logsdon, 1969; Roedder, 1971; Nash & Theodore, 1971; Nash, 1976; Eastoe, 1978, 1979). The pH of the ore fluids, in most cases, was buffered by the K-feldspar-sericite-quartz assemblage (Meyer & Hemley, 1967; Lowell & Guilbert, 1970). The oxidation state of the fluids can be as high as the hematite-magnetite buffer (Eastoe, 1979).

In the majority of cases the solutions which deposited copper sulphides were predominantly of magmatic origin (Taylor, 1974; Sheppard & Taylor, 1974; Batchelor, 1976; Ford, 1976; Eastoe, 1979). Ore constituents were probably transported mostly as chloride complexes and decrease in temperature was probably the major cause of ore-mineral precipitation (Eastoe, 1979).

2.4 EPITHERMAL VEIN-TYPE DEPOSITS

The term "epithermal" was used by Lindgren (1933) for hydrothermal deposits formed at relatively shallow depth and low temperature. White (1955, 1967, 1974) summarised the geochemistry of a number of these deposits and concluded that they were formed by solutions similar to those in present-day geothermal systems. They are generally associated with mafic to intermediate volcanic rocks and occur in the immediate vicinity of the volcanic centres. Very little gold is produced at present from these deposits and it appears unlikely that they will be a significant factor in future gold production.

The space-time distribution of these deposits is very sharply defined and three major categories can be recognised.

(i) Circum-Pacific Belt: The largest group of deposits occurs in the Tertiary volcanics surrounding the Pacific Ocean. Some of the notable examples are the Emperor, Fiji (this study); Hauraki, New Zealand (Williams, 1974); Tui, New Zealand (Robinson, 1974); Acupan, Philippines (Callow & Worley, 1965; Bryner, 1969); Redjang-Lebong, Indonesia (Emmons. 1937); Teine, Japan (Watanabe, 1952); Yatani, Japan (Hattori, 1975); several deposits in the southwestern U.S.A. (Kelly & Goddard, 1968; Nash, 1972; O'Neil *et al.*, 1973; Casadevall, 1976; Casadevall & Ohmoto, 1977; Barton *et al.*, 1977); Finlandia, Peru (Kamilli & Ohmoto, 1977).

(ii) Carpathian and Transylvanian Alps: These deposits are similar to those in group (i) and include some of the classic occurrences described in a number of text books. Almost all of these deposits have now been exhausted. Some important occurrences are Mazarron, Spain (Emmons, 1937); Schmnitz and Kremnitz, Hungary (Beyschlag *et al.*, 1916); Nagyag, Rumania (Emmons, 1937); Hanes, Fata Ball, Muncaceasca, Bradisor, Stanjia, Baia Sprie and Donrogea in Rumania (Borcos, 1966; Borcos & Manilici, 1965).

(iii) Precambrian Greenstone Belts: Considerable tonnage is being produced from deposits of this group. Many of these deposits have undergone metamorphism since deposition. Some important examples are Kalgoorlie, Australia (Markham, 1960; Woodall, 1965; Finucane, 1965; Hall & Baker, 1965; Ward, 1965; Bartram & McCall, 1971; Nickel, 1977; Golding, 1978); Vubachikwe, Rhodesia (Fripp, 1976); Moro Velho, Brazil (Emmons, 1937; Gair, 1962); Mahd Adh Dhab, Saudi Arabia (Worl, 1978a, 1978b); Ashanti, Ghana (Emmons, 1937); Kolar, India (Narayanaswami *et al.*, 1960); deposits in the Yellowknife area, Canada (Boyle, 1955, 1960), and the Kirkland Lake area, Canada (Thompson, 1949; Goodwin, 1965).

The host rocks associated with these deposits are mainly basalt and andesite, more felsic types being less frequent. In most cases the rocks show regional propylitic alteration. In many cases propylitization appears to have been the earliest phase of alteration followed by sericitization and silicification (Burbank, 1960).

In most cases the ores are open-space fillings, though there is commonly some replacement of the vein wall by ore minerals. Notable exceptions are the disseminated and replacement deposits of Nevada and Idaho in western U.S.A. (Roberts *et al.*, 1971).

Gold occurs either in native form or as gold-silver tellurides. Amongst the Precambrian deposits, those situated in high grade metamorphic terrains contain native gold and traces of tellurides while deposits in low grade metamorphic terrains carry significant proportions of Au-tellurides. At Kalgoorlie, for example, the metamorphic grade ranges from low to middle greenschist facies (Binns *et al.*, 1976). The deposits in this area contain abundant tellurides. On the other hand the Kolar gold field of India, situated in volcanic rocks which have been metamorphosed to amphibolite facies (Naqvi, 1976), contains no tellurides.

Experimental data of Markham (1960), Cabri (1965) and Kracek *et al.* (1966) show that an assemblage containing sylvanite, petzite and hessite (the most common of the gold-silver tellurides) will melt at temperatures between 300 and 400°C at atmospheric pressure. Presence of other constituents such as sulphur, selenium, water and CO_2 would probably not change these temperatures significantly (Markham, 1960; Cabri, 1965). Increase in pressure would probably raise the melting temperatures by 15 to 20°C per 1000 atmospheres (Cabri, 1965).

The temperature and pressure limits of greenschist facies metamorphism are 250 to 450°C, and 2 to 9 kb (Turner, 1968). It is suggested here that gold-silver tellurides are probably stable within the limits of the greenschist facies but at higher grades (e.g. amphibolite facies) breakdown of tellurides occurs and tellurium is lost from the system.

Many of the previous workers have placed the Precambrian deposits in the "hypothermal" class (Lindgren, 1933; Emmons, 1937; Park & McDiarmid, 1964). It is suggested that a great number of these occurrences are "epithermal" type whose character has been modified by metamorphism and complex tectonic history.

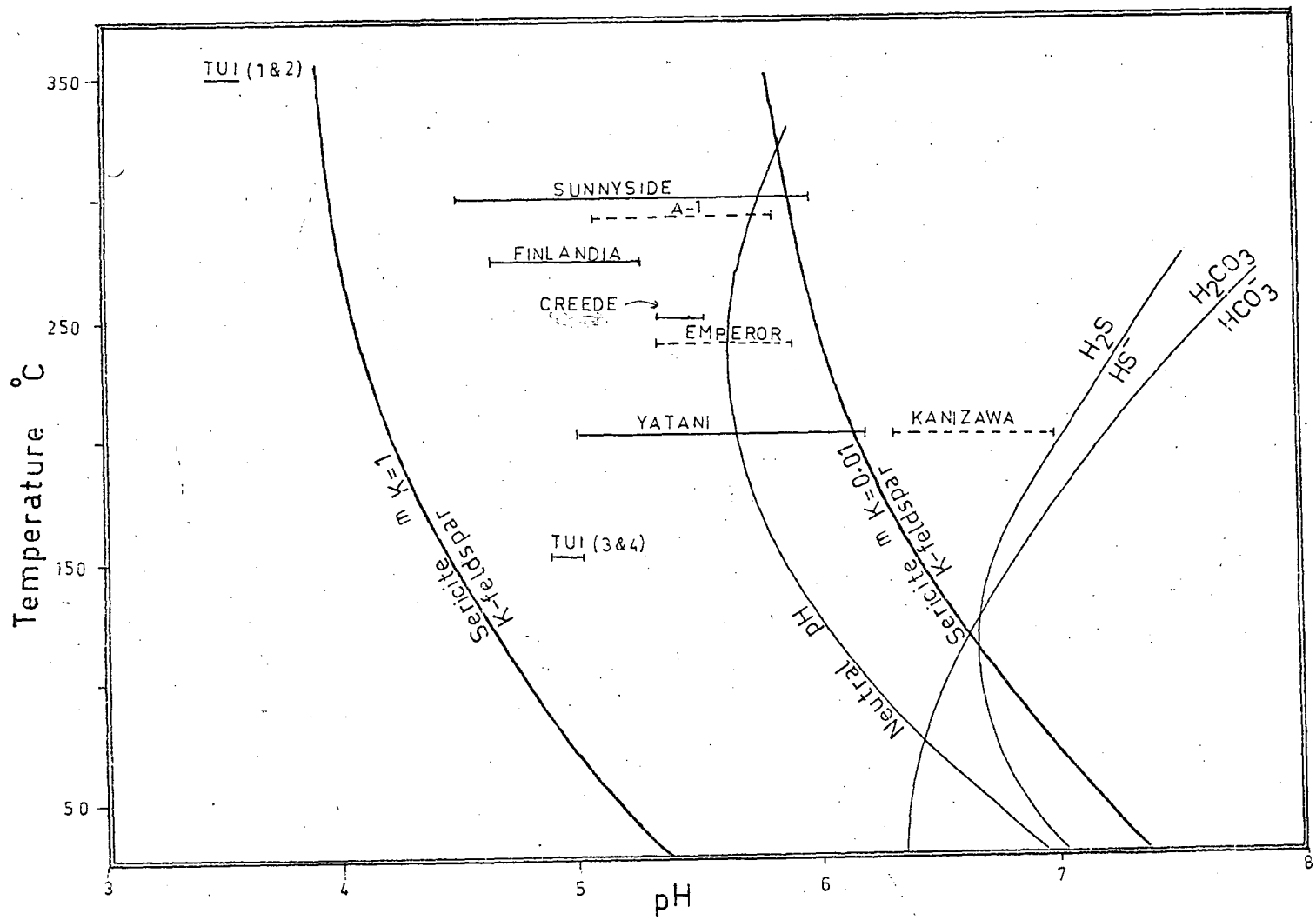

Fig. 2.3 T-pH diagram showing the regions of ore-fluids stability for hydrothermal gold deposits. Sources of data are given in Table 2.1. Mineral and aqueous species boundaries are based on the data given in Appendix E-2.

(a) Au-Ag-Pb-Zn-Cu association

These deposits are mined for one or more of the base metals, but both gold and silver occur in significant proportions. Notable examples of this association, on which a certain amount of geochemical data is available, are Sunnyside (Casadevall, 1976; Casadevall & Ohmoto, 1977), OH vein (Barton *et al.*, 1977; Roedder, 1960), Tui (Robinson, 1974), Yatani (Hattori, 1975), Mayflower (Nash, 1973), Copper Canyon (Nash & Theodore, 1971), and Finlandia (Kamilli & Ohmoto, 1977).

The majority of these deposits formed at temperatures between 170 and 400°C (Table 2.1) and the salinity of the ore-fluids ranged from 0 to 15 wt. % eq. NaCl. Fluid inclusions evidence indicates that at the Sunnyside mine, the OH vein, and at Finlandia , the ore fluids were close to the boiling curve. The pH of the ore-fluids is generally slightly acid (Fig. 2.3; Table 2.1), apparently rather more acid than the base-metal deficient Au-Ag-Te deposits.

The minerals present include native gold, gold-silver tellurides, pyrite, sphalerite, galena, chalcopyrite, tetrahedrite-tennantite, rare bornite. The common gangue minerals are quartz, calcite, dolomite, sericite, rare adularia, rhodochrosite, rhodonite, hematite, barite, anhydrite and rare magnetite and pyrrhotite.

Stable isotope studies indicate that in most cases the ore-fluids were predominantly heated meteoric waters. The sulphur and metals in these deposits were probably derived from the surrounding rocks.

Experimental data of Henley (1973) and Seward (1973) shows that a significant amount of gold can be transported as gold-chloride and gold-sulphur complexes. Casadevall (1976) and Casadevall & Ohmoto (1977) suggested that in Sunnyside ore-fluid, gold chloride complexes were dominant. At Yatani, on the other hand, gold was transported mainly as

Table 2.1

Temperature, salinity, pressure and pH of gold ore forming fluids.

Deposit	Temperature range °C	Salinity range wt.% eq. NaCl	Pressure range bars	pH range	Reference
(A) Au-Ag-Pb-Cu-Zn association					
Sunnyside, U.S.A.	170-320	0.0-3.6	110-220	4.3-5.9	Casadevall & Ohmoto, 1977; Casadevall, 1976.
OH vein, U.S.A.	190-268	6-15	50	5.4	Barton *et al.*, 1977; Roedder, 1960a
Mayflower, U.S.A.	220-300	0.3-11	90	-	Nash, 1973.
Idardo, U.S.A.					
(a) Veins	249-315	0.1-7.9	-	-	Nash, 1975.
(b) Replacements	204-319	0.2-11.2	-	-	" "
(c) Pipes	216-318	0.2-1.6	-	-	" "
Tui, New Zealand	280-400	-	-	3.5	Robinson, 1974.
Yatani, Japan	200-250	0.2-0.5	-	5-6	Hattori, 1975.
Finlandia vein, Peau	140-270	2-7	74	4.7-5.5	Kamilli & Ohmoto, 1977.
(B) Au-Ag-Te association					
Gold Acres, U.S.A.	160-265	5.4-7.3	-	6-6.5*	Nash, 1972.
Round Mt., U.S.A.	250-260	0.2-1.4	-	6*	" "
Aurora, U.S.A.	220-255	0.2-1.7	-	6-6.3*	" "
Manhattan, U.S.A.	210-235	0.2-1.9	-	6.2*	" "
Tenmile Dt., U.S.A.	245-330	0.4-7.3	-	6*	" "
Baia Sprie, Rumania	205-290	-	-	6*	Borcos & Manilici, 1965
Hanes, Rumania	253-346	-	-	6*	" " ; Borcos, 1966
Dobrogea, Rumania	112-292	-	-	6-6.2*	Borcos & Manilici, 1965

Table 2.1 cont.

Deposit	Temperature range °C	Salinity range wt.% eq. NaCl	Pressure range bars	pH range	Reference
Fata Baii, Rumania	268-318	-	-	6*	Borcos, 1966.
Muncacesca, Rumania	250-346	-	-	6*	" "
Bradisor, Rumania	224-347	-	-	6*	" "
Stanija, Rumania	240-342	-	-	6*	" "
Emperor, Fiji	200-317	4.6-7.1	6-32	5-6	this study
Kanizawa, Japan	200-250	0.2-0.5	-	6-7	Hattori, 1975.
(C) Gold-quartz veins					
Al mine, Australia	295-385	1-9	200-1260	5-6	Jahnke, 1976.
Irokinda, U.S.S.R.	200-400	5-50	820-1100	-	Lyakhov & Popivnyak, 1978.
Lebedinoye, U.S.S.R.	110-270?	-	-	-	Koltun, 1965.
Kochkar, U.S.S.R.	110-230	-	-	-	" "
? , U.S.S.R.	195-450	-	75-1250	-	Andrusenko *et al.*, 1978.
Berezovskoye, U.S.S.R.	80-410	31.49	600	-	Koltun, 1965.

* Calculated assuming K-feldspar (adularia) and sericite occur in equilibrium and potassium concentration is 0.01 moles/kg H_2O. Adularia and sericite occur in all of these deposits and low salinity probably corresponds to low potassium concentrations. No salinity data is available for the Rumanian deposits and it is assumed that they are similar to the deposits in the U.S.A.

gold-sulphur complexes (Hattori, 1975). No data, experimental or thermodynamic, are available for gold-carbonate and gold-tellurium complexes, which may contribute significantly toward gold solubility.

(b) Au-Ag-Te association

In these deposits, the base-metal sulphides are rare and the ore minerals are essentially native gold and gold-silver tellurides. Notable examples of this association for which geochemical data is available, are the Emperor Mine (this study), Gold Acres, Jaferson, Round Mountains, Auroha, Manhattan (Nash, 1972), several deposits in the Jamestown district (Kelly & Goddard, 1968), Bala Sprie, Hanes, Dobrogea, Fata Baii, Munesceascia, Bradisor and Stanija (Borcos, 1966; Borcos & Manilici, 1965).

The majority of these deposits are formed at temperatures between 200 and 300^{o}C (Table 2.1) and salinity of the ore-fluids ranged from 0 to 8 wt. % eq. NaCl (Table 2.1). Fluid-inclusions at the Emperor mine indicate the fluid was boiling, which suggests a pressure between 6 and 32 bars (this study). The pH of the ore-fluids at the Emperor mine was near neutral (Fig. 2.3). The pH of the ore-fluids at the other deposits is not known, but occurrences of adularia and sericite in the mineral assemblages of these deposits together with the low salinity (and hence low K concentrations in the ore-fluids), suggest near-neutral to slightly alkaline pH values (Table 2.1).

The most common minerals in this association are native gold, gold-silver tellurides, and native tellurium. Amongst the sulphides, pyrite, arsenopyrite, marcasite, sphalerite, galena, chalcopyrite, and tetrahedrite-tennantite are common. The common gangue minerals are quartz, sericite, adularia, calcite, dolomite, ankerite, magnetite, hematite and roscoelite.

Stable-isotope studies on a number of Tertiary deposits indicate that the ore-fluids were predominantly heated meteoric waters and that the ore constituents were probably derived from the surrounding rocks O'Neil & Silberman, 1974; this study).

The remarks made above concerning the solubility of gold are valid for the deposits of this association also. However the mineral assemblages indicate pH values slightly greater than those of the base-metal-rich deposits. This suggests that the gold-sulphur complexes may have played a significant role in gold transportation.

Mineralogical and fluid-inclusion evidence indicates that a decrease in temperature and/or an increase in pH and fO_2 may be the causes of precipitation of the ore minerals.

2.5 GOLD-QUARTZ VEINS

In these deposits gold generally occurs in native form and is closely associated with quartz and iron sulphides. These deposits are found in virtually every continent and are related to granite and granodiorite intrusives. Ore generally occurs as narrow streaks within the intrusions and alteration effects are not pronounced.

Amongst the examples of which some information is available about the geochemistry of the ore-fluids are the Al mine, Victoria, Australia (Jahnke, 1976), Irokinda, Russia (Lyakhov *et al.*, 1978), Darasun, Russia (Sakkarova, 1969), Kara, Russia (Kolosova & Onischuk, 1971), Lebedinoye Russia (Koltun, 1965), and Kochkar, Russia (Anufriyev *et al.*, 1974).

Andrusenko *et al.* (1978) described a deposit (possibly from the Urals) in which both temperature and pressure decreased with time resulting in distinct chemical changes. The composition changed from gold-tungsten (290 to 350°C) to gold-molybdenum (200 to 450°C) to gold-sulphide (200 to 340°C) to gold-antimony (195 to 350°C) to antimony-

carbonate (105 to 270°C). The pressure changed from 1215 to 175 atmospheres.

Homogenisation temperatures of the fluid-inclusions in the productive veins ranged between 110 to 450°C, pressures ranged from 75 to 1260 bars, and salinity ranged from 1 to 50 wt. % eq. NaCl (Table 2.1). Many deposits contain a separate CO_2 phase in the fluid-inclusions and in a number of occurrences solid phases (halite and sylvite) are observed. The pH of the ore-fluids at Al mine was between 5 and 6 (Jahnke, 1976).

The common minerals present in these deposits are native gold, pyrite, arsenopyrite, pyrrhotite, magnetite, chalcopyrite, graphite, quartz, sericite, chlorite, and various carbonates. A few deposits contain tourmaline, scheelite and molybdenite. In a deposit in Ust-Kara area, Russia, native gold is associated with magnetite which is the most dominant gangue mineral (Kolosova & Ynischuk, 1971). Gold-silver tellurides have been noted in some occurrences (Sakkarova, 1969).

The remarks concerning solubility of gold made in the preceding section apply also for this class of deposit. The possible role of gold-carbonate complexes is, however, worth emphasising because CO_2 occurs in the fluid inclusions in significant concentrations.

Stable-isotope data is not available for this class of deposit and the origin of ore solutions and ore constituents is uncertain.

Chapter 3

GOLD, SILVER AND TELLURIUM ABUNDANCES IN IGNEOUS ROCKS, MINERALS AND NATURAL WATERS

3.1 GENERAL

The common association of gold-silver telluride deposits with mafic and intermediate volcanics has been described in Chapter 2. Stable-isotope evidence shows that a number of these deposits were formed from hydrothermal solutions of meteoric origin (e.g. O'Neil *et al.*, 1973; O'Neil & Silberman, 1974; Casadevall, 1976; Casadevall & Ohmoto, 1977; Taylor, 1974; White, 1974; Kamilli & Ohmoto, 1977; this study). It is possible that the ore constituents were leached from the country rocks. The purpose of this chapter is to summarise available data on gold, silver and tellurium abundances.

3.2 GOLD ABUNDANCES

A number of studies of gold abundances have been made in recent years (e.g. Shcherbakov & Perezhogin, 1964; Voskresenskaya & Zvereva, 1968; Dalvetov & Dzhakshibayev, 1970; Gottfried *et al.*, 1972; Tilling *et al.*, 1973).

Amongst the plutonic rocks, granite and quartz monzonite have an average gold content of about 0.75 ppb, and gabbro an average of about 6.5 ppb. There is a general tendency for the gold content to decrease from mafic to felsic rocks. This tendency is also reflected in the volcanic rocks but significant differences are observed in the gold contents of basaltic associations from different tectonic settings. On an average the circum-Pacific basalts (average 5.5 ppb Au) have more gold than the continental tholeiites (average 3.25 ppb Au). The alkali basalts and oceanic tholeiites average about 0.5 ppb Au.

The calc-alkalic andesites average about 4.5 ppb Au and alkalic andesites about 3 ppb Au. Rhyolite, rhyodacite and dacites average about 1 ppb Au.

Published data on common rock-forming minerals indicate that mafic varieties (magnetite average 4 ppb, amphibole 2 ppb, biotite 3 ppb and pyroxene 10 ppb Au) tend to be higher in gold than the felsic varieties (feldspar average 0.4 ppb and quartz 1 ppb Au).

After a comprehensive survey of the available data on gold abundances, Tilling *et al.* (1973) concluded that gold is not concentrated in the residual silicate melt during the differentiation of calc-alkaline magma.

Amongst natural waters, sea water averages 0.01 ppb Au (Shutz & Turekian, 1965). Surface water from Colorado Front Range averages 0.022 ppb Au (Gosling *et al.*, 1971), but this value is from a gold-rich area and can not be taken as average for fresh waters. Turekian (1969) gave an average value of about 0.002 ppb Au for surface waters. Geothermal waters from the Taupo volcanic zone, New Zealand, contain about 0.04 ppb Au (Weissberg, 1969) and the geothermal waters at Yellowstone, U.S.A., contain between 0.01 and 0.1 ppb Au (Gottfried *et al.*, 1972). Both these geothermal waters are precipitating gold-rich siliceous sinters. In the Taupo volcanic zone these auriferous sinters contain from 0.001 to 85 ppm Au (Weissberg, 1969; Ewers & Keays, 1977) and at Yellowstone they contain from 0.0003 to 6 ppm Au (Gottfried *et al.*, 1972).

3.3 SILVER ABUNDANCES

Vinogradov (1962) gave the following estimates of silver in the major groups of igneous rocks:

Ultramafic rocks	50 ppb Ag
Mafic rocks	100 ppb Ag
Intermediate rocks	70 ppb Ag
Felsic rocks	50 ppb Ag

Turekian & Wedepohl (1961) gave similar results. Boyle (1968) did not find any striking correlation between the silica content and silver. Flanagan (1969), in compiling analyses of the standard reference rocks, showed that silver is highest in andesite (60 to 110 ppb Ag), lowest in ultramafic rocks (5 to 53 ppb Ag) and intermediate in basalt (20 to 81 ppb Ag). Amongst the plutonic rocks, granites have the lowest silver values (40 to 53 ppb) and granodiorite, the highest (20 to 100 ppb Ag).

Studies of the Skaergaard intrusion (Vincent & Adams, unpublished data in Frueh & Vincent, 1974) indicate no systematic variations in the silver concentration with progressive fractionation.

Greenland & Fones (1971) investigated the distribution of silver at intervals along a drill core in the Great Lake dolerite sheet of Tasmania. The average silver content is given as 86 ppb. The authors point to a steady increase in the silver concentration in rocks with fractionation. This is in contrast to that in some of the Siberian "traps" investigated by Nesterenko *et al.* (1969) where silver was concentrated in the most mafic rocks and its abundance closely correlated with the presence of sulphides.

Boyle (1968) compiled the available data on the silver contents of a number of silicate minerals. It appears that silver is concentrated in mafic minerals (olivine 1000 ppb, hornblende 850 ppb, chlorite 950 ppb,

biotite 660 ppb Ag). Quartz, feldspar and muscovite have less than 50 ppb Ag. Albite has an average silver content of about 290 ppb. Ag replaces Na, Fe and Ca in silicates (Boyle, 1968; Taylor, 1965).

The silver content of sea water ranges from 0.13 to 0.69 ppb (Shutz & Turekian, 1965) and that of stream water averages about 0.3 ppb (Kharkar *et al.*, 1968). The geothermal water from Taupo volcanic zone, New Zealand, contain about 0.7 ppb Ag and are precipitating siliceous crusts containing up to 350 ppm Ag (Weissberg, 1969; Ewers & Keays, 1977). Concentrated brines from the Salton Sea geothermal area contain between 0.8 and 2 ppm Ag. They are precipitating siliceous scales containing up to 6% Ag (Skinner *et al.*, 1967).

3.4 TELLURIUM ABUNDANCES

Vinogradov (1962) estimated the average crustal abundance of tellurium to be about 0.001 ppm. Sindeeva (1964) analysed a large number of rocks for tellurium but the tellurium contents were always below the detection limit (0.01 ppm). Ganapathy *et al.* (1970) analysed a pyroxene gabbro from the Adirondack intrusive and obtained a value of 10 ppb.

Beaty & Manuel (1973) analysed a variety of rocks by atomic absorption methods and reported the following results:

Ultrabasic rocks	
Peridotite	8 ppb
Dunite	15 ppb
Mafic rocks	
Basalt	88-154 ppb (2 analyses)
Andesite	16 ppb
Gabbro	58-70 ppb (2 analyses)
Felsic rocks	
Syenite	74-82 ppb (2 analyses)
Granodiorite	20 ppb
Granite	132-210 ppb (2 analyses)

Sedimentary rocks

Limestone	1009-1726 ppb (2 analyses)
Shale	42-789 ppb (2 analyses)
Sandstone	26-28 ppb (2 analyses)

More recently Golding (1978) analysed the unmineralized volcanic and sedimentary rocks around the Kalgoorlie gold field, Western Australia, by neutron-activation methods. She obtained the following results:

Serpentinite	15-220 ppb	(2 analyses)
Basalt	41-33 ppb	(2 analyses)
Dolerite	3-50 ppb	(16 analyses)
Black shale	380-4100 ppb	(3 analyses)
Calcareous sediments	2500 ppb	(1 analysis)
Cherty sediments	2200-16000 ppb	(2 analyses)

The sedimentary rocks contain pyrite and other sulphides and the higher tellurium concentration may be related to sulphides. The sedimentary rocks are interbedded with volcanics and are probably derived from them.

No analysis is available for the tellurium content of sea water, Leutwein (1974) analysed the surface water from the Elbe River near Hamburg, Germany, and found 0.05 ppm Te.

Sinters from the Taupo geothermal area, New Zealand, contain between 0.06 and 0.18 ppm tellurium (Ewers & Keays, 1977), but the tellurium concentration in the geothermal waters precipitating these sinters is not known.

Chapter 4

GEOLOGY

4.1 GENERAL

Fiji comprises more than three hundred islands situated between latitudes 16°S and 21°S and longitudes 177°E and 178°E. Suva, the capital city, is located on the southeast coast of Viti Levu, the largest island of the group.

There are a number of short reports and notes describing the geology and lithology of the various rock units exposed on the island of Viti Levu. Wichmann (1882) reported on many of the volcanic and plutonic rock types and metallic mineralization, and Brock (1924) named different rock formations. Ladd (1934) defined formations, and after studying fossils systematically throughout the island, concluded that most of the rocks of Viti Levu were Tertiary. Shackleton (1936) compiled a general reconnaissance map of the island. Phillips (1965) revised the geological map and arranged the various formations into Groups. Rodda (1967) elaborated Phillip's nomenclature and compiled a detailed geological map of the island at the scale of 1:500,000 (Fig. 4.1). Ibbotson (1967) mapped the area around the Tavua caldera and described the petrology of the various rock types.

The area around the Emperor gold mine has been the subject of detailed mapping and several petrological studies. Blatchford (1953) described the geology and lode structure at the Tavua gold field. M. Cohen (1962) described the petrology of the altered rocks and E.M. Cohen (1962) revised the geology and described the lode structure. Denholm (1967a, 1967b, 1967c) described the lode structures and the controls of mineralization.

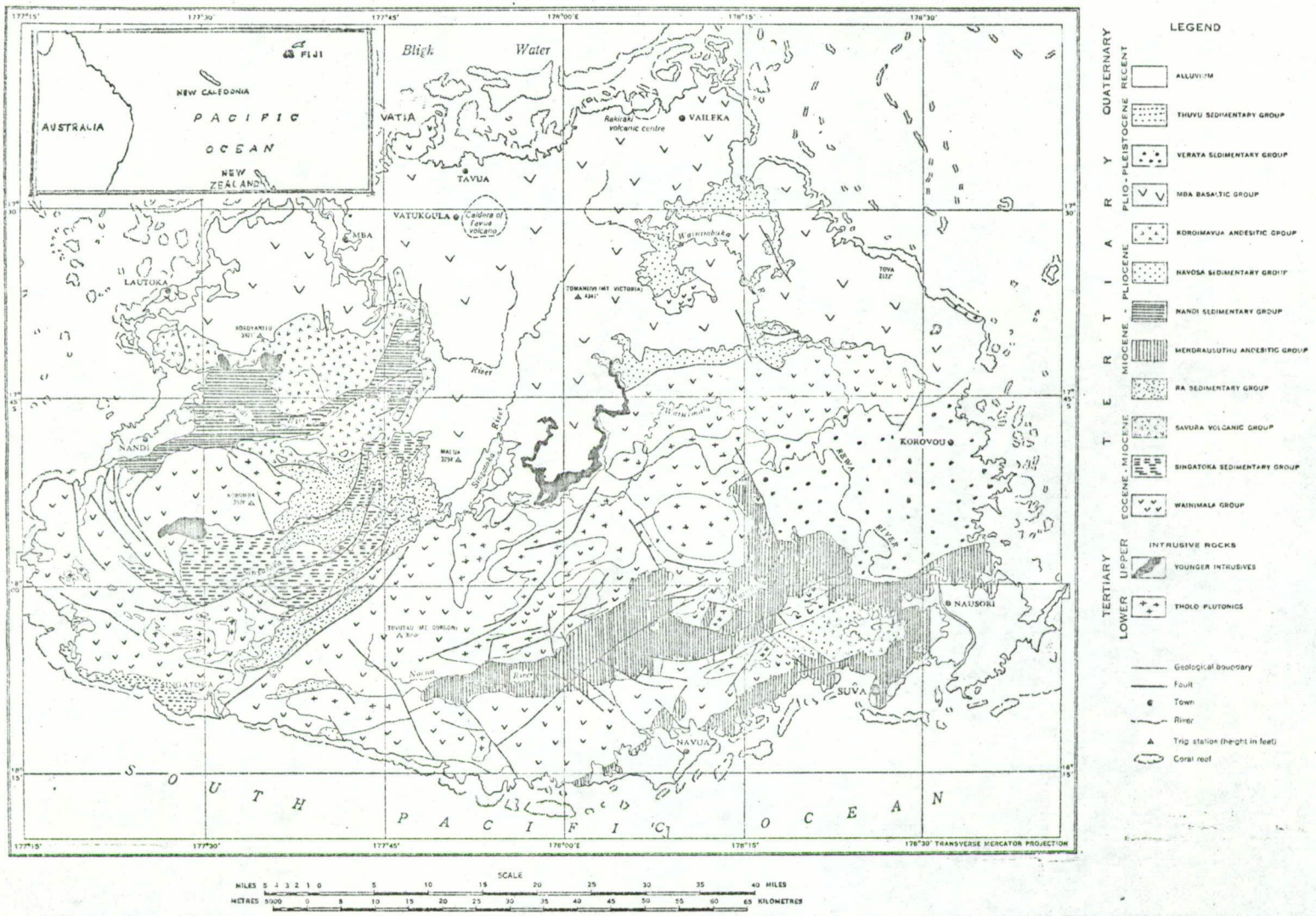

Fig. 4.1 Geological map of Viti Levu, after Rodda(1967)

4.2 OUTLINE OF THE GEOLOGY OF VITI LEVU

The oldest known rocks exposed on Viti Levu belong to the Wainimala Group. They are exposed in the southern part of the island (Fig. 4.1). On palaeontological evidence, Cole (1960) assigned an upper Eocene to lower Oligocene age to these rocks (Table 4.1). They are predominantly volcanic in origin and consist of andesite, basalt, volcanic conglomerates, tuffs, pillow lavas and pillow breccias. Minor sandstone and limestone beds are observed towards the top of the succession. The Wainimala rocks are generally metamorphosed to greenschist facies.

The lower units of the Wainimala Group are intruded by plutons of the Tholo Plutonic Suite. The stocks range from olivine gabbro to biotite tonalite and trondhjemite. Radiometric dating (Rodda *et al.*, 1967) suggests that there are at least two distinct periods of emplacement, one from 50 to 30 m.y. (represented by the stocks southeast of Nandi), and the other taking place about 10 m.y. ago and represented by most of the other stocks.

In southwestern Viti Levu, the Wainimala rocks are conformably overlain by the Singatoka Sedimentary Group. This group is predominantly sedimentary in origin and consists of sandstone, mudstone and limestone. The age of these rocks is uncertain.

In southeastern Viti Levu, the Wainimala rocks are overlain by the Sauvra Volcanic Group. The most common rock types of this group are andesitic conglomerate and breccia, but pillow lava and pillow breccia also occur within the sequence. The age of this Group is uncertain.

In the northeastern part of the island, the Wainimala and possibly Singatoka rocks are unconformably overlain by the Ra Sedimentary Group. This group is predominantly sedimentary in origin and consists of conglomerate, sandstone, mudstone and limestone. Some pyritic beds have been observed. Palaeontological evidence suggests a late Miocene age for this group (Rodda, 1967).

Table 4.1

Stratigraphic succession, Viti Levu Island

Compiled after Rodda (1967)

Age	Group name	Lithological description
Pliocene-Pleistocene	Thuvu Sedimentary Group	Marl and limestone
	Verata Sedimentary Group	Sandstone
	Mba Volcanic Group	Basalt, andesite, tuff and conglomerate, volcanic greywacke
Miocene-Pliocene	Koroimavua Andesitic Group	Andesite with minor sedimentary beds
	Navosa Sedimentary Group	Sandstone, mudstone with minor andesite flows
	Nandi Sedimentary Group	Conglomerate, marl and limestone with minor andesite flows
	Mendrausuthu Andesitic Group	Andesite, volcanic breccia, conglomerate
	Ra Sedimentary Group	Sandstone, mudstone with minor limestone
Eocene-Miocene	Suvra Volcanic Group	Andesitic conglomerate and breccia
	Singatoka Sedimentary Group	Sandstone, mudstone with minor limestone
	Tholo Plutonic Group	Olivine gabbro, tonalite
	Wainimala Group	Spilite, keratophyre, conglomerate and minor limestone

In southwestern Viti Levu, the rocks of the Wainimala Group and the Tholo Plutonic Suite are overlain by the Mendrausuthu Andesitic Group. This group consists of andesitic lavas, volcanic breccia, conglomerate and tuff. Towards the top of the succession sandstone, mudstone, marl, and limestone are common. Palaeontological evidence suggests an upper Miocene age for this group (Ibbotson, 1960).

In northeastern Viti Levu, the rocks of the Singatoka Sedimentary Group are overlain by the Nandi Sedimentary Group. This group consists of conglomerate, marl and limestone, but andesitic rocks occur in many places. This group has been described under Suva Series by Rickard (1963), who has shown them to continue beneath the Mba volcanics. Their age is uncertain.

The Nandi rocks are unconformably overlain by the Koroimavua Andesitic Group, which in turn is overlain by the rocks of the Mba Volcanic Group. The rocks of the Koroimavua Andesitic Group have been radiometrically dated as 4.8 to 5.3 m.y. old (McDougall, 1963). They are predominantly andesitic flows grading into sandstones towards the southeast.

The Singatoka rocks are overlain by the rocks of the Navosa Sedimentary Group. The rocks include polymict conglomerate and sandstone, with limestone and mudstone being more common in the upper part of the succession. Their age is uncertain.

The northern half of Viti Levu is covered by the rocks of the Mba Volcanic Group. This group includes widespread basalt and andesite as well as sedimentary rocks. The basalt and andesite are the host rocks of the gold mineralization at the Emperor mine. The volcanic activity during Mba time took place from a number of centres, and four main volcanic centres and several minor vents have been recognised. The rocks range from olivine basalt to trachyandesite. The sedimentary rocks belonging to this group are of two types:-

(a) minor lenses of volcanic sandstone and grit within the volcanic sequence;

(b) thick sequences of volcanoclastic greywacke, mudstone and sandstone, flanking the basaltic rocks to the south, east and west.

The second type has been included under the Vatukoro Greywacke Formation by Rodda (in press). These rocks probably continue beneath the volcanics in the Emperor mine area (Rodda, pers. comm., 1977). They include rather thinly bedded calcareous greywacke, sandstone, siltstone, mudstone, marl and limestone (Plate 4.1). Field and laboratory investigations of these rocks indicate that the majority have significant carbonate content (in some cases up to 20%), but the rocks exposed to the east of the Emperor mine are generally less calcareous. The common minerals observed are quartz, chlorite, carbonates, relicts of unaltered pyroxene and plagioclase. Carbonate usually occurs in the form of calcareous fossils, but in some cases calcareous cement is observed. Nine samples were analysed for major and trace elements by XRF methods during the course of this study (Appendix C.4). The sample locations are given in Appendix A-2. The chemical composition of these rocks is similar to that of altered basalt (Appendix C.2).

K-Ar age determinations indicate that Mba volcanic activity commenced over 10 m.y. ago and ceased at about 4.3 m.y. ago (Rodda *et al.*, 1967).

In the western Viti Levu, the rocks of the Mba Volcanic Group grade into the conglomerate and sandstone of the Verata Sedimentary Group. Their age is uncertain.

Along the southern coast of Viti Levu there are exposures of conglomerate, sandstone and marl of Pliocene age, grouped together as the Thuvu Sedimentary Group.

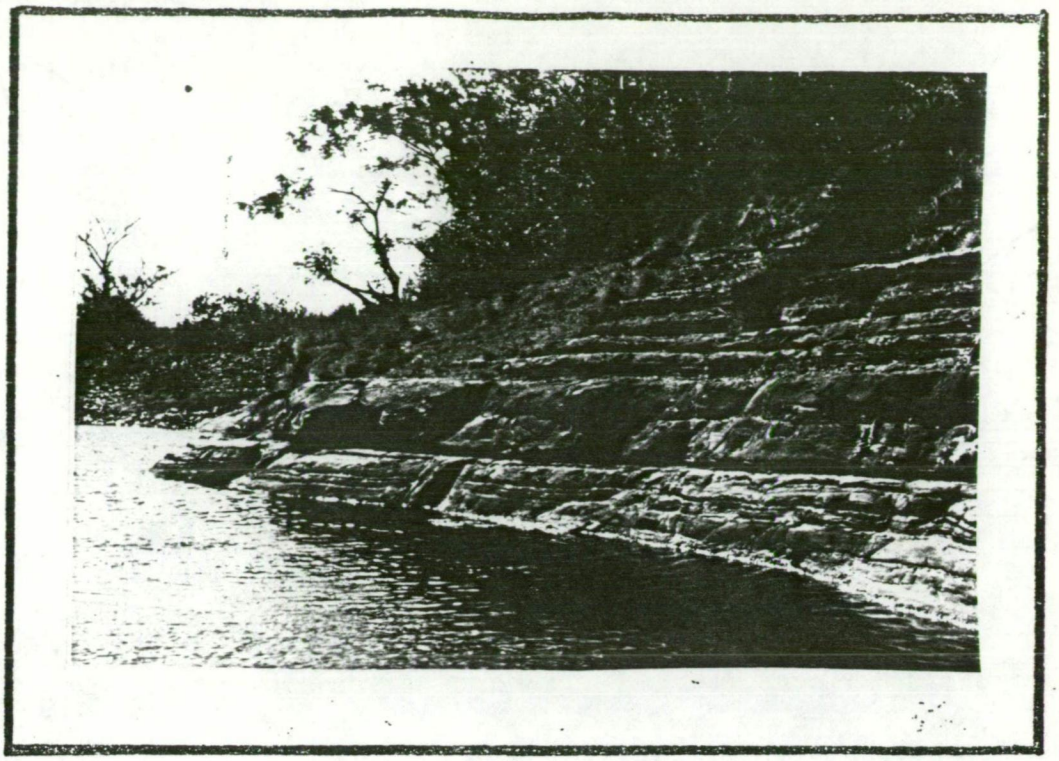

Plate 4.1 Photograph showing bedded calcareous greywacke, sandstone and mudstone of the Vatukoro formation. Locality: Mba river valley 5 km south of Mba township.

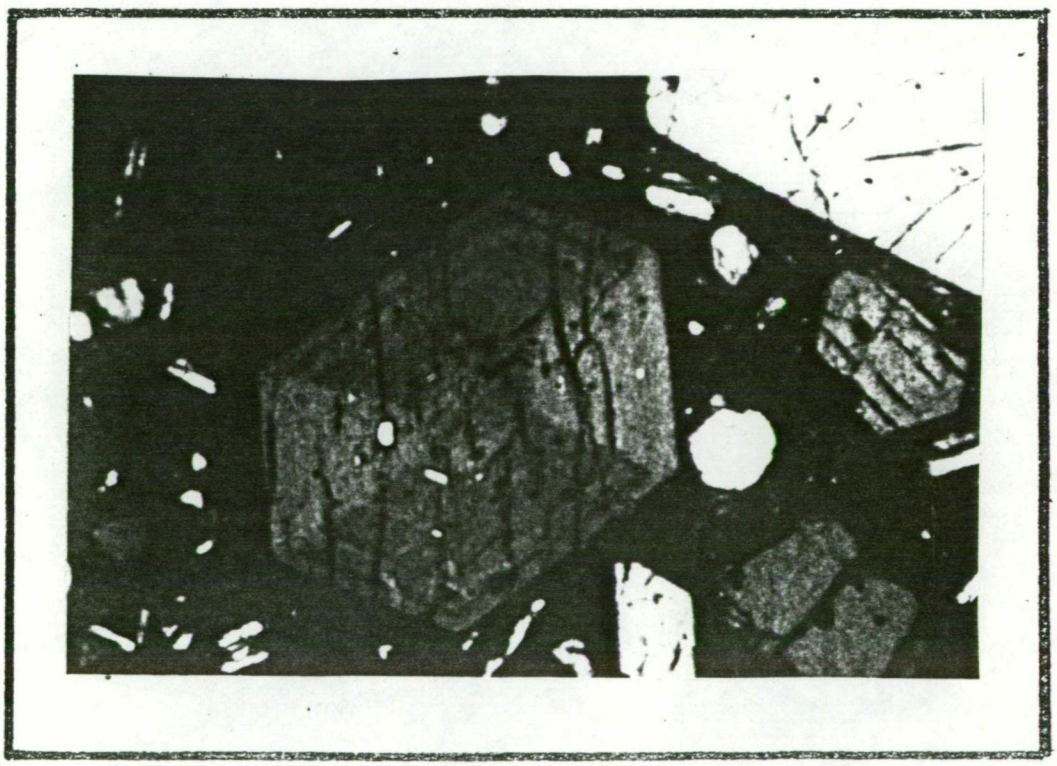

1 mm

Plate 4.2 Photomicrograph of olivine basalt showing zoned phenocrysts of pyroxene (brown and yellow), olivine (bright red and green) and plagioclase (light yellow). Sample 47288, Nasivi River crossing 1 km south-west of Homeward Bound. Cross nicols.

Rodda (1967) has used the term "Younger Intrusives" for all the intrusive rocks not classified as part of the Tholo Plutonic Suite. They range in composition from basalt to andesite and from gabbro to micro-granite and monzonite. K-Ar dating indicates that the Younger Intrusives are about 4.5 to 5 m.y. old (Rodda *et al.*, 1967).

4.3 GEOLOGY OF THE TAVUA CALDERA

The geology of the Tavua caldera (also known as the Tavua Basin) has been described by Blatchford (1953), Cohen (1962), Ibbotson (1967) and Denholm (1967a, 1967b, 1967c), and the following description relies heavily on their observations.

The rocks exposed in and around the caldera belong to the Mba Volcanic Group. Ibbotson (1967) suggested that the volcanic rocks near the caldera are at least 1500 m thick and Rodda (pers. comm., 1977) indicated a minimum thickness of about 2000 m. The Emperor mine workings extend to a depth of about 700 m through rocks which are mainly olivine basalt flows. The maps and sections (Figs. 4.2, 4.3, 4.4) are based upon the data given in Blatchford (1953), Cohen (1962), Rodda (1967), Ibbotson (1967) and Denholm (1967a, 1967b, 1967c). It is assumed that the volcanic rocks are thickest near the caldera and that the thickness is about 2000 m.

The caldera measures about 7 km by 5 km. The caldera boundary is a zone of brecciation about 10 m in thickness and is marked by a strong lithologic break that separates andesitic (and predominantly pyroclastic) rocks from basaltic (mostly flow) rocks.

Ibbotson (1967) recognised five phases of volcanic activity at the Tavua caldera, viz.

Phase V	Monzonite and trachyte intrusions.
Phase IV	Bictite trachyandesite flows and pyroclastics.
Phase III	Augite trachyandesite cone sheets, tuff and breccia.
Phase II	Trachybasalt flows and pyroclastics.
Phase I	Olivine basalt flows, pyroclastics, volcanic greywackes and conglomerate.

There were two major periods of cauldron collapse (Ibbotson, 1967). The first accompanied phase-I volcanism and the second commenced during phase-III volcanism and continued through cone-sheets emplacement and the extrusion of phase-IV lavas. The present caldera boundary was probably formed during the second period of cauldron collapse. The cauldron collapse took place on a series of inward-dipping faults and slide planes, many of which can still be recognised. A caldera lake was formed by the time of phase-III volcanic activity and the pyroclastics within the caldera were deposited under lacustrine conditions (Denholm, 1967a).

4.4 ROCK DESCRIPTIONS

The olivine basalt of phase I

In hand specimen, the basalt is dark grey to black and usually massive. Individual flows have an average thickness of about 1.5 m. Most of the flows are holocrystalline but they differ in groundmass, texture and modal composition. The phenocrysts are commonly of olivine and pyroxene with rare plagioclase (generally zoned), while the groundmass includes plagioclase, pyroxene, olivine and opaque minerals (Plate 4.2). In many instances, the olivine is altered to iddingsite and iron oxide (magnetite?) but the pyroxene is nearly always fresh.

Five samples of fresh olivine basalt were analysed by XRF methods during the present study for major and trace elements (Appendix C.1). Some feldspar and pyroxene grains were also analysed by electron microprobe (Appendix D.4).

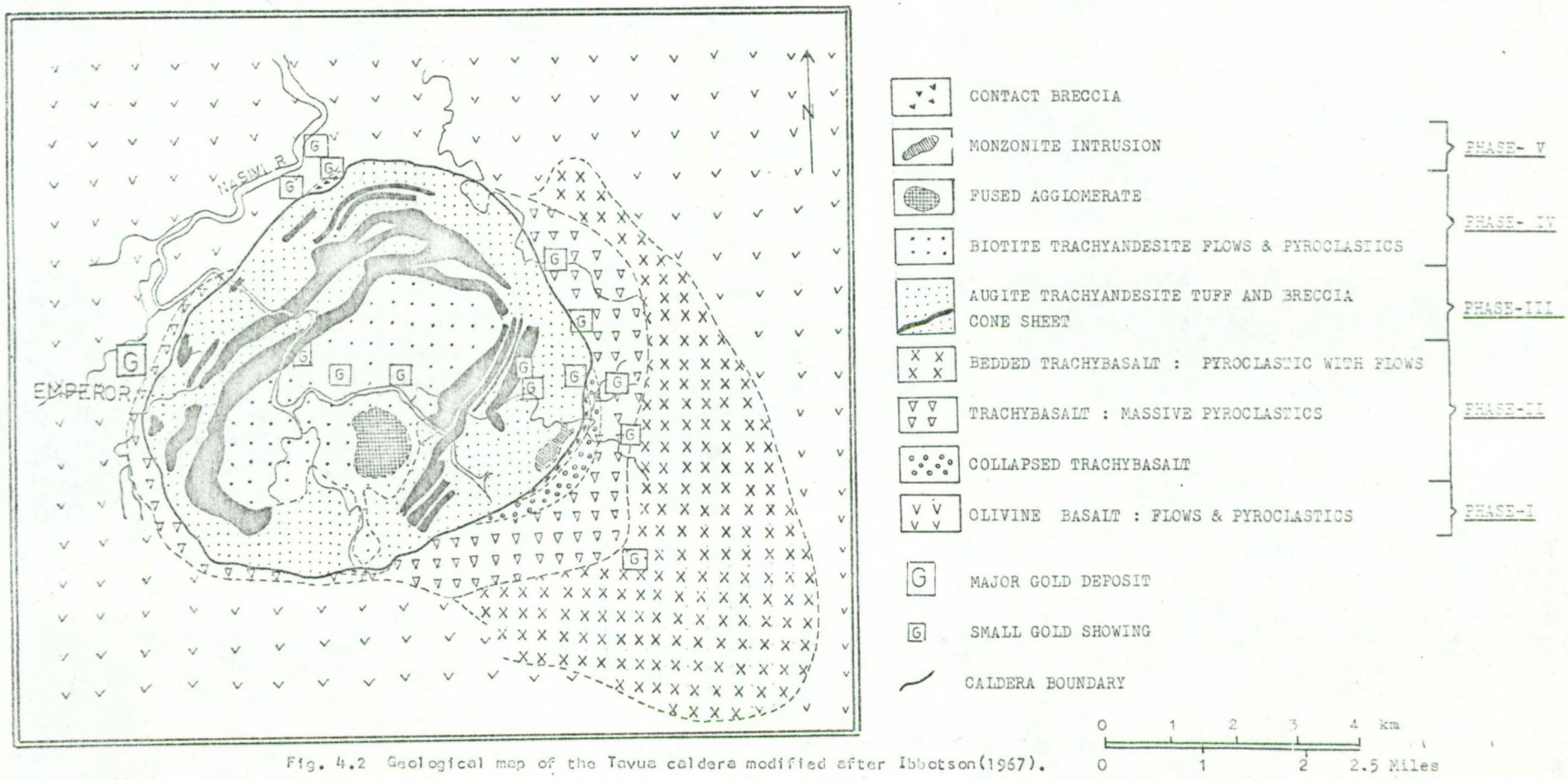

Fig. 4.2 Geological map of the Tavua caldera modified after Ibbotson(1967).

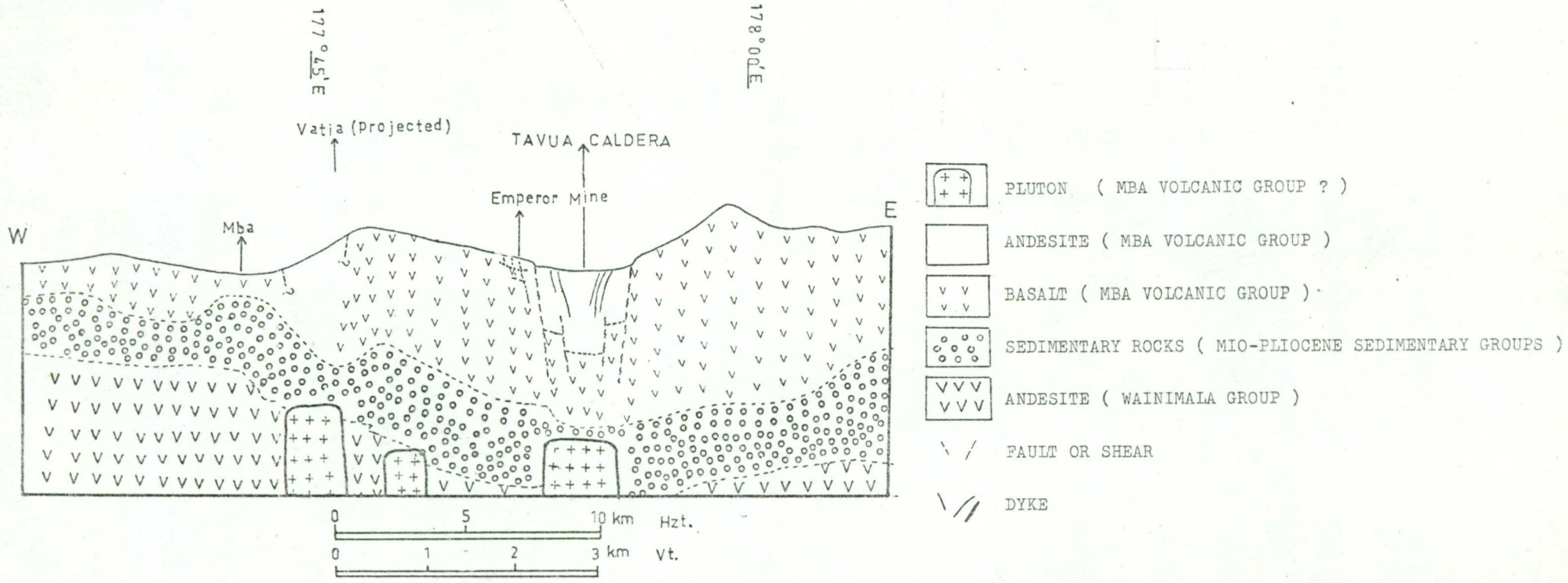

Fig. 4.3 Digrammatic section across the Tavua cauldron.

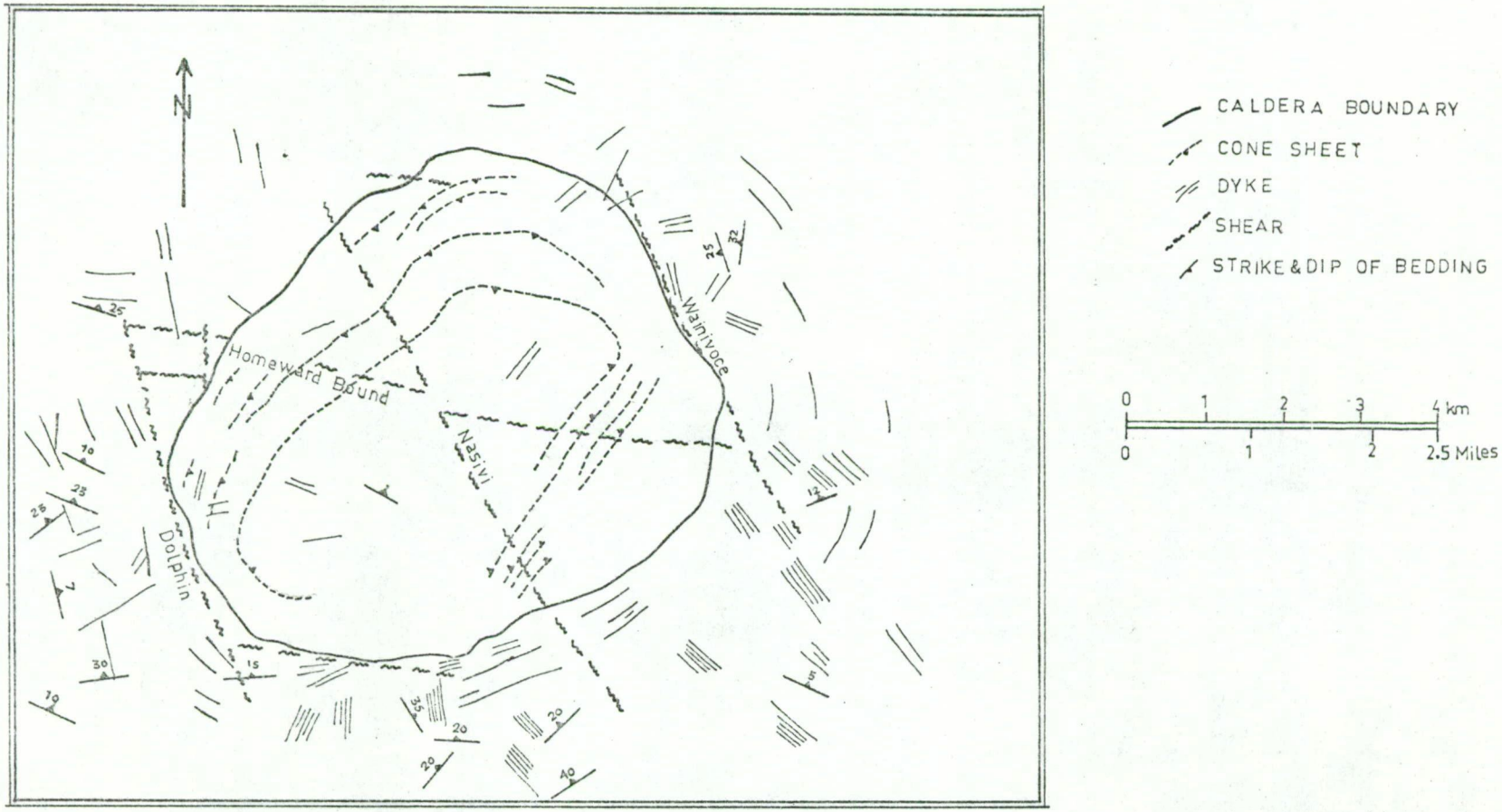

Fig. 4.4 Structural elements of the Tavua cauldron, after Ibbotson(1967) and Denholm(1967).

Both olivine and nepheline appear in the norm and Ibbotson (1967) classified these rocks as alkali olivine basalts.

The phase-I rocks near the Tavua caldera have an average dip of about 10^{o} north, which has been ascribed to regional tilting (Ibbotson, 1967).

Pyroclastic rocks belonging to phase-I volcanic activity include agglomerate, volcanic breccia, tuffaceous agglomerate, tuff and ash beds.

The trachybasalt of phase II

The phase-II rocks are predominantly pyroclastic trachybasalt. The trachybasalt is grey to grey-black and usually contains phenocrysts of feldspar and pyroxene. Some flows are fine grained and non-porphyritic.

Some rocks of phase II are heavily altered; feldspar and pyroxene phenocrysts are pseudomorphed by calcite and zeolite (which also occurs in amygdales) and by chlorite.

The augite trachyandesite of phase II

The phase-III rocks outcrop within the limits of the present caldera boundary and include tuff, ash beds, volcanic breccia and augite andesite in cone sheets.

Augite andesite is grey to light green and has a subhedral porphyritic texture. Pyroxene is the most common phenocryst with a modal variation of 10 to 35%. Porphyritic feldspar is present in many sheets.

The pyroclastics have an average dip of about 20^{o} towards the centre of the caldera. At the surface the cone sheets dip towards the centre of the caldera at angles of up to 50^{o} whereas in the deeper levels of the mine they steepen to 80^{o}.

The biotite trachyandesite of phase IV

The phase-IV rocks occur in the form of a shallow saucer-shaped outcrop in the central part of the Tavua caldera. These rocks can be divided into an earlier pyroclastic type and a later effusive type.

The biotite trachyandesite is white to buff, fine-grained porphyritic rock containing phenocrysts of biotite, feldspar and rare hornblende.

The pyroclastics are estimated to be about 160 m thick and their maximum dip is about 10° towards the centre of the caldera.

The intrusive rocks of phase V

The phase-V rocks are represented by dykes of trachyte and small plugs of monzonite and trachyte.

The trachyte of phase V is distinguished from phase-IV trachyandesite by its lack of ferromagnesian phenocrysts. It is grey, white or greenish, cryptocrystalline and feldspathic. Ferromagnesian minerals occur in the groundmass.

The monzonite is holocrystalline, porphyritic and rich in mafic minerals. Pyroxene and feldspar are abundant, and olivine and biotite rare. Potash feldspar is commonly observed as small laths in the groundmass.

4.5 DYKES

Dykes belonging to all the five phases of volcanic activity occur in and around the Tavua caldera (Fig. 4.4). They have an average width of about 2 m and generally have very steep dips (usually more than 80°). In the Emperor mine area, the majority of steep lodes are associated with dykes. The dykes can be divided into two categories on the basis of geographical position and strike direction:-

(a) Concentric dykes - dykes running parallel to the caldera boundary, e.g. the cone sheets of phase-III augite trachyandesite exposed within the caldera, and a number of dykes occurring outside the caldera.

(b) Radial dykes - dykes running radially from the caldera centre, the majority being phase-I olivine basalt.

No distinction is made in Fig. 4.4 between the dykes associated with the various phases of volcanic activity. The majority of dykes surrounding the caldera belong to phase-I or phase-II volcanic activity. The phase-I olivine basalt dykes are more common towards the south and southwest and phase-II trachybasalt dykes are more common towards the east. The trachyandesite dykes of phase-III occur both within and outside the caldera. Outside the caldera they are more common towards the south and southwest, and within the caldera they generally occur as cone sheets. A few biotite trachyandesite dykes of phase-IV are observed within the caldera. Monzonite and trachyte dykes belonging to phase-V volcanic activity are rare. Few monzonite dykes have been observed in the Emperor mine workings.

Ibbotson (1967) showed that the dykes and dyke swarms are more common between altitudes of 120 and 213 m (up to 73% of the total) and are uncommon below or above these altitudes.

4.6 STRUCTURE AND MINERALIZATION

The shears shown in Fig. 4.4 are taken from Denholm (1967a, 1967b, 1967c). No detailed information on these structures is available. The Dolphin shear is exposed in the Emperor mine workings but its extensions are unknown. The Homeward Bound shear is exposed towards the northwestern margin of the caldera, but again its extensions are doubtful. The Nasivi shear is exposed in the centre of the caldera for about 1000 m. No data is available concerning the Wainivoce shear.

As shown in Fig. 4.2 a number of minor gold occurrences have been noted, both inside and along the periphery of the caldera. The geology and mineralogy of these prospects is not known but Denholm (1967a, 1967b) described the mineralization as fracture controlled and occurring at the intersection of more than one fracture or a fracture and a dyke.

The samples of core drilled on these prospects were not accessible during this study. Chief Geologist J.R. Ekstrom (pers. comm., 1977) stated that pyrite is relatively more abundant in these prospects than at the Emperor mine. None of the prospects proved to be economic.

4.7 AGE DETERMINATIONS

Age determinations by the K-Ar method were carried out on rocks from Viti Levu at the Overseas Division, Institute of Geological Sciences, London. Potassium was determined by flame photometry and argon by stable-isotope dilution. The results of these determinations are reported by Rodda *et al.* (1967). Eight age determinations are available for the rocks belonging to the Mba group. Seven of them are on the rocks exposed in and around the Tavua caldera and one is on the Vatia andesite exposed about 16 km northwest of the Tavua caldera. The ages obtained are listed below.

Material used	Rock type	Age (m.y.)	Phase	Location
whole rock	basalt	7.5 ± 1	I	Emperor mine
feldspar	andesite	9.2 ± 2	I ?	Vatia
biotite	trachyandesite	10 ± 0.5	I	Emperor mine
biotite	trachyandesite	5 ± 0.2	II	NE margin of Tavua caldera
whole rock	trachybasalt	4.7 ± 0.2	II	NE margin of Tavua caldera
whole rock	trachyandesite	4.3 ± 0.2	III	Emperor mine
biotite	trachyandesite	4.7 ± 0.2	IV	inside Tavua caldera
biotite	monzonite	4.7 ± 0.2	V	Emperor mine

It must be noted that the trachyandesite dyke (age 10 ± 0.5 m.y.) is included under phase-I. It has been suggested that this dyke represents an earlier andesitic phase than that seen at the surface. Rodda *et al.* (1967) have suggested that the sequence basalt-trachybasalt-trachyte may have

been repeated several times, the latest repetition constituting its most prominent development. This trachyandesite dyke may therefore belong to the first phase of volcanic activity.

Vatia has been suggested as one of the major centres of volcanic activity during Mba times. The volcanic activity at this centre may be contemporaneous with one of the older periods of volcanic activity at Tavua (Rodda *et al.*, 1967).

It seems that the Tavua area witnessed two major periods of igneous activity, the first between 10 and 7.5 m.y. and the second between 5 and 4.3 m.y.

Chapter 5

GEOLOGY OF THE MINE AREA

5.1 GENERAL

The geology and lode structures at the Emperor mine have been described in detail by Blatchford (1953), Cohen (1962), Denholm (1967a, 1967b, 1967c) and Forsythe(1967).

Fig. 5.1 is the geological map of the mine area. This map is based on Blatchford's (1953) data but has been updated. The mineralized lodes are located to the southwest of the Tavua caldera and they all lie within about 2000 m of the caldera boundary. The host rocks are olivine basalt flows and andesite dykes.

5.2 ROCK DESCRIPTIONS

The fresh olivine basalt is greenish grey, massive and markedly porphyritic, with phenocrysts of augite, plagioclase and olivine (Plate 4.2). The groundmass consists of interlocking crystals of plagioclase, pyroxene and olivine. Both pyroxene and plagioclase are zoned. Augite crystals showing perfect hour-glass textures are frequently observed. In most samples, olivine is partly altered to iron oxide and iddingsite. Magnetite grains are common.

In most samples examined the olivine basalt is altered to an assemblage containing chlorite, ankerite, dolomite, magnetite, serpentine and tremolite with rare pyrite (Plate 5.1). This assemblage is termed propylitic. As the mineralized zone is approached, the intensity of alteration increases and the mineral assemblage finally becomes quartz, sericite, potassium feldspar, dolomite and pyrite (Plates 5.2, 5.3). This assemblage has been termed the K-silicate assemblage. The mineralized

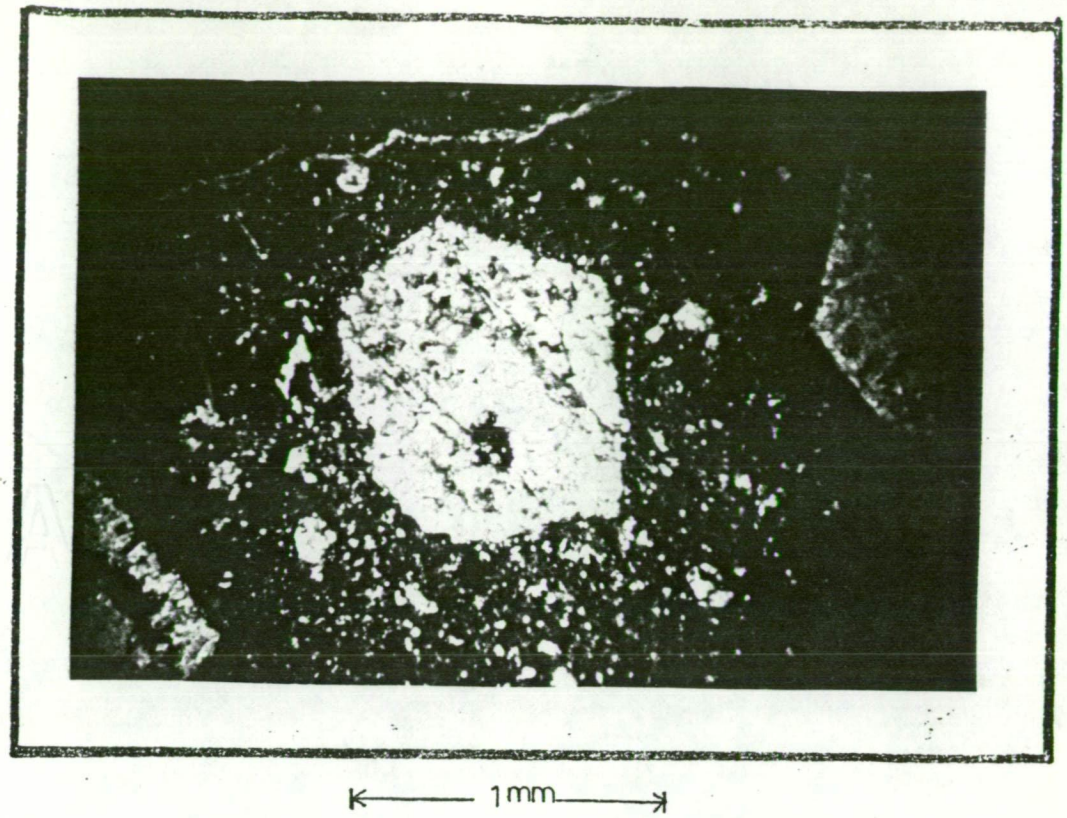

Fig. 5.1 Photomicrograph of altered olivine basalt showing the pseudomorphs of ankerite and minor chlorite after pyroxene. Sample 47215, DDH MA-56. Crossed nicols.

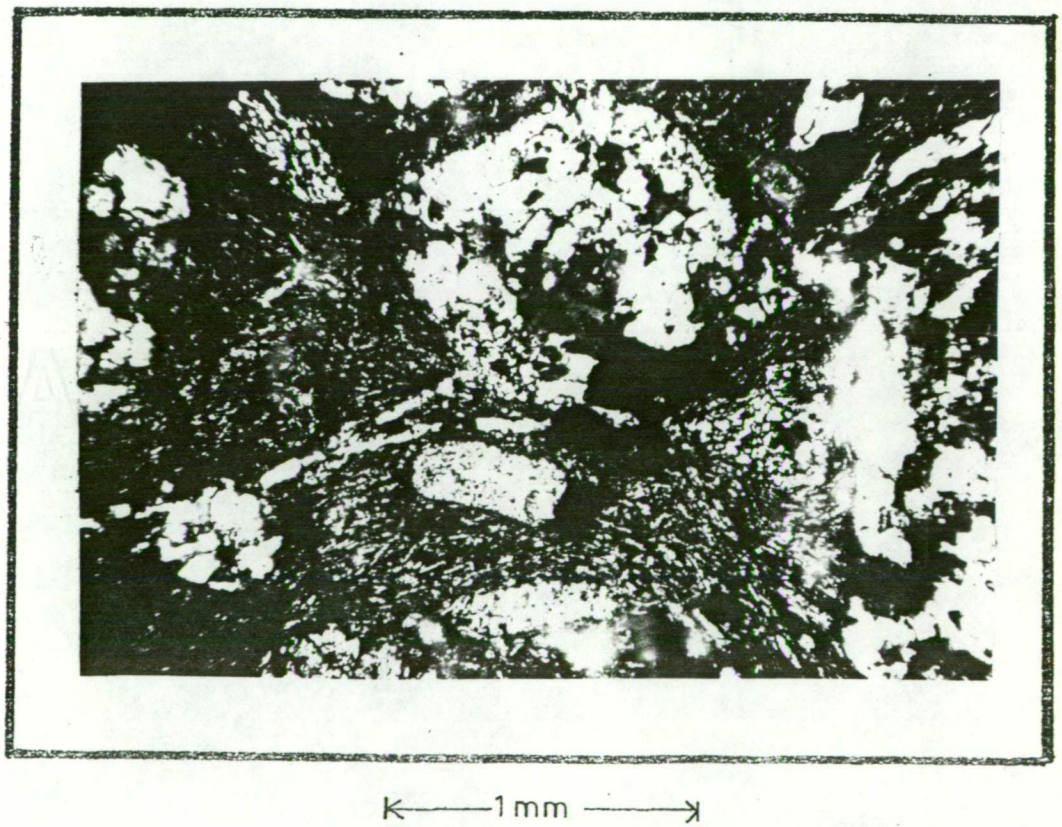

Fig. 5.2 Photomicrograph of altered olivine basalt showing the pseudomorphs of quartz, ankerite, sericite and minor adularia (rhomb shaped grains in the bottom left hand corner). Sample 103336, State flatmake, 2 level, crossed nicols.

←——1mm ——→

Plate 5.3 Photomicrograph showing pseudomorphs of sericite and dolomite after plagioclase. Note the cross cutting, late-stage quartz vein. Sample 103308, P.O.W. lode, 10 level.

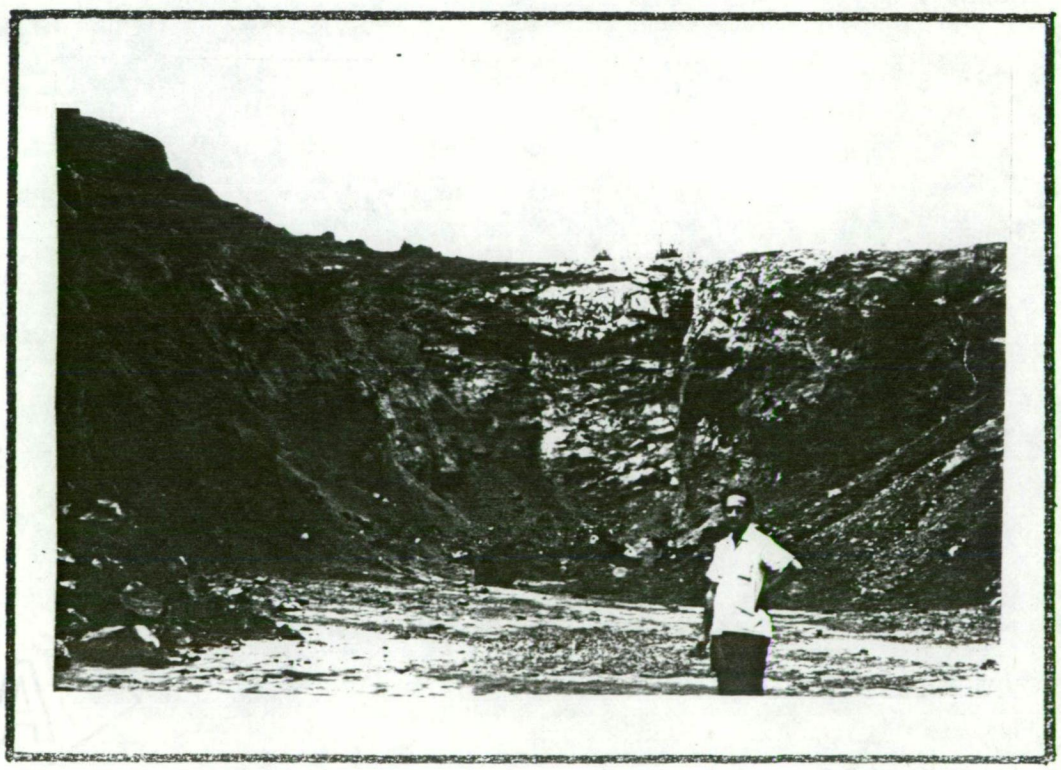

Plate 5.4 Photograph showing the steeply dipping President dyke. Location: Loloma open cut, looking north.

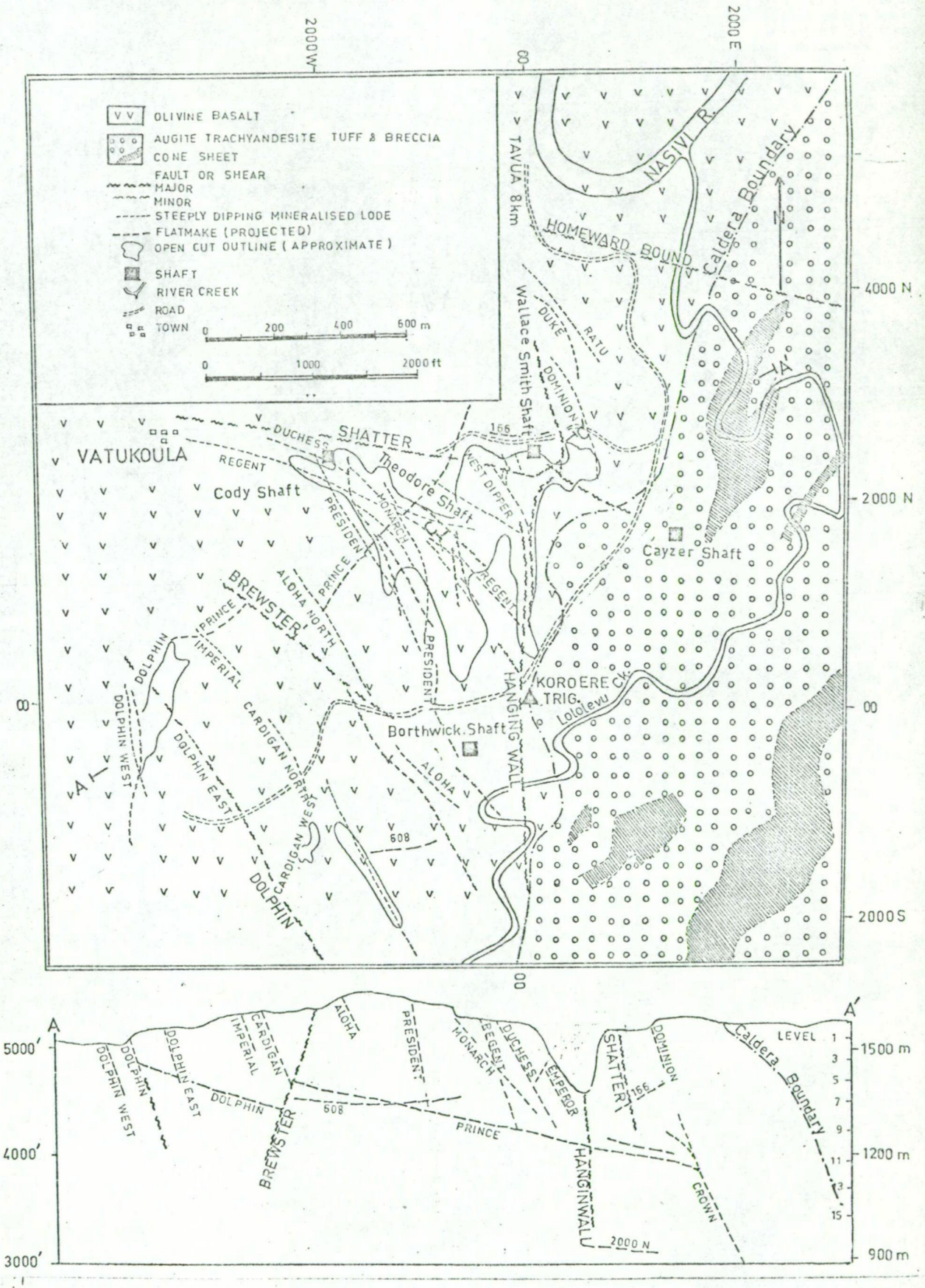

Fig. 5.1 Geological map of the Emperor mine area and cross section A-A'

lodes cover an area of about 1.5 sq. km and it appears that the majority of rocks in the mine area are propylitized, although the degree of alteration varies from place to place.

Individual flows probably average about 1.5 m in thickness (Ibbotson, 1967), although Blatchford (1953) described flows up to 30 m thick from the underground workings. Individual flows have an average dip of about 10° north and a general east-west strike.

The basalt flows are interbedded with rare ash or tuff beds. Individual beds range from 1 to 15 m in thickness (Blatchford, 1953) and the majority appear to be of limited extent.

The andesite is greenish grey coloured, massive, holocrystalline and contains phenocrysts of zoned pyroxene and plagioclase. The alteration pattern is similar to that of olivine basalt. The contact with the olivine basalt is sharp and is marked by a zone of brecciation about 5 cm thick (Plates 5.4, 5.5). The majority of these dykes have a northwest trend and dip at steep angles to the northeast. Their average thickness is about 5 m.

5.3 STRUCTURE AND MINERALIZATION

The caldera boundary in the Emperor mine area trends from north-south to northeast and dips east. The dip near the surface is about 50° but steepens to about 80° at depth. It is a zone of brecciation about 10 m in thickness. In the mine workings disseminated pyrite is commonly observed but the zone is only weakly auriferous. It separates phase-I olivine basalt from the later phases of volcanic activity.

Three major shears have been mapped in the mine workings, viz. the Shatter shear, the Hanging Wall shear and the Brewster shear. No economic concentrations of gold have been observed in these shears, although disseminated pyrite is common.

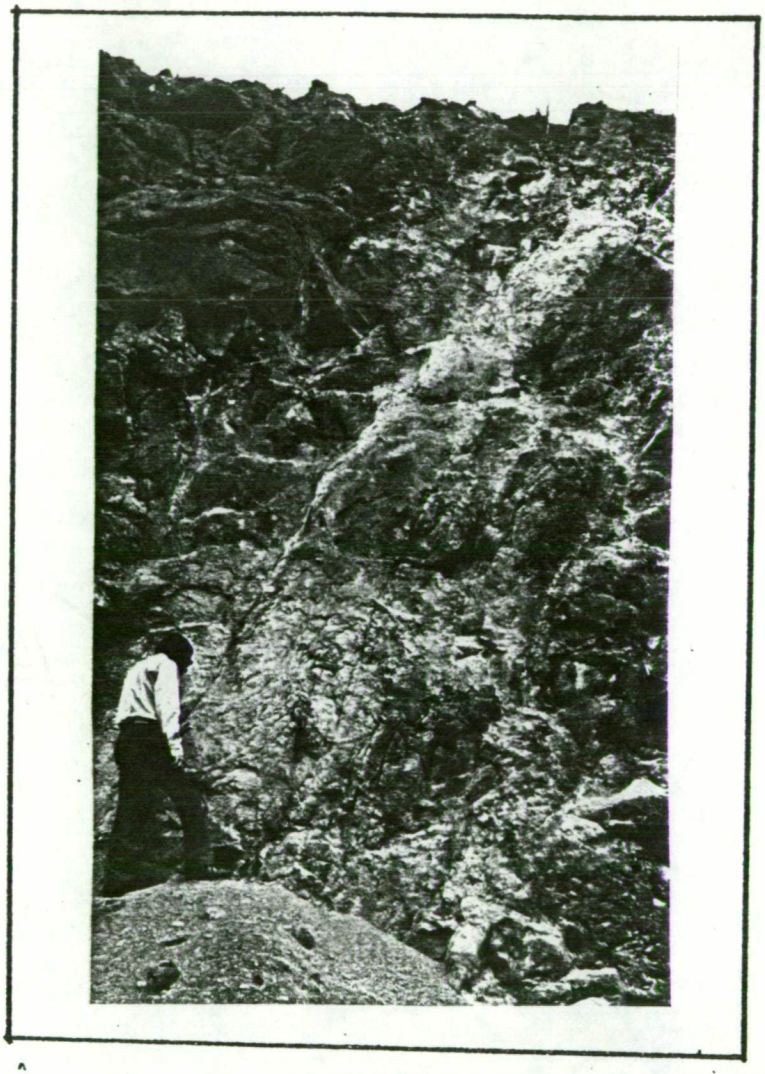

Plate 5.5 Photograph showing the Duchess dyke. Note that the hanging-wall contact with basalt is strongly sheared and has acted as the loci for the ore-mineralization. The hanging-wall basalt is also bleached (brown coloured) while the footwall basalt (grey coloured) does not show any change in colour. Location: Loloma open cut.

The rocks exposed to the east of the caldera boundary belong to phase III and are represented by augite-andesite cone sheets and tuffs (Fig. 5.1). The tuffaceous rocks dip at low angles to the east. The cone sheets dip at an angle of about 50° near the surface but steepen to about 80° in the underground workings. No productive mineralized lodes have been located in the rocks east of the caldera boundary.

There are three types of lodes from which most of the gold in the Emperor mine area has been won. They are:-

(a) Steep northwest shears
(b) Flatmakes
(c) Shatter structures.

5.3.1 Steep northwest shears

As mentioned previously the olivine basalt is intruded by a number of andesite dykes. In the mine area the majority of these dykes have a northwest trend and dip steeply to the northeast. An interesting feature of these dykes is that on the contact (usually the hanging wall) they are strongly sheared (Plate 5.5). The width of these dykes ranges from 2 to 4 m while the width of the shear zone ranges from a few centimetres to a few tens of centimetres.

The shears running parallel to the dykes have served as loci for gold mineralization. The Crown lode, striking northwest, is associated with an andesite dyke and is mineralized over a strike length of about 760 m and a vertical range of about 360 m. The lode has an average dip of about 75° due northeast. The lode width ranges from 10 cm to about 1 m. This lode has yielded approximately 500,000 tons of ore assaying about 15 dwt/ton Au. The other lodes of similar kind but of less economic importance are Cardigan, Duchess, Monarch, Regent, Prince of Wales and several others (Figs. 5.1, 5.2, 5.3).

5.3.2 Flatmakes

Mineralized lodes dipping at angles less than 45° have been termed "flatmakes". The average dip is about 25°. Cohen (1962) has suggested that they are thrust faults along which movements of a few metres have taken place. These flatmakes are influenced in some degree by the crude layering of lava flows, ash beds and flatly dipping dykes. Individual lodes usually range in thickness from 1 to 10 cm.

The Prince-Dolphin flatmake strikes east-northeast and dips about 25° southeast (Figs. 5.1, 5.2, 5.3). It is mineralized over a strike length of about 2300 m and a similar dip length. In contrast with the steep lodes, crustification textures and open vughs are frequently observed. This flatmake has yielded about 2 million tons of ore averaging 9 dwt/ton Au.

The 608 flatmake is similar to the Prince-Dolphin flatmake. It strikes east-west and dips from 25 to 30° north. It is mineralized over a strike length of about 450 m and a dip length of about 1200 m. It has yielded about 1,300,000 tons of ore averaging between 5 and 10 dwt/ton Au.

Other flatmakes of similar type but less economic importance are State, B17A, 2000N, 460E, 166, Princess etc.

5.3.3 Shatter structures

The shatter structures are aggregates of numerous discontinuous, flatly dipping cracks. These are believed to be produced when basalt blocks were wedged by a series of shears and left partly suspended. The resulting resettling produced a number of tension joints of which the majority dip easterly at low angles (Cohen, 1962; Denholm, 1967a).

The shatter structures contained some of the bonanza ore bodies on which the earlier mining activity concentrated.

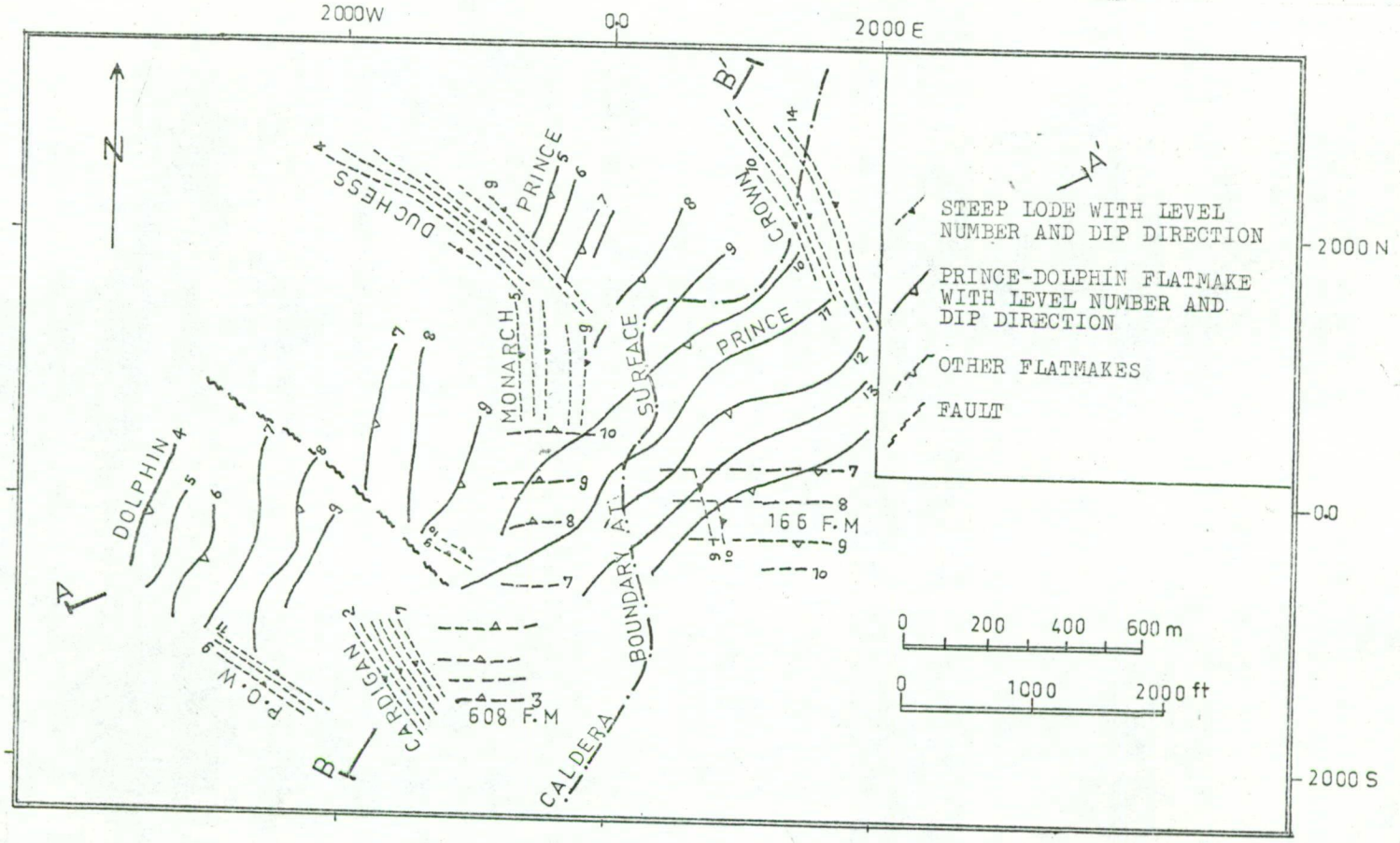

Fig. 5.2 Simplified composite plan of lodes at the Emperor mine.

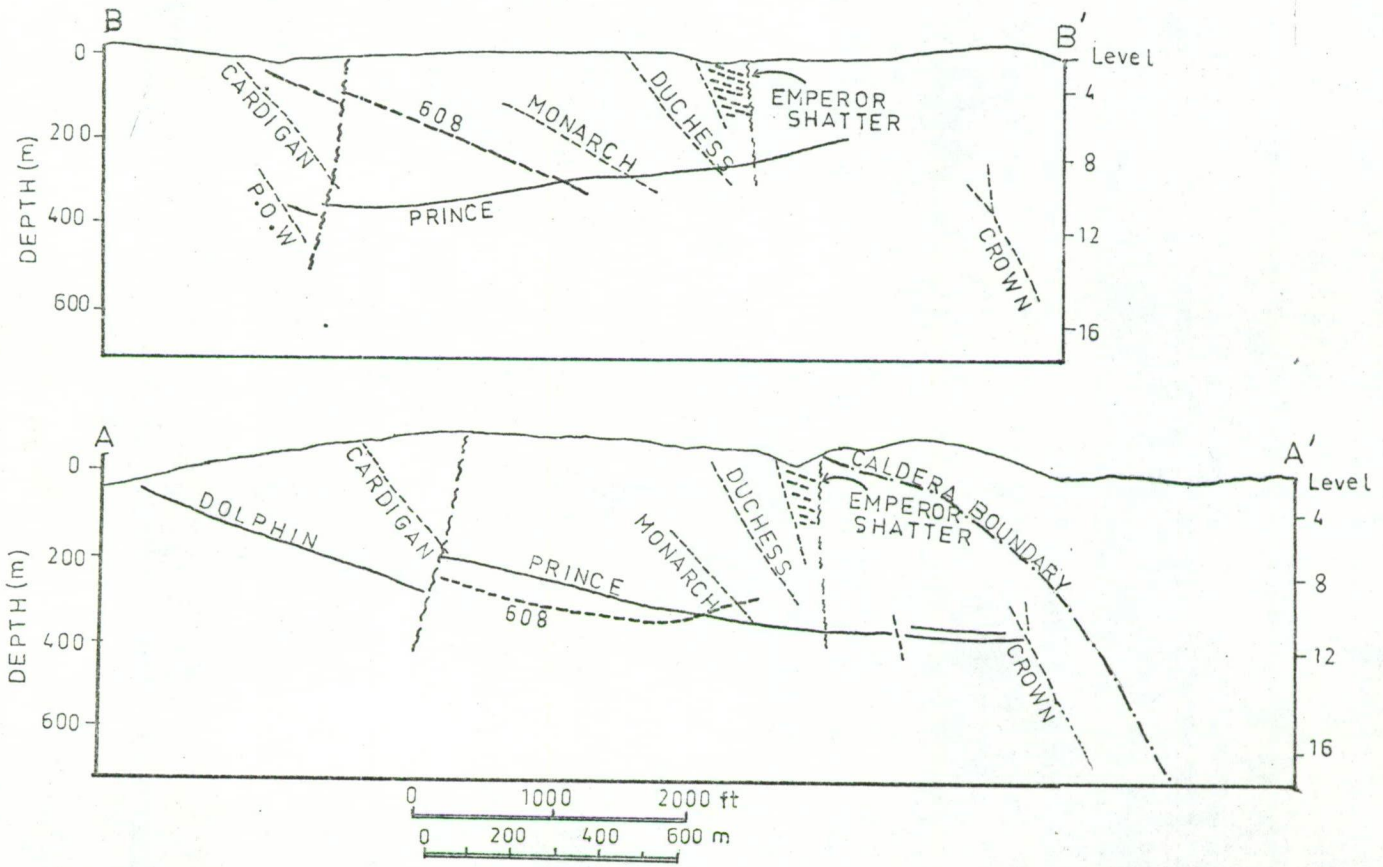

Fig. 5.3 Cross sections A-A' and B-B' in Fig.5.2

The Emperor Shatter ore body (Figs. 5.6, 6.3) has yielded 2,500,000 tons of ore and the 1030 Shatter has yielded about 200,000 tons of ore assaying about 10 dwt/ton Au.

5.4 AGE OF MINERALIZATION

Age determinations by the K-Ar method (Chapter 4, Section 4.7) indicate that igneous activity at Tavua occurred from about 10 m.y. to 4.3 m.y. These age determinations also suggest two major periods of igneous activity, the first between 10 and 7.5 m.y. and the second between 5 and 4.3 m.y.

Previous workers (e.g. Cohen, 1962; Denholm, 1967a, Ibbotson, 1967) have suggested that the mineralization at the Emperor mine took place after the igneous activity subsided. These suggestions are probably based on the assumption that the mineralized lodes follow the andesite dykes which belong to phase-III or phase-IV volcanic activity. The age determinations on andesite dykes, however, indicate that they may belong to phase-I volcanic activity. One andesite dyke from the Emperor mine workings, gave an age of about 10 m.y., whereas the age on the phase-III and phase-IV andesite is between 4.7 and 4.3 m.y. (Rodda *et al.*, 1967). More age determinations on the andesite dykes associated with the Emperor mineralization are needed, but the available data indicate that the mineralization may not be later than phase III or phase IV.

Srinivasan *et al.* (1972) determined an age of 7.2 ± 0.94 m.y. for a telluride sample from the Emperor mine by the Te^{130}-Xe^{130} method. They used a composite sample weighing about 3.2 kg. The nature and type of telluride minerals present in this sample are not known. The method relies on the double beta decay of Te^{130} which produces Xe^{130}. The half life for this decay is estimated on a sample from Kalgoorlie, Western Australia to be $(2.83 \pm 0.30) \times 10^{21}$ years. They also determined ages for tellurides

from Facebaja, Roumania and Moctezuma, Mexico. The ages obtained from these samples are comparable to the geological age.

The only available data thus indicates that the bulk of the mineralization probably occurred towards the end of, or slightly later than, the first period of igneous activity. Minor gold occurrences within the Tavua caldera are probably related to the second period of igneous activity because they occur as fracture fillings in the phase-III volcanics which have been dated at 4.3 ± 0.2 m.y. (Section 4.7).

Chapter 6

THE LODES

6.1 GENERAL

As described in Chapter 5, the majority of the steep lodes follow the andesite dykes. The ore in these lodes generally occurs in or along the walls of the dykes as a single or several near-parallel strands, commonly branching into a network within the limits of the dyke, or meandering from wall to wall. In general, if the dyke is displaced by a fault the lodes are also displaced (Figs. 6.1B, 6.3) i.e. the faulting is post-mineralization. In some cases the lode crosses the fault and traverses through the basalt for a short distance, indicating pre-mineralization faulting (Fig. 6.1A).

The majority of steep lodes are tabular in shape and are confined to narrow channels a few centimetres to a few tens of centimetres wide. In places several near-parallel strands increase the width of the mineralized zone to about 1 m or more. The Diadem lode, for example, with its numerous short-lived north-south trending fractures (Fig. 6.3), has been stoped successfully over a width of about 6 m.

The gently-dipping lodes (flatmakes) generally do not follow any particular lithological boundary though in a few cases they tend to follow a less steeply dipping dyke for a short distance (Figs. 6.2A, 6.3). Some flatmakes tend to follow ash beds. When a flatmake encounters a steeply dipping dyke, it generally breaks up into numerous short-lived strands (Fig. 6.2B), thereby increasing the payable stoping width.

The flatmakes are tabular in shape with the width of the payable zone ranging from a few centimetres to a few tens of centimetres, but again branching or splitting may increase this width to a couple of metres.

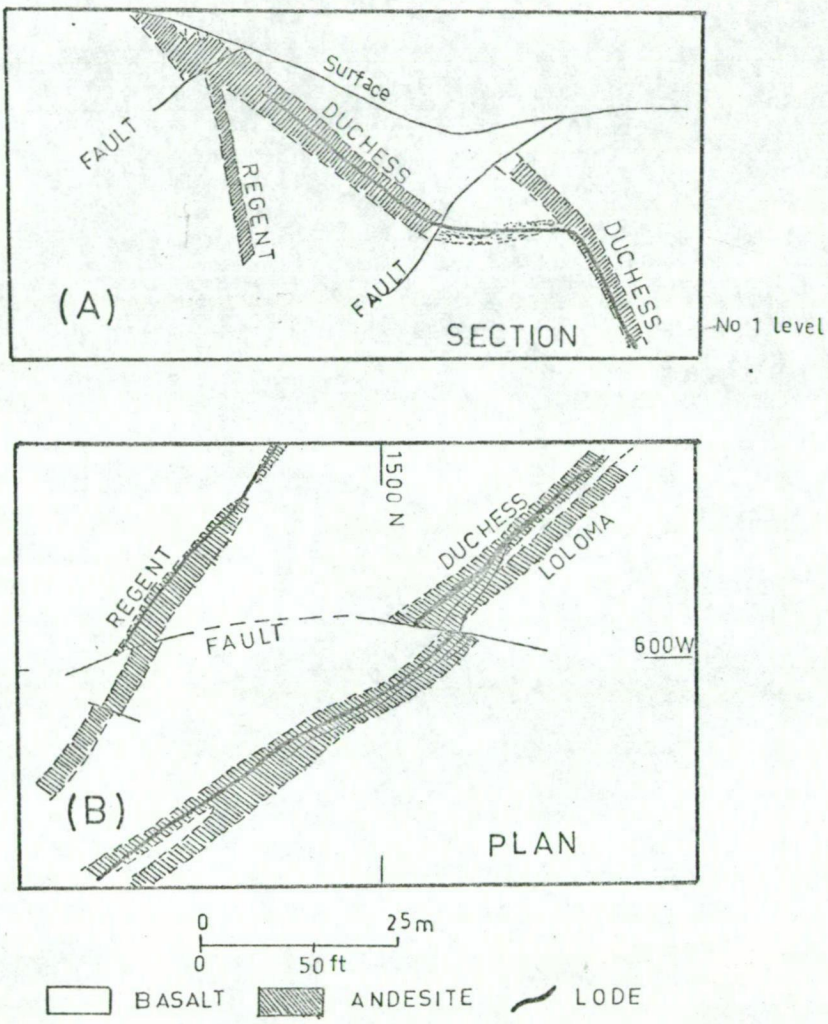

Fig. 6.1 Detailed section and plan showing the nature of the lodes, after Blatchford(1953). (A) Cross section showing the continuation of the Duchess lode through basalt in between the displaced parts of the andesite dyke. (B) Plan showing the displacement of the Duchess lode by a post-mineralization fault.

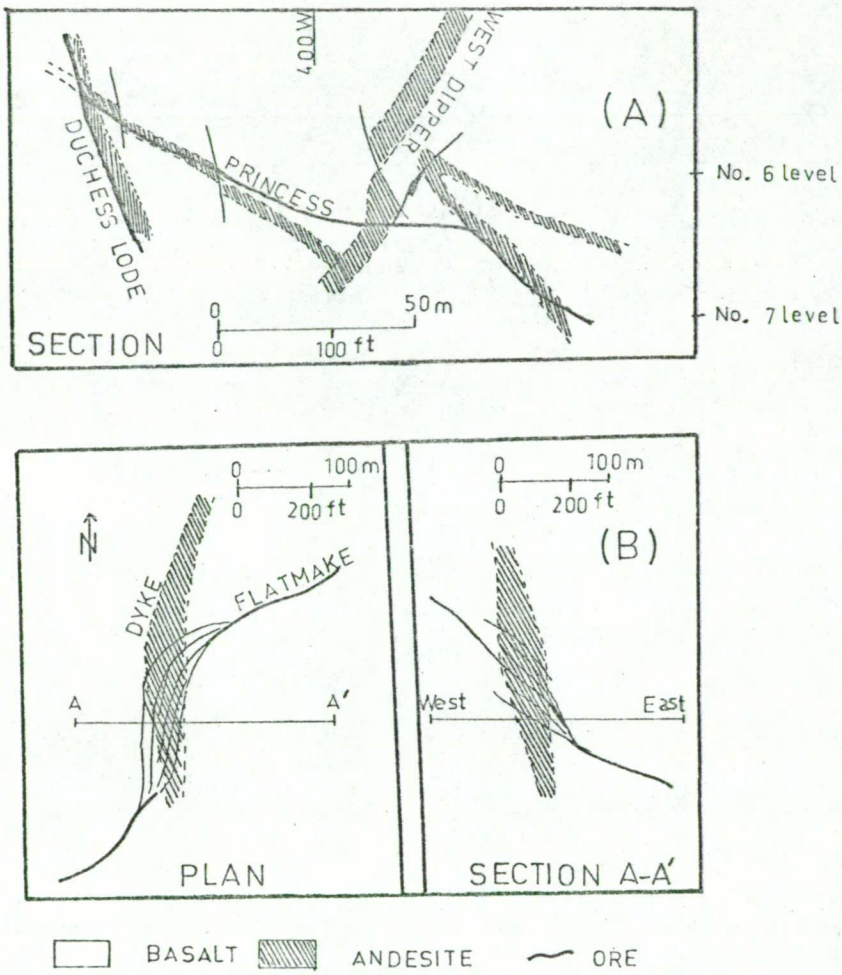

Fig. 6.2 Detailed section and plan showing the nature of the lodes. (A) Section showing the influence of a less steeply dipping dyke on the Princess flatmake, after Blatchford(1953). (B) Section and plan showing the splitting of a flatmake at its intersection with a steeply dipping dyke, location not known, after Denholm(1967a).

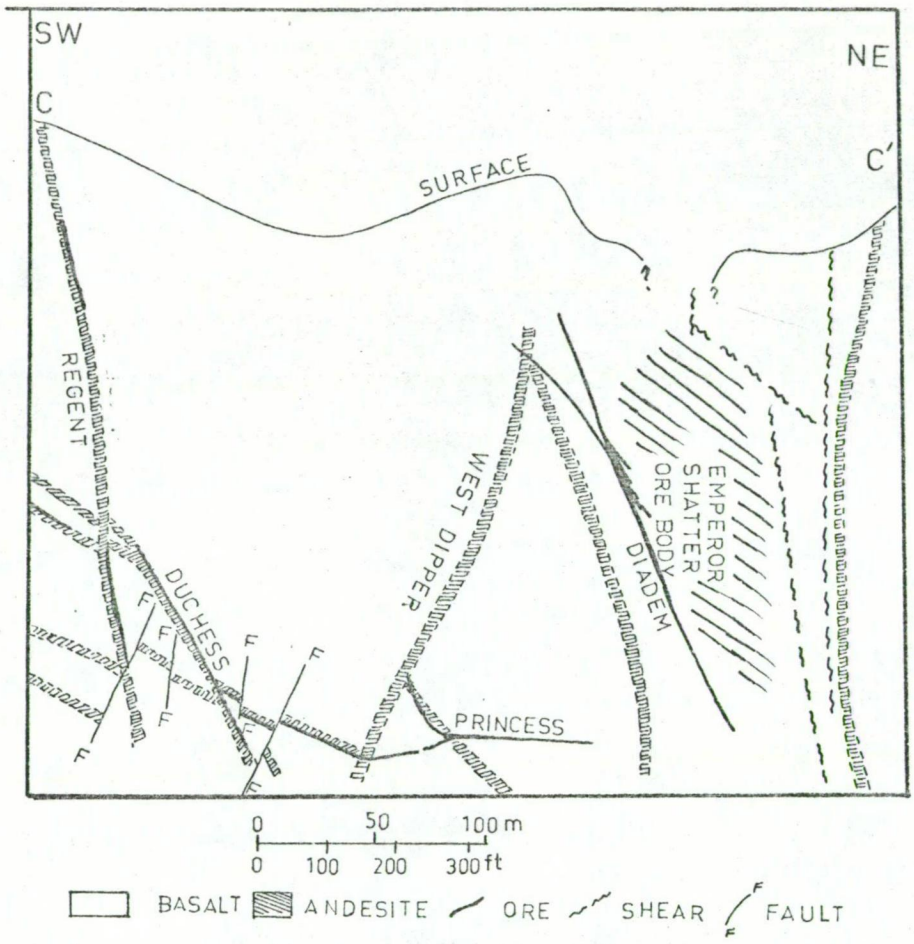

Fig. 6.3 Cross section C-C' in Fig. 5.1, modified from Blatchford(1953) to show the location and nature of the Emperor shatter ore-body. Note also the displacement of the Princess flatmake by faults.

The most important lode (or more appropriately a cluster of lodes) is the Emperor Shatter ore body. This ore body is a cluster of several gently dipping mineralized strands occupying an inverted cone-shaped area between Diadem (Emperor) lode, the Shatter shear and the Hanging Wall shear. This ore body tails out around No.8 level near the intersection of the above-mentioned structures (Fig. 6.3).

Bottoming of most of the steep lodes and flatmakes is mineralogical rather than structural. In most cases the structure continues but payability of the lode decreases due to fading out of the ore minerals. As a general rule most of the steep lodes are not payable below their intersection with the Prince-Dolphin flatmake. The only exception to this is the Crown lode which continues to be payable much below its intersection with the Prince-Dolphin flatmake.

In longitudinal sections (Fig. 6.4), most of the lodes show an irregular outline, but generally, the horizontal extent is greater than the vertical. These lodes generally do not have a homogeneous grade throughout, but they have pockets of relatively high grade material which generally coincide with the intersection of more than one fracture. Usually the intersections of flatmakes and steeply dipping dykes are richly mineralized (Denholm, 1967a).

The strike, dip, vertical extent and other pertinent data on a number of important lodes (i.e. lodes which have high tonnage) are given in Table 6.1. The tonnage values given in this table are only approximate and are based on the data given in Blatchford (1953) and Denholm (1967a) The exact amount of material actually mined, probably does not deviate much from these values. Prince of Wales, 166 and Wunawali lodes are being mined and exact figures for these lodes are not available.

Most of the steep lodes trend north-west, they generally follow andesite dykes. The majority of the steep lodes are exposed at the surface. The vertical extent of these lodes range from 70 to 730 m

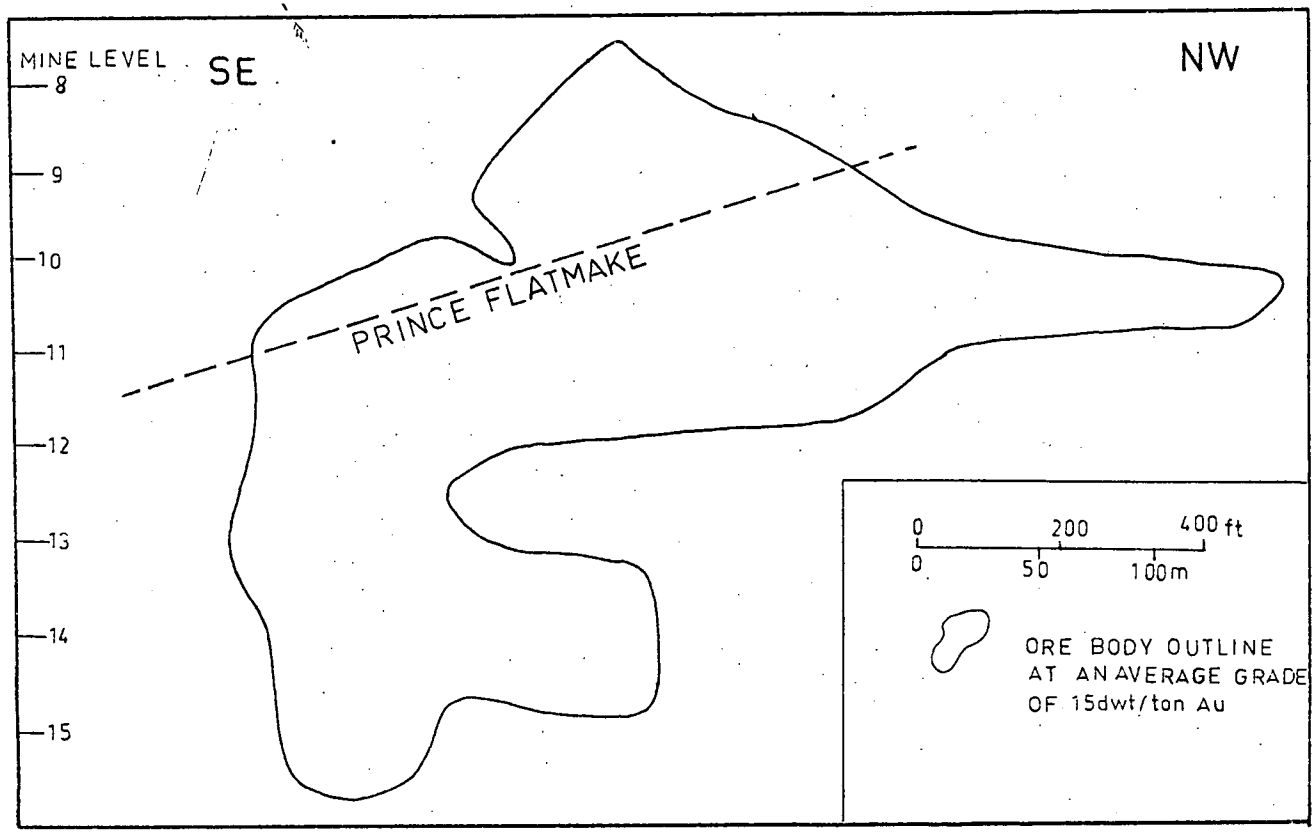

Fig. 6.4 Longitudinal section showing the outline of the Crown lode, after Forsythe (1967)

Table 6.1

Data on some important lodes.

Lode	Strike	Dip	Maximum vertical extent,	Maximum horizontal extent,	Location*	Host* rock	Approximate total reserves, tons	Average grade or range, dwt/t
Emperor Shatter	diverse		236	182	o	B some T and A	2,588,000	7-8
Diadem (Emperor)	NW-SE to N-S	50-70° to E	196	365	o	B some A	46,100	10-12
Princes Flatmake	N-S	20-50° to E	80	300?	c	B some T and A	34,500	20-25
Duchess Flatmake	N-S	25-45° to E	121	152?	c	Mostly A some B	34,300	20-40
Duchess lode	NW-SE	50-60° to N	236	762	o	A	306,200	20-30
Regent	NW-SE	75-80° to N	236	762	o	A	33,400	15-20
Monarch	NW-SE to N-S	45-55° to E	731	60	c	A	20,600	9-12
Cardigan	NW-SE	70° to E	364	840	o	A some B	86,500	5-8
Prince-Dolphin flatmake	NE-SW	25° to E	523	2310	c	B	2,000,000	9
Crown-Crescent	NW-SE	70-80° to E	365	762	c	A some B	500,000	15

608 flatmake	E-W	25-30° to N	521	457	o	B	1,300,000	5-10
166 flatmake	E-W	25-30° to S	100?	304?	c	B	?	?
Prince of Wales	NW-SE	70° to E	100?	304?	c	A	?	?
Wunawali	N-S	65° to E	70	200	c	A	?	?

---

* o - outcropped

c - concealed

A - andesite

B - basalt

T - tuff

Table 6.2

Minerals observed at the Emperor gold mine, Fiji.

(A) OPAQUE MINERALS	
Calaverite	$AuTe_2$
Krennerite	$(AuAg)Te_2$
Sylvanite	$AuAgTe_4$
Petzite	Ag_3AuTe_2
Hessite	$AgTe_2$
Empressite	Ag_5Te_3
Coloradoite	HgTe
Melonite	NiTe
Altaite	PbTe
Tellurium	Te
Gold	Au
Magnetite	Fe_3O_4
Anatase	TiO_2
Pyrite	FeS_2
Marcasite	FeS_2
Arsenopyrite	FeAsS
Sphalerite	ZnS
Galena	PbS
Chalcopyrite	$CuFeS_2$
Bournonite	$CuPbSbS_{13}$
Tetrahedrite	$(CuAg)_{12}(SbAs)_4S_{13}$
Pyrargyrite	Ag_3SbS_3
Proustite	Ag_3AsS_3
Polybasite	$Ag_{16}Sb_2S_{11}$
Stibnite	Sb_2S_3
Realgar	As_2S_3
(B) TRANSPARENT MINERALS	
Chlorite	$(MgAlFe)_{12}[(SiAl)_8O_{20}](OH)_{16}$
Quartz	SiO_2
Sericite	$KAl_2(AlSi_3)O_{10}(OH)_2$
K-feldspar	$KAlSi_3O_8$
Roscoelite	$KV_2(AlSi_3)O_{10}(OH)_2$
Ankerite	$(Ca,Mg,Fe)_2(CO_3)_2$
Dolomite	$CaMg(CO_3)_2$
Calcite	$CaCO_3$

and the horizontal extent ranges from 200 to 840 m. The dip of most of these lodes is generally towards the northeast, and ranges from 45 to 80°.

The dip and strike direction of the flatmakes is variable but the amount of dip generally ranges from 25 to 45°. Except the Prince-Dolphin flatmake, all the other flatmakes have relatively small dip and strike extent. The flatmakes are difficult to locate on the surface and are only recognised in mine workings or drill cores. Almost all the flatmakes follow shallow fractures in basalt.

Fracture filling is characteristic of these lodes although some replacement along the vein wall has occurred. In many instances open cavities ranging up to 30 cm in width have been observed with vein quartz crystals projecting from both sides. In general flatmakes have larger cavities than the steep lodes. Hot water having temperatures up to 63°C, has been observed flowing through these cavities (Denholm, 1967b).

In hand specimens, well grown vein quartz crystals form the bulk of the vein with thin bands of tellurides, sulphides and carbonates more common near the edge of the vein (Plates 6.1 to 6.6). Native gold is generally not observed in hand specimens and where seen it occurs as thread-like bodies. Silvery white prismatic crystals of tellurides or masses of such crystals are generally visible to the unaided eye. Calcite commonly occurs as scalenohedral or rhombohedral crystals growing over barren quartz (Plate 6.7).

Microscopically, the lode material contains a fairly large number of minerals (Table 6.2). Almost all of these have been confirmed by either X-ray diffraction or electron microprobe methods or by a combination of these two techniques. From an economic view point only a small number of these minerals are important. In the order of abundance they are sylvanite, petzite, krennerite, hessite, native gold, native tellurium and calaverite. Amongst the gangue minerals, the order of abundance is

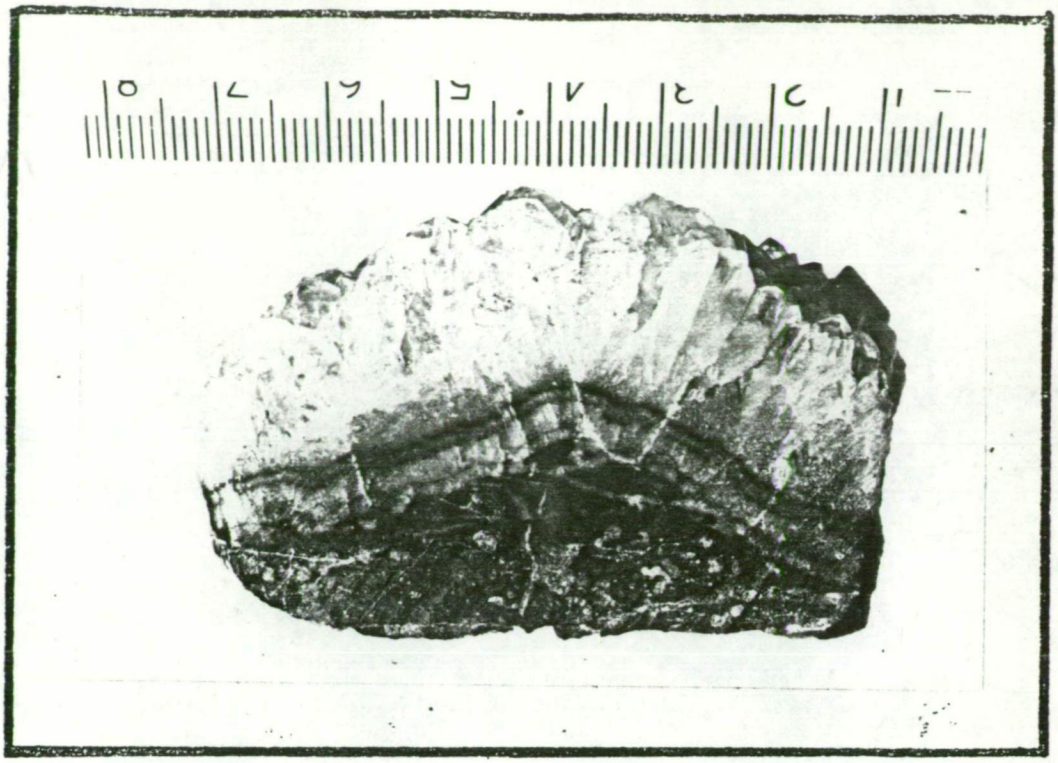

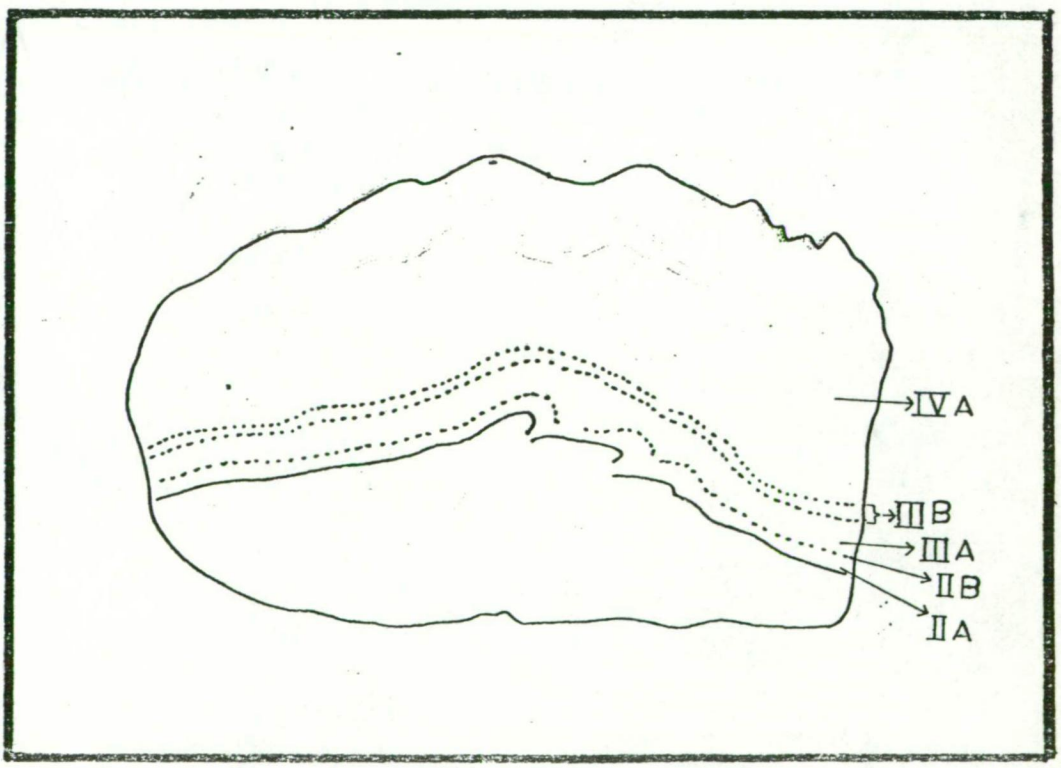

Plate 6.1 Crustification texture in vein quartz. Bands of white quartz are outlined by interveining bands of ore minerals. Roman numerals refer to the stages in the paragenetic sequence. Sample 103297. 166 flatmake, 7 level.

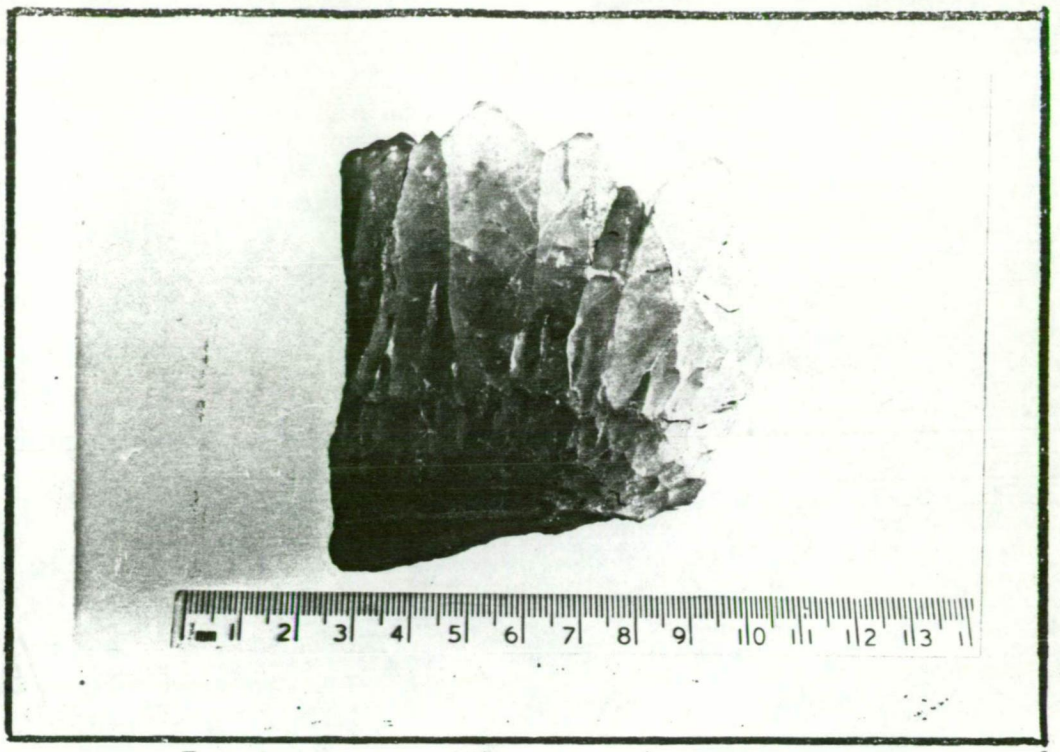

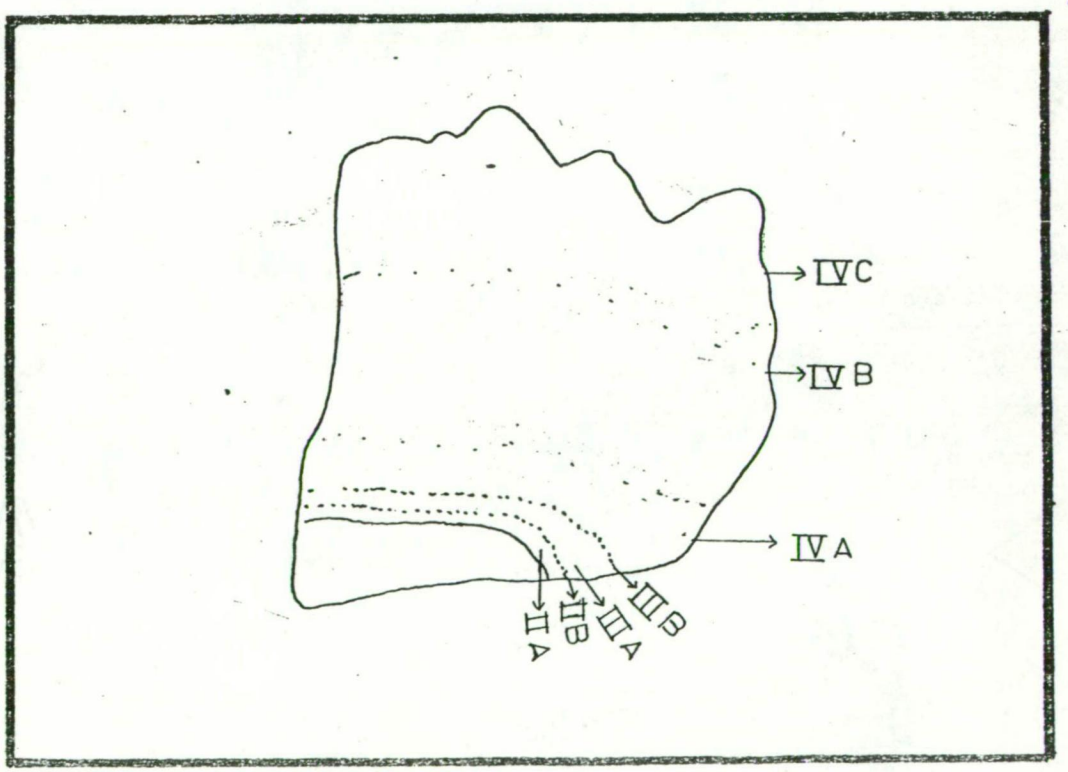

Plate
~~Fig~~. 6.2 Crustification texture in vein quartz. Bands of white quartz are outlined by bands of ore minerals. Roman numerals refer to stages in the paragenetic sequence. Stage IV quartz is nearly all barren. Sample 103296, 166 flatmake, 7 level.

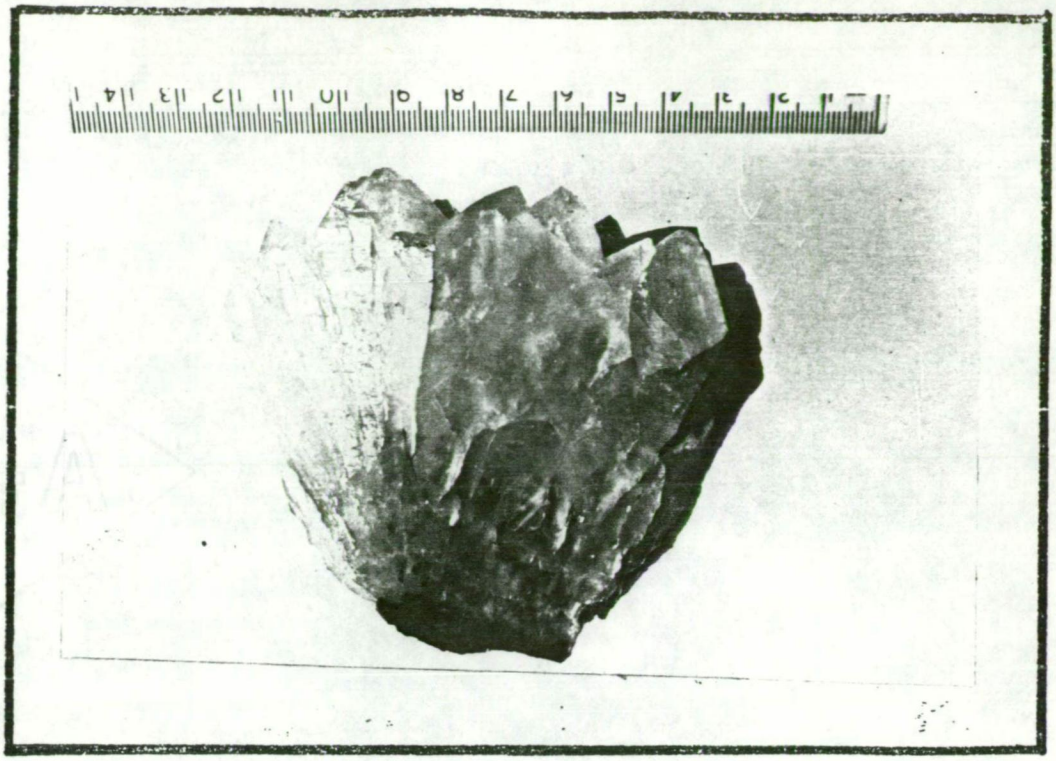

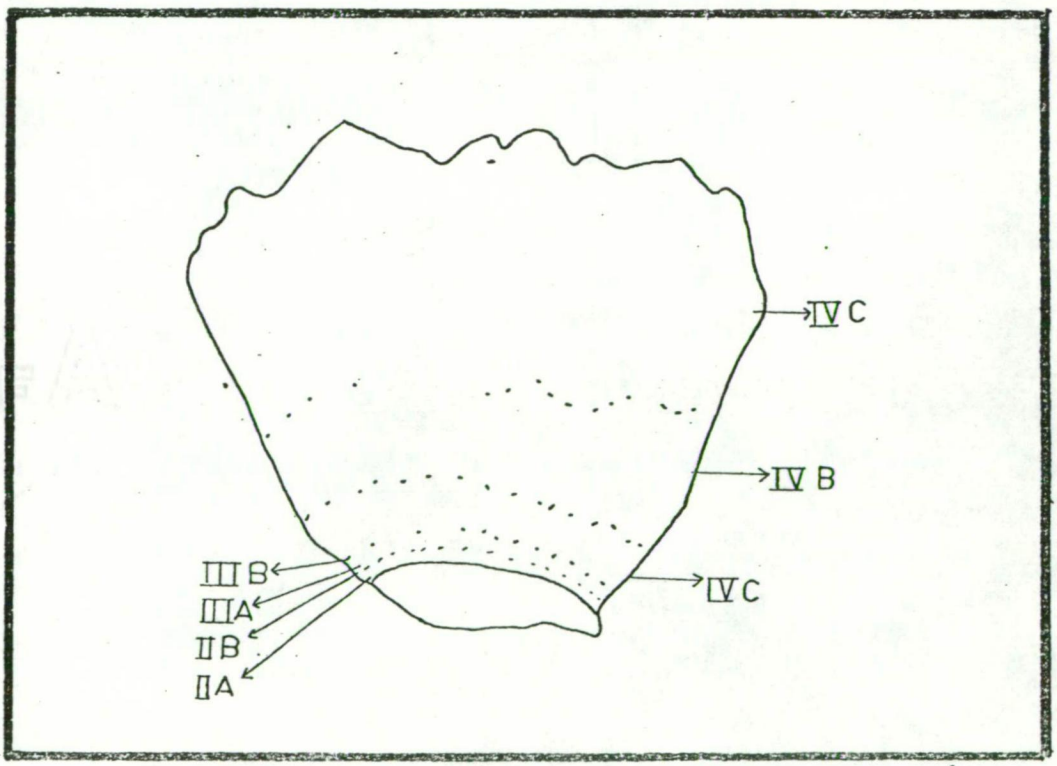

Plate 6.3 Crustification texture in vein quartz. Note the absence of dark bands of ore minerals between the various layers of quartz (cf. Plate 6.2). Both samples are from 166 flatmake. It is thought that one (Plate 6.2) formed against the footwall of the vein and collected ore minerals which were suspended in the ore-fluid and settling under gravity, while the other (Plate 6.3) formed against the hanging-wall. Sample 103296, 166 flatmake, 7 level.

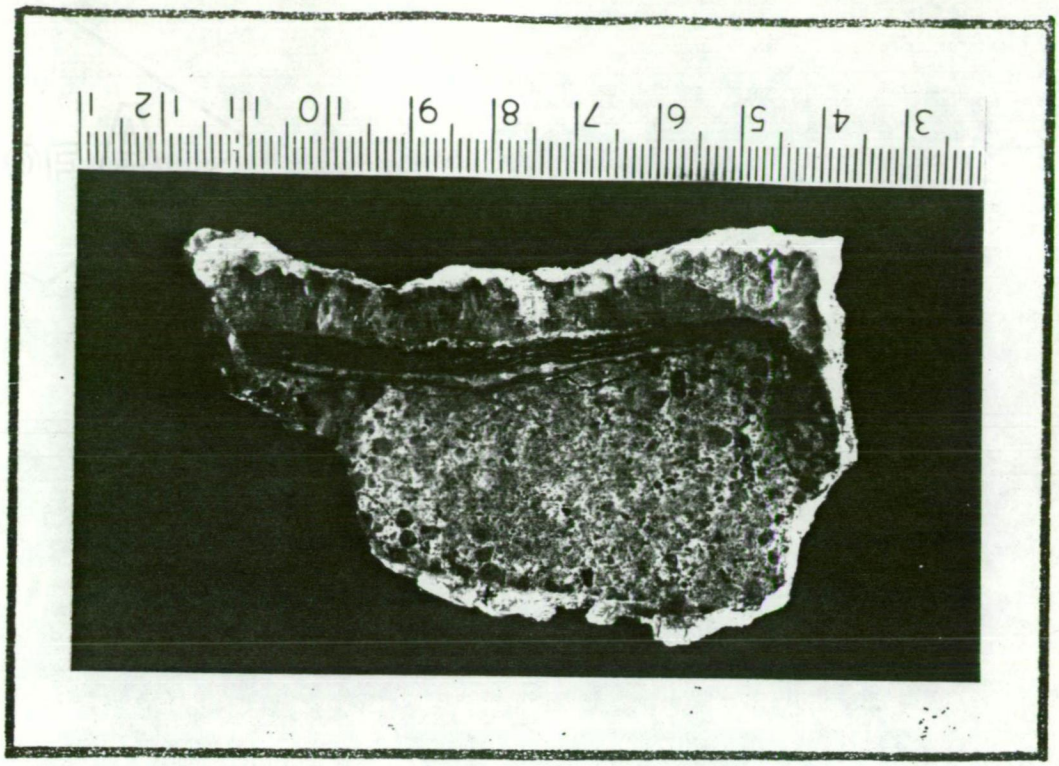

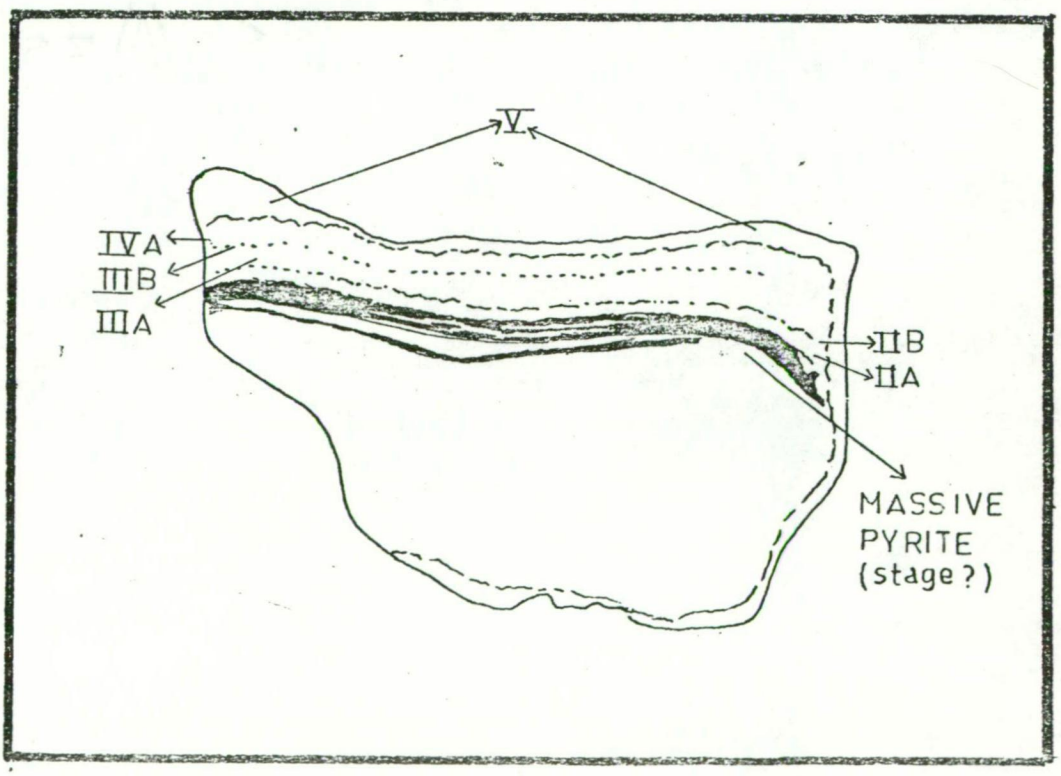

Plate 6.4 Crustification texture in vein quartz. Note the position of stage V calcite. The massive pyrite bands at the edge of the vein may represent a stage earlier than IIA (possibly IB). Note also the silicified pseudomorphs of pyroxene in the wall rock. Sample 103329, Crown lode, 14 level.

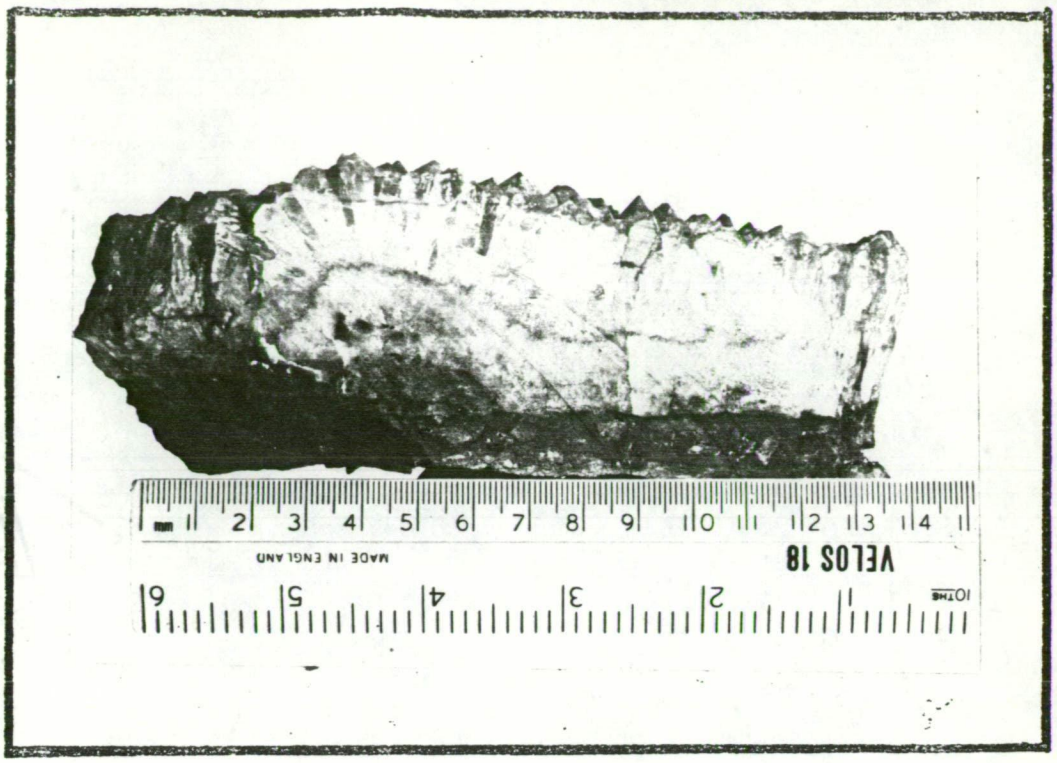

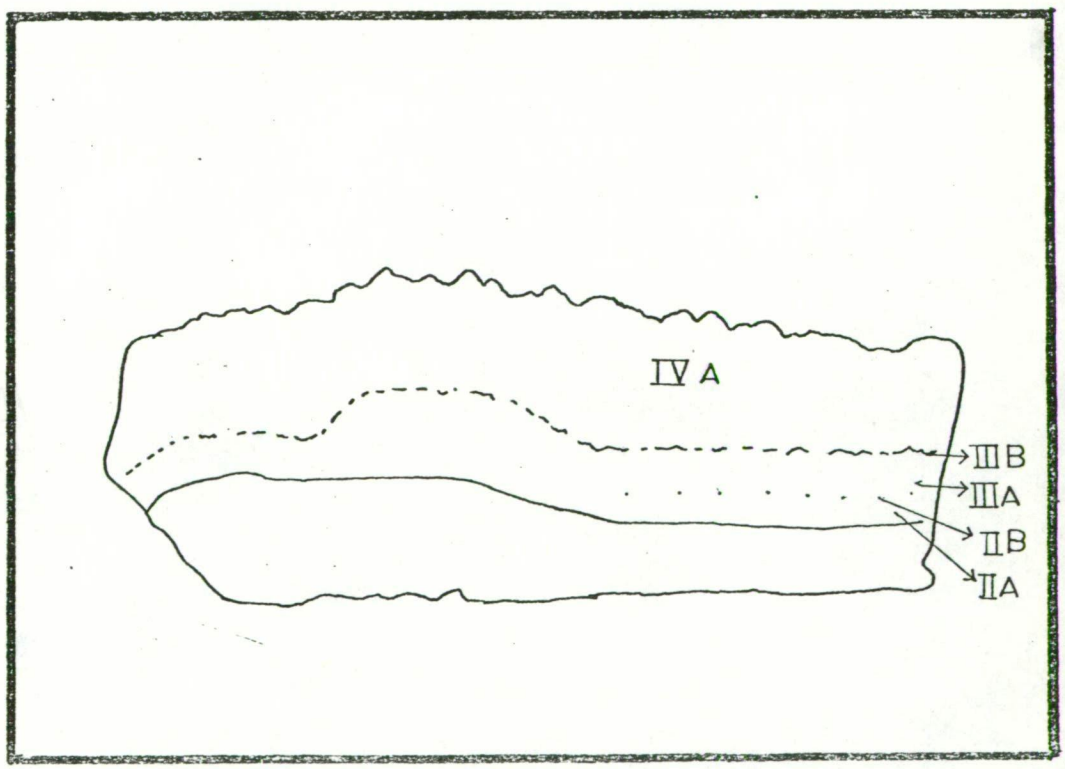

Plate 6.5 Crustification texture in vein quartz. Note that the dark band belonging to the stage IIB is virtually absent in this specimen. Sample 103368, Wunawali lode, 9 level.

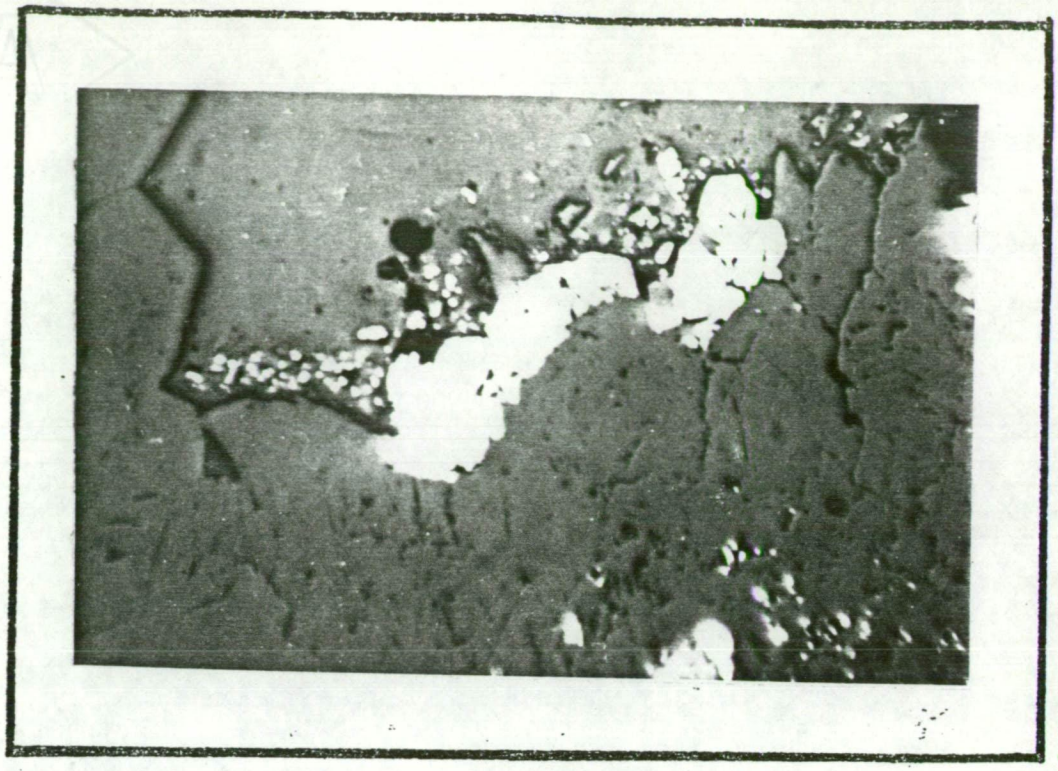

1 mm

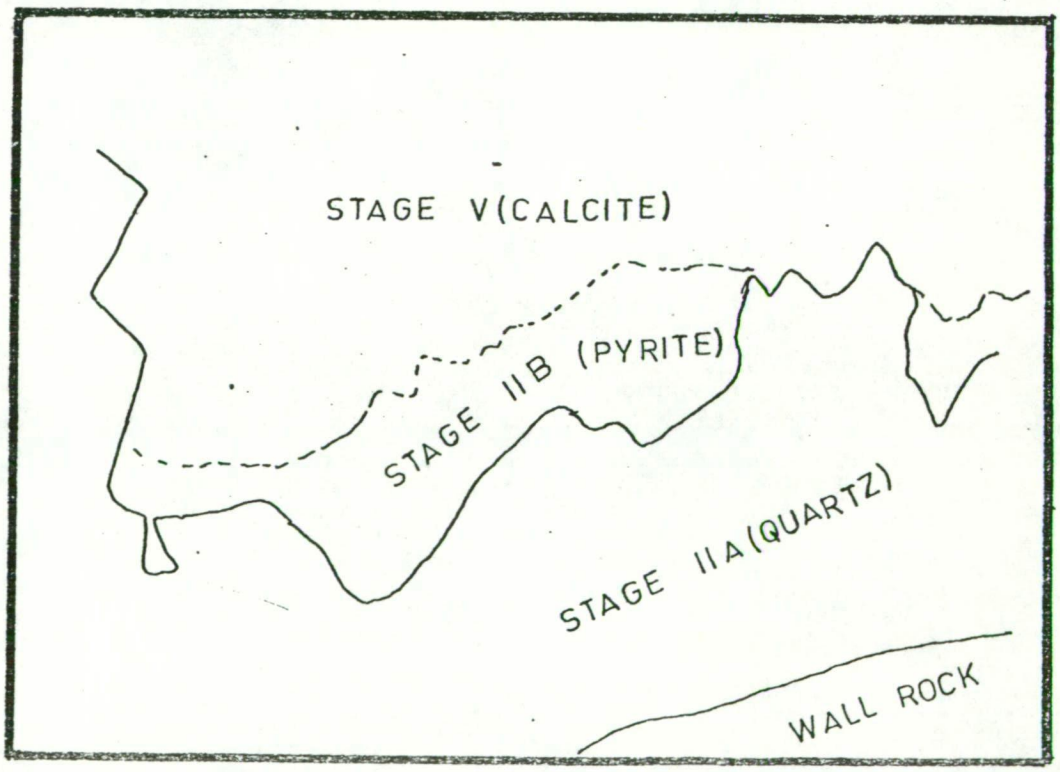

Plate 6.6 Photomicrograph showing grains of stage IIB pyrite between barren quartz of stage IIA and calcite of stage V. Sample 103410, Crown lode, 11 level.

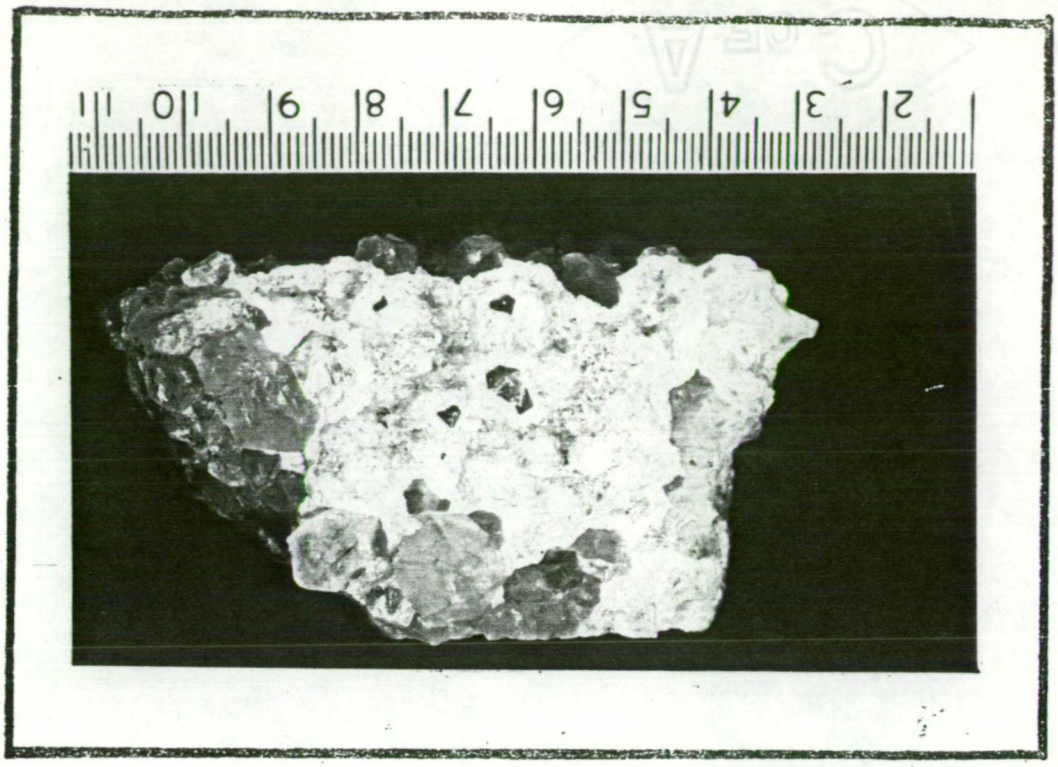

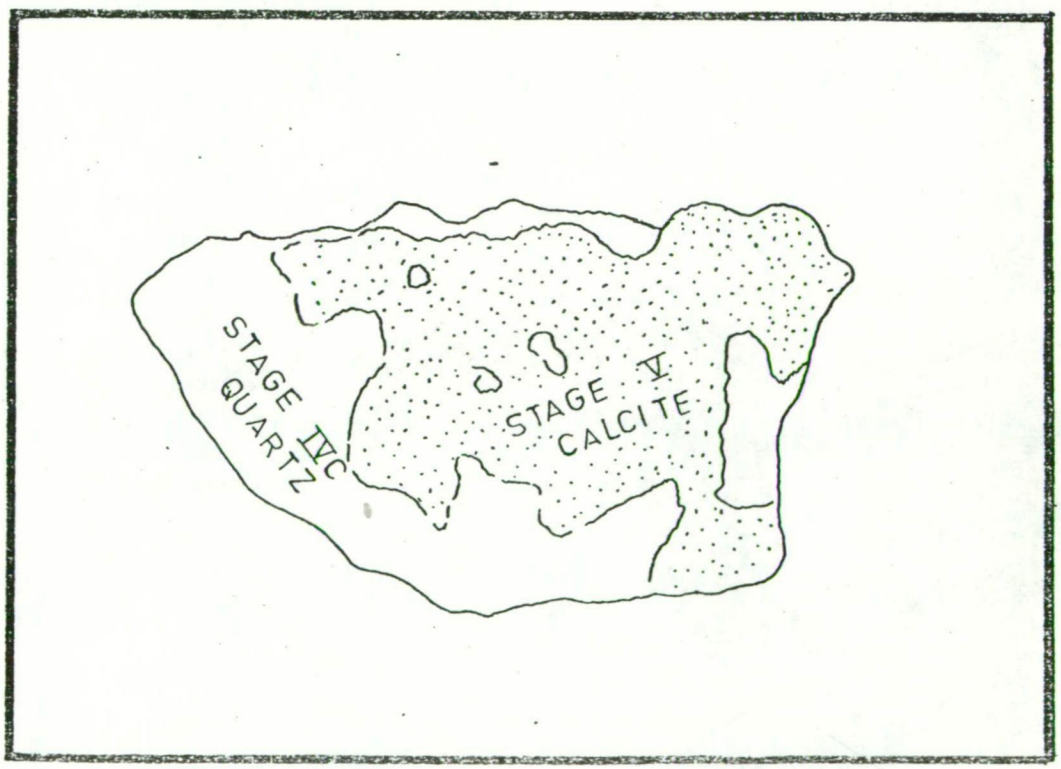

Plate 6.7 Photograph showing stage V calcite coating stage IVC quartz. Sample 103292, 166 flatmake, 9 level.

quartz, dolomite, calcite, sericite, potassium feldspar, chlorite and roscoelite. Quartz ranges up to 90% of the gangue material.

6.2 ALTERATION

The rock surrounding the vein is generally bleached. Starting from the centre of the vein to the fresh rock the following zones are usually observed.

Zone		Width	Description
I.	Barren carbonates	up to 0.5 cm	White coloured barren calcite.
II.	Barren quartz	up to 6 cm	White or amber coloured quartz with minor pyrite and dolomite.
III.	Mineralized vein quartz	up to 2 cm	Pale green coloured consisting mainly of quartz, dolomite, sericite, adularia, roscoelite, sulphides and tellurides.
IV.	Mineralized wall rock	up to 5 cm	Light greenish to white coloured consisting mainly of quartz, sericite, adularia, roscoelite, traces of chlorite, sulphides, tellurides and carbonates (mainly dolomite) rare ankerite and magnetite.
V.	Carbonatized wall rock	up to 1 m	Greenish grey with white spots of phenocryst minerals replaced by carbonates. Common minerals are ankerite, dolomite, quartz, chlorite, K-feldspar (orthoclase?), pyrite and rare magnetite.
VI.	Chloritized wall rock	variable	Greenish grey with light green spots. Common minerals are chlorite, tremolite, rare epidote, rare ankerite, magnetite and rare pyrite.
VII.	Fresh rock	variable	Greenish grey. Common minerals are pyroxene, plagioclase, olivine.

With several mineralized strands running parallel, the total width of zone I to zone V may range up to a few metres. If no other fracture

is observed, zone VI may extend up to about 30 m but this rarely happens as other fractures (may be weakly mineralized or even unmineralized) generally repeat the zonal sequence. As a result, completely fresh volcanics are seldom observed in the mine area.

Zone II and zone III can be grouped together as a zone of silicification, because quartz is the principal mineral (up to 99% by volume). Zone IV and part of zone III can be grouped together as a potassium silicate assemblage. Zone V is actually a zone of carbonatization, but in later discussions this has been grouped with zone VI under a general term of propylitic alteration (Chapter 8).

The quartz and dolomite of zone II and zone III contain a number of two-phase fluid inclusions, but inclusions in the calcite of zone I are rare and are usually single phase (water only).

6.3 PARAGENESIS

Stillwell & Edwards (1946) and Stillwell (1949) observed that sulphides were deposited very early in the paragenetic sequence, sylvanite being the first telluride to form and native tellurium the last. Hessite was in part contemporaneous with sylvanite and in part later.

Markham (1960) showed that the tellurides generally replace sulphides but he considered that all the tellurides were precipitated contemporaneously.

Forsythe(1967), after a comprehensive study of the ore minerals from the Crown lode, concluded that mineralization occurred in two stages, differing mainly in the nature of tellurides. The first stage includes calaverite, krennerite, sylvanite and native tellurium with possibly minor petzite. The second stage includes petzite, hessite and native gold.

Stumpfl (1970) examined a few samples from the Emperor mine and suggested that telluride mineralization probably occurred in two stages.

All of the above-mentioned studies are limited to the examination of polished slabs and no details are available on the temporal relationship amongst the transparent minerals. One hundred and twenty-three polished slabs from Forsythe's (1967) collection were re-examined during the present study and where required polished thin sections were prepared. In addition, 53 polished thin sections were prepared. Polished slabs prepared for fluid-inclusion studies were also examined for ore and gangue minerals. The generalised paragenetic sequence constructed from the present study is given in Fig. 6.5. In order to make this sequence more complete, alteration assemblages have been included. Five stages of ore and gangue mineral precipitation have been recognised. The first four of them have been further subdivided into substages on the basis of differences in either colour or in mineralogy. The system of numbering of the paragenetic stages is arbitrary, being based on an earlier field classification, I - V (i.e. the stages IA, IB, IIA, IIB ... are of equivalent rank and could have been labelled 1, 2, 3, 4 ...). Stages II and III commence with the precipitation of barren quartz and terminate with the precipitation of sulphides, tellurides and carbonates. Stage IV is essentially barren quartz with minor carbonates and sulphides. Stage V is essentially calcite and is devoid of any silicates, sulphides and tellurides. One feature of the paragenetic sequence is the almost continuous precipitation of quartz from Stage IB to Stage IV while precipitation of sulphides, tellurides and carbonates appears to be discontinuous.

Not all stages can be recognised everywhere and the proposed paragenetic sequence (Fig. 6.5) is composed from observations on samples from a number of lodes. For example, in the deeper parts of Crown lode (12 level and below) sub-stage IIB is not observed. Stage IV is inconspicuous in the majority of lodes, but is well developed in samples from the 166, Wunawali and 1010 lodes.

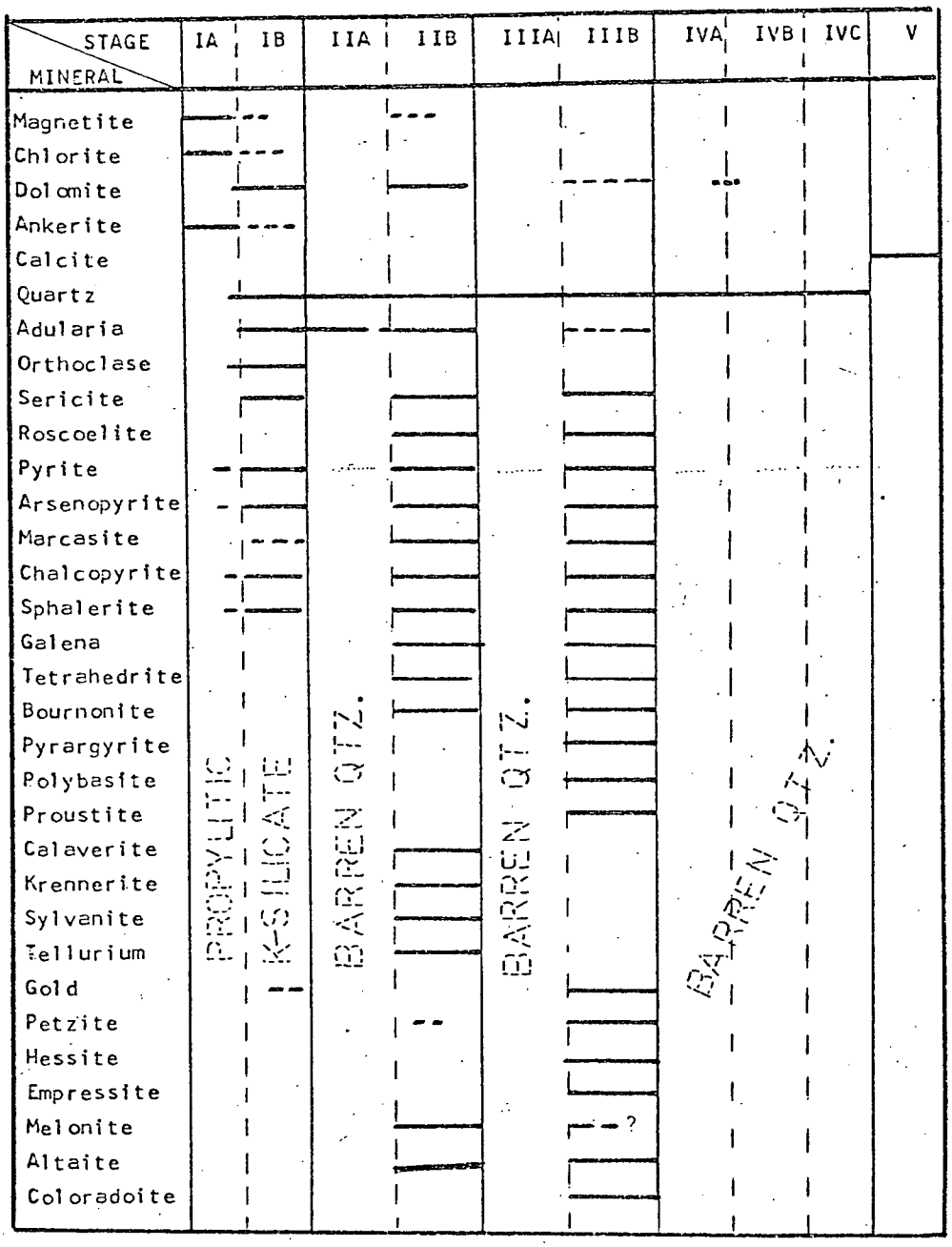

Fig. 6.5 Generalised paragenesis diagram for the lodes at the Emperor mine, Fiji.

The criteria used in the construction of the proposed paragenetic sequence are crustification and/or replacement textures. The former is used for deciding the age relationship in the vein and the latter in the mineralized wall rock.

6.3.1 Crustification Textures

The majority of the samples from the Emperor mine show well developed crustification textures (Plates 6.1 to 6.9; Fig. 6.6). Starting from the vein wall to the centre, the following sequence is typically observed:-

(a) A layer of white barren quartz up to about 5 mm thick

(b) A layer of sulphides, tellurides, carbonates and silicates up to about 1 mm thick. This layer contains sylvanite, calaverite and kremmenite as the principal tellurides and they are commonly associated with native tellurium. The most common sulphide is pyrite, followed in abundance by sphalerite, chalcopyrite and tetrahedrite. Amongst the carbonates, dolomite is most common but some ankerite also occurs. Amongst the silicates adularia, sericite and roscoelite are commonly observed. Other minerals occurring within this layer are galena, tetrahedrite, melonite, altaite, bournonite and coloradoite.

(c) A layer of white barren quartz up to about 1 cm thick. Rare pyrite is sometimes observed within this layer.

(d) A layer of sulphides, tellurides, carbonates and silicates up to about 1 mm thick. This layer contains petzite, hessite and possibly rare sylvanite as the most common tellurides. These tellurides often occur in close association with native gold. Sulphides, carbonates and silicates are the same as in layer (b).

(e) A layer of white barren quartz up to about 2 cm thick. Rare pyrite is sometimes observed within this layer.

	IIA	IIB	IIIA	IIIB	IV	V
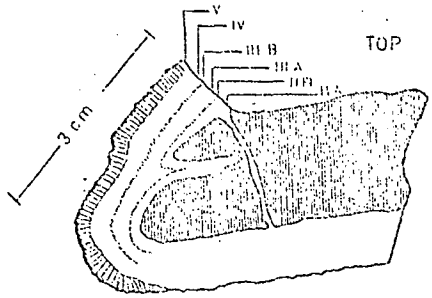 SAMPLE No. 103298	QUARTZ	QUARTZ DOLOMITE ROSCOELITE SYLVANITE KRENNERITE CHALCOPYRITE PYRITE SPHALERITE	QUARTZ	QUARTZ DOLOMITE NATIVE GOLD PETZITE CHALCOPYRITE PYRITE SPHALERITE	QUARTZ	CALCITE
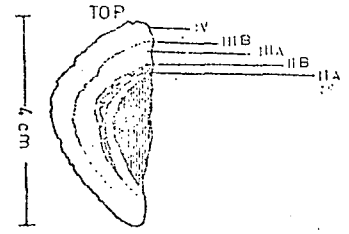 SAMPLE No. 103343	QUARTZ	QUARTZ DOLOMITE ADULARIA PYRITE SPHALERITE	QUARTZ	QUARTZ DOLOMITE ADULARIA PETZITE HESSITE PYRITE SPHALERITE	QUARTZ	
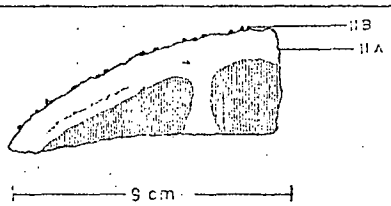 SAMPLE No. 103312	QUARTZ	QUARTZ TELLURIUM CALAVERITE KRENNERITE				
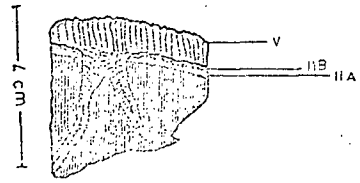 SAMPLE No. 103409	QUARTZ	QUARTZ DOLOMITE PYRITE KRENNERITE SYLVANITE				CALCITE
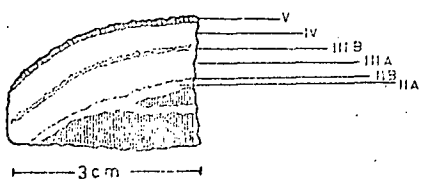 SAMPLE No. 103292	QUARTZ	QUARTZ DOLOMITE KRENNERITE PYRITE	QUARTZ	QUARTZ DOLOMITE ADULARIA PYRITE SPHALERITE	QUARTZ	CALCITE
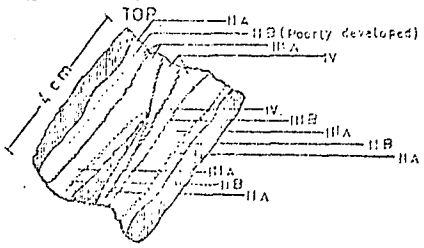 SAMPLE No. 103306	QUARTZ	QUARTZ DOLOMITE ROSCOELITE PYRITE	QUARTZ	QUARTZ DOLOMITE ROSCOELITE PYRITE	QUARTZ	

Wall rock
Vein quartz
Vein calcite

Fig. 6.6 Crustification textures in the samples from the Emperor mine. Roman numerals refer to stages of the paragenetic sequence.

(f) A layer of amber coloured quartz up to about 2 cm thick. A few isolated grains of pyrite are observed within this layer.

(g) A layer of white barren quartz up to about 2 cm thick.

(h) A layer of white barren calcite up to about 0.5 cm thick.

The crustification structures therefore clearly indicate two well defined periods of telluride precipitation, which also coincide with major sulphide and carbonate precipitation. Quartz precipitation was probably continuous from layer (a) to layer (g) as the quartz crystals have grown in optical continuity and layer (b) and layer (d), usually follow the growth zones within the quartz crystals.

As can be seen from Fig. 6.6, the development of these layers is incomplete in many of the samples and there are pronounced "unconformities". In sample number 103409, layer (b) is directly followed by layer (h). In sample 103312, on the other hand, precipitation was arrested during the time of layer (b). Layer (h) is absent in a number of samples.

The layers described above relate to the paragenetic sequence given in Fig. 6.5 as follows:-

Layer	Stage
(a)	IIA
(b)	IIB
(c)	IIIA
(d)	IIIB
(e)	IVA
(f)	IVB
(g)	IVC
(h)	V

An interesting feature of layers (b) and (d) is their asymmetric development (Fig. 6.6; samples 103298, 103343 and 103306; Plate 6.8) i.e. one side of the vein shows strong development of layer (b) and layer (c) while the other side is practically devoid of these layers.

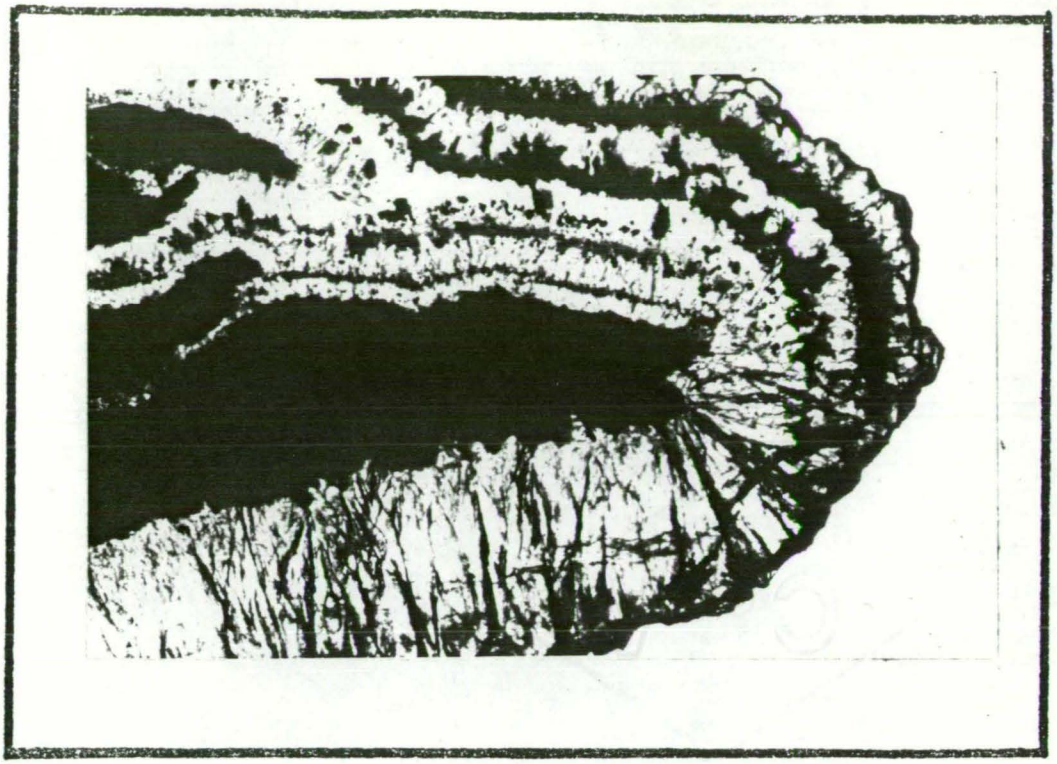

1 cm

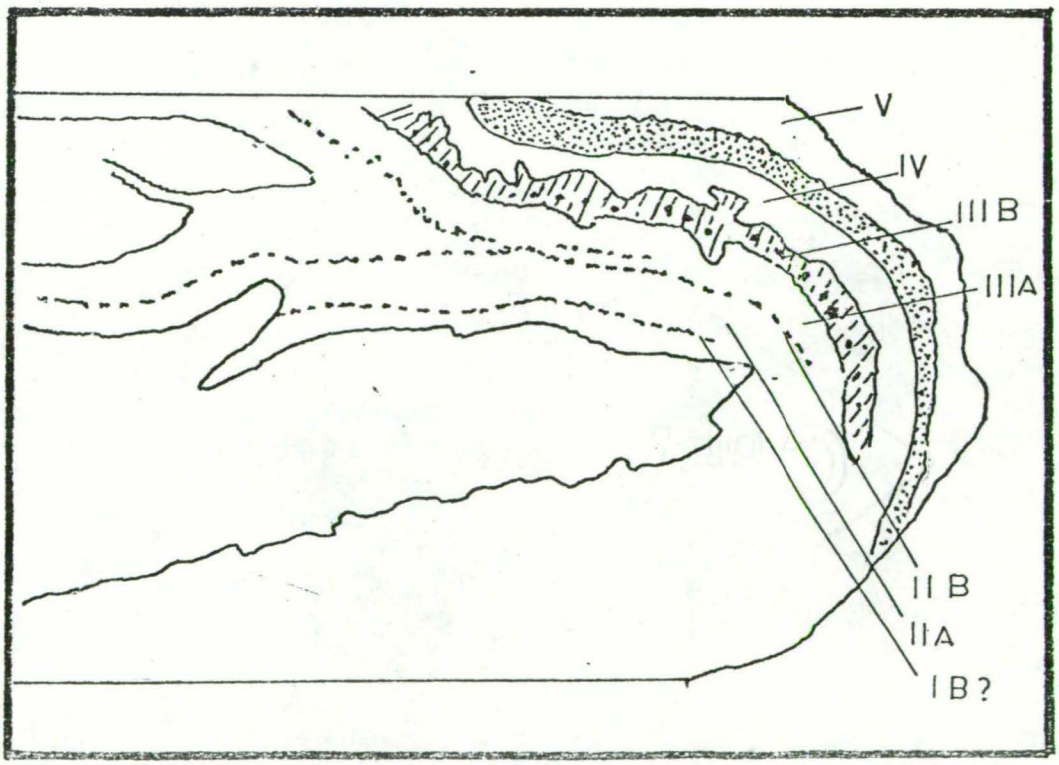

Plate 6.8 Photomicrograph showing crustification texture in vein quartz. Stage IIIB includes dolomite (hatched in the sketch) and pyrite (small black dots) and appears as a thick dark layer in the photograph. The heavily stippled layer in the sketch is the contact between stage V calcite and stage IV quartz and appears as a thick black layer in the photograph due to total internal reflection. The section is about 1.5 mm thick. Sample 103298, 166 flatmake, 7 level.

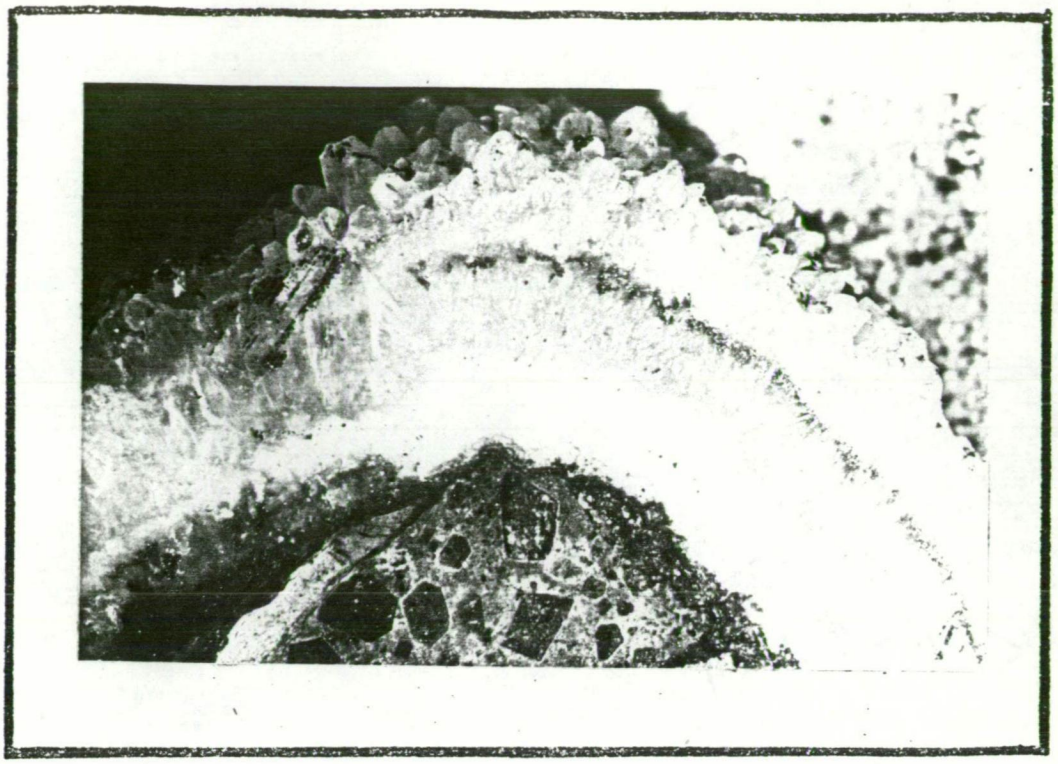

1 cm

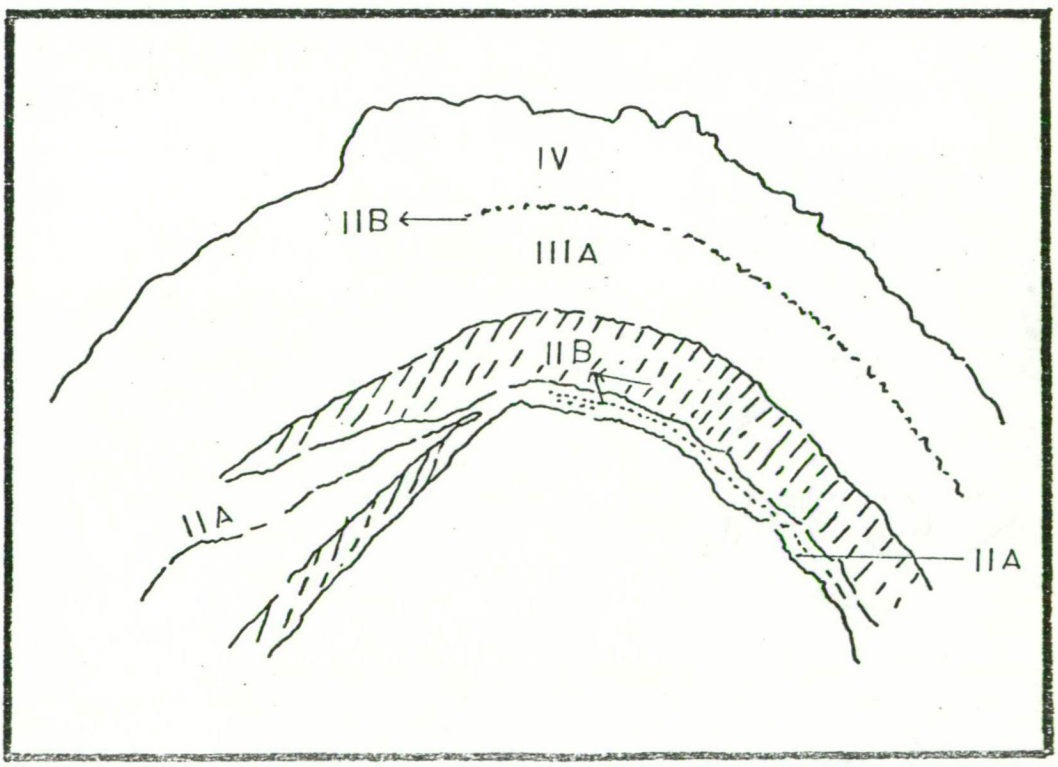

Plate 6.9 Photomicrograph showing crustification texture in vein quartz. Hatched areas represent dolomite which appears as a white band in the photograph. The dolomite vein in the wall rock probably belongs to stage IIB. For mineralogy refer to Fig. 6.6. Note the asymmetric development of stage IIIB and quartz-carbonate pseudomorphs after pyroxene in the wall rock. Sample 103343, 608 flatmake, 7 level.

Barton *et al.* (1971) have described similar features in the samples from the OH vein, Colorado, due to gravitational settling. Although oriented samples were not collected in the present study, it is suggested that gravitational settling may be the main cause of the asymmetrical development of layers (b) and (d). Assuming this to be the case, the top of the samples is indicated in Fig. 6.6.

6.3.2 Replacement Textures

Replacement textures have been described in great detail by Forsythe (1967). These textures are most common in the mineralized rocks surrounding the veins. They indicate a paragenetic sequence similar to the one constructed from the crustification textures.

Amongst the opaque minerals, pyrite is the first mineral to form and much of it is probably formed at the expense of pre-existing magnetite. An interesting feature of this replacement is seen in sample 103428 (Plates 6.10, 6.11). In this sample magnetite grains are first replaced by pyrite, which in turn is veined by magnetite, which is then again veined by a later generation of pyrite. At the immediate base of the mineralised vein, however, magnetite is completely replaced by pyrite.

Among sulphides, early pyrite, chalcopyrite, sphalerite and tetrahedrite are seen to be veined or enclosed by later sulphides which in turn are veined or enclosed by a still later generation of sulphides. Thus there appear to be at least three generations of sulphide deposition.

Tellurides generally occur as vughs filling (Plate 6.13). Among them, deposition of native tellurium, calaverite, krennerite and sylvanite appears to take place first. These tellurides are often observed to be veined by petzite, hessite and native gold. An interesting case is seen in sample 103404 (Plate 6.14) in which a sylvanite crystal, the optical continuity of which is apparent from the orientation of twin lamellae, is being replaced by petzite. This crystal of sylvanite is completely

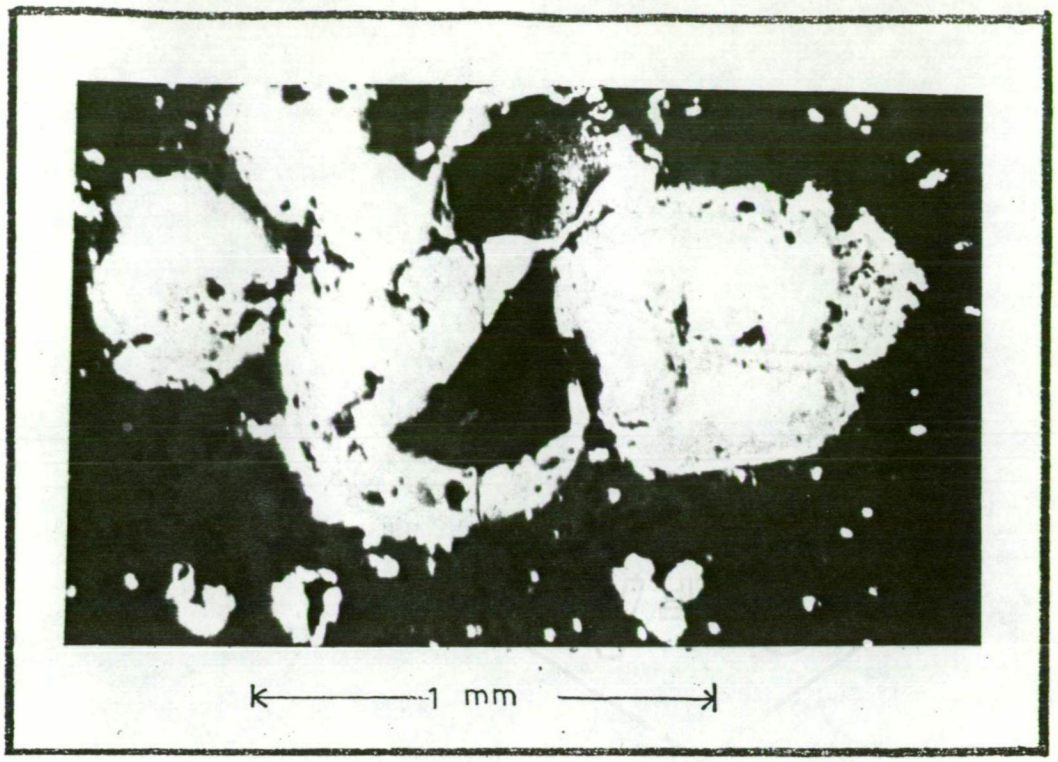

Plate 6.10 Photomicrograph showing replacement of magnetite grains (dark grey) by pyrite (light grey). Note that after the replacement of magnetite by an early stage of pyrite (the central core), magnetite was again precipitated (the rims and veins). This was then veined and enclosed by an even later stage of pyrite. Sample 103428, Crown lode, 14 level.

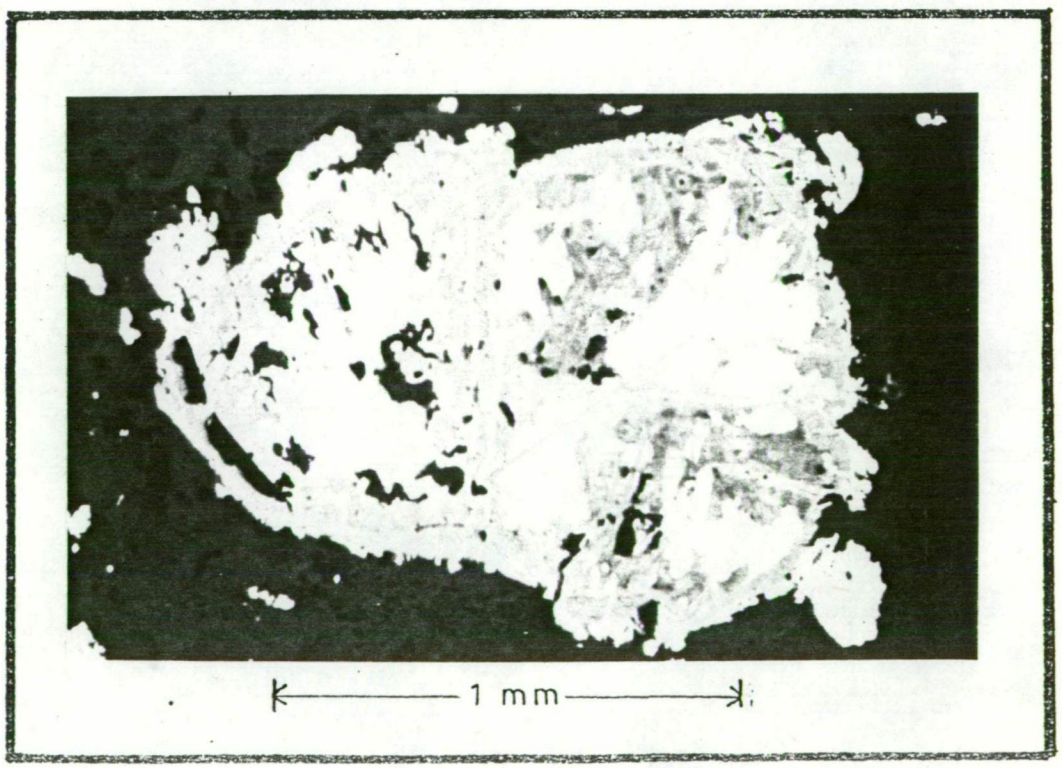

Plate 6.11 Description same as for Plate 6.8.

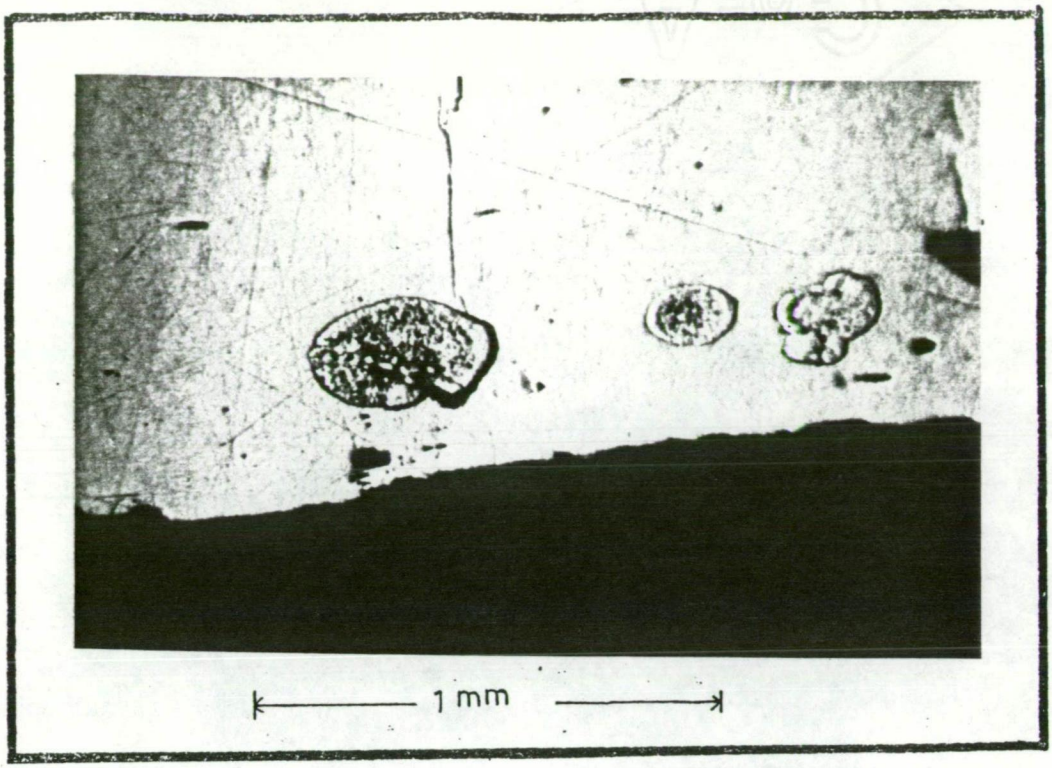

Plate 6.12 Photomicrograph showing rounded grains of melonite in a crystal of native tellurium. Sample no.F-311 from Forsythe's (1967) collection, 608 flatmake, 8 level.

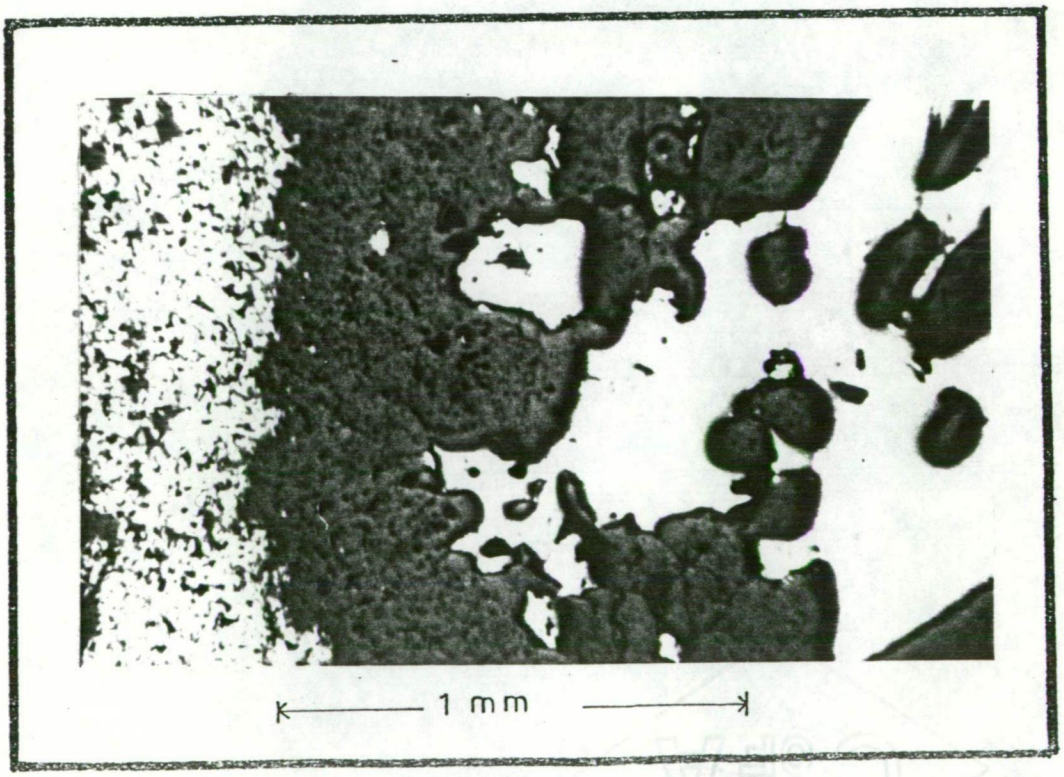

Plate 6.13 Photomicrograph showing wall rock pyrite at the edge of a vein (white, to left); vein quartz (dark grey) and krennerite. Note the habit of the krennerite which fills vugs. Sample 103345, 1600 flatmake, 10 level.

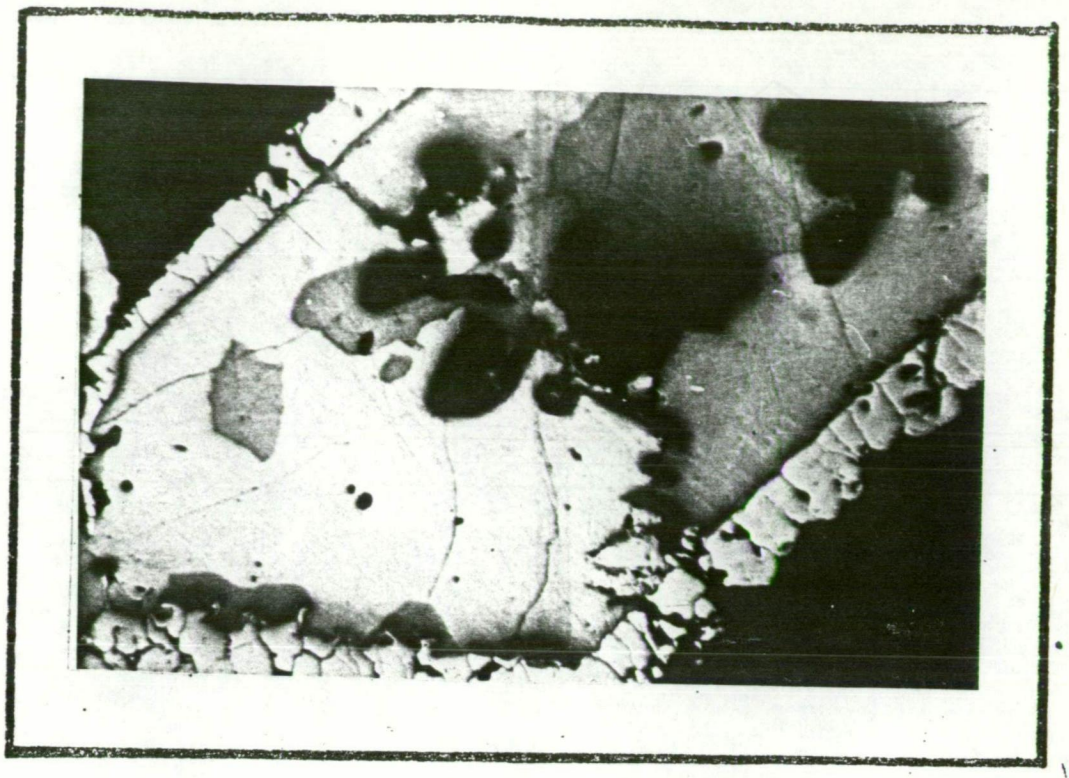

1 mm

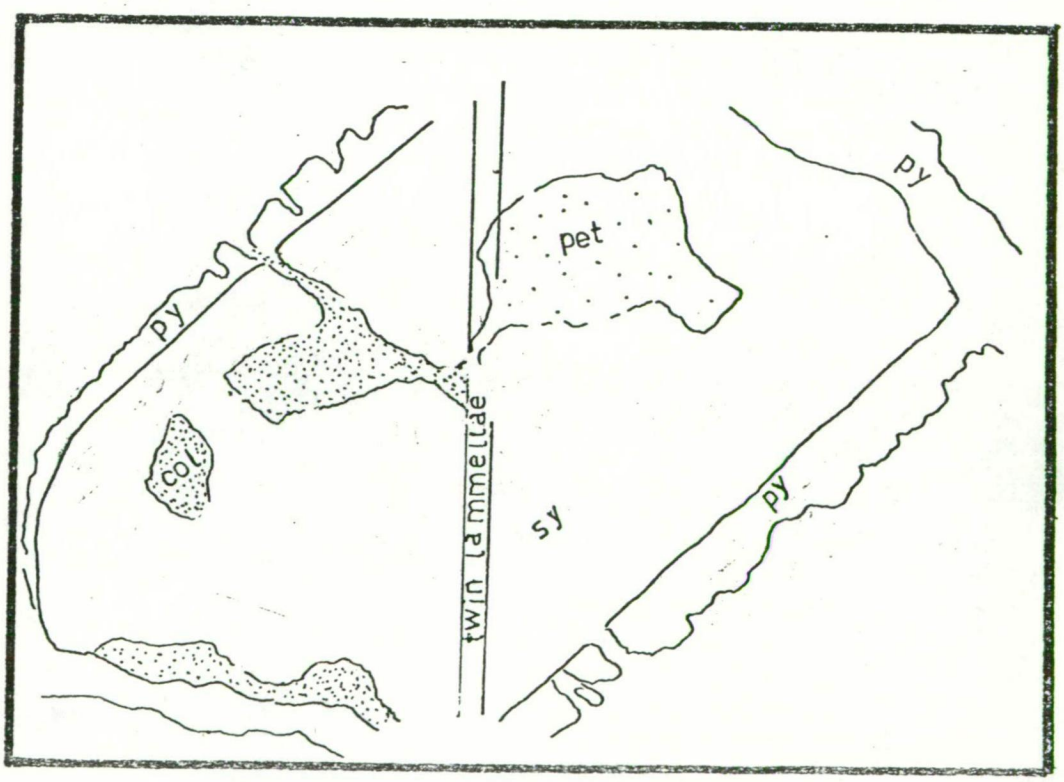

Plate 6.14 Photomicrograph showing replacement of sylvanite (sy) by petzite (pet) and coloradoite (col). All three minerals are enclosed by a later generation of pyrite (py). Note the disruption of the twin lamellae of the single crystal of sylvanite by later petzite and coloradoite. Sample no. F-109 from Forsythe's (1967) collection, Crown lode, 12 level. Black areas represent holes in the section.

enclosed by a later generation of pyrite. Native gold appears to be latest amongst the ore-minerals as it is often observed as veins in petzite and/or hessite (sample 103433). Melonite generally occurs as rounded grains in native tellurium crystals (Plate 6.12) and much of it is was probably precipitated during stage IIB.

Amongst the transparent minerals, chlorite appears first, and as the mineralised vein is approached, this is first replaced by ankerite which in turn is replaced by an assemblage containing quartz, sericite, roscoelite and K-feldspar (both adularia and orthoclase). In a number of samples, veins of late-stage quartz are often observed traversing sericitized and/or carbonatized phenocrysts. In sample 103338, for example, a sericitized feldspar phenocryst is traversed by a vein of late-stage quartz (Plate 5.3).

6.4 ORE-MINERAL ZONING

From a comprehensive study of ore minerals from the Crown lode and analyses of Ag, Au and Te, Forsythe (1967, 1971) described the following changes in the telluride assemblage with depth:

(i) Below a line midway between 12 and 13 level (depth about 400 m) native tellurium, calaverite, sylvanite and krennerite, altaite and melonite are not observed.

(ii) Petzite, hessite and native gold are distributed throughout the lode, but are more common in the deeper section of the lode.

He also analysed a number of samples for Au, Ag and Te. These analyses showed that:-

(iii) The Te/Au + Ag weight ratio is nearly constant (average about 0.5) up to 12 level, but increases sharply above this level (average about 1.5).

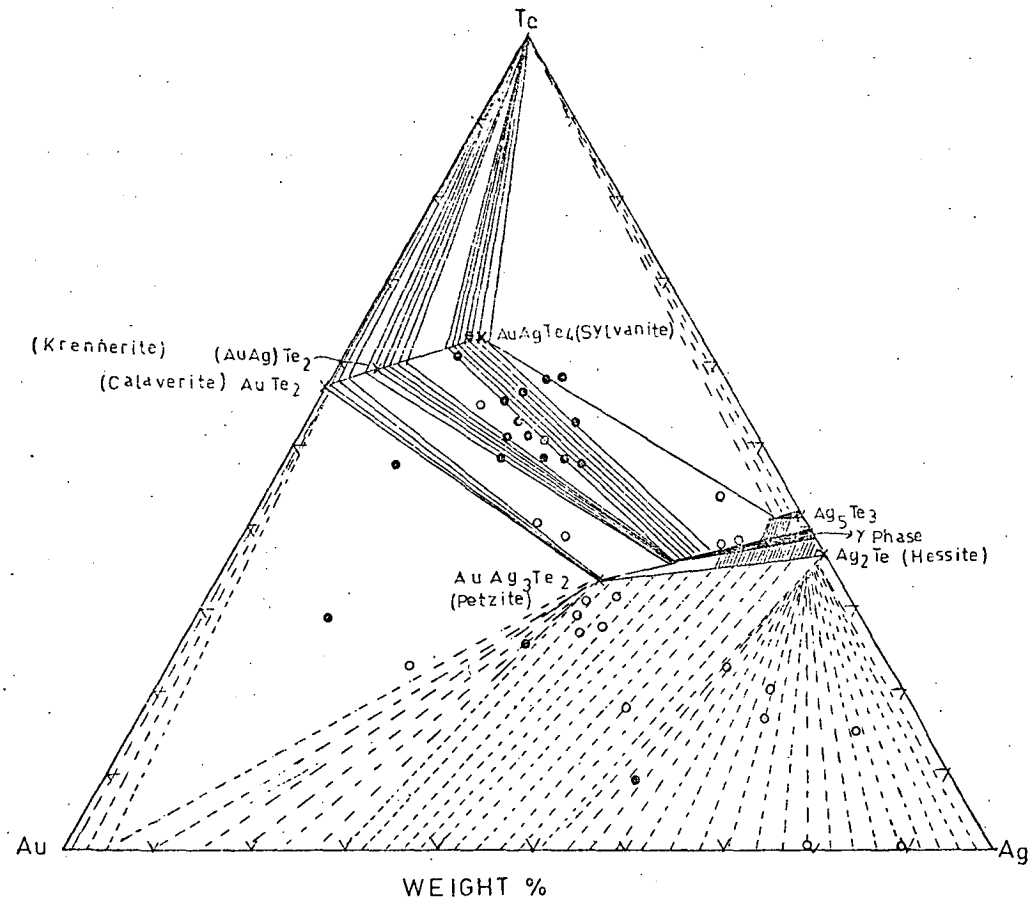

Fig. 6.7 A plot of the bulk composition of samples from the Crown lode on an Au-Ag-Te triangle. Open circles: samples from 13 level and below; filled circles, samples from 12 level and above. Also shown are the phase relationships for the 290°C isotherm of the synthetic system Au-Ag-Te, after Cabri(1965). All analyses from Forsyth(1967). Note that the majority of samples from 12 level and above indicate sylvanite, krennerite and native tellurium as the predominant stable minerals, while the majority of sample from lower levels indicate hessite, petzite and native gold (electrum) as the stable minerals.

(iv) The Te/Ag weight ratio is nearly constant (average about 0.5) up to 12 level but increases sharply above this level (average about 3).

(v) The Ag/Au weight ratio is nearly constant (average about 2.5) up to about 12 level but decreases sharply above this level (average about 1).

It is apparent from a plot of the analyses given in Forsythe (1967), shown in Fig. 6.7, that there is very pronounced change in the abundances of Au, Ag and Te with depth. The experimental tie lines in the system Au-Ag-Te as observed by Cabri (1965) are also shown in Fig. 6.7. This figure suggests that the upper level assemblage should be dominated by calaverite, sylvanite, krennerite and native tellurium while the assemblage from lower levels should be dominated by petzite, hessite and Au-Ag solid solutions. This is precisely what is found.

6.5 THE OPAQUE MINERALS

The opaque minerals from the Emperor mine have been described in a number of previous studies (e.g. Stillwell & Edwards, 1946; Stillwell, 1949; Forsythe, 1967, 1971; Markham, 1960; Stumpfl, 1970).

Magnetite

Magnetite is fairly widespread in the propylitic rocks. It is grey coloured with a brownish tint, isotropic and generally occurs as idiomorphic cubes and octahedrons. Electron microprobe spectra show the presence of considerable amounts of vanadium and titanium.

With the advancement of alteration magnetite is gradually replaced by pyrite. Replacement starts at the margin of the magnetite grain and in many cases the central core is unreplaced. Alongside mineralized veins most of the magnetite is replaced by pyrite. In some cases alternate rings of magnetite and pyrite are observed within a single grain. In some sections (e.g. sample 103327) all stages of magnetite replacement

are observed within a distance of about 4 cm. Sample 103428 (Plates 6.10, 6.11) shows magnetite grains replaced by pyrite, which in turn is replaced by magnetite and a yet later generation of pyrite replaces the magnetite again.

Anatase

Anatase is fairly common in the propylitic rocks but has not been observed in the vicinity of mineralized rocks. It is pinkish brown in colour and occurs as rhomb-shaped idiomorphic grains. In thin sections it is brown in colour. In some cases it is found as clusters surrounding partly replaced magnetite grains.

Pyrite

Pyrite is the most common sulphide in the Emperor mine. Forsythe (1967) estimated it to be about 2.1 wt. % of the ore.

Two types of pyrite can be recognised:-

(a) Pyrite formed as a result of replacement of magnetite presumably without addition of iron.

(b) Pyrite formed independently of magnetite with addition of both iron and sulphur from the hydrothermal solutions.

Type (a) pyrite is more common in the propylitic rocks while type (b) is confined to the base of mineralized veins and between barren quartz layers.

Marcasite

Marcasite occurs as laths (commonly in clusters) up to 1 mm in length and closely associated with type (b) pyrite.

Arsenopyrite

Arsenopyrite is a fairly common mineral and it occurs as diamond-shaped anisotropic grains. It is most commonly associated with type (b) pyrite.

Chalcopyrite

Chalcopyrite occurs as irregular laths. It is a common mineral but subordinate in amount to sphalerite and tetrahedrite. As with pyrite, chalcopyrite precipitation occurred in four distinct stages but it appears to be more common during the later stages (Fig. 6.5).

Sphalerite

Sphalerite is fairly widespread. It is grey, isotropic and shows internal reflections in shades of brown and yellow. In thin sections it is yellowish brown in colour. Fluid inclusions were noted in a few grains but they were too small to be of any practical use. Sphalerite is commonly associated with chalcopyrite and pyrite and within a particular stage (crustification layer) all three minerals appear to be in equilibrium. They usually occur in contact with each other.

Electron microprobe analyses of sphalerite carried out during the present study indicate the presence of minor amounts of copper, iron, cadmium and chromium (Appendix D.1).

Occurrences of chalcopyrite inclusions have been observed in a few grains but in most cases the sphalerite is free of such inclusions.

Galena

Galena is a rare mineral and is recognised in only a few specimens. It is generally pure PbS but in some grains minute amounts of silver were noted in the electron microprobe spectrum.

Galena is commonly associated with altaite. Most of the galena is associated with type (b) pyrite, tetrahedrite, chalcopyrite, and with both generations of tellurides (i.e. substages IIB and IIIB).

Tetrahedrite-Tennantite

With the help of electron-microprobe analysis and X-ray diffraction studies, Forsythe(1967) calculated the following formula for the mineral present at the Emperor mine:-

$$(Cu_{10.125}Ag_{1.875})(Sb_{2.2}As_{1.88})S_{13}$$

He suggested that the mineral is argentian tetrahedrite (friebergite).

It is observed in most of the specimens and occurs generally in association with type (b) pyrite. Commonly earlier pyrite is enclosed by later tetrahedrite. Other minerals commonly associated with tetrahedrite are chalcopyrite, sphalerite, bournonite, proustite, pyrargyrite, polybasite, petzite, hessite, native gold and altaite.

Bournonite

Bournonite is rare. It is grey or bluish tinted greenish grey, anisotropic and characteristically exhibits polysynthetic twinning.

It is commonly associated with tetrahedrite, pyrite, altaite, chalcopyrite, petzite, hessite and native gold.

Stibnite

Previous workers have reported the presence of rare stibnite from near-surface workings (Garetty, 1936; Stillwell, 1949; Forsythe, 1967).

Groups of radiating needles and felted masses of stibnite were observed in a specimen collected from the Cardigan open cut (sample 103452).

Pyrargyrite, proustite, polybasite and pearsite

These minerals have been described by Forsythe (1967) but they have not been confirmed in this study. According to Forsythe they are very rare and are probably more common in the deeper part of the Crown lode. They are associated with silver-rich telluride and native gold.

Realgar

Realgar was reported by Forsythe (1967) in a near-surface sample. It is probably of supergene origin.

Calaverite

Calaverite is a rare mineral in the Emperor mine and it is only found in 12 level and above (Forsythe, 1967). It is cream coloured, anisotropic and shows distinct reflection pleochroism. Anisotropy is considerably weaker than that of sylvanite and slightly greater than

krennerite. Sylvanite generally shows lamellar twinning and can be easily distinguished from calaverite.

Calaverite is seen in contact with krennerite, coloradoite and native tellurium. Coloradoite and petzite occur as veinlets and marginal areas in calaverite and are therefore younger in paragenesis. Forsythe (1967) observed native gold in association with calaverite and considered it to be a possible oxidation product. The sulphide associates of calaverite are pyrite, chalcopyrite, sphalerite and tetrahedrite.

Krennerite

Krennerite is observed in a number of specimens from the upper levels. It is cream coloured, anisotropic and shows weak reflection pleochroism.

It is found in association with sylvanite, calaverite, native tellurium and rarely with petzite. Vein-like and marginal areas of petzite, hessite and coloradoite are commonly observed (e.g. sample 103386). Krennerite grains are generally completely enclosed by later pyrite.

Electron microprobe analyses of several krennerite grains are given in Appendix D.2.

Sylvanite

Sylvanite is the most common and easily identifiable telluride. It is common in the samples from the upper levels (12 level and above). It is cream coloured, strongly anisotropic and commonly shows lamellar twinning. Reflection pleochroism is fairly strong.

It is commonly associated with krennerite, petzite and native tellurium. In the majority of the specimens studied hessite, petzite, empressite and coloradoite are observed to be replacing sylvanite and are therefore younger. Altaite and melonite were locally intergrown with the replacing minerals.

Electron microprobe analyses of several grains of sylvanite were carried out during the present study (Appendix D.2). In comparison with other deposits, sylvanite from the Emperor mine is low in silver (Markham, 1960; Cabri, 1965; Stumpfl, 1971). Cabri (1965) suggested the use of the silver content of sylvanite to indicate the temperature of ore deposition when sylvanite occurs in equilibrium with a more silver-rich phase e.g. petzite or hessite. The temperatures estimated from Cabri's (1965) calibration curve for the Emperor mine sylvanite are much higher (>350^{o}C) than those obtained from fluid-inclusions in the associated quartz. This probably indicates that the sylvanite is not in equilibrium with petzite or hessite and this is consistant with the textural data, which usually indicates veining relationships.

Empressite

Empressite is a rare mineral in the Emperor mine. It is grey in colour, highly anisotropic and shows distinct reflection pleochroism.

It is closely associated with petzite, hessite and native gold and is observed replacing the early gold-rich tellurides.

Petzite

Petzite is fairly common mineral. It is pale grey in colour, very soft and weakly anisotropic. It resembles hessite in colour but hessite is highly anisotropic. It occurs in close association with hessite and native gold. Amongst the sulphides, tetrahedrite, chalcopyrite and sphalerite are common associates. Late pyrite is often observed to be enclosing petzite. In some cases sylvanite grains having veins of petzite are completely enclosed by pyrite (Plate 6.13). Some of the native gold is probably later than petzite as it veins the petzite grains.

Unlike calaverite, krennerite, sylvanite and native tellurium petzite is observed throughout the vertical extent of the mine workings.

Analyses of several grains of petzite are given in Appendix D.2

Hessite

Two polymorphs of hessite are known. At room temperature, hessite is possibly orthorhombic (Rowland & Barry, 1951), probably monoclinic (Fruech, 1959), but certainly anisotropic (Cabri, 1965). At temperatures above 145°C, hessite is cubic but inverts to orthorhombic or monoclinic upon cooling. In this process it may retain cubic crystal form but not structure. Due to inversion from high to low temperature the mineral shows either mottled, irregular or lamellar textures. The presence of such textures puts a minimum limit on the temperature of deposition of 145°C.

Hessite it subordinate in amount to petzite. It is observed throughout the vertical extent of the mine working. It is brownish grey in colour, very soft, takes rather poor polish and is strongly anisotropic.

Hessite is commonly associated with petzite, native gold and coloradoite. In many samples it is observed replacing calaverite, krennerite, sylvanite and native tellurium. Amongst the sulphides, tetrahedrite, chalcopyrite and sphalerite are the most common associates.

Coloradoite

Coloradoite is rare. It is greyish white, isotropic and takes very good polish. It is commonly associated with petzite, hessite and native gold. The electron microprobe spectrum shows mercury and tellurium to be the only elements present.

Melonite

Melonite is a very rare mineral. It is light grey to cream coloured with a pinkish tint and is distinctly anisotropic. It is commonly associated with native tellurium (sample 103459; Plate 6.12), calaverite and krennerite. Amongst the sulphides, chalcopyrite is the most common associate.

The electron microprobe spectrum of this mineral shows tellurium and nickel to be the only elements present.

Altaite

Altaite is also rare. It is creamy white in colour, isotropic and resembles native tellurium, but the non-basal sections of native tellurium are distinctly anisotropic.

Forsythe (1967) described three associations of altaite from the Emperor mine:-

(a) Bournonite-altaite-chalcopyrite-tetrahedrite

(b) Altaite-galena

(c) Altaite-native tellurium.

The latter two associations are used in Chapter 10 to constrain the depositional environment. Altaite is observed in association with both the gold-rich and silver-rich tellurides and was probably precipitated throughout the paragenetic sequence.

Electron microprobe spectrum of this mineral shows lead and tellurium to be the only elements present.

Gold

Gold in native state is not very common in the Emperor mine. In polished sections the colour, reflectivity and isotropic nature makes it the most easily identifiable mineral.

Three types of gold occurrences have been observed:-

(a) Submicroscopic gold

Stillwell & Edward (1946) examined the pyritic concentrate from the Dolphin lode and concluded that gold was included in pyrite and arsenopyrite either as minute submicroscopic inclusions or in solid solution. Electron microprobe studies failed to reveal any gold-rich phase in either pyrite or arsenopyrite and it is suggested that gold is probably included within the structure of these sulphides.

(b) Visible gold

Large microscopic grains of gold are observed in a number of specimens. This gold is generally associated with petzite, hessite, chalcopyrite and tetrahedrite.

(c) Dendritic gold

Dendritic and thread-like forms of brownish yellow gold are observed on joint planes. This gold is probably of supergene origin.

Tellurium

Native tellurium is fairly common in the specimens examined. It has a creamy white colour and high reflectivity. It is strongly anisotropic in non-basal sections. Reflection pleochroism is distinct, with the tint varying from light grey to black.

Native tellurium is commonly associated with sylvanite and krennerite. In a few specimens sylvanite is observed to be moulded around native tellurium crystals and it appears that native tellurium pre-dates the precipitation of sylvanite. Hessite, petzite and native gold are observed veining native tellurium. Melonite and altaite are associated with native tellurium in a few specimens (Plate 6.12).

Native tellurium is more common in the specimens from the upper levels (12 level and above).

6.6 TRANSPARENT MINERALS

Chlorite

Chlorite is a very common mineral in the propylitic rocks. It is green coloured, slightly pleochroic and has low birefringence. It generally occurs as fibrous aggregates.

Electron microprobe analysis of chlorite carried out during the present study on a number of specimens is given in Appendix D.4 and is plotted on Hey's (1954) diagram (Fig. 6.8). It can be seen that there

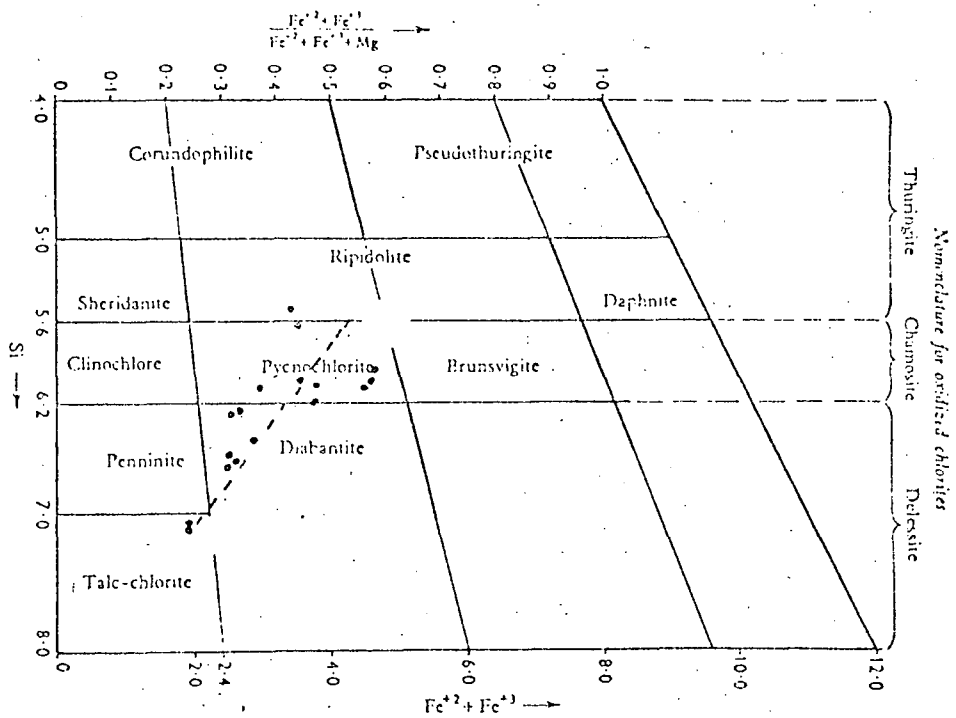

Fig.6.8 Variation in the composition of chlorite plotted on the diagram of Hey(1954). For details refer to Appendix D-4.

are considerable variations in composition. The chlorite in the relatively unaltered rocks is high in magnesium and low in iron, while in the completely altered rocks in the vicinity of mineralized rocks, it is relatively lower in magnesium and higher in iron.

Chlorite is generally formed at the expense of pyroxene and plagioclase. Complete pseudomorphs after these two minerals are frequently observed.

In the mineralized veins chlorite is very rare. The green micaceous mineral described by the previous workers (e.g. Cohen, 1962; Forsythe,1968; Ibbotson, 1967) from the mineralized veins is actually roscoelite and not chlorite.

Chlorite is generally associated with magnetite, ankerite, dolomite and pyrite. Quartz and sericite are not generally observed in association with chlorite.

Quartz

Quartz is the most abundant gangue mineral. In size it varies from very small microscopic grains in the wall rock to crystals as long as 6 cm in the mineralized vein. In colour it varies from white to amber. Some samples from the P.O.W. lode show colloidal banding.

There appears to be at least five periods of barren vein quartz precipitation (i.e. sub-stages IIA, IIIA, IVA, IVB and IVC). These periods can be worked out by simply counting the individual layers in the hand specimens (Plates 6.1 to 6.9; Fig. 6.6) and are separated by precipitation of carbonates, sulphides and tellurides. All of these periods are not observed everywhere and it appears that some fractures were sealed up earlier than the others. Most of the specimens show at least the first two periods. Samples from 166 flatmake generally exhibit all five periods (Plates 6.1 to 6.3).

Apparently there was no break in the quartz precipitation but there were times when the solutions precipitated carbonates and ore minerals along with quartz.

Sericite

Sericite occurs as small flakes dusting the wall rocks adjacent to the mineralized veins. Complete pseudomorphs after plagioclase are common but in a number of cases the margins of plagioclase are left intact and only the central part is replaced.

Sericite is associated with vein quartz, adularia, sulphides, telluride and carbonates. The width of the sericitized rocks varies from a few millimetres to a few centimetres and is related to the width of the mineralized vein and the nature of the host rock. The dyke rocks (andesite) show comparatively more sericitization than the basalt.

Although adularia is the common vein feldspar, the wall rock feldspar in many samples is orthoclase. This orthoclase in many samples is dusted with sericite. Analyses of sericite from a number of samples are given in Appendix D.4.

Adularia

The K-feldspar occurring as rhombs at the edge of mineralized veins (Plate 5.2) and between barren quartz layers is tentatively identified as adularia. Sufficient material was not available to confirm the suggested identification by X-ray diffraction methods. Electron microprobe analyses (Appendix D.4) suggest a potassium feldspar.

Orthoclase

The lath-shaped K-feldspar in the altered wall rocks is tentatively identified as orthoclase but positive confirmation by X-ray diffraction methods was not possible. Electron microprobe analyses (Appendix D.4) suggest a potassium feldspar.

Roscoelite

Roscoelite is a common mineral in the mineralized veins. It is green, strongly pleochroic and highly birefringent. It has been confirmed by electron microprobe analyses (Appendix D.4) and X-ray powder diffraction patterns.

It is generally associated with tellurides and in many samples, tellurides are observed to be preferentially replacing roscoelite.

Epidote

Epidote was described by Cohen (1962) from a few samples of relatively unaltered rocks, but it is very rare. It is observed to be replacing plagioclase and pyroxene phenocrysts. No epidote was observed in the mineralized rocks (K-silicate assemblage).

Ankerite and dolomite

Ankerite and dolomite are hard to distinguish under the microscope. Electron microprobe analyses carried out during the present study, on several grains from a number of samples (Appendix D.3) show that both ankerite and dolomite are present in the samples studied. As suggested by Dear *et al.* (1971), the term "ankerite" is used for those carbonates in which the magnesium to iron ratio is less than 4.

Ankerite is probably the very first carbonate to form in the slightly altered rocks at the expense of pyroxene and plagioclase. The replacement starts along the cleavage planes and cracks and as the vein is approached complete pseudomorphs after pyroxene and plagioclase are observed (sample 47215; Plate 5.1). In many plagioclase grains, the central core is completely replaced but the margins are intact, indicating that the replacement was dependent on the "on site" availability of calcium. The core being more calcic was replaced first.

The analyses of carbonates are plotted on a Ca-Mg-Fe triangle (Fig. 6.9) along with the analyses of augite. It is obvious that during

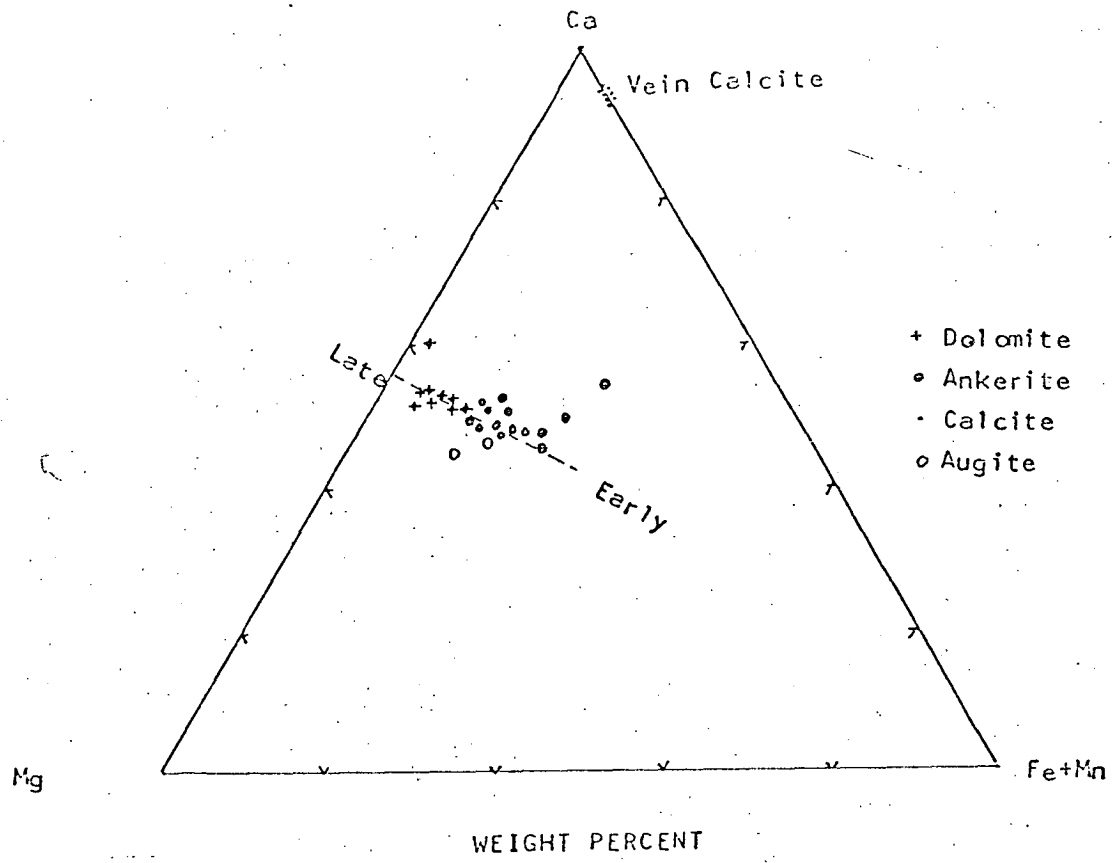

Fig. 6.9 Triangular plot of analyses of dolomite, ankerite, calcite and augite.

the replacement of augite by ankerite no real transfer of Ca, Mg and Fe was involved.

Dolomite is observed at the edge of mineralized veins and between barren quartz layers. There appears to be a decrease in the iron contents of these carbonates with time (Fig. 6.9). Early carbonates occurring at the base of mineralized veins have an average iron content of about 9.8 wt. %, while those occurring between barren quartz layers have an average iron content of about 3.8 wt. %.

Calcite

Calcite is a very late mineral. It is fairly widespread and occurs as rhombohedral or scalenohedral crystals gowing over post-mineralization quartz.

The electron microprobe analyses (Appendix D.3) show it to be almost pure $CaCO_3$ with up to 3 wt. % iron.

Except for rare grains of marcasite, no other sulphides or tellurides were seen to be associated with calcite.

Chapter 7

FLUID-INCLUSION STUDIES

7.1 GENERAL

Fluid-inclusions were found in vein and wall rock quartz, dolomite, calcite, sphalerite and K-feldspar (adularia ?). Those in wall rock quartz, sphalerite and K-feldspar were too small for homogenisation studies and the calcite of stage-V contains small inclusions without a visible vapour phase (i.e. water and no bubble). Thirty-six samples of vein quartz and one of dolomite contained inclusions large enough for homogenisation temperatures to be determined with reasonable care. The location of these samples is shown in Fig. 7.5A. The samples are from a number of veins and cover a total vertical extent of about 500 m and a lateral extent of about 1800 m. In a number of samples more than one paragenetic stage is present.

Roedder (1967) discussed several criteria for distinguishing primary, secondary and pseudosecondary inclusions. In this study the inclusions belonging to the following categories have been considered as primary or pseudosecondary:-

(i) Isolated inclusions not related to any fracture plane (Plates 7.1 and 7.2).

(ii) Inclusions related to growth zones of the crystal (Plate 7.3)

(iii) Inclusions related to small fractures not obviously extending to the crystal surface (Plates 7.5 and 7.6).

Most quartz samples consist of large crystals projecting into open vughs, so that growth zones and/or crystal margins are fairly well defined. The homogenisation temperatures in a single plate generally fall within a range of 30°C and in the few cases tested this range is not

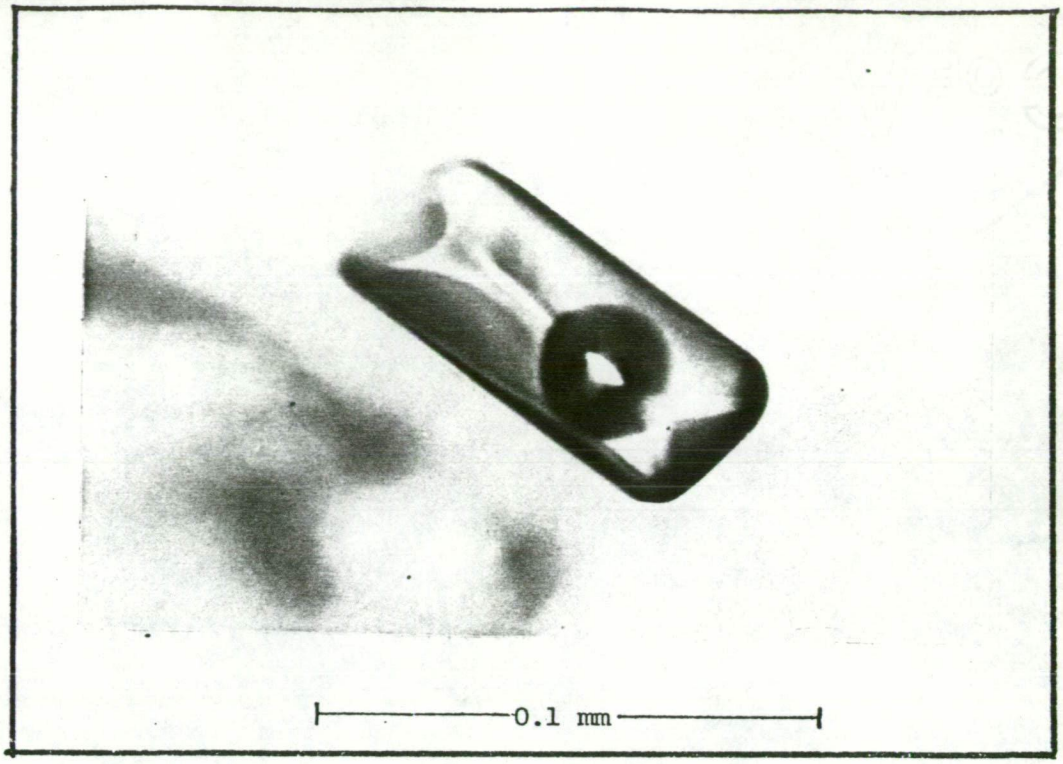

Plate 7.1 Isolated type A fluid inclusion in the form of negative crystal. Sample 103346, 1010 lode, 9 level.

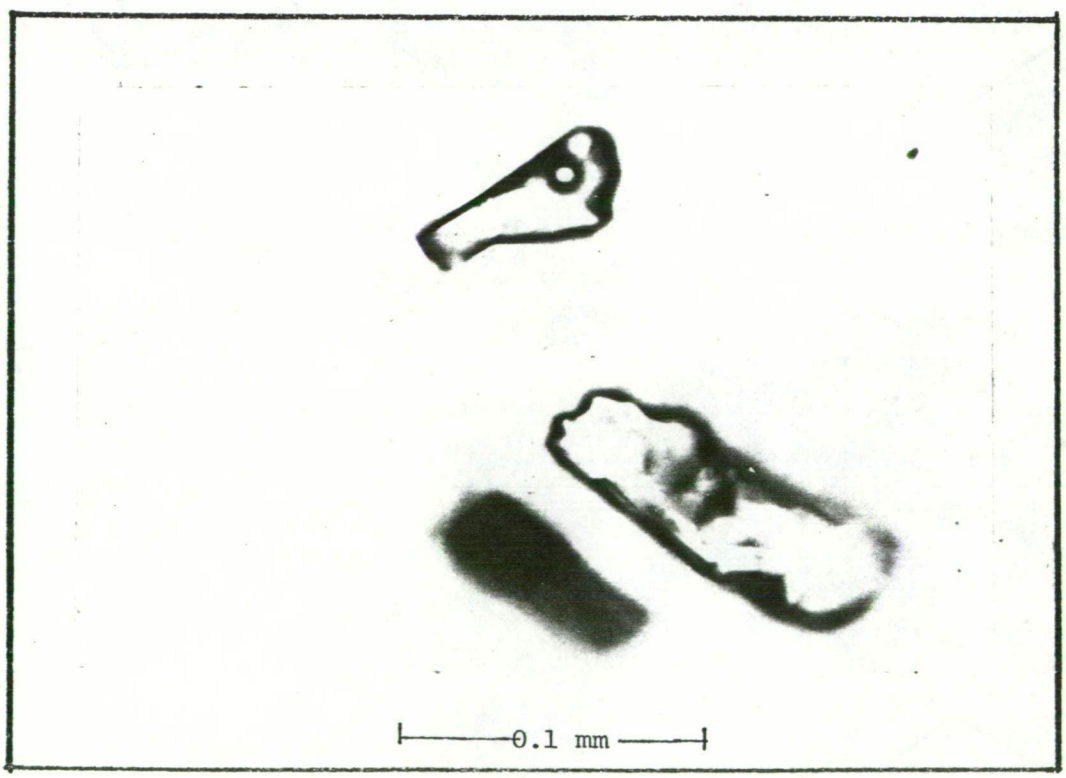

Plate 7.2 Irregular, isolated type A inclusions. Sample 103346, 1010 lode, 9 level.

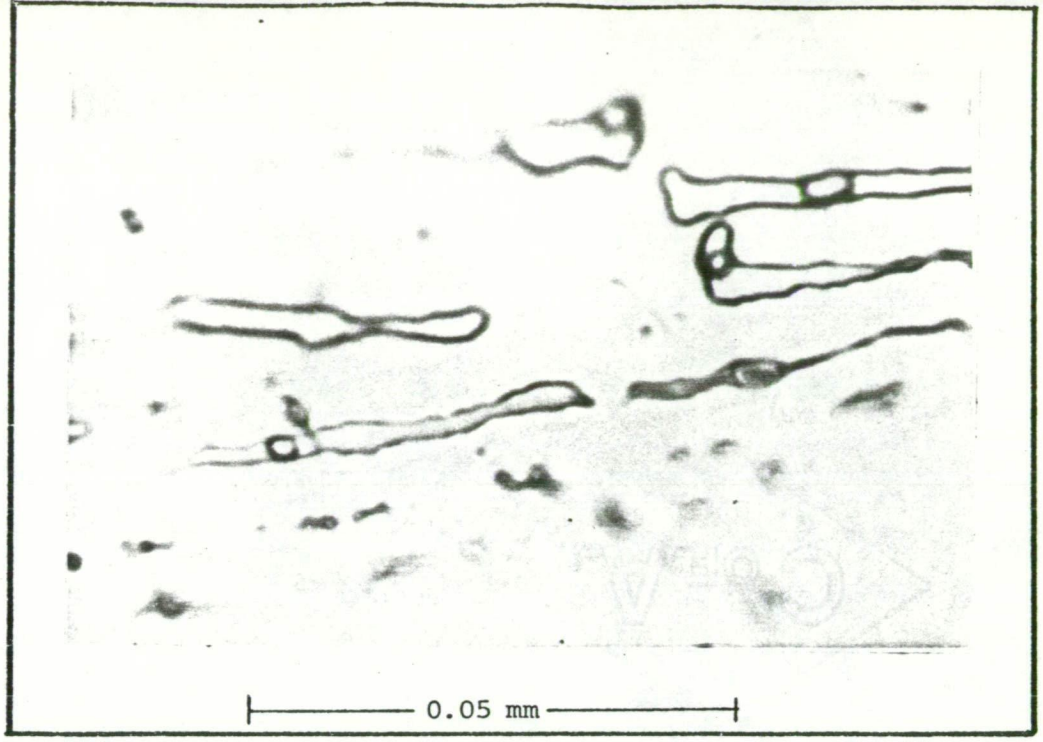

Plate 7.3 Tubular type A fluid inclusions along growth zones in quartz. Sample 103346, 1010 lode, 9 level.

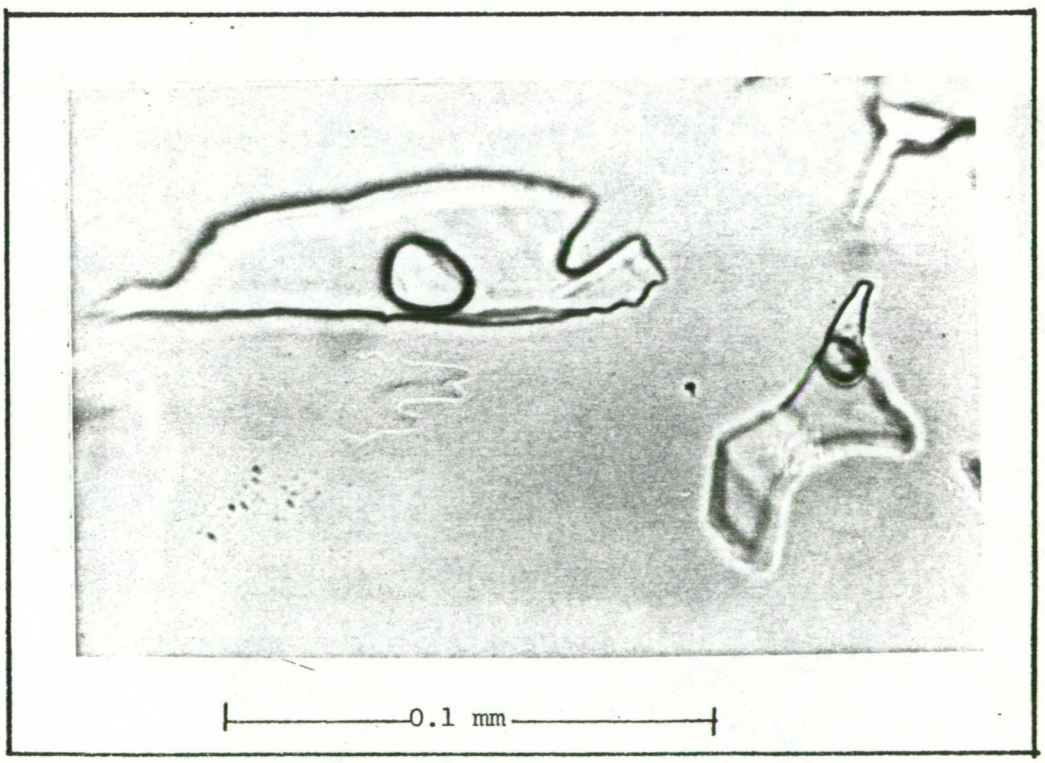

Plate 7.4 Irregular amoeboid type A fluid inclusions in vein quartz. Sample 103346, 1010 lode, 9 level.

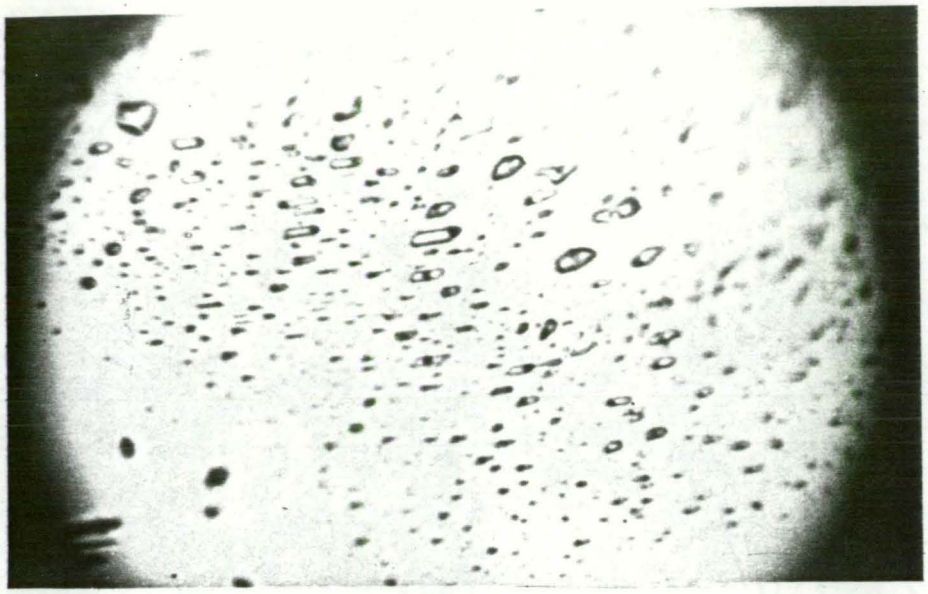

Plate 7.5 Type A inclusions in the form of negative crystal along a healed fracture plane. These inclusions are probably pseudosecondary. Sample 103298, 166 flatmake, 7 level.

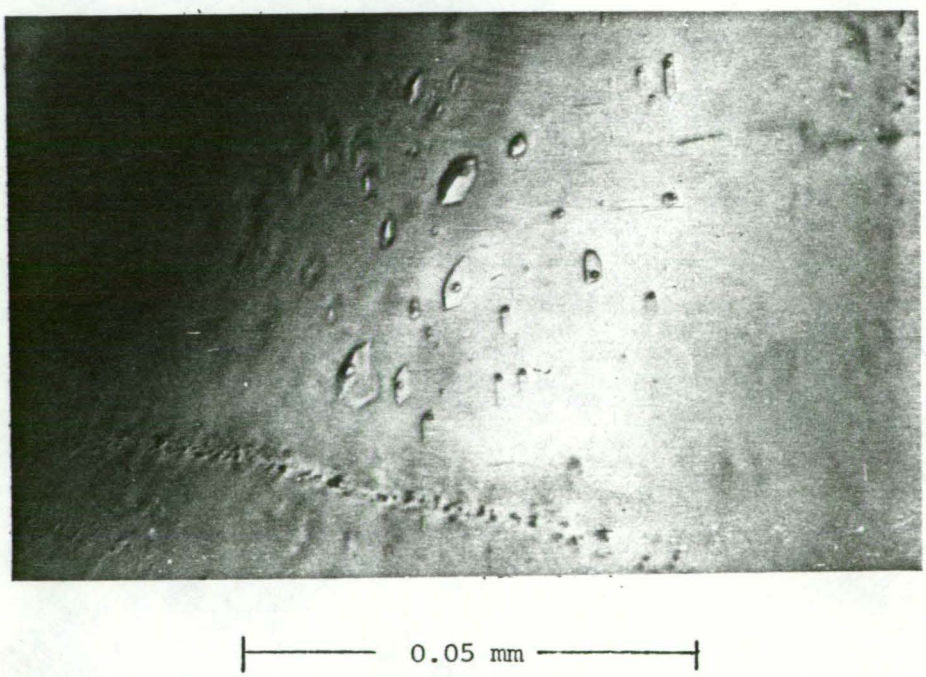

Plate 7.6 Description same as for Plate 7.7. Sample 103298, 166 flatmake, 7 level.

increased by measuring all visible inclusions whether deemed primary, pseudosecondary or secondary. Wherever possible, inclusions showing evidence of necking-down have been discarded.

The fluid-inclusions were heated and frozen on a Chaixmeca apparatus, and also on a heating stage built at the University of Tasmania. The comparison in temperatures obtained on these two stages is excellent ($\pm$ 2^{o}C). These stages were calibrated relative to the melting points of pure substances and Merk standards. The readings are accurate to $\pm$ 0.2^{o}C for freezing temperatures and $\pm$ 3^{o}C for homogenisation temperatures.

7.2 SHAPE AND SIZE OF THE INCLUSIONS

On the basis of shape, three main types of inclusions can be recognised. They are:-

(i) Irregular amoeboid (Plate 7.4)

(ii) Negative crystals (Plates 7.1, 7.5 and 7.6)

(iii) Tubular (Plate 7.3).

Though all three types do occur together in some samples it is possible to make the following generalisation.

The majority of inclusions related to cracks and certain growth zones are irregular and fairly large in size, ranging from a few microns to 0.5 mm in diameter.

Isolated inclusions and those related to minor cracks generally have a negative crystal shape. They are relatively smaller in size, ranging from a few microns to a few tens of microns in diameter.

Tubular inclusions are generally associated with growth zones and are usually cylindrical in shape. The width of these inclusions generally ranges from 1 to 5 microns and the length from a few tens of microns to as large as 0.05 mm (Plate 7.3).

7.3 PHASES OBSERVED IN INCLUSIONS

On the basis of phase ratio and the number of phases present, the inclusions studied can be classified into four types:-

Type A Two-phase inclusions (water and vapour) with an almost constant phase ratio (Plates 7.1 to 7.6).

Type B Single- (vapour only) and two-phase inclusions of water and vapour with a variable phase ratio (Plates 7.9 and 7.10).

Type C Three-phase inclusions of water, vapour and solid (Plates 7.7 and 7.8).

Type D Single-phase inclusions filled with water only.

Type-A inclusions

All inclusions used for temperature and salinity determinations are of this type. These inclusions trapped a homogeneous liquid and separation into two phases occurred as a result of cooling.

Type-B inclusions

These inclusions are either filled with vapour (Plates 7.9, 7.10) or with various proportions of vapour and liquid. They commonly occur in groups. Isolated inclusions of this type are hard to differentiate from type-A inclusions and can give spurious temperatures. These inclusions were not homogeneous when trapped and they therefore indicate the solutions were boiling. Two inclusions of this type homogenised in the vapour phase at temperatures comparable to those of the type-A inclusions in the same sample (sample 103340).

Type-C inclusions

In addition to water and vapour, this type of inclusion also contains radiating clusters of a highly birefringent mineral (Plates 7.7,

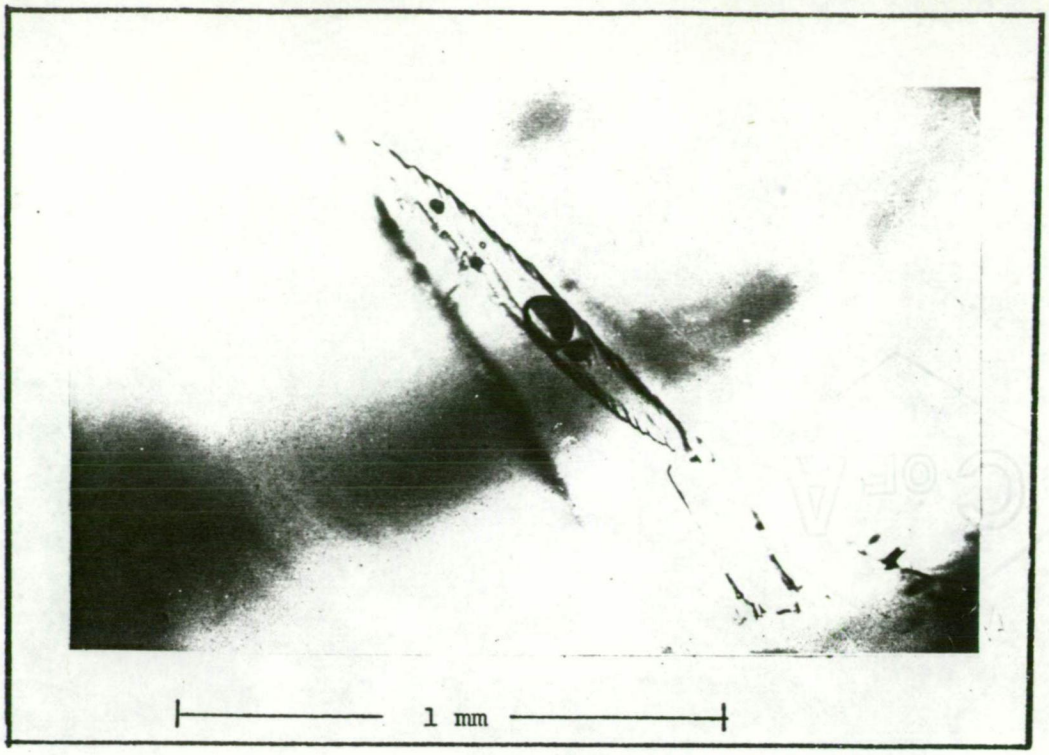

Plate 7.7 Type C inclusion showing aggregates and clusters of a solid phase which may be roscoelite. Sample 103296, 166 flatmake, 7 level.

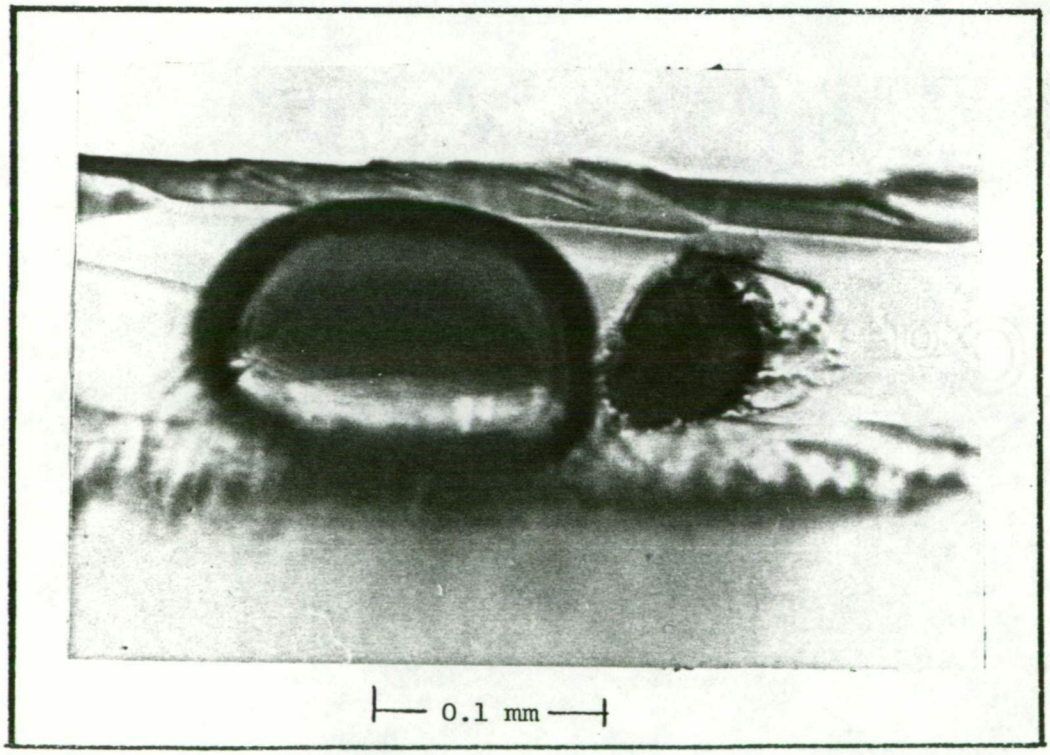

Plate 7.8 Same as in Plate 7.5 at a higher magnification.

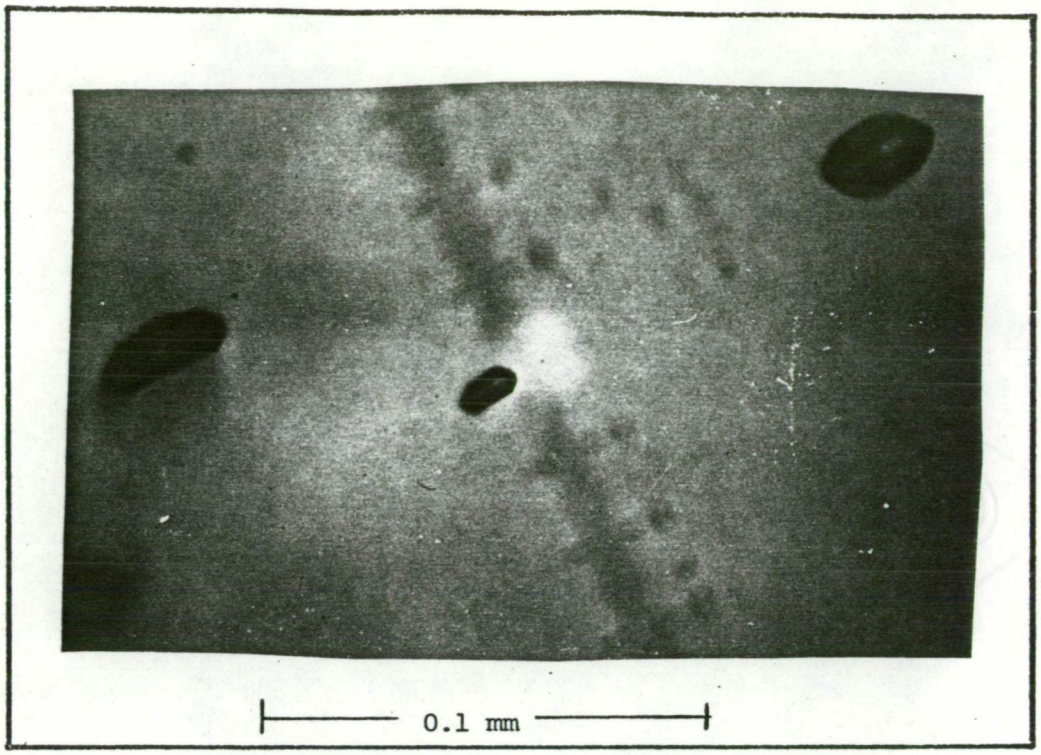

Plate 7.9 Type B inclusion in vein quartz filled with vapour only. Sample 103340, Cardigan lode, 3 level.

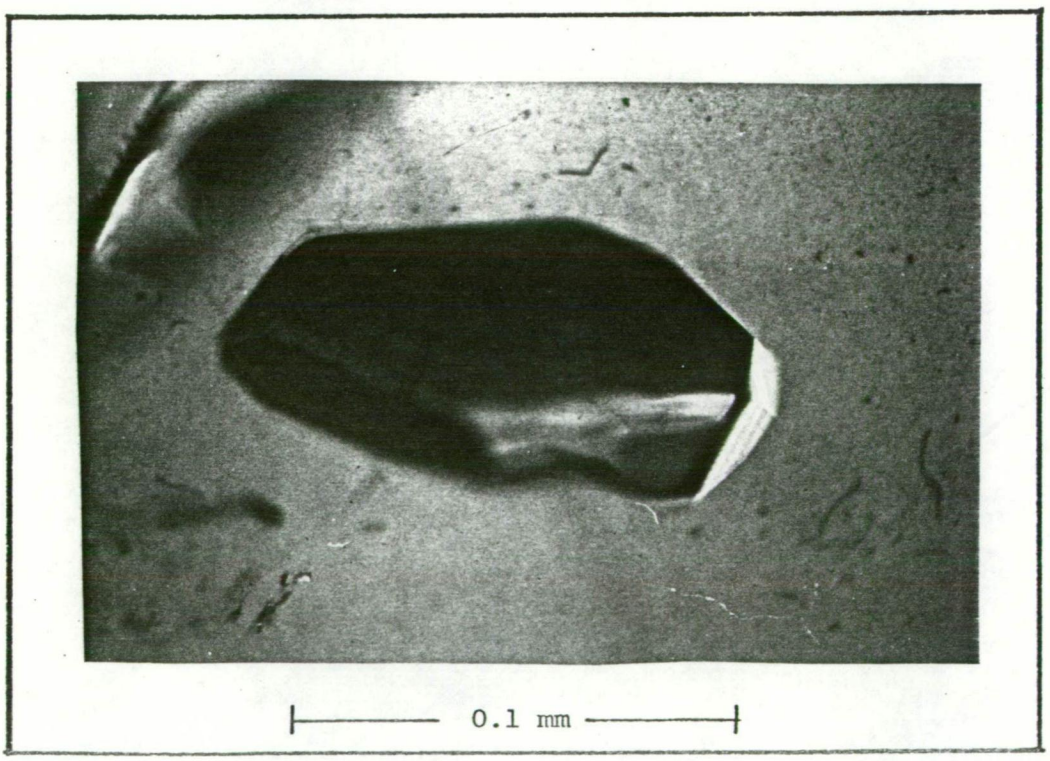

Plate 7.10 A large type B inclusion filled with vapour only. Sample 103300, 04S lode, 3 level.

7.8). Rye & Sawkins (1974) described similar material from the Casapalca deposit as dawsonite. This solid commonly occupies almost one third of the inclusion cavity. Abnormal concentrations of Na and Al would be required if these crystals had grown inside the inclusions after trapping. The optical properties of these crystals resembles very much those of roscoelite and it is suggested that this mineral was accidently trapped along with the liquid.

Type-D inclusions

These inclusions are single phase and contain only water. They are commonly observed in stage-V calcite but they also occur in quartz and here they are related to very large cracks and are obviously secondary in origin. As no visible vapour phase has separated, it can be assumed that they were formed at very low temperatures. The inclusions in calcite are very small in size (usually less than a micron across).

7.4 HOMOGENISATION TEMPERATURES

The homogenisation temperatures are summarised in Table 7.1 and are plotted in Figs. 7.1, 7.2 and 7.3. As shown in the following sections the salinity of these solutions was about 5.5 wt. % eq. NaCl and the pressure was generally less than 32 bars. The temperature corrections required for non-boiling liquids at such low pressure and salinity are almost negligible and are within the limits of uncertainty. No corrections are therefore applied to the temperatures given in Table 7.1.

Stage IIA

As shown in Table 7.1 and in Fig. 7.1 the temperatures during this stage range from 205 to 317^{o}C, a fairly wide range compared to other stages. This may be for two reasons:-

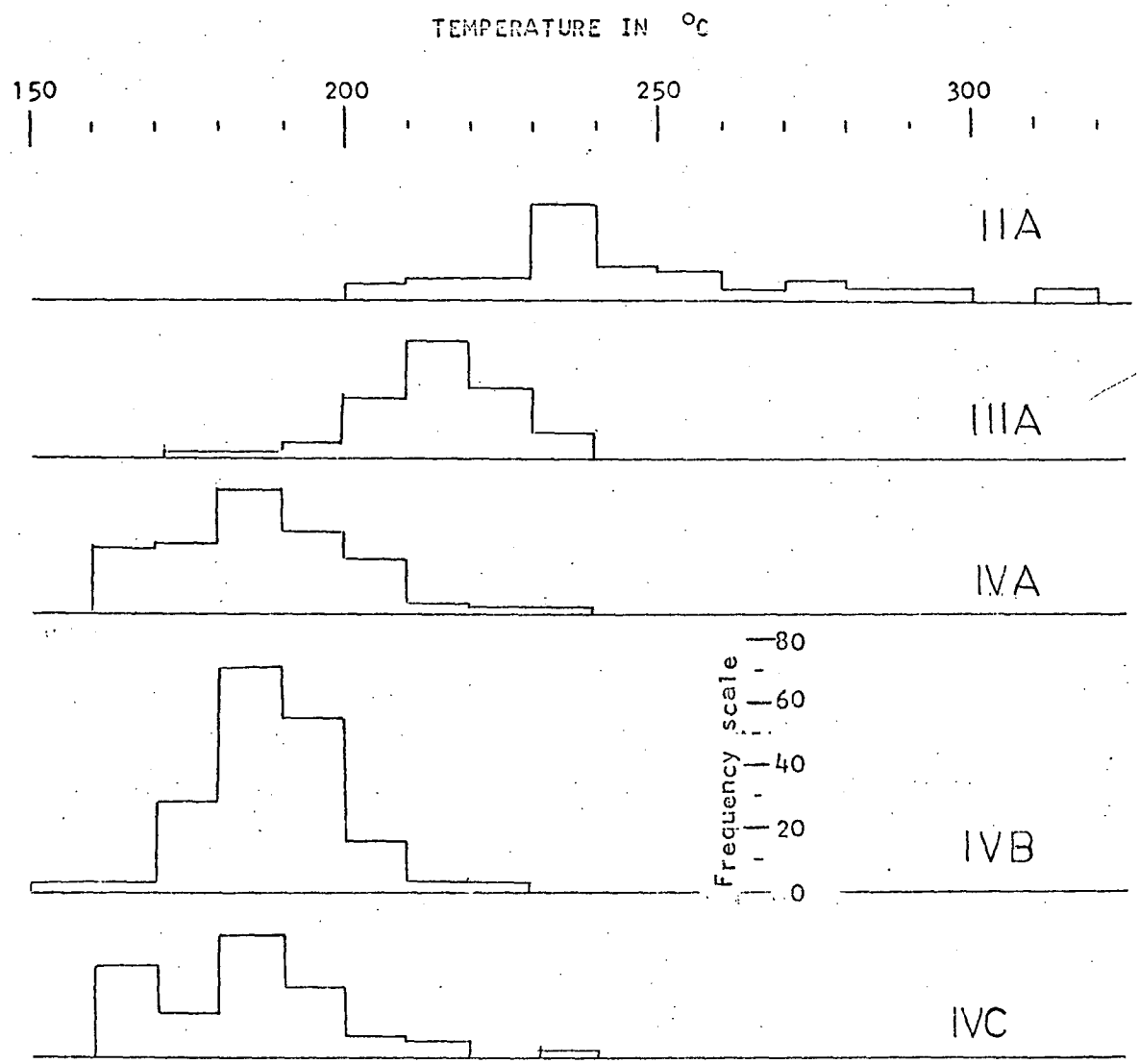

Fig.7.1 Fluid-inclusion homogenisation temperatures during various stages of mineralization. For details refer to Table 7.1

Table 7.1

FLUID-INCLUSION DATA

Specimen Number	Mineral	Location	Filling temperatures °C				Salinity wt.% eq. NaCl			Type-B inclusion
			Stage	No. incls.	Temp. range	Av. temp.	No. incls.	Saln. range	Mean saln.	
103296	Quartz	7 level, 166	IIA/ IIIA	4	216-262	233				present
103310	Quartz	10 level, P.O.W.	IIA/ IIIA	19	217-255	231	12	5.08-5.82	5.75	?
103313	Quartz	11 level, P.O.W.	IIA	12	205-248	235	12	4.92-6.54	5.68	present
103329	Quartz	14 level, Crown	IIA	8	238-281	249				absent
103334	Quartz	9 level, 608	IIA	6	230-278	243				present
103433	Quartz	14 level, Crown	IIA	15	235-308	255	16	4.90-7.10	5.83	absent
103434	Quartz	16 level, Crown	IIA	6	220-317	265				absent
103446	Quartz	15 level, 2000N	IIA	5	257-300	278				absent
103291	Quartz	9 level, 608	IIIA	2	220-230	225				?
103292	Quartz	9 level, 166	IIIA	5	210-230	219				present
103303	Dolomite	8 level, Monarch	IIIA?	13	170-214	196				?
103303	Quartz	8 level, Monarch	IIIA	17	172-222	184				?
103306	Quartz	8 level, 1010	IIIA	3	220-235	226	6	4.78-5.52	5.39	present
103312	Quartz	8 level, 1010	IIIA	5	205-220	212				present
103318	Quartz	9 level, Crown	IIIA	11	210-234	218				?
103325	Quartz	12 level, Crown	IIIA	4	211-225	206				?
103329	Quartz	14 level, Crown	IIIA	9	210-234	215				present
103340	Quartz	3 level, Cardigan	IIIA	13	205-211	211				present

Table 7.1 cont.

Specimen Number	Mineral	Location	Filling temperatures °C				Salinity wt.% eq. NaCl			Type B inclusion
			Stage	No. incls.	Temp. range	Av. temp.	No. incls.	Saln. range	Mean saln.	
103346	Quartz	9 level, 1010	IIIA	18	200-224	218	7	4.62-7.10	5.72	present
103392	Quartz	8 level, Crown	IIIA	8	207-225	214				?
103420	Quartz	15 level, Crown	IIIA	4	225-230	228				?
103430	Quartz	14 level, Crown	IIIA	3	210-230	216				absent
103446	Quartz	15 level, 2000N	IIIA	6	216-232	221				absent
103292	Quartz	9 level, 166	IVA	8	159-179	166				present
103296	Quartz	7 level, 166	IVA	40	168-198	180	10	6.25-6.82	6.30	present
103297	Quartz	7 level, 166	IVA	4	178-221	198				present
103462	Quartz	10 level, P.O.W.	IVA	9	165-204	178				absent
103316	Quartz	10 level, Crown	IVA	18	170-205	177				present
103339	Quartz	3 level, Cardigan	IVA	11	184-202	193				?
103341	Quartz	4 level, Shatter	IVA	14	170-208	194				present
103342	Quartz	5 level, Cardigan	IVA	8	163-212	186				present
103343	Quartz	7 level, 608	IVA	2	185-202	193				present
103433	Quartz	14 level, Crown	IVA	9	167-240	198				
103292	Quartz	9 level, 166	IVB	12	184-210	189				present
103293	Quartz	9 level, 166	IVB	11	172-210	184	11	5.22-5.97	5.56	present

Table 7.1 cont.

Specimen Number	Mineral	Location	Filling temperatures °C				Salinity wt.% eq. NaCl			Type B inclusion
			Stage	No. incls.	Temp. range	Av. temp.	No. incls.	Saln. range	Mean saln.	
103296	Quartz	7 level, 166	IVB	44	174-198	184				present
103297	Quartz	7 level, 166	IVB	21	174-200	190	11	5.37-6.25	5.61	present
103305	Quartz	8 level, 166	IVB	5	183	183				present
103364	Quartz	9 level, Wunawali	IVB	10	148-180	176				present
103365	Quartz	9 level, 166	IVB	22	183-196	190				present
103367	Quartz	9 level. 166	IVB	16	172-210	184				present
103368	Quartz	9 level, 166	IVB	6	188-205	196	2	5.67	5.67	present
103370	Quartz	10 level, 166	IVB	11	178-232	184				present
103371	Quartz	10 level, 166	IVB	20	180-232	192	6	5.67	5.67	present
103296	Quartz	7 level, 166	IVC	64	165-210	179	16	5.07	5.07	present
103297	Quartz	7 level, 166	IVC	24	165-210	175	9	4.4-6.24		present
103366	Quartz	9 level, 166	IVC	12	196	196				present
103369	Quartz	10 level, Wunawali	IVC	15	160-235	207				present

(i) The stage-IIA quartz crystals are relatively small and useful inclusions are generally rare. The criteria for differentiating primary and secondary inclusions can not be very rigourously applied. It is possible that some of the inclusions actually formed during later stages and are therefore secondary with respect to stage IIA.

(ii) In Fig. 7.2 fluid inclusion temperatures are plotted against depth. It can be seen that the temperatures on stage-IIA quartz from 7 to 11 levels (depth 180 to 360 m) range from 205 to 278°C, while between 14 and 16 levels (depth 480 to 550 m) they range from 220 to 317°C. This suggests that the temperatures during this stage increase with depth. This increase in temperatures is also contributing towards increasing the range shown in Fig. 7.1.

Stage IIIA

Temperatures from this stage show less scatter ranging from 170 to 232°C (Table 7.1; Figs. 7.1, 7.2). There is a slight indication of an increase in temperature with depth (Fig. 7.2).

The stage-IIIA quartz occurs as large crystals up to 1 cm in length. The criteria for distinguishing between primary and secondary inclusions can be more rigourously applied to this quartz and hence, possibly there is less scatter in the homogenisation temperatures.

Some of the inclusions are very close to the tellurides of stage IIIB and there is no difference between the temperatures obtained from these inclusions and those from the barren quartz i.e. stage IIIA proper.

Stage IV

The homogenisation temperatures of stages IVA, IVB and IVC lie in a narrow range of 159 to 235°C (Table 7.1; Figs. 7.1, 7.2) and there is again a slight indication of an increase of temperature with depth (Fig. 7.2).

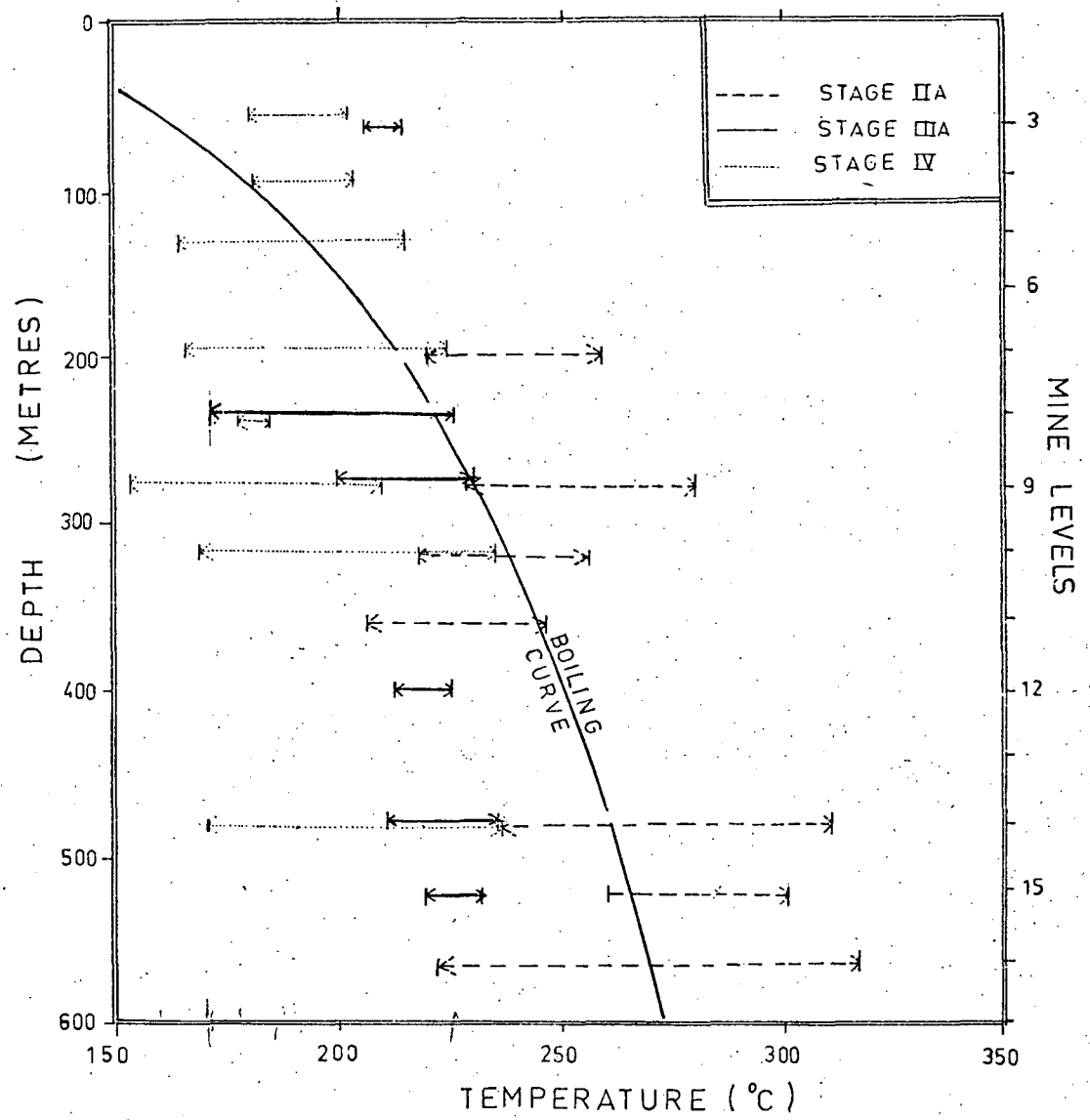

Fig. 7.2 Fluid-inclusion homogenisation temperatures versus depth. The boiling curve for solutions containing 5 wt% NaCl is from Haas(1971). For details refer to Table 7.1.

The stage-IV quartz occurs as large crystals up to 6 cm long. The sub-stages can be identified by colour differences and rare carbonate-sulphide layering (Plates 6.1 to 6.5). Stage-IVB quartz is generally of an amber colour while that of stage IVB and IVC is commonly white. The quartz crystals continue to grow in optical continuity but they enclose carbonate-sulphide layers as discontinuous bands.

Temperature determinations across one of the crystals (sample 103296) are shown in Fig. 7.3. It appears that minor fluctuations in temperature (between 165 and 200°C) did occur during the growth of this crystal. According to the modal temperature estimates, the temperature was about 195 ± 5°C during stages IVA and IVB, dropped to about 165°C at the beginning of stage IVC (marked as 'b' in Fig. 7.3) but rose again to about 190°C towards the end of stage IVC (marked as 'a' in Fig. 7.3).

7.5 FREEZING TEMPERATURES

Only large and clearly visible inclusions were frozen, and this considerably reduced the number of suitable inclusions. In most cases heating runs were made immediately after freezing.

Most of the inclusions did not freeze until about -30°C. No separate CO_2 phase appeared upon cooling. Inclusions filled with vapour only were frozen to temperatures as low as -90°C, and except for a few crystals of ice which formed at about -30°C no other phase developed. Three phase inclusions (type C) froze at about -10°C.

The temperatures of melting of the last crystals of ice have been converted to wt. % eq. NaCl using the equation given in Potter *et al.* (1978). The salinities so obtained are given in Table 7.1 and are plotted in Fig. 7.4. It can be seen that the salinities range between 4.6 and 7.1 wt. % eq. NaCl, averaging about 5.5 wt. % eq. NaCl. There is no apparent variation in the salinity with time or depth.

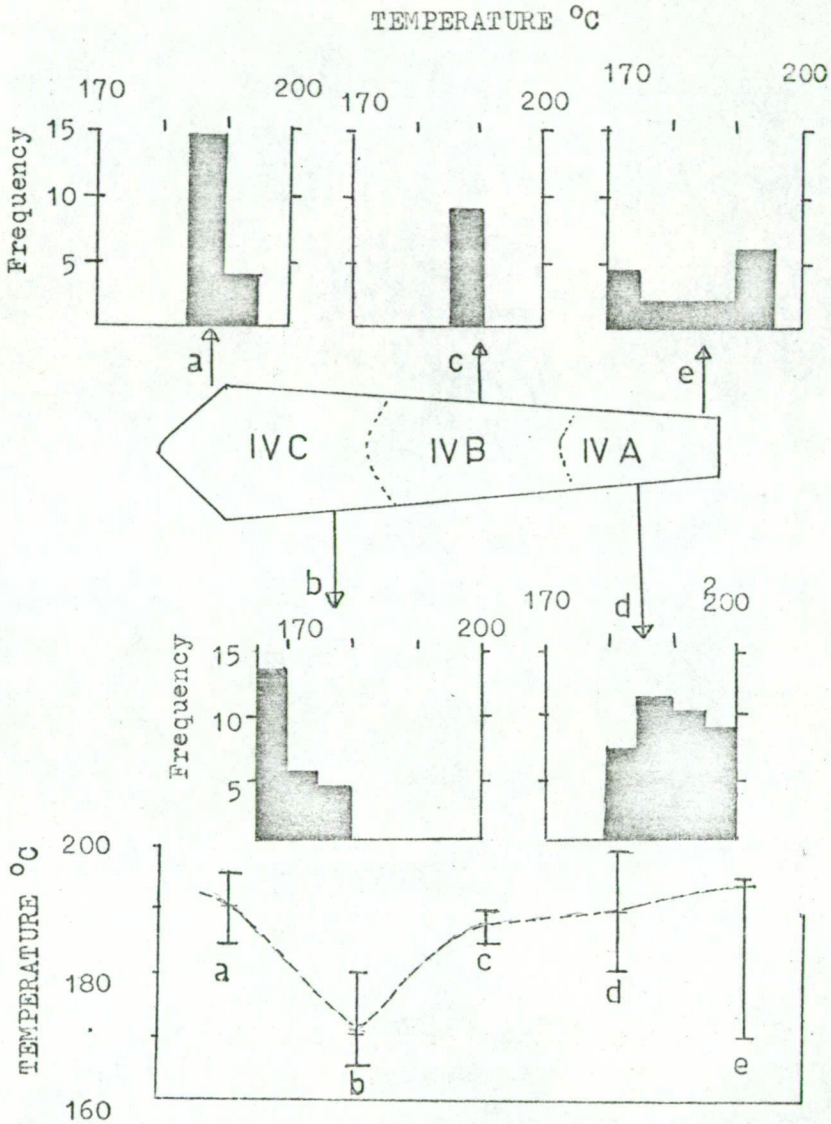

Fig. 7.3 Temperature variations along a single quartz crystal. The curve in the bottom figure links the modal values of the various sets of measurements. Sample No. 103296.

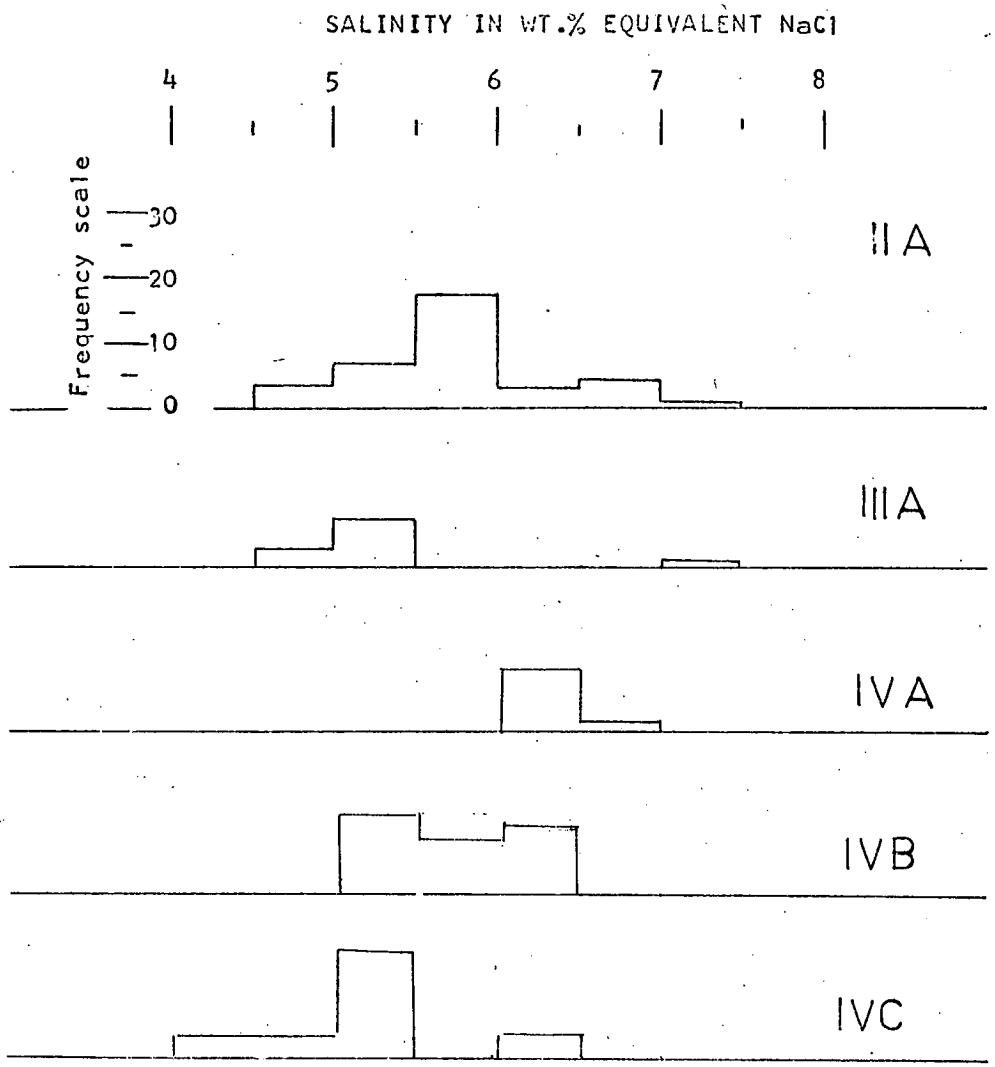

Fig.7.4 Salinity as determined from the freezing-point depression of fluid-inclusions. Roman numerals refer to stages of mineralization. For details refer to Table 7.1.

Freezing studies on inclusions in stage-V calcite were not successful because of the very small size of the inclusions.

7.6 BOILING

The presence of type-B inclusions in most of the samples indicates that the fluids boiled intermittently. The open spaces in the vein suggest that the fluids probably circulated freely and the pressure was mainly hydrostatic. These two observations indicate that the fluid may have remained close to the boiling point-depth curve. The temperature-pressure relationships of a 5% NaCl solution on the boiling curve (given in Haas, 1971) can therefore be used to approximate the depth of the water table at the time of quartz growth. As shown in Table 7.1, the temperature range for the majority of samples of stage IIA is about $\pm$ 30^{o}C or less, and that of stages IIIA, IVA, IVB and IVC is $\pm$ 10^{o}C or less. Such a spread (at about 250^{o}C) may produce an uncertainty of $\pm$ 250 m for stage IIA and of $\pm$ 75 m for other stages in the calculated height of the water table. It is possible that the lower temperatures (in single samples) are of solutions which may not be boiling and the higher temperatures (in single samples) may be the result of trapping of minor amounts of vapour along with the fluids. In the following presentation, which may be treated as preliminary, average temperatures given in Table 7.1 are used.

A summary of the depth, pressure (hydrostatic) and density of the solutions calculated from the average temperatures for samples containing type-B inclusions (Table 7.1) is given below. All calculations are with respect to 5% NaCl solutions (from Haas, 1971).

	Stage IIA	Stage IIIA	Stage IV
Temperature range, ^{o}C	222-243	206-225	166-218
Pressure range, bars	22-32	20-25	6.5-22
Depth range, m	237-354	214-264	62-237
Density range, gm/cm^3	0.88-0.86	0.89-0.88	0.94-0.88

A plot of the fluid-inclusion temperatures versus depth (Fig. 7.2) suggests that the data for stage IIA are more or less compatible with the boiling point-depth (BPD) curve based on the water table about 50 m below the present surface. However the stage IIIA and stage IV data can not be explained in the same way as substantial departures from the BPD curve are present.

In Figs. 7.5, 7.6 and 7.7 the sample positions are shown in plan and sections for the various stages of quartz formation and the sections also show the water table heights calculated for average temperatures of each sample.

Stage IIA Samples from 14 level and below in the Crown lode and 2000N flatmake do not contain type-B inclusions (Table 7.1). Samples from 11 level and above in the P.O.W. lode, 608 flatmake and 166 flatmake indicate that fluids were boiling. These observations suggest that boiling probably commenced between 14 and 11 levels. The height of the water table is therefore minimum above the Crown lode (Fig. 7.5B) and may be approximately equal to the present surface above the other lodes (Fig. 7.5B). It would appear that the water table was convex upward (above the Crown lode) and probably followed the topography of the volcano. This suggests that the Tavua caldera probably formed after stage IIA.

Stage IIIA The occurrence of type-B fluid-inclusions in samples from the Crown lode indicates that boiling was common down to level 14 (Table 7.1) but the available samples from 15 level do not contain type-B

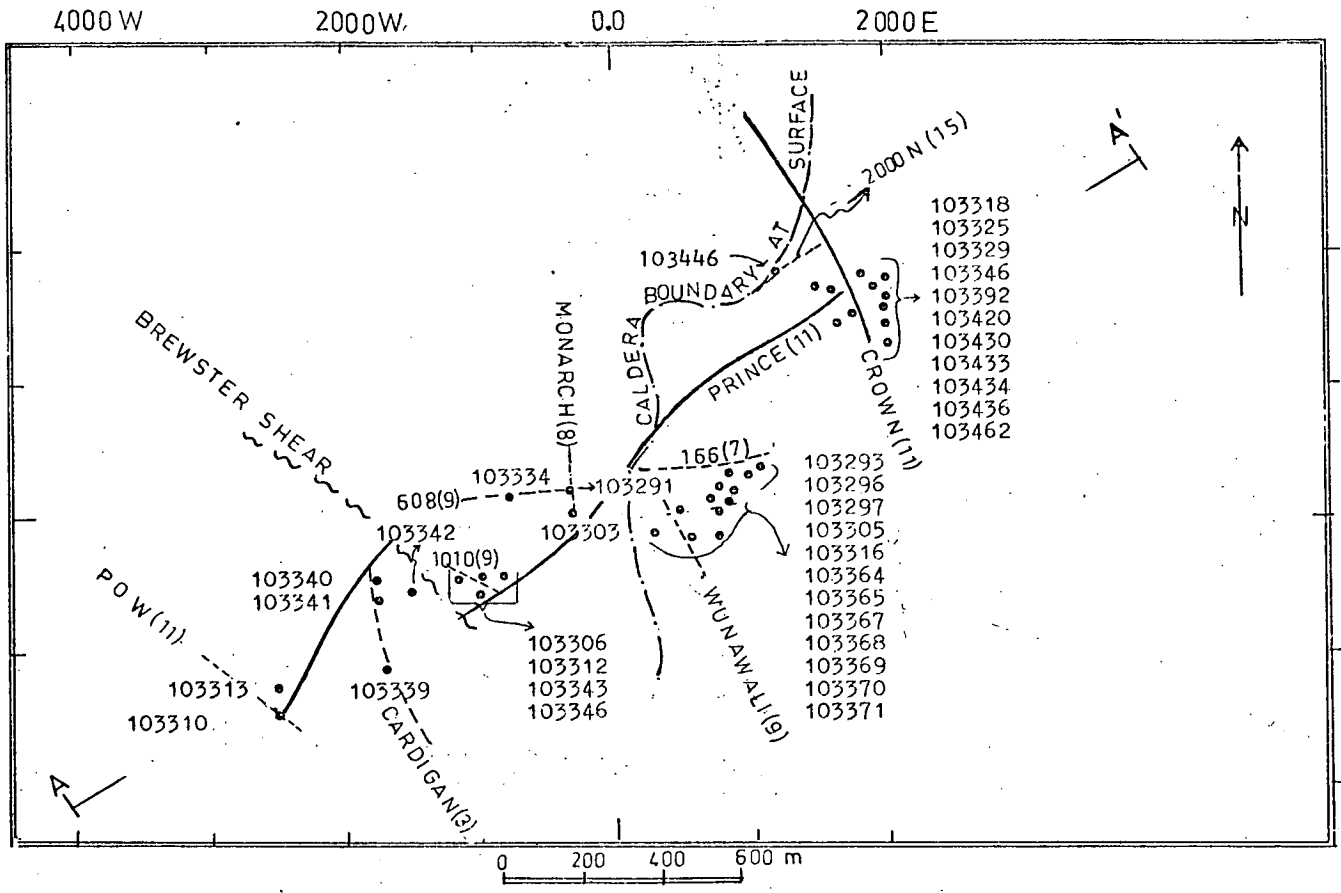

Fig. 7.5A Simplified level plan showing the location of samples used for fluid-inclusion studies. Filled circles: sample location with numbers; heavy solid lines: principal lodes with level of projection in brackets; broken lines: minor lodes with level of projection in brackets.

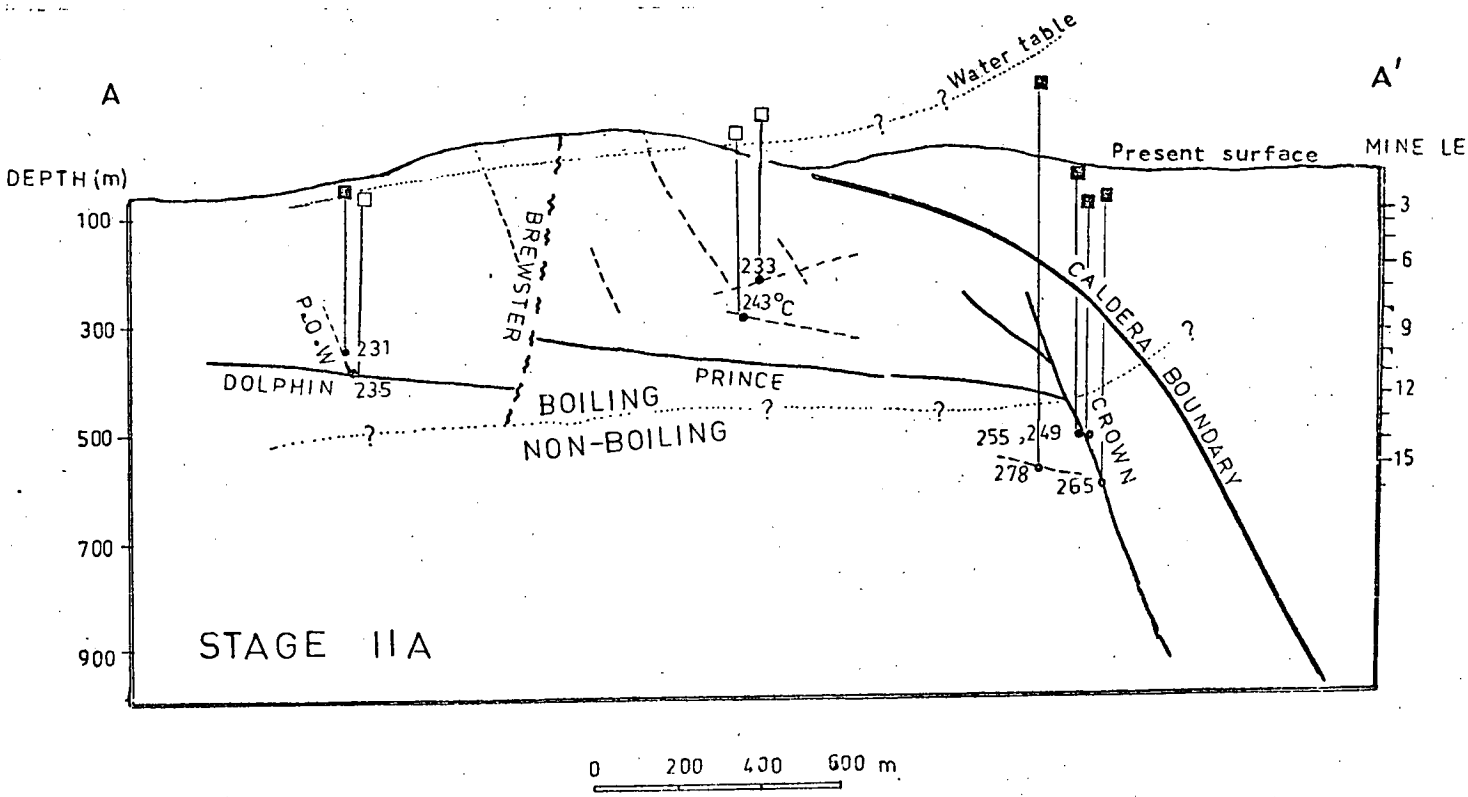

Fig. 7.5B Cross-section A-A' in Fig. 5.5A showing the average fluid-inclusion temperatures (Table 7.1), approximate position of water table and the probable depth of commencement of boiling. Filled squares: minimum depth of water table for samples lacking type B inclusions; open squares: approximate position of water table calculated for samples containing type B inclusions.

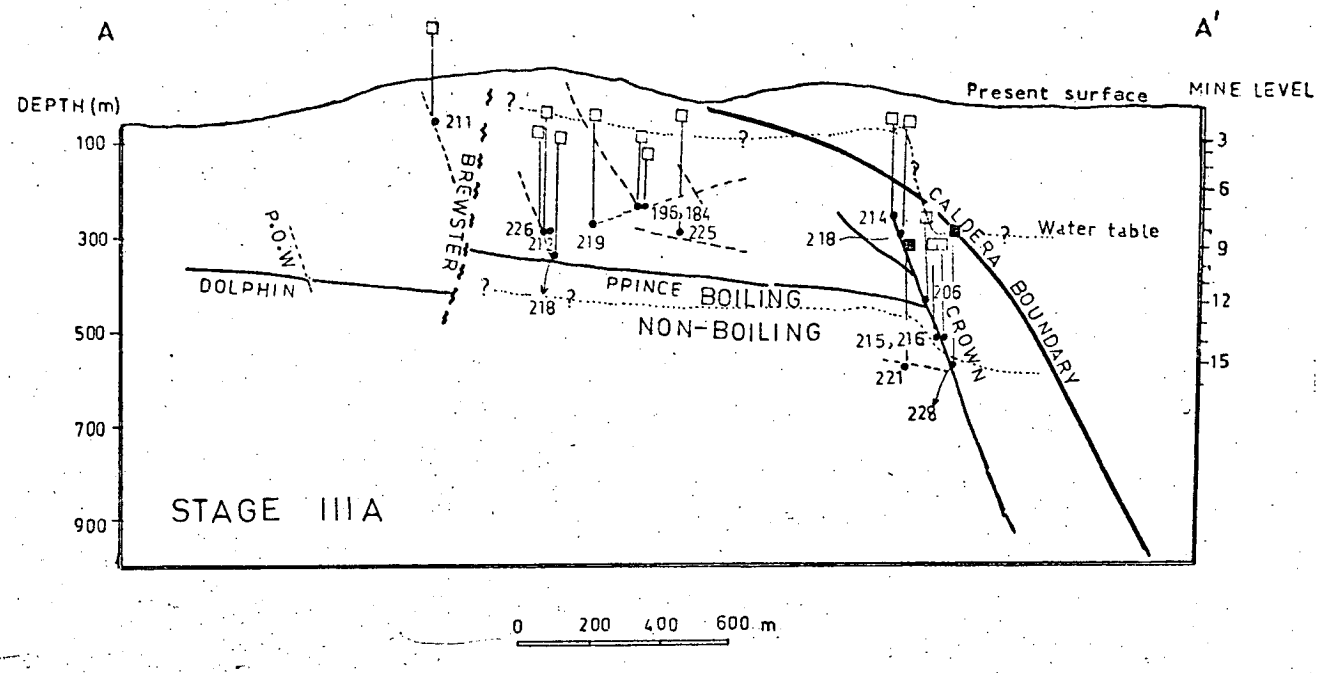

Fig. 7.6A Cross section A-A' in Fig.7.5A. Description same as for Fig.7.5B.

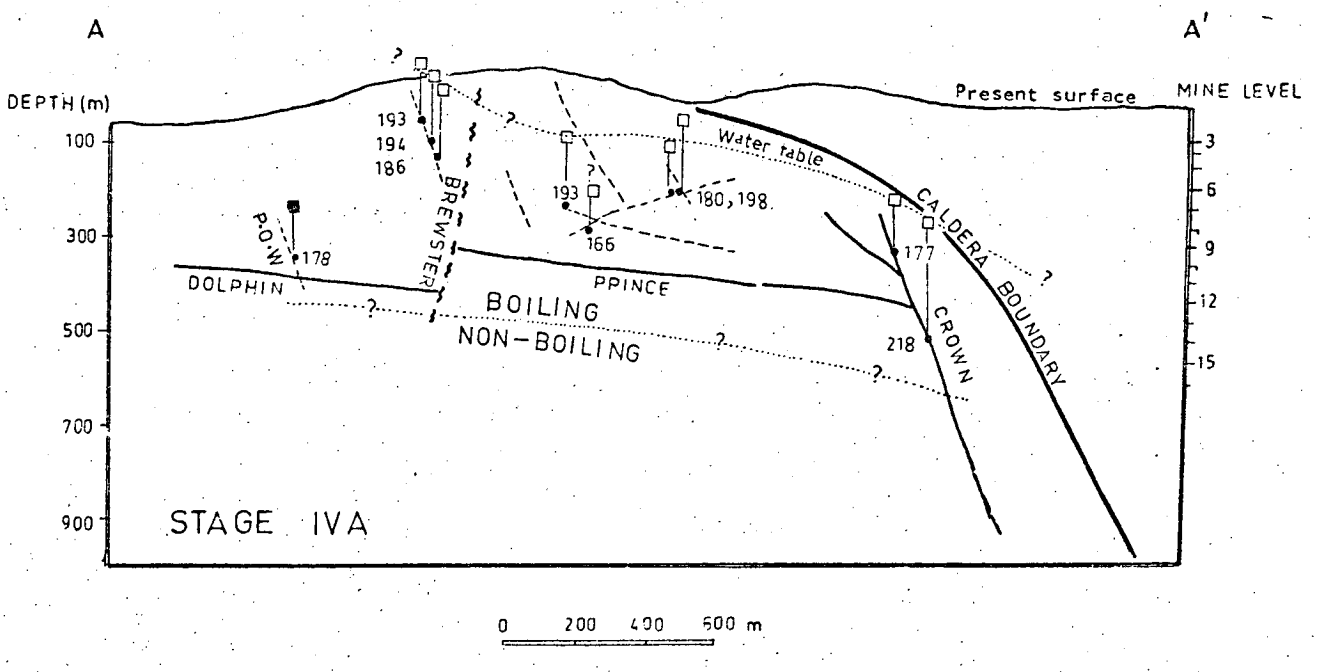

Fig. 7.6B Cross section A-A' in Fig.7.5A. Description same as for Fig.7.5B.

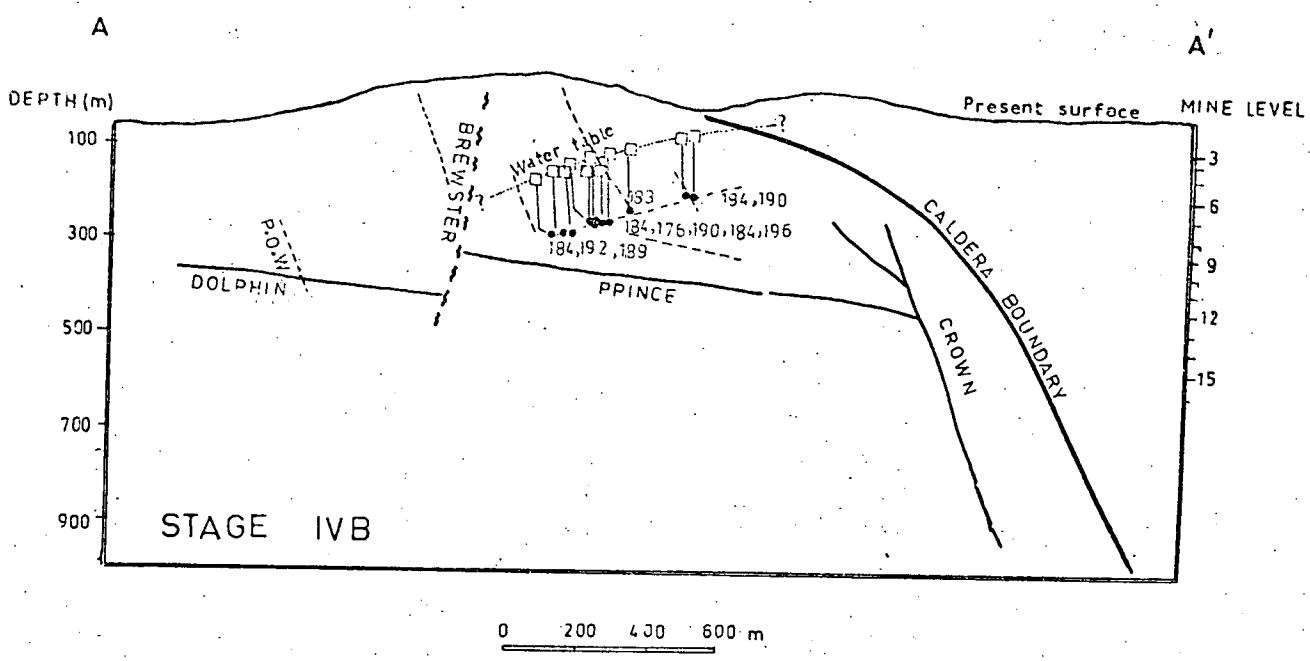

Fig.7.7A Cross section A-A' in Fig. 7.5A. Description same as for Fig.7.5B.

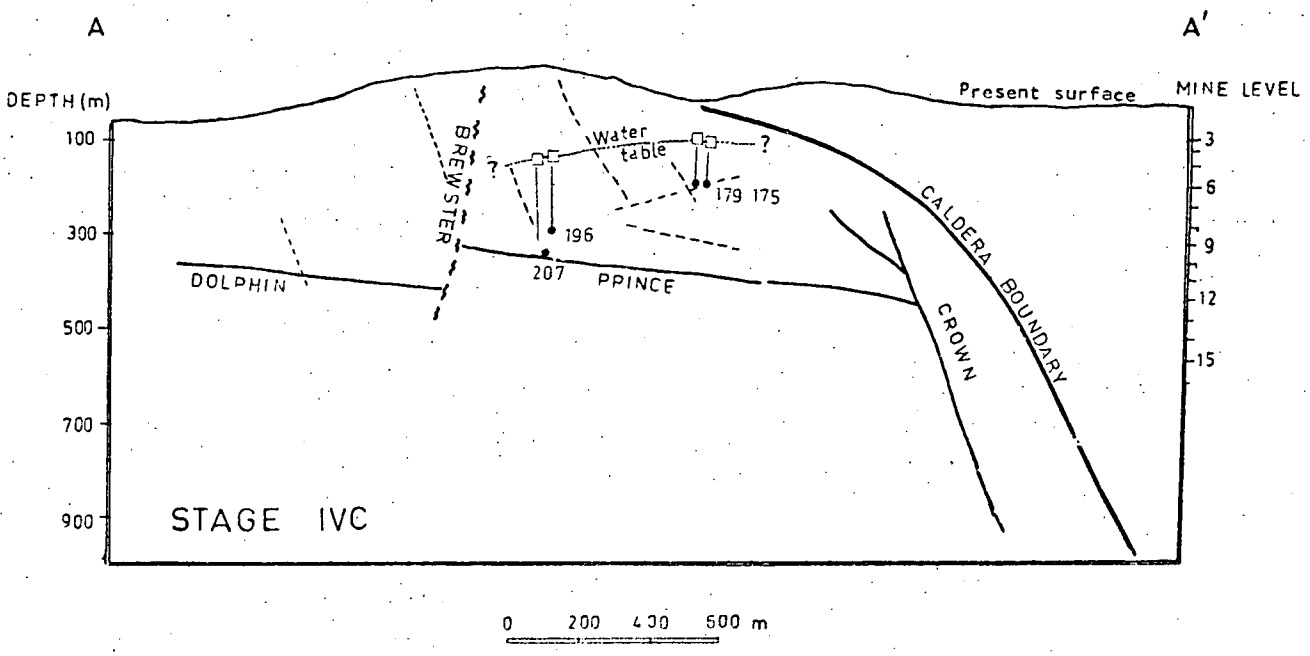

Fig.7.7B Cross section A-A' in Fig. 7.5A. Description same as for Fig.7.5B.

inclusions. Apparently boiling commenced between 15 and 14 levels near the Crown lode (Fig. 7.6A). This lowering may reflect cauldron collapse during or just prior to stage IIIA. If this has happened the boiling horizon (level of commencement of boiling) may still be at relatively higher elevations in areas away from the caldera. The calculated height of the water table (Fig. 7.6.A) indicates a sudden drop above the Crown lode which may also be due to cauldron collapse.

Stage IVA All samples (except 103310) contain type-B inclusions indicating boiling at least down to 14 level. The water table (Fig 7.6B) indicates a gentle slope towards the caldera suggesting relatively settled conditions after an abrupt period of caldera subsidence.

Stage IVB All samples contained type-B inclusions. As samples from lower levels are not available the lower limit of boiling is not known. The water table shows a slope away from the caldera which could be due to opening of the Brewster shear (Fig. 7.7A).

Stage IVC All samples contain type-B inclusions. As with stage IVB, the lower limit of boiling could not be established. The slope of the water table is still away from the caldera (Fig. 7.7B) but it is apparently not as steep as during stage IVB, suggesting a return to normal conditions after a period of activation of the Brewster shear.

7.7 LEACHATE ANALYSIS

For leaching analyses 10 samples of vein quartz were selected that were relatively free of impurities like carbonates, silicates, sulphides and tellurides. Samples weighing betwen 23 to 43 g were placed in cold HF for two hours to remove any alkali feldspar. These samples were then:-

(1) Boiled in concentrated HNO_3 for two hours

(2) Boiled in deionised water for two hours

(3) Placed in the cleaning U-tube (Fig. 7.8) until current readings comparable to the deionised water were obtained. This process took up to 8 hours.

The samples were then placed in stainless steel tubes which had been:

(a) Cleaned in an ultrasonic cleaner for half an hour with soapy water,

(b) Cleaned with dilute HNO_3 for two hours,

(c) Placed in deionised water for two hours,

(d) Filled with deionised water. The purity of this water was checked using the cleaning U-tubes; the process was repeated until current readings comparable to deionised water were obtained.

The samples were crushed inside the tube by a heavy-duty press. The crushed samples were then leached with 15 to 30 ml of deionised water. The leachate was collected in plastic bottles cleaned by processes (a) to (d) described above, and the filter papers used were washed with:

(i) dilute HNO_3,

and (ii) deionised water (the purity of the filtered water being checked using the cleaning U-tube).

Blank samples were prepared by leaching uncrushed quartz. The leachates were analysed for Na, K, Ca, Mg and Li by atomic absorption methods. Lithium concentrations were found to be below the detection limit (0.001 ppm). Chlorine analysis of the leachates was attempted by ion selective electrode and by an absorptiometric method described by Swain (1956). The ion selective method did not prove to be successful because of the small volume of the leachate (less than 10 ml). Determination by the absorptiometric method suffered because of suspended fine particles of quartz of colloidal dimensions and small volumes. Four analyses of relatively clear solutions are given in Table 7.2.

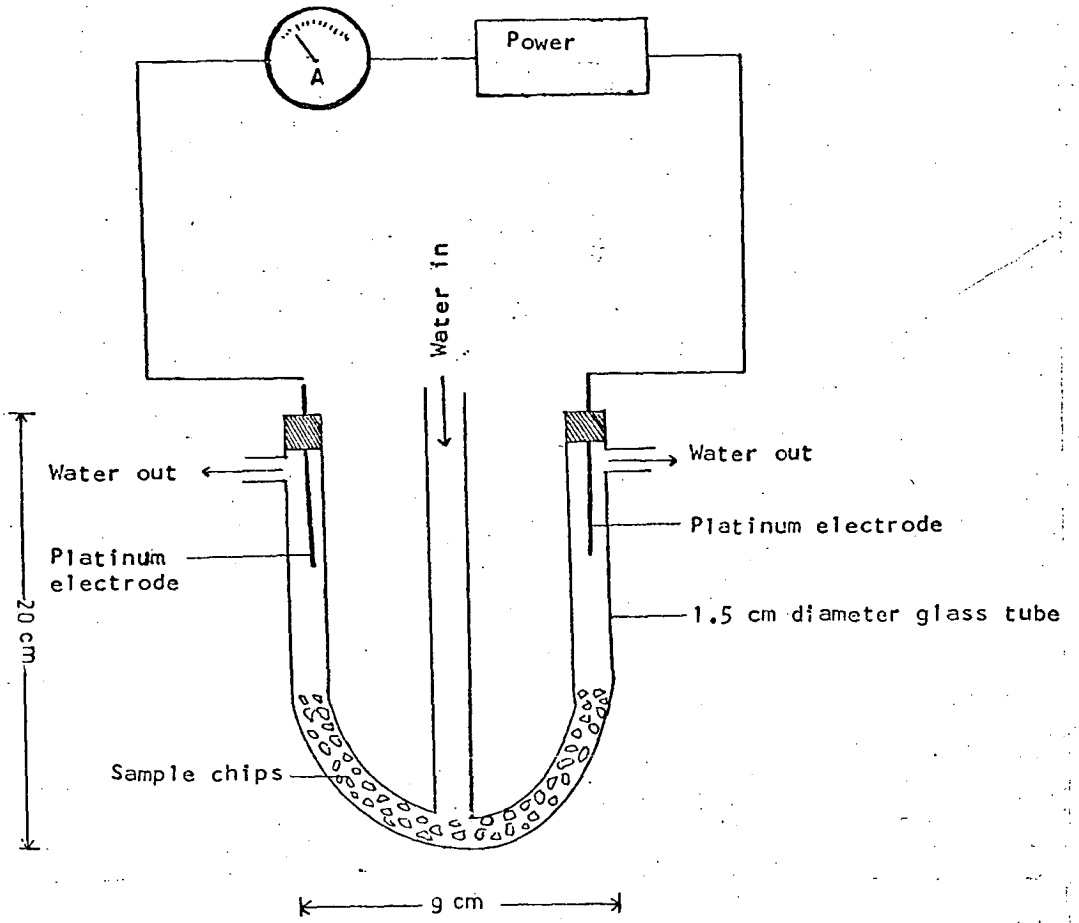

Fig. 7.8 Tube for cleaning fluid-inclusion chips.

Table 7.2

Analyses of Leachates.

Specimen number	Stage	Sample weight (gm.)	Volume Water (ml.)	Concentrations in ppm					Equivalent concentrations of chlorides, ppm				Weight proportions of chlorides.				Weight proportions adjusted to 5.5% total salts.				Cations (%)				Molality			
				Na	K	Ca	Mg	Cl*	NaCl	KCl	$CaCl_2$	$MgCl_2$	NaCl	KCl	CaCl	MgCl	NaCl%	KCl%	CaCl %	MgCl %	Na	K	Ca	Mg	Na	K	Ca	Mg
103206	IIA	25	15	3.25	1.50	3.35	.085	14	8.19	2.64	9.69	.33	3.10	1	3 48	.13	2.21	.71	2.48	.09	.88	.37	.89	.023	.38	.09	.22	.009
103430	IIIA	30	15	0.90	1.00	3.35	.012	13	2.26	1.89	9.15	.05	1.20	1	4.85	.03	.93	.78	3.77	.02	.37	.41	1.35	.005	.16	.10	.34	.002
103433	IIIA	24	15	4.50	1.45	3.30	.073	-	11.35	2.74	9.05	.28	4.14	1	3.30	.10	2.67	.64	2.12	.06	1.06	.34	.76	.015	.46	.09	.19	.006
103297	IVA	24	15	1.45	1.00	1.70	.036	10	3.65	1.84	4.66	.14	1.93	1	2.47	.08	1.94	1.00	2.47	.08	.77	.52	.89	.020	.33	.13	.22	.008
103296	IVB	38	20	1.75	1.10	3.70	.037	9	4.41	2.07	10.15	.14	2.13	1	4.90	.07	1.45	.68	3.33	.05	.58	.36	1.20	.013	.25	.09	.30	.005
103297	IVB	40	20	2.00	1.50	4.00	.027	-	5.05	2.84	10.98	.10	1.77	1	3.86	.04	1.46	.82	3.18	.03	.58	.43	1.15	.008	.25	.11	.29	.003
103377	IVB	23	15	2.55	1.30	4.20	.061	-	6.43	2.45	11.53	.24	2.62	1	4.71	.10	1,71	.65	3.07	.07	.68	.34	1.11	.018	.30	.09	.28	.007
103377	IVC	28	15	6.60	1.20	4.35	.097	-	16.65	2.27	11.95	.38	7.33	1	5.26	.17	2.92	.40	2.10	.07	1.16	.21	.76	.018	.50	.05	.19	.007
103296	IVC	43	30	2.10	1.11	4.35	.073	-	5.20	2.07	11.94	.28	2.56	1	5.77	.14	1.49	.58	3.35	.08	.59	.30	1.21	.020	.26	.08	.30	.008
103297	IVC	40	30	2.65	1.15	2.90	.012		6.68	2.18	7.95	.05	3.06	1	3.65	.02	2.17	.71	2.60	.01	.86	.37	.94	.003	.37	.09	.23	.001

* Analysis doubtful

The analyses of leachates are given in Table 7.2 and are plotted on a K-Na-Ca triangle in Fig. 7.9.

The K-Na-Ca concentrations can be used to approximate the temperatures of the ore fluids. Using the methods outlined in Fournier & Truesdell (1973), a temperature range from 171 to 242°C is obtained. These temperatures differ slightly from fluid-inclusion temperatures, but the variations appear to be within the limits of uncertainty.

If it is assumed that the Na-K-Ca-Mg proportions of the leachates are the same as those of the hydrothermal solutions and these are re-adjusted to the average salinity (5.5 wt. % eq. NaCl) the molalities of these elements in the ore fluids can be approximated. The molalities calculated in this manner are given in Table 7.2. The average values so obtained are 0.35 molal Na, 0.1 molal K, 0.26 molal Ca and 0.005 molal Mg. These calculations assume that cations are totally balanced by chloride ion. Mineral stability data (Chapter 11) indicates sulphur and carbon concentrations of 10^{-3} and 10^{-2} molal respectively, suggesting insignificant proportions of sulphates and carbonates in comparison to chloride.

It can be seen from Fig. 7.9 and Table 7.2 that the Emperor ore fluids have a fairly constant Ca/K ratio which averages about 2.5.

The following reaction can be written for the assemblage present at the Emperor mine:-

$$\tfrac{1}{2}KAl_3Si_3O_{10}(OH)_2 + CaMg(CO_3)_2 + 3SiO_2 + K^+ + 3H^+ =$$
$$3/2\ KAlSi_3O_8 + Ca^{2+} + Mg^{2+} + 2H_2O + 2CO_2\ (g)$$

$$\log K_{250^\circ C} = 13.76 \quad \text{(Appendix E.2)}$$

Assuming the following

$m_{Mg} = 0.005$ (average from Table 7.2)

$f_{CO_2} = 2.5$ (see Chapter 10)

pH = 5.5 (see Chapter 10)

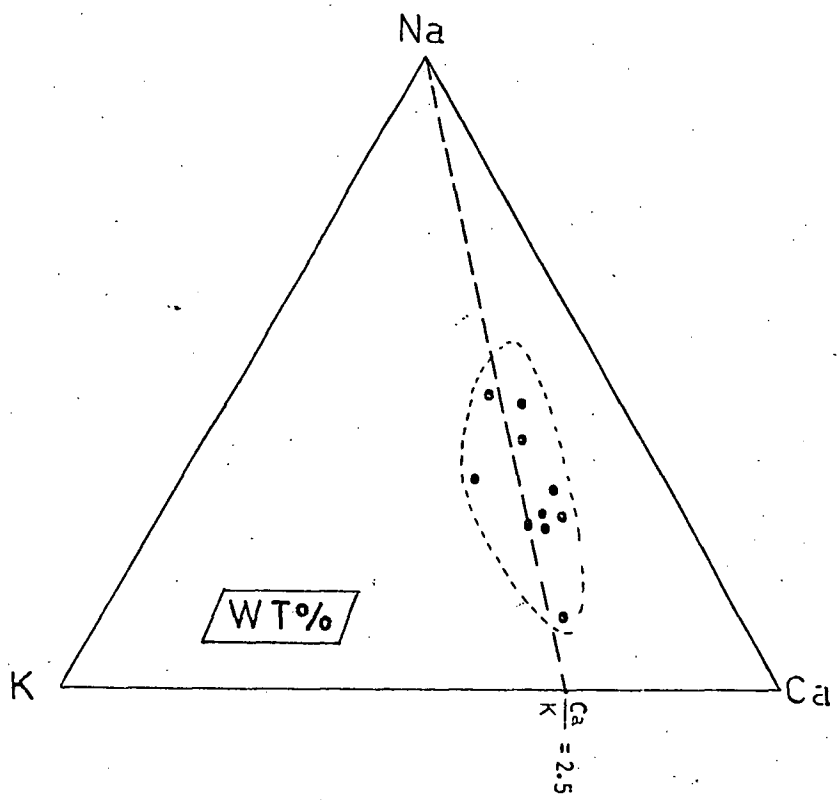

Fig. 7.9 Analyses of leachates plotted on a Na-K-Ca triangle. For details refer to Table 7.2.

and using the activity coefficients given in Appendix E.3, an m_{Ca}/m_K ratio of 2.6 is obtained. This is close to that obtained from leachate analyses. This approximation assumes constant values for pH, f_{CO_2} and temperature, which is unlikely. In natural hydrothermal systems, like Emperor, where intermittent boiling occurred, both pH and total carbon in solution tend to fluctuate but they have opposite effects on the above equilibrium. Boiling of CO_2 will reduce f_{CO_2} but it will also increase pH. This assists in keeping the m_{Ca}/m_K ratio more or less constant.

Chapter 8

WALL-ROCK ALTERATION

8.1. GENERAL

M. Cohen (1962) studied the altered rocks from the Emperor mine and concluded that the condition of augite provides the simplest and most satisfactory basis for describing the progressive alteration of the host-rock basalt. She identified six stages of augite alteration, as follows:

Stage 1 Fresh, though cracked.

Stage 2 Altering along edges and along irregular cracks, to calcite and some serpentinite/chlorite.

Stage 3 Advanced but not complete alteration to cloudy calcite. There may be small quantities of chlorite, serpentine, quartz and perhaps sericite.

Stage 4 Completely altered, calcite being the principal replacement mineral with small amounts of serpentine, chlorite, magnetite, kaolin and actinolite.

Stage 5 Quartz is present in the replaced augite phenocrysts. Minute amounts may have been seen before, but now it is becoming prominent. Calcite is still predominant, and there may be some chlorite and serpentine.

Stage 6 Augite pseudomorphs are completely replaced by quartz.

The sequence given above is generally correct except that kaolin was not observed in the present study and the calcite referred to is ankerite and/or dolomite.

In the present study the wall-rock alteration assemblages are divided into two groups, i.e. the propylitic assemblage and the potassium-silicate assemblage (or K-silicate assemblage), more or less following the usage of Meyer & Hemley (1967).

8.2 PROPYLITIC ALTERATION

The propylitic assemblage at the Emperor mine includes chlorite, ankerite, dolomite, actinolite, serpentine and magnetite. Pyrite is found locally in the vicinity of mineralized veins. Epidote is very rare in the specimens studied. This assemblage may include stages 1 to 4 described above. The width of fairly intense alteration is a few metres, beyond which there is a fairly widespread but weak alteration with epidote, actinolite and serpentine.

8.3 POTASSIUM-SILICATE ALTERATION

The potassium-silicate assemblage at the Emperor mine includes sericite, potassium feldspar, quartz, carbonates, pyrite and rare chlorite and magnetite. Magnetite is largely replaced by pyrite. Roscoelite (vanadium mica) invariably occurs with telluride-rich ores.

Orthoclase (?) commonly occurs as prismatic crystals in the wall rock and adularia (?) as rhombic grains near the vein base and between barren quartz layers. Both of these minerals are identified on the basis of crystal habit and electron microprobe analysis (Appendix D.4) but sufficient material could not be separated to confirm the suggested identification by X-ray diffraction method.

Sericite generally occurs as small flakes dusting both plagioclase and potassium feldspar. Commonly the central part of the plagioclase grain is sericitized and the rims are relatively unaltered.

Chlorite of this assemblage is relatively richer in iron and lower in magnesium (Fig. 6.8) than the chlorite of the propylitic facies.

The low iron content of carbonates from this assemblage has already been described (Chapter 6); most of the carbonate is dolomite rather than ankerite.

The width of the K-silicate assemblage ranges from a few millimetres to a few centimetres and is related to the width of the mineralized vein and the nature of the host rock, being wider in andesite than in basalt.

In many samples, stringers of vein quartz are observed cutting across the pseudomorphs of sericite and ankerite (Plate 5.3), suggesting that wall-rock alteration may be earlier than the silicification and mineralization.

8.4 CHEMICAL EXCHANGE BETWEEN HYDROTHERMAL SOLUTIONS AND WALL-ROCKS

Major and trace element analyses of altered and fresh rocks are given in Appendices C.1 to C.3. All analyses were done by X-ray fluorescence techniques except that CO_2 analyses given in Appendix C.5 were made by the method described in Shapiro (1975). Specific gravity determinations on fresh and altered rocks are given in Appendix C.6.

From the analyses, changes in the (chemical) composition of the samples due to alteration have been calculated. They are expressed in mg/cc (assuming that no volume change has resulted due to alteration). The average specific gravity, for fresh and altered rock, used in these calculations are obtained from the measurements given in Appendix C.6. The chemical gains and losses are plotted in Figs. 8.1, 8.2. and 8.3, and some salient features are discussed below.

Iron

The analyses plotted in Figs. 8.1 and 8.2 are actually total iron converted to Fe_2O_3. It is evident that iron is depleted in the altered rocks, with the propylitic rocks less depleted than the K-silicate rocks. Minor depletions in the propylitic rocks are probably the result of the replacement of pyroxene and olivine by chlorite and ankerite.

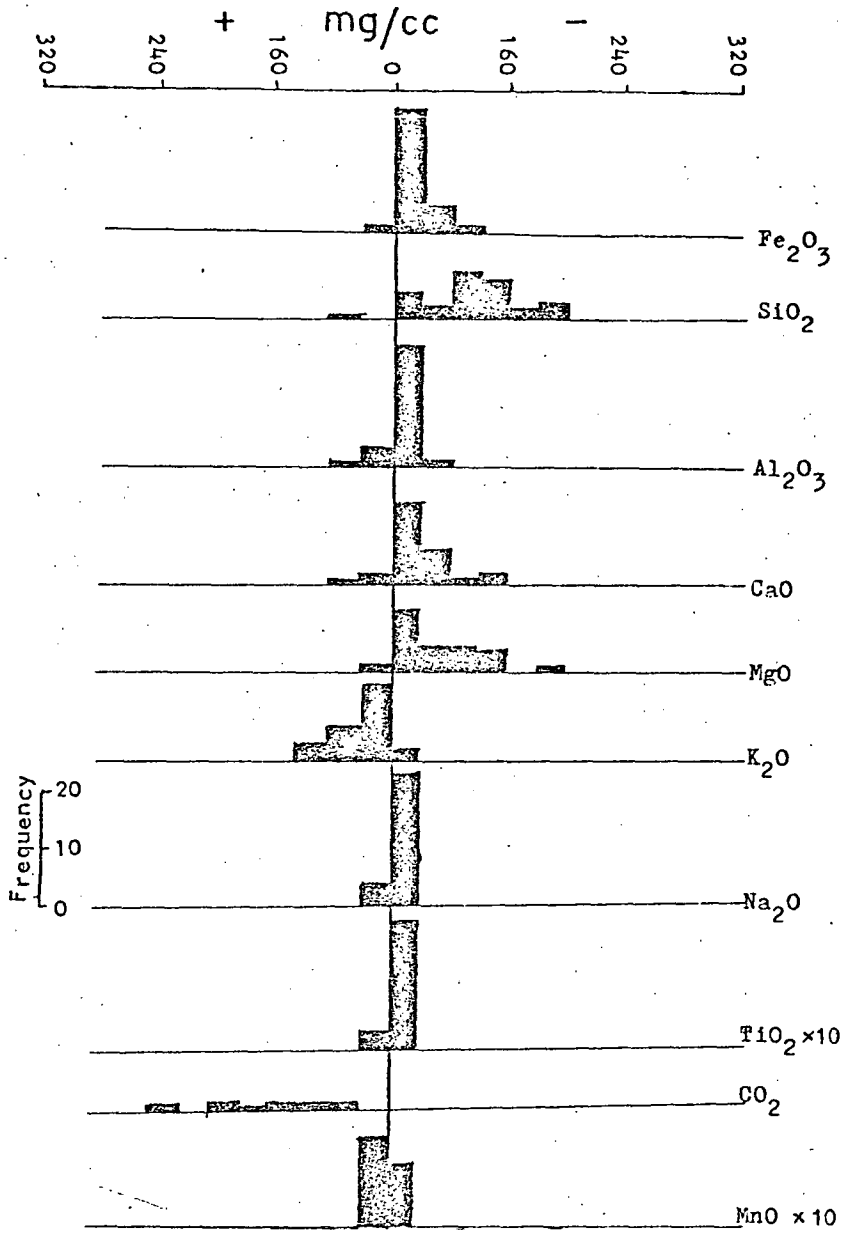

Fig.8.1 Changes in major element abundances during propylitic alteration.

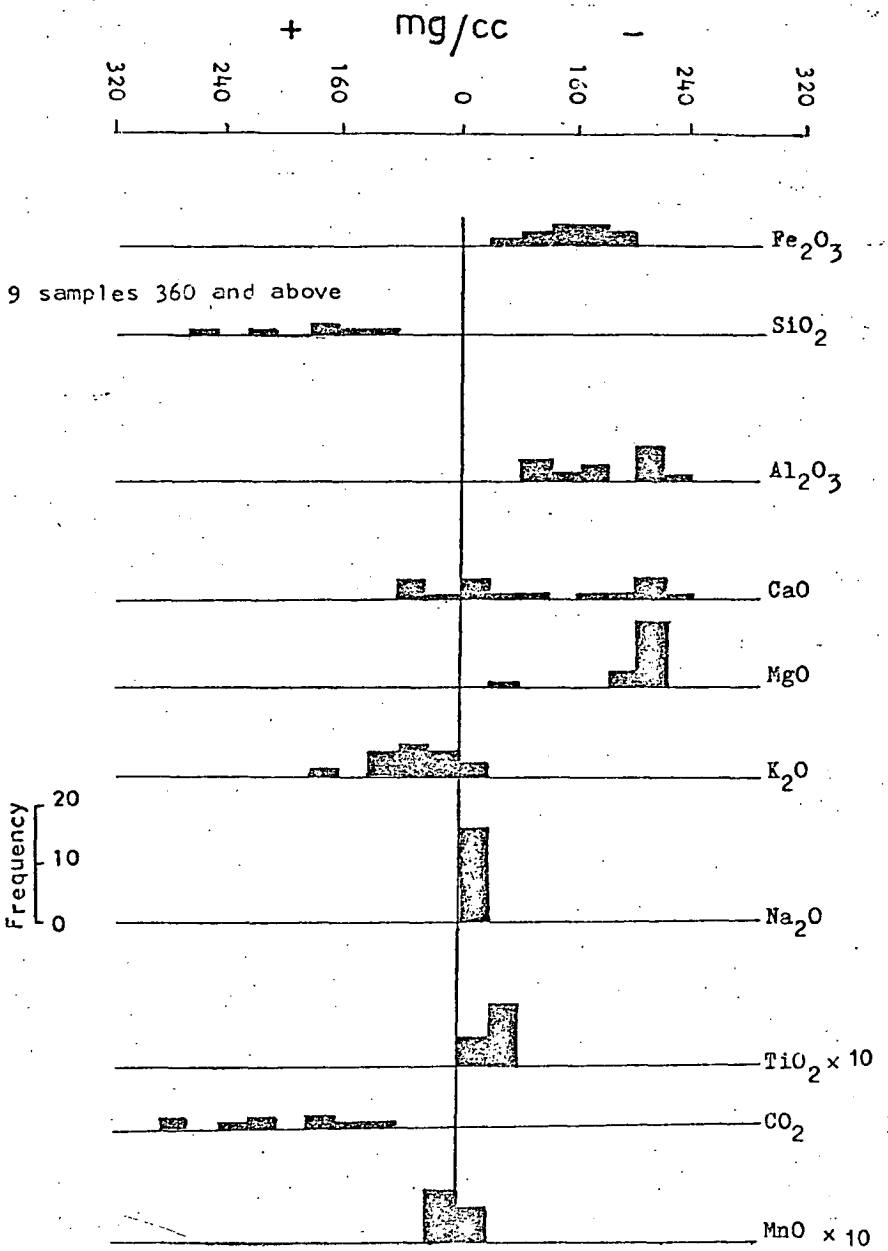

Fig.8.2 Changes in major element abundances during K-silicate alteration.

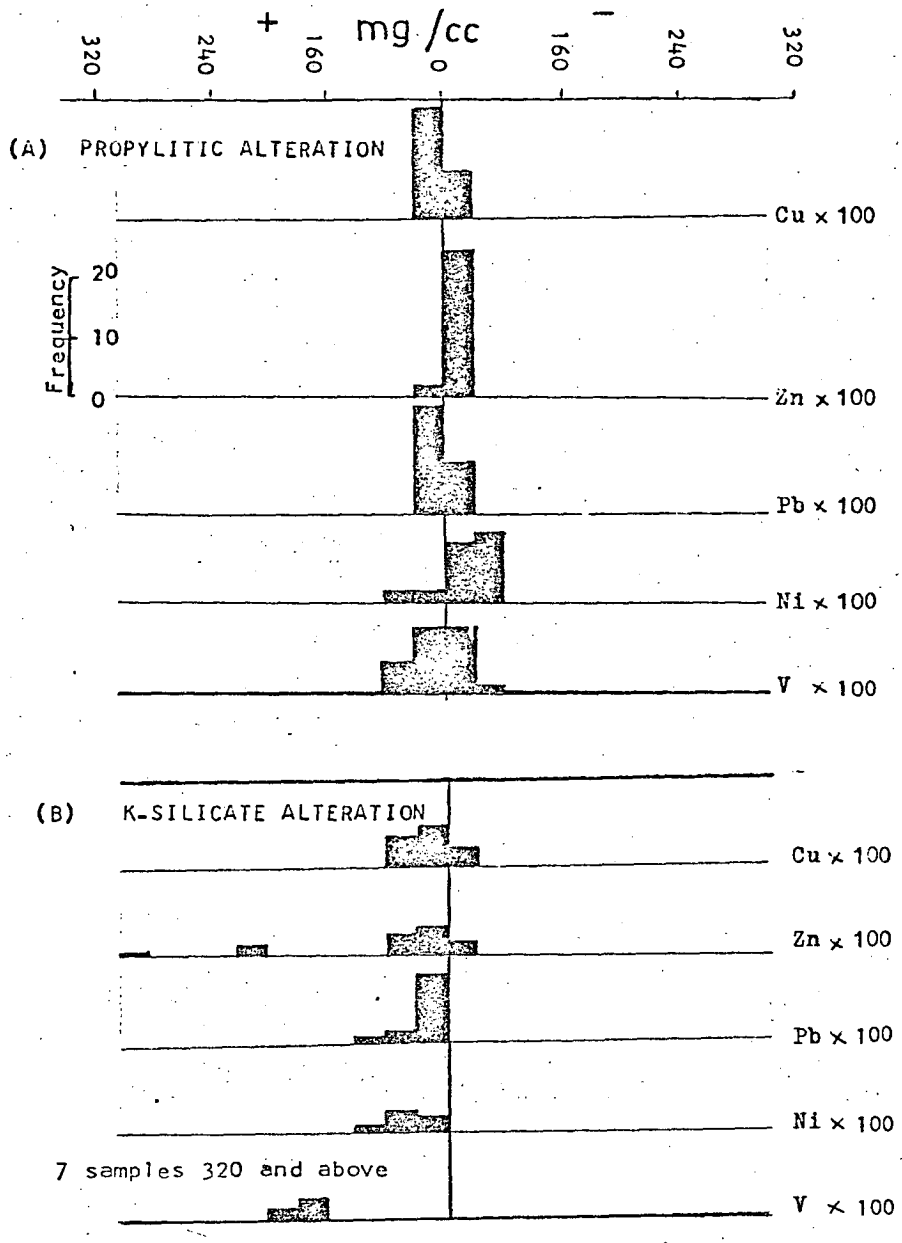

Fig.8.3 Changes in trace element during propylitic and K-silicate alteration.

Extensive depletions in the K-silicate rocks reflect the replacement of chlorite and ankerite by quartz, sericite, K-feldspar and dolomite.

Silica

Silica is depleted in the propylitic rocks (up to a maximum of 240 mg/cc) but the K-silicate rocks show extensive enrichment in silica. The depletion of silica in the propylitic rocks demand some explanation. The solubility of silica appears to be essentially independent of f_{O_2}, pH and ionic strength of the aqueous solution in most geological situations, and certainly those at the Emperor mine. It is a function of temperature (Kennedy, 1950; Kitahara, 1960; Morey & Hesselgessar, 1951; Morey *et al.*, 1962; Weill & Fyfe, 1964; Anderson & Burnham, 1965) and increases with increasing temperature except near the critical point. If silica-saturated solutions moving through the veins were hotter than the enclosing rocks, then as they diffuse into the rocks cooling must have occurred and silica been deposited in most situations. Because silica is depleted from the propylitic rocks it appears that early solutions were undersaturated with silica. The later solutions (which were responsible for the K-silicate alteration) must have been saturated with silica.

Aluminium

Al_2O_3 is only slightly depleted in the propylitic rocks (up to a maximum of 60 mg/cc) but major depletion (up to a maximum of 300 mg/cc) occurs in the K-silicate rocks. As plagioclase is the main aluminium-bearing phase in the fresh rocks, slight depletion in the propylitic rocks may be attributed to the replacement of this mineral by ankerite. In the K-silicate rocks, replacement of chlorite, residual plagioclase and even potassium feldspar by quartz probably releases aluminium to the solutions. Textural evidence for such replacements is frequently observed in thin section.

Calcium and magnesium

Both calcium and magnesium are progressively depleted in the altered rocks with the K-silicate rocks more depleted than the propylitic rocks.

Minor depletions in the propylitic rocks are possibly due to the desctruction of olivine and pyroxene. Some calcium will also go into solution as a result of replacement of plagioclase by chlorite. Most magnesium and calcium will, however, be retained in ankerite and dolomite.

In the K-silicate rocks, replacement of dolomite and ankerite by quartz is a possible reason for the loss of substantial calcium and magnesium.

Potassium and sodium

Potash is added to both assemblages up to a maximum of 180 mg/cc, largely because it is retained in potassium-feldspar, sericite and roscoelite. Na_2O shows depletions up to a maximum of about 40 mg/cc (i.e. nearly all the Na_2O in these rocks has been leached away). This reflects the lack of Na-bearing phases in both alteration assemblages.

Carbon dioxide

Carbon dioxide has been added to both the assemblages up to a maximum of about 460 mg/cc. This is expected because of extensive carbonatization of both pyroxene and plagioclase.

Manganese

Some samples show slight depletion in MnO_2, while others a slight enrichment, so manganese concentrations probably remained more or less constant.

Copper, lead and zinc

In the propylitic rocks, some samples show minor depletions while others minor addition (Fig. 8.3). The concentrations of these three elements probably remained more or less constant in the propylitic rocks.

In the K-silicate rocks all three elements show considerable enrichment as a result of precipitation of base-metal sulphides.

Nickel

The majority of the propylitic rocks show a depletion in nickel, while all the samples from the K-silicate rocks show enrichment. A large part of the nickel in volcanic rocks resides in the pyroxene and olivine (Wagner & Mitchell, 1951; Mason, 1958) and it is suggested that during the hydrothermal alteration of these minerals most of the nickel is released to the solutions. In the K-silicate rocks, however, most of it is probably deposited in melonite.

Vanadium

In the propylitic rocks some samples show depletion in vanadium concentration while others show slight enrichment. It appears that vanadium concentration did not appreciably change during propylitic alteration. The K-silicate rocks on the other hand show considerable enrichment in vanadium, present mainly in roscoelite.

The high vanadium contentsof magnetite at the Emperor mine have already been mentioned in Chapter 5. Vanadium was probably present in magnetite and during its replacement by pyrite it was probably released to the solutions.

Titanium

The majority of the samples from the propylitic rocks show minor depletions, though a few show slight enrichment. Virtually all the titanium has been leached out of the K-silicate rocks.

In the basaltic rocks most of the titanium resides in the pyroxene. This titanium is released to the solutions during the replacement of pyroxene by ankerite or dolomite. A large part of the titanium will, however, be retained in magnetite and anatase. In the K-silicate rocks extensive replacement of magnetite and anatase by pyrite has released almost all the titanium to the solutions.

Chapter 9

STABLE-ISOTOPE STUDIES

9.1 GENERAL

The purpose of the stable isotope measurements was to establish the source of the hydrothermal solutions and dissolved constituents and to place constraints on the f_{O_2}-pH-T conditions of the depositing environment. This work involved measurements of $\delta^{34}S$ on sulphides; $\delta^{18}O$ on bulk rock, quartz and carbonates; $\delta^{13}C$ on carbonates; δD on fluid-inclusion water, and combined δD and $\delta^{18}O$ on local waters. These analyses were carried out at the Institute of Nuclear Sciences, Wellington, New Zealand.

9.2 SAMPLE PREPARATION

Coarse-grained pyrite was hand picked and checked for impurities under the microscope. It was found to be free of any other sulphides. Pyrite from thin veins in the wall-rock was extracted using a dentist's drill and was powdered in the process. Minor carbonate and silicate impurities were present in these samples.

Vein quartz, dolomite and calcite occur as large crystals of about 99% purity and they did not require any special treatment.

No physical separation was possible for wall-rock carbonates (ankerite and/or dolomite). Whole-rock samples were reacted with 100% H_3PO_4 and the CO_2 evolved was used for $\delta^{13}C$ and $\delta^{18}O$ measurements on these carbonates. It was however checked that no veinlets of stage V calcite occurred in these samples. Similar procedures were used for the determination of $\delta^{13}C$ and $\delta^{18}O$ of the carbonates in the sedimentary rocks.

Clear quartz and calcite chips were used for the extraction of fluid-inclusion water.

The local waters were collected by the staff of Emperor Gold Mines Ltd., and were sent to the laboratory in sealed plastic bottles.

9.3 ANALYSIS

The sulphur for isotopic measurements from pyrite was extracted as SO_2 by reaction with Cu_2O at 1000°C by techniques described in Robinson & Kusakabe (1975). Galena was converted to Ag_2S which was treated as for pyrite (Rafter, 1957a, 1957b). The SO_2 was analysed on the G.P. mass spectrometer built at the Institute of Nuclear Sciences, Wellington, New Zealand, using techniques described in Hulston & Shilton (1958).

The oxygen for isotopic measurements from quartz and bulk-rock samples was extracted by reaction with bromine pentafluoride and converted quantitatively to CO_2 by a modification of the technique given in Clayton & Mayeda (1963). Five samples could be treated simultaneously, but in practice, four samples and one laboratory standard (R-4150) were used with each batch.

CO_2 gas was extracted from carbonates by reaction with 100% H_3PO_4 at 25°C by methods described in McCrea (1950). Reaction time was about 24 hours for calcite and about two weeks for dolomite and ankerite. The CO_2 samples were analysed in a NAA 6-60 RMS, 15 cm radia, 60° sector mass spectrometer.

Fluid-inclusion water for δD measurements was collected by first outgassing 20 to 64 g of sample in stainless steel tubes. Sealed tubes were then removed from the vacuum line and crushed in a heavy-duty press to open the fluid-inclusions. These tubes were then connected to the vacuum line and the inclusion fluid was collected in a liquid nitrogen trap to check the presence of non-condensable gases (e.g. CH_4). No such gases were detected. The water was then separated from condensable gases (e.g. CO_2) with an acetone-dry ice trap. The proportions of CO_2 present were negligible and not enough to measure or analyse for $\delta^{13}C$ or $\delta^{18}O$.

Fluid-inclusion and local waters were reduced to hydrogen by passing over zinc held above its melting point, in a matrix of sand (Lyon & Cox, 1975).

The δD measurements were made on a Micromass 602C mass spectrometer.

The $\delta^{18}O$ determinations of local waters were made on CO_2 gas which had been equilibrated with the water samples at 25°C by techniques described in Epstein & Mayeda (1953).

The $\delta^{18}O$ and δD values are reported with respect to Vienna SMOW, the $\delta^{13}C$ values are reported with respect to PDB, and $\delta^{34}S$ values are reported with respect to CDT.

The δD and $\delta^{18}O$ measurements on local waters are correct to ± 0.3‰ and 0.14‰ respectively. The δD measurements on fluid-inclusion waters are probably less precise because of minute amounts of water available for analysis. The $\delta^{18}O$ measurements on silicates and carbonates are correct to ± 0.4‰ as is indicated by the variations in the $\delta^{18}O$ values of laboratory standard R-4150. The $\delta^{13}C$ and $\delta^{34}S$ values are probably correct to ± 0.3‰ and ± 0.2‰ respectively, as is indicated from the analyses of duplicate samples.

9.4 RESULTS

9.4.1 Silicates

The $\delta^{18}O$ measurements on quartz and whole rock are given in Table 9.1. The $\delta^{18}O$ values of relatively unaltered volcanic rocks range from +5.6 to +7.1‰. The $\delta^{18}O$ values of propylitic rocks range from +9.1 to +12.4‰ and the $\delta^{18}O$ values of the K-silicate rocks range from +14.2 to +17.1‰. The $\delta^{18}O$ values of vein quartz range from +15.8 to +20.9‰.

The $\delta^{18}O$ values of whole-rock and vein quartz are plotted in Fig. 9.1. It can be seen that there is a gradual increase in $\delta^{18}O$ values from fresh rocks to K-silicate rocks. The $\delta^{18}O$ values of vein quartz are more or less

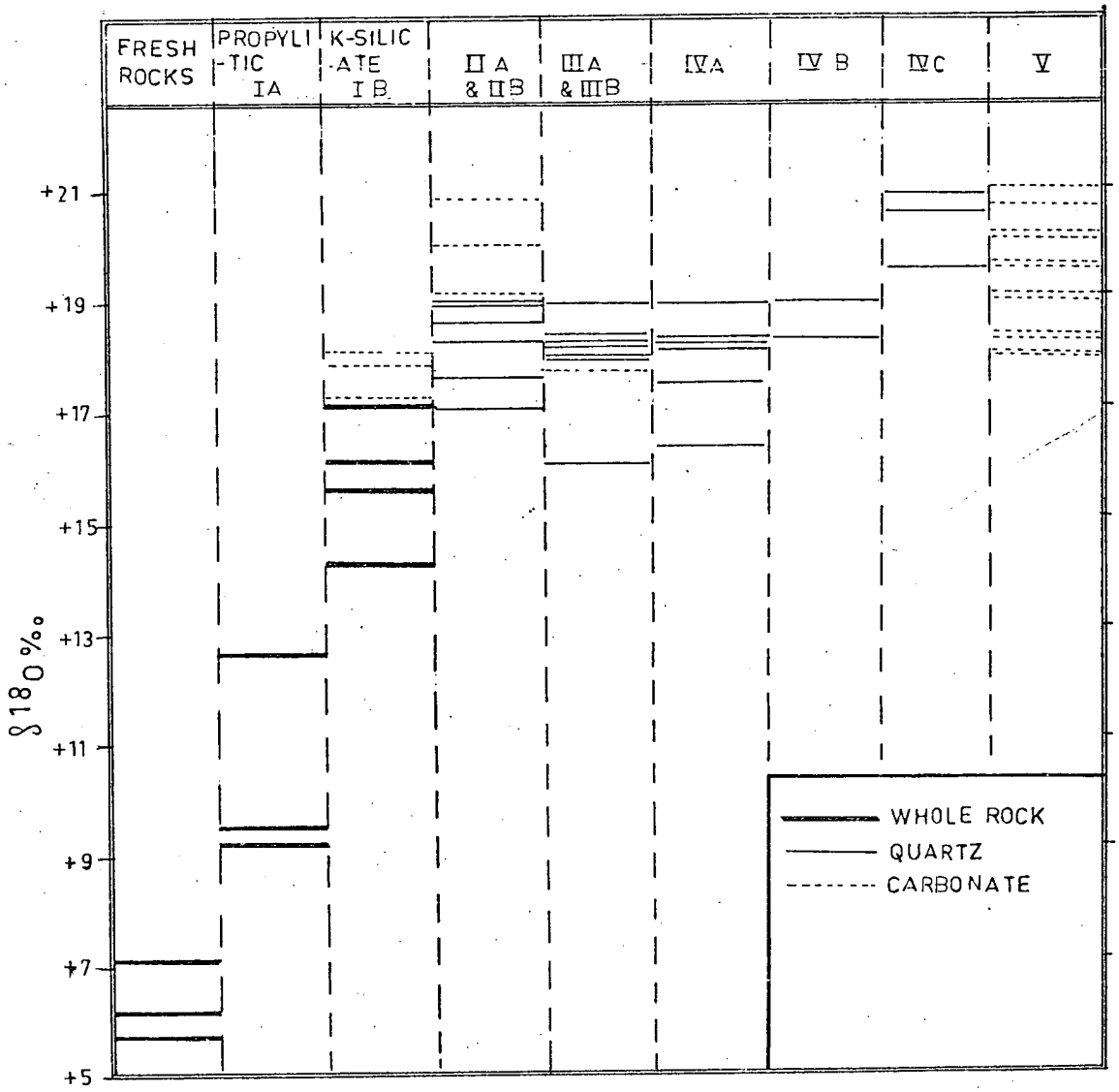

Fig. 9.1 Oxygen isotope data on whole rock, quartz and carbonates. Roman numerals refer to stages in the paragenetic sequence. For details refer to Table 9.1 and 9.2 .

Table 9.1

Oxygen isotope data on quartz and whole rock samples.

Specimen Number	Location	Stage	$\delta^{18}O$ ‰	$\delta^{18}O$ ‰ of H_2O (calculated)	Average fluid-inclusion temperatures °C
(A) Quartz					
103329	14 level, Crown	IIA	+18.8	+7.9	249
103296	7 level, 166 F.M.	IIA	+16.9	+4.6	222
103297	7 level, 166 F.M.	IIA	+17.9	+5.6	222
103313	11 level, P.O.W.	IIA	+17.2	+5.6	235
103446	15 level, Crown	IIA	+18.2	+8.7	278
103433	14 level, Crown	IIA	+17.5	+7.0	255
103329	14 level, Crown	IIIA	+18.8	+6.1	215
103296	7 level, 166 F.M.	IIIA	+18.0	+5.7	222
103297	7 level, 166 F.M.	IIIA	+18.1	+5.6	222
103313	11 level, P.O.W.	IIIA	+17.9	+6.2	235**
103433	14 level, Crown	IIIA	+15.8	+5.3	255**
103392	13 level, Crown	IIIA?	+18.3	+5.6	214
103340	3 level, Cardigan	IIIA	+17.2	+4.1	211
103329	14 level, Crown	IVA	+16.3	+5.4	249**
103296	7 level, 166 F.M.	IVA	+18.2	+3.0	180
103297	7 level, 166 F.M.	IVA	+17.9	+4.1	198
103433	14 level, Crown	IVA	+17.4	+3.6	198
103339	3 level, Cardigan	IVA	+18.9	+4.7	193
103343	7 level, 608 F.M.	IVA	+18.2	+4.0	193

Table 9.1 cont.

Specimen Number	Location	Stage	$\delta^{18}O$ ‰	$\delta^{18}O$ ‰ of H_2O (calculated)		Average fluid-inclusion temperatures °C
103296	7 level, 166 F.M.	IVB	+19.0	+4.6		184
103297	7 level, 166 F.M.	IVB	+18.3	+3.7		190
103340	3 level, Cardigan	IVC	+20.9	+6.7		211***
103296	7 level, 166 F.M.	IVC	+20.6	+5.3		179
103297	7 level, 166 F.M.	IVC	+19.5	+3.8		175
(B) Fresh volcanic rocks						
47288	Augite andesite from Nasivi River crossing 1 mile east of Cayzer shaft.		+6.0			
47286	As above, 1 mile N.E. of Cayzer shaft.		+5.6			
47261	Olivine basalt from DDH MA-56 at 1034 feet.		+7.1			
(C) Propylitic rocks				at 350°C*	at 250°C*	
103333	Basalt, 9 level		+9.1	+5.7	+2.9	
47255	Basalt, DDH MA-56 at 1025 feet.		+9.4	+6.0	+3.2	
47237	Basalt, DDH MA-56 at 1005 feet.		+12.6	+9.2	+6.3	
(D) Rocks with potassium silicate assemblages				at 250°C*		
103398	Basalt, 9 level, Crown		+15.5	+9.2		
103461	Basalt, 13 level, Crown		+14.3	+7.8		
103436	Basalt, 16 level, Crown		+16.1	+9.8		
103336	Basalt, 2 level, Cardigan		+17.1	+10.8		

Table 9.1 cont.

Specimen Number	Location	Stage	$\delta^{18}O$ ‰
(E) Miscellaneous			
47289	Tuff, Nasivi River crossing 1 mile east of Cayzer shaft.		+10.9
47290	Altered biotite andesite, 1 mile S.E. of Cayzer shaft.		+15.5

* Temperatures are assumed (see text).

** Temperatures are assumed to be equal to IIA.

*** Temperature is assumed to be equal to IIIA.

constant (averaging about +18‰) up to stage IVB but the stage IVC quartz is about 2‰ enriched in ^{18}O.

The $\delta^{18}O$ values on single samples, representing various vein-quartz stages, are portrayed in Fig. 9.2. It can be seen that except for a single analysis (Sample 103433, stage IIIA), the $\delta^{18}O$ values of vein quartz from stages IIA to IVB are close to +17.7 ± 1.2‰ but the $\delta^{18}O$ values on stage IVC quartz are about 2‰ heavier (average +20‰).

The $\delta^{18}O$ values of waters in equilibrium with the vein quartz can be calculated at the fluid-inclusion homogenisation temperatures by using the quartz-H_2O fractionation factor. Though there are some disagreements concerning this factor (Bottinga & Javoy, 1973; Clayton *et al.*, 1972; Blattner, 1975), they are only of minor importance and do not significantly change the conclusions. In this study, the quartz-H_2O fractionation factor given in Blattner (1975) has been used. The calculated values of $\delta^{18}O_{H_2O}$ are given in Table 9.1. It can be seen that the calculated $\delta^{18}O_{H_2O}$ range from +3.5 to +7.9‰.

Temperatures of waters in equilibrium with the K-silicate rocks may be similar to the fluid-inclusion temperatures on stage IIA quartz (205-317°C). For an average temperature of 250°C, the $\delta^{18}O$ values of these waters can be calculated on the assumption that the basalt-H_2O fractionation factor is nearly the same as the plagioclase (An_{30})-H_2O fractionation factor (Taylor, 1974). Using this factor (O'Neil & Taylor, 1967), the $\delta^{18}O_{H_2O}$ values have been calculated and are given in Table 9.1. They range from +7.7 to +10.8‰. A similar approach can be applied to calculate the $\delta^{18}O$ of waters in equilibrium with the propylitic rocks, but the temperatures of these waters are not known. A temperature of 250°C gives $\delta^{18}O_{H_2O}$ values between +3.1 and +6.3‰ which are distinctly lower than those obtained for waters in equilibrium with the K-silicate rocks. A temperature of 350°C gives $\delta^{18}O_{H_2O}$ values between +5.6 and +9.1‰ which

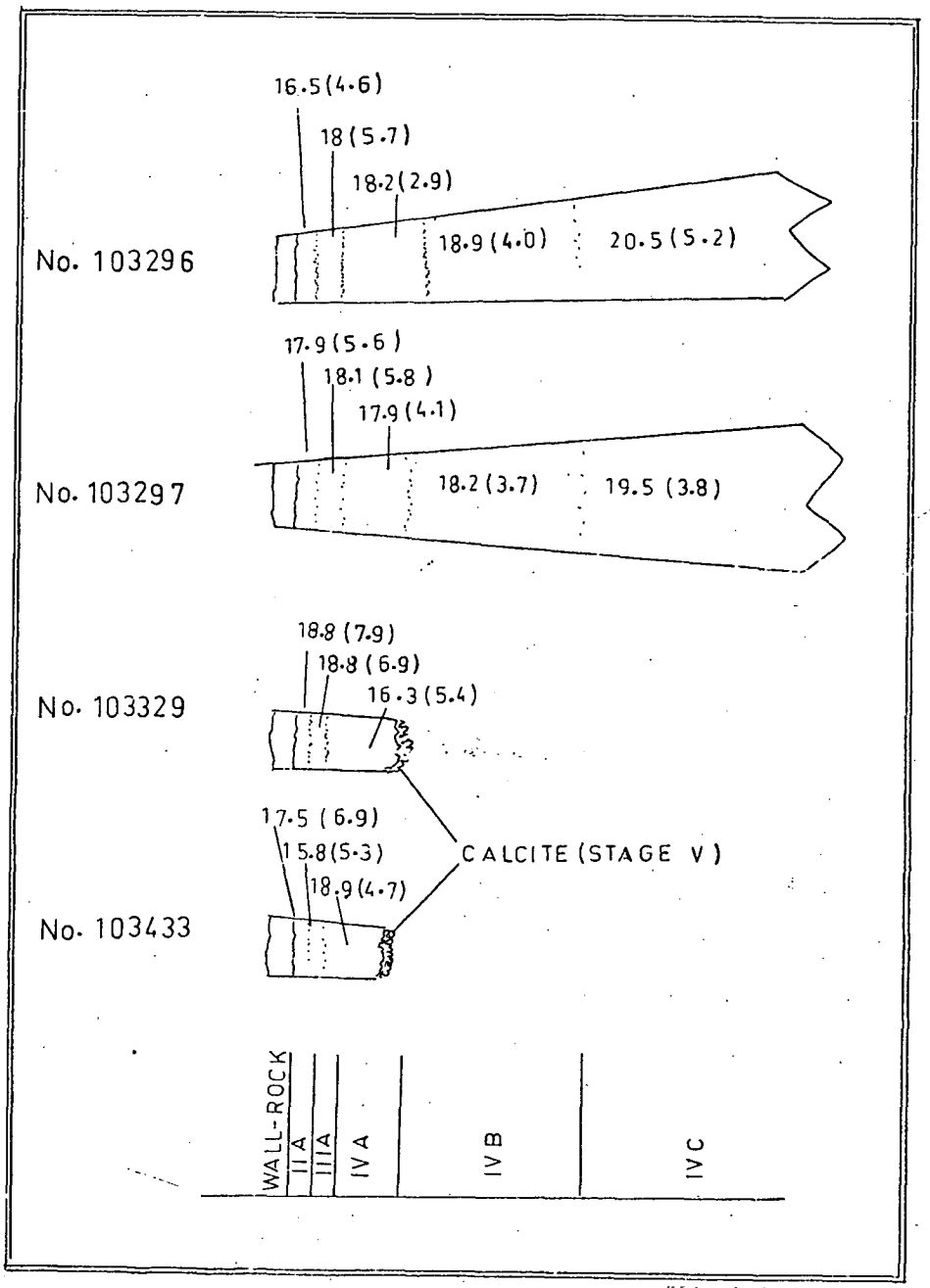

Fig. 9.2 Variation in $\delta^{18}O$ quartz and $\delta^{18}O$ H_2O(calculated, in brackets) in single samples of vein quartz. For details refer to Table 9.1.

are more or less similar to those obtained from the K-silicate rocks and so the latter set of values is preferred.

The calculated $\delta^{18}O_{H_2O}$ values are plotted in Fig. 9.3. There appears a gradual decrease in $\delta^{18}O_{H_2O}$ with time although a slight reversal in this trend has occurred during stage IVC. The calculated $\delta^{18}O_{H_2O}$ values for single samples representing various stages of vein quartz (Fig. 9.2) also indicate a similar trend.

The $\delta^{18}O$ values of vein quartz from various stages are plotted against depth in Fig. 9.4A. It appears the $\delta^{18}O$ values of stage IIA increase with depth, the largest increase occurring between 11 and 15 levels. The existing data do not indicate any significant changes during other stages, although stage IIIA quartz show a trend similar to stage IIA between 11 and 14 levels and stage IVA quartz a possible reversal.

The $\delta^{18}O_{H_2O}$ (calculated) values during various stages of vein quartz deposition are plotted against depth in Fig. 9.4B. It appears that $\delta^{18}O_{H_2O}$ increased with depth during stage IIA with a well defined trend, but during the other stages it was probably more or less constant throughout.

Assuming that the volcanic rocks were altered at temperatures between 170 and 317^{o}C (from fluid-inclusion homogenisation temperatures on stage IIA and stage III quartz) and the fractionation factor between basalt and water is equivalent to that between plagioclase (An_{30}) and water (O'Neil & Taylor, 1967), the water/rock ratios can be calculated using the equation given in Taylor (1974) for various initial $\delta^{18}O$ values of water. These calculations are plotted in Fig. 9.5. It can be seen that neither the local meteoric waters ($\delta^{18}O$ = -6‰, section 9.4.4), nor sea water ($\delta^{18}O$ = 0‰) can produce the observed $\delta^{18}O$ range of altered rocks at the assumed temperatures. However water having a $\delta^{18}O$ value of +8‰ can produce the observed $\delta^{18}O$ range at a minimum water-to-rock ratio of about 3.

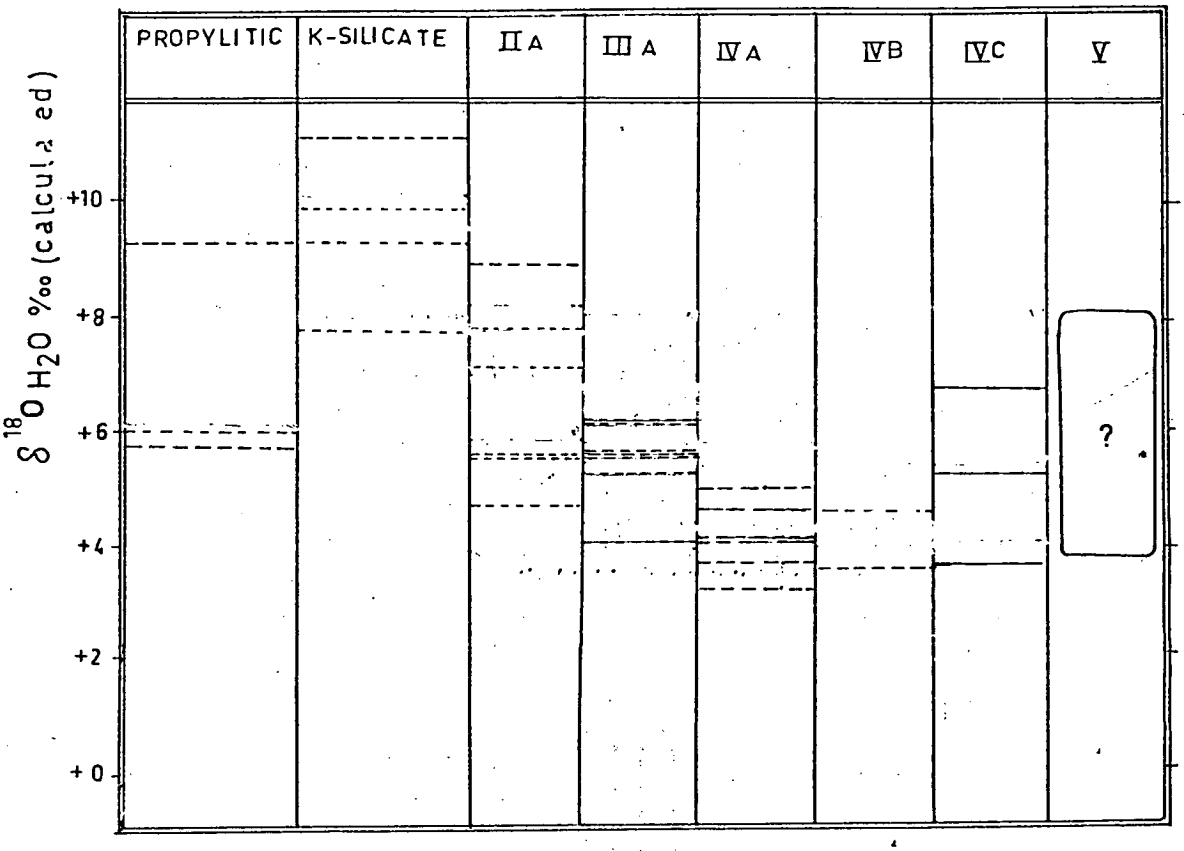

Fig. 9.3 Calculated $\delta^{18}O$ values of water during various stages of mineralization. For details refer to Table 9.1.

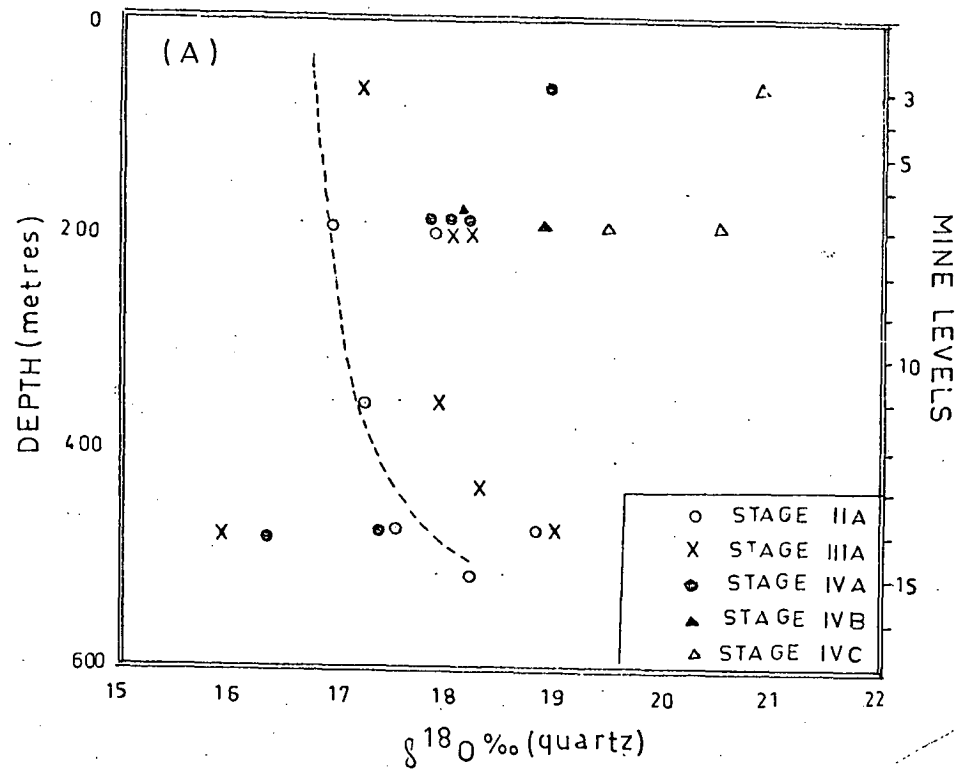

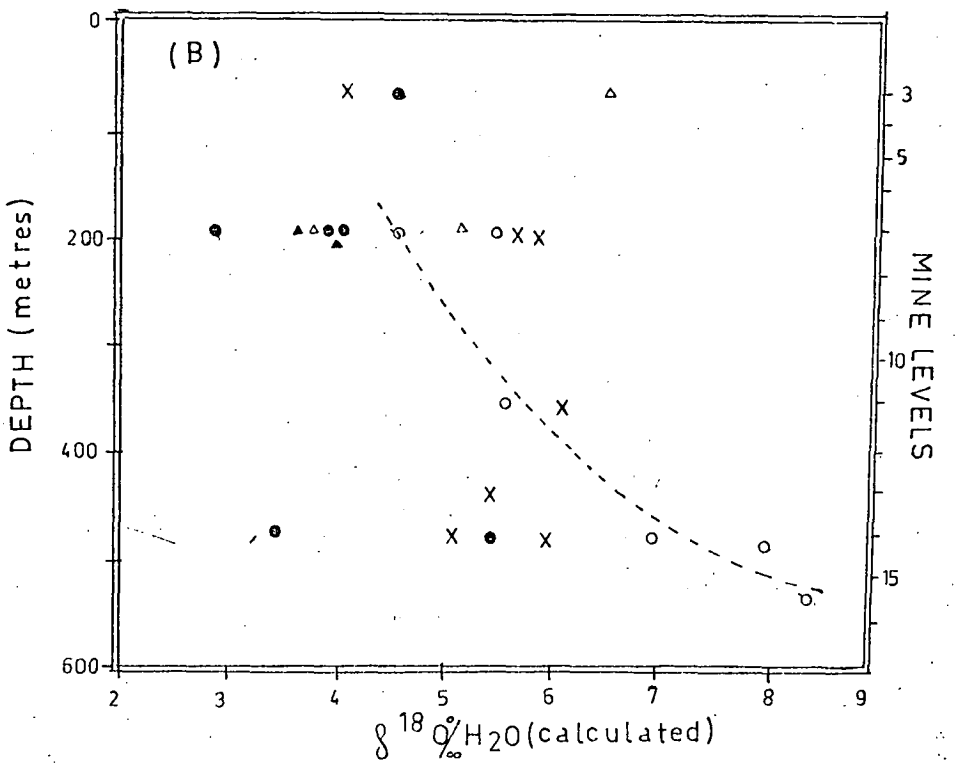

Fig. 9.4A Variations in $\delta^{18}O$ of quartz versus depth during various stages of mineralization. Note that the $\delta^{18}O$ values of stage IIA quartz show an apparent increase with depth but changes during other stages are probably insignificant.

Fig. 9.4B Variations in $\delta^{18}O$ of H_2O(calculated) versus depth during various stages of mineralization. Note that the $\delta^{18}O$ of H_2O increases with depth during stage IIA but no changes are apparent during the other stages. For details refer to Table 9.1.

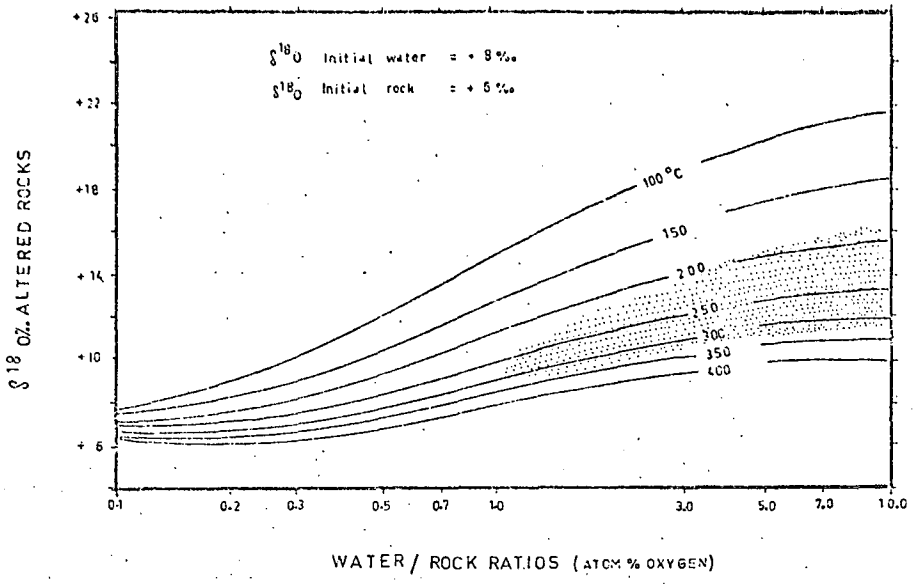

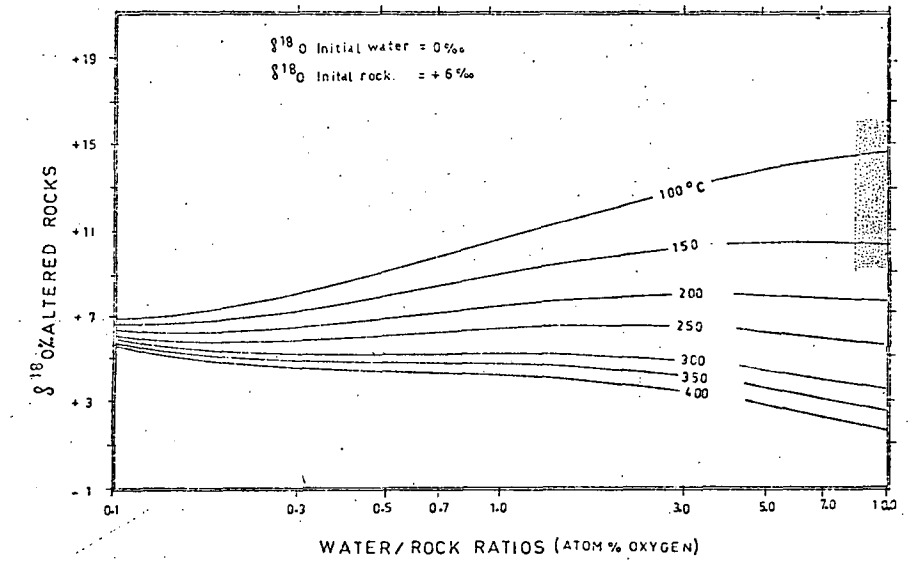

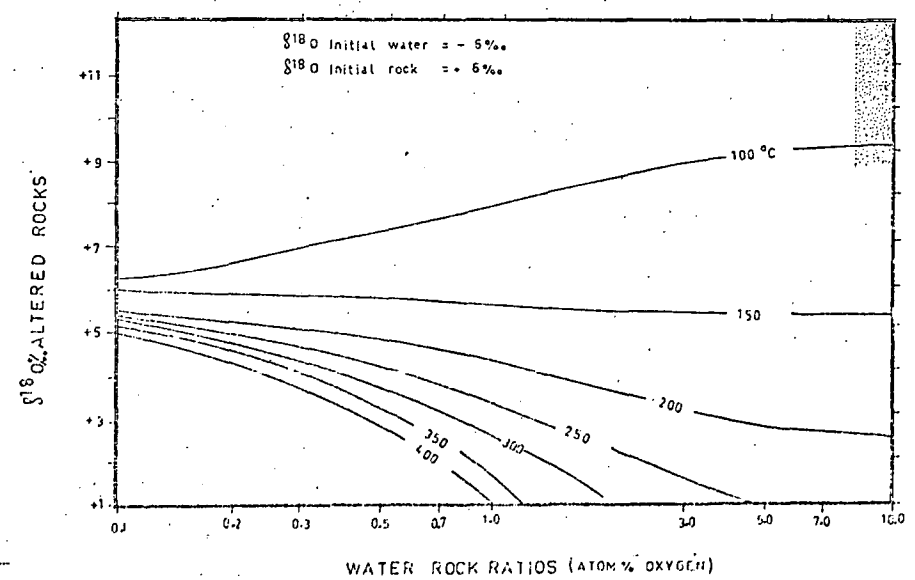

Fig. 9.5.A Plot of $\delta^{18}O$ (altered rocks) versus water/rock ratios (wt.% oxygen). Stippled area indicates the $\delta^{18}O$ values of the altered rocks at the Emperor mine.

9.4.2 Carbonates

The $\delta^{13}C$ and $\delta^{18}O$ values of carbonates (Table 9.2; Fig. 9.6) can be grouped as follows:-

(a) The $\delta^{13}C$ values of vein and wall-rock dolomite range from +0.3‰ to -1.4‰ (average, -0.7‰) and the $\delta^{18}O$ values range from +17.2 to +20.8‰ (average, +18.4‰).

(b) The $\delta^{13}C$ values of stage V calcite range from -4.1 to -8.6‰ (average, -6.8‰) and the $\delta^{18}O$ values range from +17.9 to +20.8‰ (average, +19.3‰).

(c) The $\delta^{13}C$ values of carbonates in the sedimentary rocks surrounding the Mba volcanics range from +0.8 to -4.0‰ (average, -1.9‰) and the $\delta^{18}O$ values range from +18.2 to +28.3‰ (average, +22.6‰).

The $\delta^{13}C$ and $\delta^{18}O$ values of hydrothermal carbonates (i.e. vein and wall-rock dolomite and stage V calcite) are plotted against depth in Fig. 9.7. The $\delta^{13}C$ and $\delta^{18}O$ values of stage V calcite show an apparent decrease with depth but those on vein and wall-rock dolomite are nearly constant. The decrease in the $\delta^{18}O$ and $\delta^{13}C$ values of stage V calcite probably reflects an increase in temperature with depth.

As is mentioned in Chapter 7, only one sample of vein dolomite (sample 103303) had inclusions large and clear enough for temperature determinations. However, temperatures can be calculated by using the $\delta^{18}O_{H_2O}$ values estimated from vein quartz (Table 9.1). Since major dolomite precipitation stopped towards the end of stage III, the $\delta^{18}O_{H_2O}$ values estimated from stage IIA and stage IIIA quartz can only be used for this purpose. It can be seen from Table 9.1 that the calculated $\delta^{18}O_{H_2O}$ values during stages IIA and IIIA range from +5.2 to +8.7‰ and average about +6.7‰. Using this average and the dolomite-H_2O fractionation factor given by Northrop & Clayton (1966), the temperatures of the fluid which precipitated dolomite can be approximated (Table 9.2). They range from

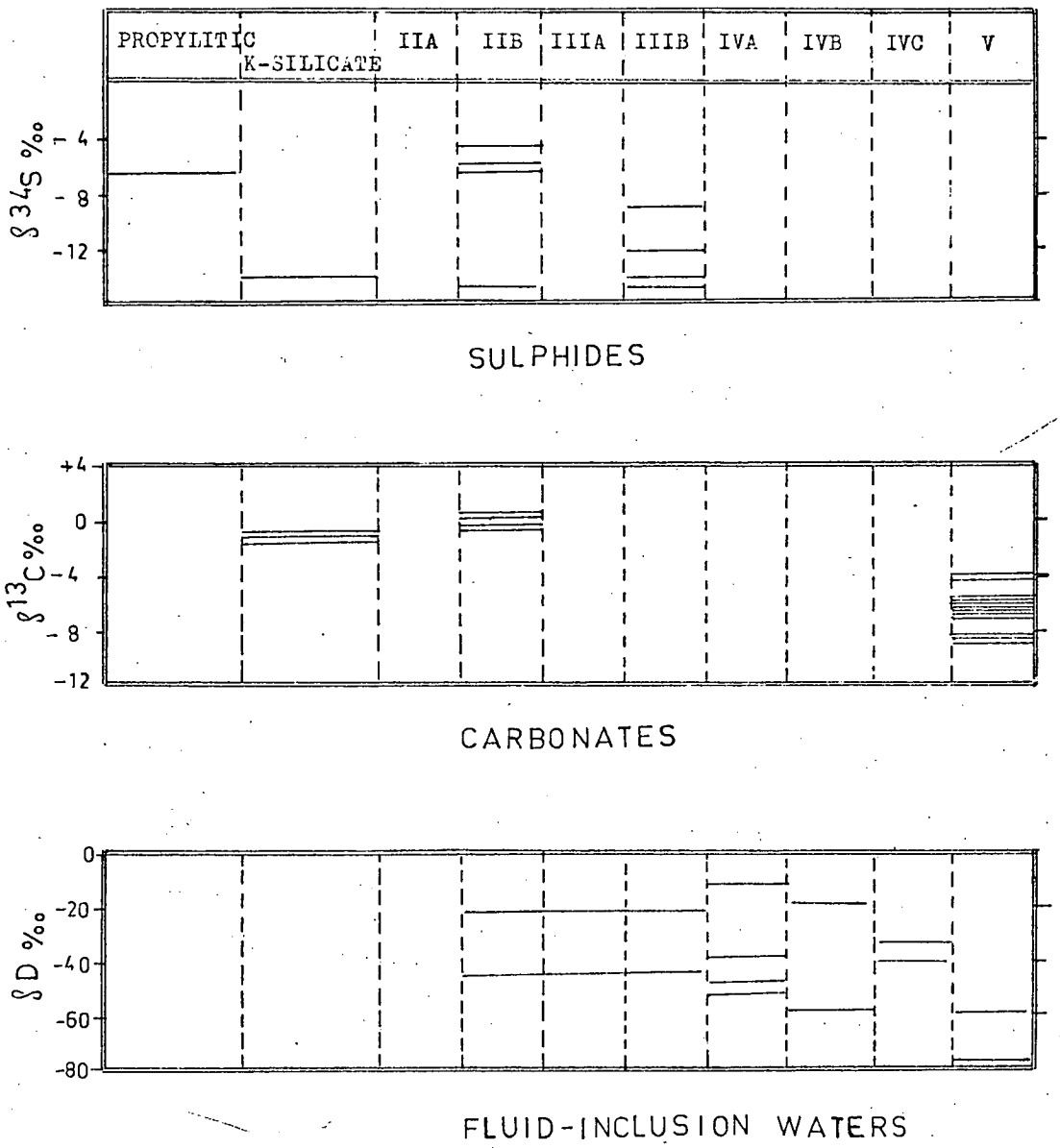

Fig. 9.6 Sulphur, carbon and hydrogen isotopic variations with time. For details refer to Table 9.2, 9.3 and 9.6.

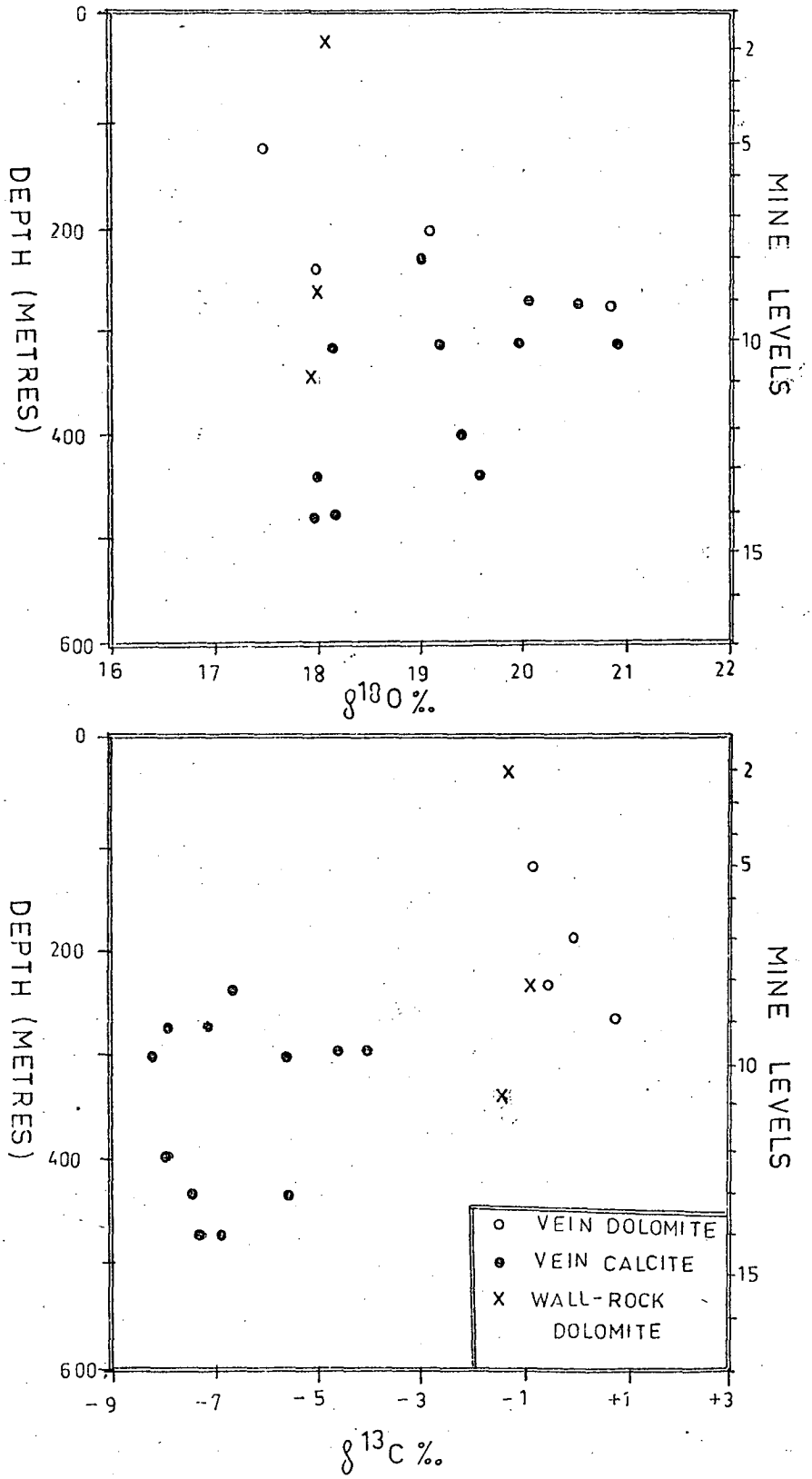

Fig. 9.7 Plot of $\delta^{18}O$ (A) and $\delta^{13}C$ (B) values of carbonates versus depth. Note that the $\delta^{13}C$ and $\delta^{18}O$ values of stage V calcite show an apparent decrease with depth but those of vein and wall-rock dolomite are near-constant. For details refer to Table 9.2.

Table 9.2

Carbon and oxygen isotope data on carbonates.

Specimen Number	Location	Stage	^{18}O ‰	^{13}C ‰	$\delta^{13}C$ ‰ H_2CO_3(ap) (calculated)	$T^{o}C$ calculated	Depth (m)
(A) VEIN DOLOMITE							
103343	7 level, 608 F.M.	IIB	+19.1	-0.1	-0.3	196	196
103342	5 level, Cardigan	IIB	+17.6	-1.0	-0.7	223	125
103334	9 level, 608 F.M.	IIB?	+20.8	+0.3	-0.6	170	277
103303	8 level, Monarch	IIIA?	+18.1	-0.7	-0.6	214	236
(B) WALL ROCK DOLOMITE							
103336	2 level, 1399 F.M.	IB?	+18.1	-1.2	-1.1	214	61
47237	DDH MA-56 at 1005'	IB?	+17.9	-1.4	-1.3	217	306
103394	8 level, Crown	IB?	+17.2	-1.1	-0.7	230	277
(C) VEIN CALCITE							
103292	9 level, 166 F.M.	V	+20.1	-6.2	-9.4	104	277
103329	14 level, Crown	V	+18.0	-7.2	-9.1	127	482
103442	13 level, Crown	V	+17.9	-8.6	-10.6	128	483
103307	10 level, Dolphin	V	+20.1	-6.4	-9.5	105	317
103309	10 level, Dolphin	V	+19.2	-4.8	-7.4	113	317
103328	14 level, Prince	V	+18.3	-7.0	-9.1	124	483
103326	8 level, President	V	+19.0	-6.6	-9.0	116	440
103327	13 level, Prince	V	+19.6	-7.5	-10.3	110	440
103409	12 level, Crown	V	+19.4	-8.1	-10.8	112	400
103387	10 level, Crown	V	+20.9	-4.1	-7.7	97	317
103398	9 level, Crown	V	+20.7	-7.1	-10.5	99	277
103457	Recent calcite growing over a copper wire, 9 level, Dolphin.		+22.3	+1.3	-	-	-

Table 9.2 cont.

Specimen Number	Location	Stage	^{18}O ‰	^{13}C ‰	$\delta^{13}C$ ‰ H_2CO_3(ap) (calculated)	T°C calculated	Depth (m)
(D) CALCITE IN THE SURROUNDING SEDIMENTARY ROCKS							
47297	Mudstone, Mba River Basin		+28.3	-4.0	-	-	-
47270	Siltstone, DDH MD4 at 29 metres. Damsite area.		+18.2	-0.8	-	-	-
47273	Siltstone, DDH MB/1B at 90 metres. Damsite area.		+20.7	-3.8	-	-	-
47304	Limestone, Ra Sedimentary Group.		+23.2	-0.8	-	-	-

The fractionation factors used are:-

Calcite-water (O'Neil *et al.*, 1969); Dolomite-water (Northrop & Clayton, 1966); Calcite-H_2CO_3(ap) (Botinga, 1968); Dolomite-calcite (Sheppard & Schwarcz, 1970).

170 to 230°C. The average fluid-inclusion temperature of sample 103303 is 196°C whereas the temperature calculated from the oxygen-isotope data is 214°C, well within the limits of uncertainty and assumptions.

Fluid-inclusions in stage V calcite are rare, very small and lack a visible vapour phase. No temperature determinations on these inclusions were possible. If it is assumed the $\delta^{18}O_{H_2O}$ did not change appreciably during stage IV and stage V, the temperatures of stage V fluids can be approximated. The $\delta^{18}O_{H_2O}$ values calculated for the stage IV fluids range from +2.9 to +7.7‰ and average +4.2‰. Using this average and the calcite-H_2O fractionation factor given in O'Neil *et al.* (1969), temperatures of the fluids which deposited stage V calcite can be approximated (Table 9.2). They range from 97 to 127°C.

At the f_{O_2}-pH-T conditions of the ore fluids which precipitated early carbonates (dolomite and ankerite), $H_2CO_3(ap)$ is the dominant solution species of carbon (Chapter 10) and it can be assumed that

$$m\Sigma C = m\ H_2CO_3(ap)$$

so

$$\delta^{13}C_{\Sigma C} = \delta^{13}C_{H_2CO_3(ap)}.$$

Following Ohmoto (1972) it can further be assumed that

$$\delta^{13}C_{H_2CO_3(ap)} = \delta^{13}C_{CO_2(g)}.$$

The dolomite-calcite fractionation factor for $\delta^{13}C$ given in Sheppard & Schwarcz (1970) and the calcite-CO_2 fractionation factor given in Bottinga (1968) can be added to obtain the dolomite-CO_2 fractionation factor. Using this dolomite-CO_2 fractionation factor and the temperature calculated from the oxygen isotope data, it is possible to estimate the $\delta^{13}C_{H_2CO_3(ap)}$ ($\approx CO_2 \approx \Sigma C$) values of the fluids which precipitated dolomite.

These values are given in Table 9.2. They range from -0.3 to -1.3‰. The $\delta^{13}C$ values of dolomite are plotted against temperature in Fig. 9.8A along with the contours of $\delta^{13}C_{H_2CO_3(ap)}$. It can be seen that the $\delta^{13}C$ values of dolomite are adequately defined by the $\delta^{13}C_{H_2CO_3(ap)}$ values of about -0.5 to -1.0‰. This range for $H_2CO_3(ap)$ suggests that carbon in the Emperor mine ore-fluids was derived from marine carbonate, and the most likely source is that in the sediments beneath the basalts of the mine.

The f_{O_2}-pH conditions of the stage V fluids are not precisely known. Negative values and smaller fluctuations in the $\delta^{13}C$ of stage V calcite indicate that these fluids were outside the reduced carbon field (Ohmoto, 1972). The dominant oxidized carbon species in the likely field of interest are $H_2CO_3(ap)$ and HCO_3^- (Chapter 10). It can be seen from the data given by Ohmoto (1972) that at temperatures between 100 and 130°C

$$\delta^{13}C_{CO_2(g)} \approx \delta^{13}C_{H_2CO_3(ap)} \approx \delta^{13}C_{HCO_3^-} \approx \delta^{13}C_{\Sigma C}$$

It is therefore possible to estimate the $\delta^{13}C_{\Sigma C}$ from the calcite-CO_2 [= calcite-$H_2CO_3(ap)$] fractionation factor given in Bottinga (1968). The calculated values for $\delta^{13}C_{H_2CO_3(ap)}$ are also given in Table 9.2. They range from -7.4 to -10.8‰. The $\delta^{13}C$ values of calcite are plotted against temperature in Fig. 9.8B along with the contours of $\delta^{13}C_{H_2CO_3(ap)}$. It can be seen that the majority of samples (83%) indicate a $\delta^{13}C_{H_2CO_3(ap)}$ value of -10 ± 1‰.

The $\delta^{13}C$ values of deep-seated carbon range from -5 to -8‰ as is indicated from the analyses of carbonatites (Hoefs, 1973). Data from the Providencia deposit, which is considered to be of magmatic origin, indicate a $\delta^{13}C$ value for ΣC of about -5‰ (Robinson, 1974) and the main stage carbonates from Casapalca deposit, also probably of magmatic origin, have $\delta^{13}C$ values that average -6 ± 0.5‰ (Rye & Sawkins, 1974). It can

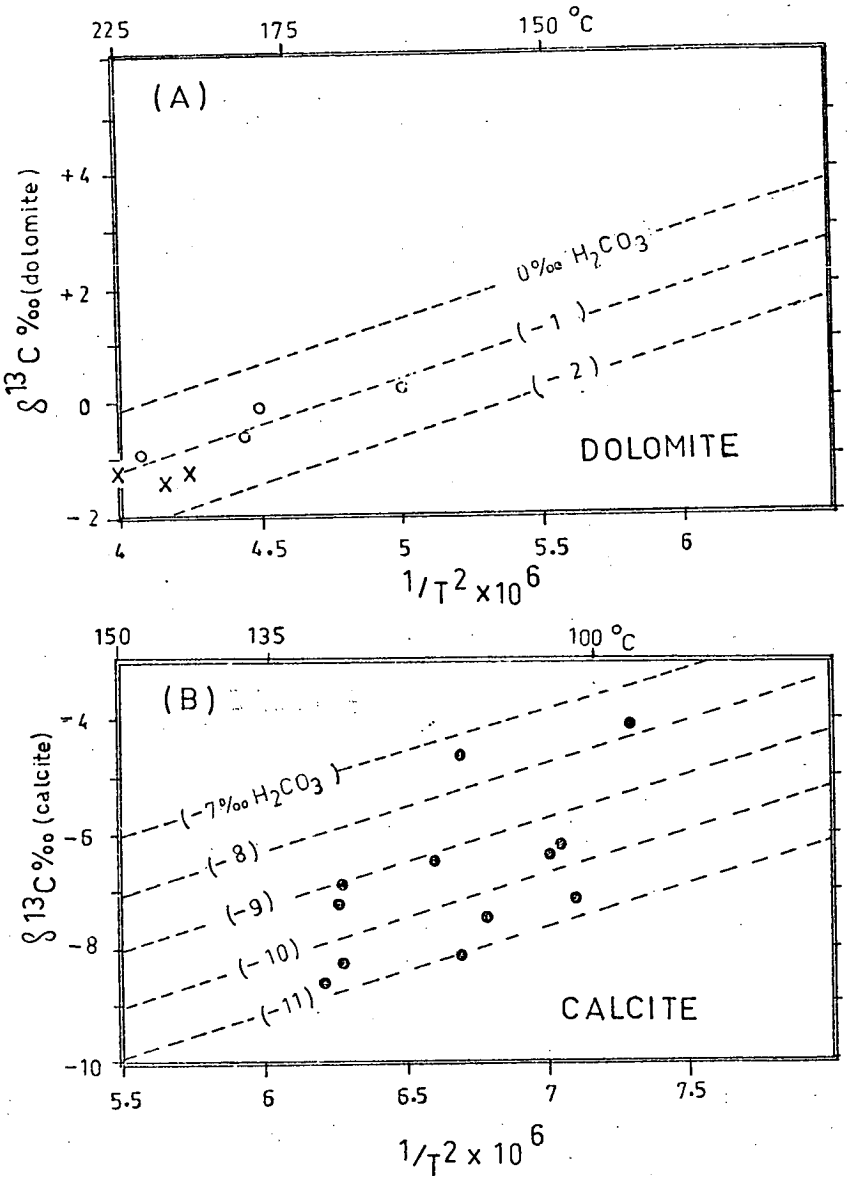

Fig. 9.8 Plot of $\delta^{13}C$ versus temperature for carbonates from the Emperor mine with contours of $\delta^{13}C\ H_2CO_3$(ap). For details refer to Table 9.2.

probably be concluded that $\delta^{13}C$ values for magmatic carbon range from -5 to -8‰. The calculated values for $\delta^{13}C_{\Sigma C}$ for the stage V fluids at the Emperor mine, therefore suggest that carbon was either derived directly from a magmatic reservoir or leached from the volcanic rocks.

It thus appears that the source of carbon in the Emperor mine ore-fluids changed markedly with time. The early carbonates (stages I to III) suggest a sedimentary source and the late carbonates (stage V) a magmatic source.

The $\delta^{13}C$ (+1.3‰) and $\delta^{18}O$ (+22.3‰) values of recent (supergene) calcite occurring as encrustations over a copper wire in the mine workings, are also given in Table 9.2. Assuming a temperature of about 30°C, the $\delta^{13}C$ value of this calcite suggests a value of -10‰ for $\delta^{13}C_{H_2CO_3(ap)}$ indicating that carbon is probably leached from the surrounding volcanics or by dissolution of stage V calcite.

9.4.3 Sulphides

The $\delta^{34}S$ values of sulphides are given in Table 9.3 and are plotted in Fig. 9.6. It can be seen that these values range from -4.2 to -15.3‰ and the existing data does not indicate any temporal or spatial changes.

One sample of galena was analysed for $\delta^{34}S$, and gave a value of -5.8‰. Unfortunately it was not possible to separate and analyse the associated sphalerite and pyrite.

9.4.4 Waters

The δD and $\delta^{18}O$ values of local meteoric waters are given in Table 9.4. The δD values of creek and mine waters range from -27 to -38‰, rain water gave a value of -4‰, and sea water from Vatia Wharf a value of +3‰. The $\delta^{18}O$ values of creek and mine water range from -5.3 to -6.5‰, rain water gave a value of -2‰, and sea water a value of +0.2‰. The δD and $\delta^{18}O$ values of rain water are significantly different from the creek and mine waters and are probably due to non-equilibrium precipitation.

Table 9.3

Sulphur isotope data.

Specimen No.	Location	Description	Stage	^{34}S CDT. ‰
47243	DDH MA-56 at 1012 feet.	Massive pyrite vein in propylitic rock.	IA?	-6.6
103349	2 level, Cardigan	Pyrite associated with quartz vein.	IIB	-5.5
103460	Cardigan area?	"	IIB	-4.2
103329	14 level, Crown	Pyrite at the base of stage IIA quartz.	IB?	-13.4
103455	Cardigan area?	Euhedral marcasite crystal on fracture plane.	IIIB	-14.9
103456	?	Massive pyrite vein in sericitised rock.	IIIB?	-9.7
103404	12 level, Crown	Massive pyrite below stage V calcite.	IIIB	-12.1
103409	12 level, Crown	"	IIB	-15.3
103442	13 level, Crown	"	IIIB	-14.2
103443	10 level, Scepter	Galena.	IIB?	-5.8

Table 9.4

δD and $\delta^{18}O$ values of waters from the Emperor mine area.

R.No.*	^{18}O* No.	Description	$\delta^{18}O$‰	δD‰
5314/1	RF1	Vatukoula rainwater 18.3.76	-2.03±0.13	-4.1
5314/2	RF2	Lololevu Creek 18.3.76	-5.29±0.15	-27.3
5314/3	RF3	Seepage no.10 level, flowing through 166 flatmake	-6.26±0.12	-35.9
5314/4	RF4	No.3 level, flowing through 608 flatmake	-5.56±0.10	-33.9
5315/5	RF5	No.7 level, flowing through 166 flatmake	-6.61±0.11	-39.4
5314/6	RF6	No.14 level, flowing through Prince flatmake	-6.43±0.11 -6.42±0.14	-38.4
5314/7	RF7	No.9 level Dolphin Flat	-6.51±0.14	-36.8
5314/8	RF8	No.7 level, flowing through 608 flatmake	-6.51±0.14	-38.4
5314/9	RF9	Vundraviloa Creek - river water near mine	-5.88±0.11 -6.07±0.14	-35.2
5314/10	RF10	Sea water, Vatia Wharf	+0.19±0.10	+3.0

* Numbers referred to are from the Institute of Nuclear Sciences, Wellington, New Zealand.

Table 9.5

δD and $\delta^{18}O$ values of hot springs and river water from Vanua Levu, Fiji.

R.No.*	^{18}O* No.	Description	$\delta^{18}O$‰	δD‰
5257/1	GF1	Waigele Springs 98°C	-5.73±0.05	-36.5
5257/2	GF2	Waigele Springs 90°C	-5.09±0.08 -5.15±0.08	-34.1 -33.1
5257/3	GF3	Waigēle Springs 93°C	-5.55±0.09	-31.6
5257/4	GF4	Waigele Springs 93°C	-5.56±0.08	-33.7
5257/5	GF5	Waigele Springs 96°C	-5.54±0.08 -5.62±0.08	-31.0 -35.0
5257/6	GF6	Waigele Springs 93°C	-5.52±0.08	-33.3
5258/1	GF7	Waigele River	-5.45±0.08	-33.6
5258/2	GF8	Batinikama River	-4.93±0.15	-29.0
5258/3	GF9	Sabeto River	-5.13±0.08	-32.5
5258/4	GF10	Sabeto No.2 (Spring?)	-5.67±0.11	-35.8

Std. deviation for D/H = 1.0‰

* Numbers referred to are from Institute of Nuclear Sciences, Wellington, New Zealand.

Table 9.6

δD and $\delta^{18}O$ values of fluid-inclusion water.

Specimen Number	Mineral	Stage	Location	Sample wt. (g)	Water extracted (mg)	$\delta^{18}O_{H_2O}$, ‰ (calculated)	δD ‰	Average fluid-inclusion temp. (^{o}C)
103297	quartz	IIA&IIIA	7 level 166 F.M.	64	5.7	+5.6	-48	222
103433	quartz	IIA&IIIA	14 level Crown	25	3.8	+7.0	-26	255
103339	quartz	IVA	3 level Cardigan	60	4.4	+4.7	-53	193
103296	quartz	IVA	7 level 166 F.M.	39	7.0	+3.0	-47	180
103297	quartz	IVA	7 level 166 F.M.	30	2.8	+4.1	-10	198
103433	quartz	IVA	14 level Crown	50	11.6	+3.6	-41	198
103296	quartz	IVB	7 level 166 F.M.	64	6.0	+4.6	-58	184
103297	quartz	IVB	7 level 166 F.M.	55	4.6	+3.7	-20	190
103296	quartz	IVC	7 level 166 F.M.	54	3.5	+5.3	-42	179
103297	quartz	IVC	7 level 166 F.M.	58	3.0	+3.8	-37	175
103442	calcite	V	14 level Crown	30	1.4	?	-79	?
103329	calcite	V	14 level Crown	30	5.1	?	-60	?

These values are therefore not considered in the following discussions.

Hot spring and river waters from the Vanua Levu island, Fiji, were analysed by Cox & Hulston (J.R. Hulston, pers. comm., 1976) at the Institute of Nuclear Sciences, Wellington, New Zealand. Their results are given in Table 9.5. The δD values of hot spring waters (temperature about $90^{o}C$) range from -31 to -36.5‰ and those of the river waters from the surrounding area range from -29 to -35.8‰. The $\delta^{18}O$ values of hot spring waters range from -5.1 to -5.7‰ and those of the river waters range from -4.9 to -5.6‰.

The δD values of fluid-inclusion waters are given in Table 9.6. The δD values for inclusion water in quartz of stages II to IV range from -10 to -58‰. Only two samples of fluid-inclusion waters from stage V calcite were analysed and they gave values of -60 and -79‰. The small amounts of water extracted did not allow measurement of $\delta^{18}O$ but these values can be calculated at the fluid-inclusion homogenisation temperatures by using the quartz-H_2O fractionation factor. A similar approach to calculate the $\delta^{18}O_{H_2O}$ for stage V fluids is not feasible because the temperatures of these fluids are not precisely known. It can probably be assumed that $\delta^{18}O_{H_2O}$ of the stage V fluids was approximately similar to stage IV fluids (i.e. between +3‰ and +7‰ - see section 9.4.2 above and Table 9.2). The $\delta^{18}O$ values calculated using the quartz-H_2O fractionation factor given in Blattner (1975) for the stage II to stage IV fluids are also given in Table 9.6. They range from +3 to +7‰.

The δD and $\delta^{18}O$ values for the Emperor mine ore-fluids, local meteoric waters and hot spring waters (from Vanua Levu) are plotted in Fig. 9.9 along with the data on several other epithermal deposits and the range for primary magmatic waters. It can be seen that the fluid-inclusion waters from the Emperor mine fall very close to the magmatic water range but are all slightly richer in ^{16}O. The stage II to stage IV fluids have

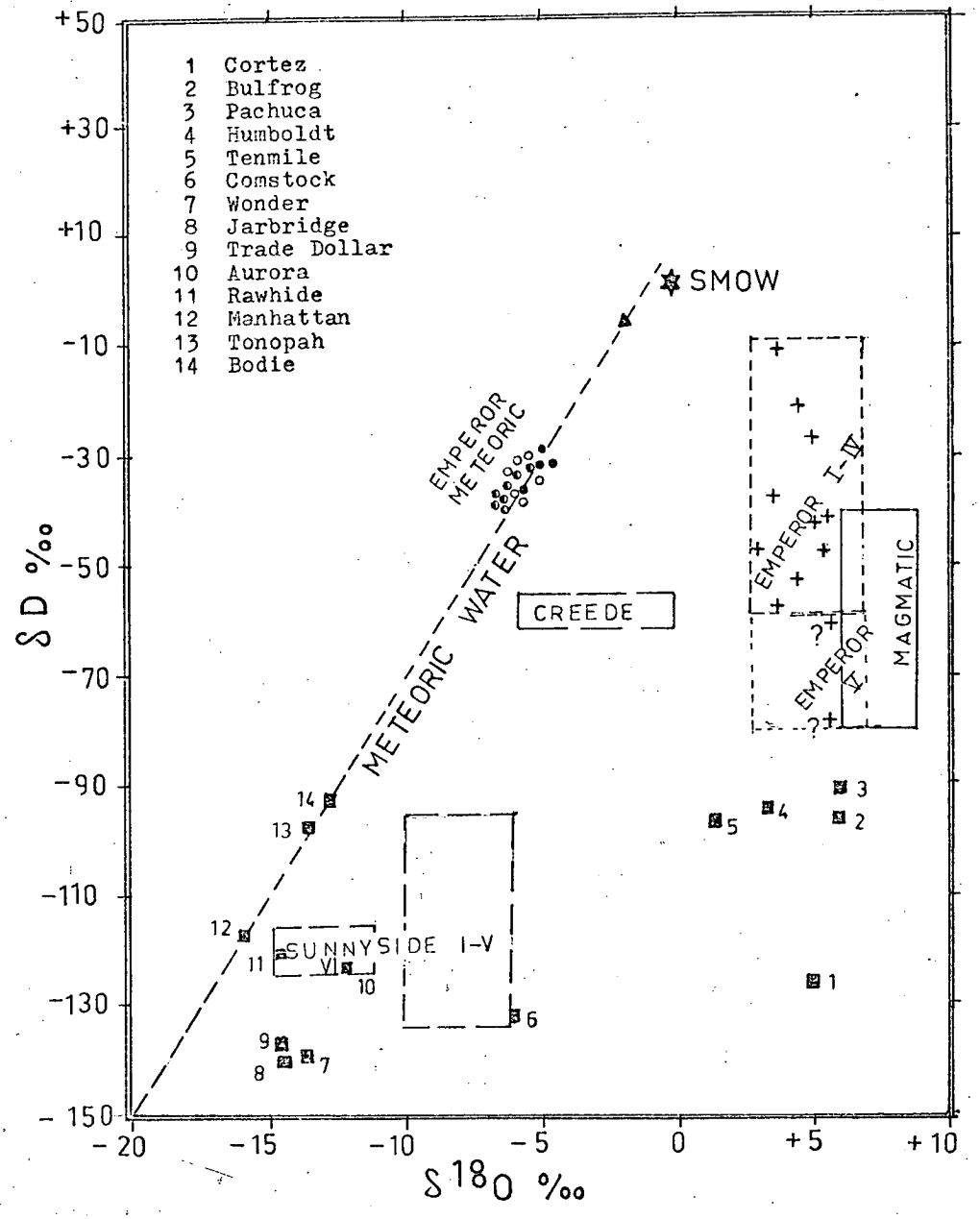

Fig. 9.9 Hydrogen isotope versus oxygen isotope composition diagram. Open circles: hot spring waters from Vanua Levu (Table 9.5); filled circels: river waters from Vanua Levu(Table 9.5); half filled circles: mine and river water from the Emperor mine area(Table 9.4); filled traingle: rain water from the Emperor mine area(Table 9.5); crosses: fluid inclusion waters from the Emperor mine(Table 9.6). Also shown are the range for "primary magmatic waters"(Taylor, 1974) , the meteoric water line(Craig, 1961) and the composition of ore-fluids from a number of "epithermal" deposits. Sources of data: Sunnyside(Casadevall and Ohmoto,1977); Creede (Bethke et al.,1973); Cortez(Rye et al., 1974) and deposit No. 2 to 14(listed and numbered, O'Neil and silberman, 1974).

δD values higher than that of magmatic waters and the stage V fluids have δD values similar to the magmatic waters.

9.5 DISCUSSION

9.5.1 Source of carbon

As shown in section 9.4.2, the source of carbon in the Emperor mine ore-fluids has changed markedly with time. The $\delta^{13}C$ values of early carbonates (stage I to III) suggest a sedimentary source while those of late (stage V) calcite, a magmatic source.

It is suggested that the volcanic rocks at the Emperor mine are underlain by Mio-Pliocene carbonate-bearing sediments which are flanking the volcanics to the south, east and west, and that these are the source of ore-fluid carbon.

The K-Ar age determinations (Chapter 4) indicate two major periods of igneous activity in the Emperor mine area and Te^{130}-Xe^{130} age determination (Chapter 5) indicates that the ore-mineralization at the Emperor mine probably coincided with the first period of igneous activity.

It can be postulated that during the early stages (I to IV) emplacement of a heat source (pluton) during the first period of igneous activity resulted in the formation of a hydrothermal convection system involving the sub-basaltic sedimentary rocks. Carbon from these sediments was leached and precipitated as early (stage I to III) carbonates. During the second period of igneous activity (represented mainly as ring dykes and small shallow intrusives)it is suggested that the heat source was at a higher level, resulting in a shallower hydrothermal system that did not include the sediments. These late (stage V) fluids either leached carbon from the volcanic rocks or inherited it from magmatic solutions.

9.5.2 Source of sulphur

Using the fractionation factors compiled by Ohmoto (1972) between aqueous sulphur species and pyrite, the $\delta^{34}S$ values of pyrite are contoured on f_{O_2}-pH and f_{O_2}-T diagrams (Figs. 10.5B and 10.8B, Chapter 10). It can be seen that the observed variations in the $\delta^{34}S$ pyrite can be explained (at the f_{O_2}-pH-T conditions inferred from the mineral stability and other data) by assuming $\delta^{34}S_{\Sigma S}$ to be about 0‰ and this indicates a magmatic source. It appears the sulphur was either directly derived from a silicate melt (magma) or indirectly through leaching of the sulphides from the volcanic rocks.

9.5.3 Variations in the $\delta^{18}O_{H_2O}$

As shown in Figs. 9.2, 9.3 and 9.4 and Table 9.1, the $\delta^{18}O_{H_2O}$ (calculated) indicates significant temporal and spatial changes. The calculated $\delta^{18}O_{H_2O}$ values show a gradual decrease with time although a slight reversal in this trend has occurred during stage IVC. This decrease could be due to three factors, viz.

(a) As mentioned previously, the underlying sedimentary rocks are only sparingly calcareous (Chapter 4). Although some massive limestone beds occur in the succession, the bulk of these rocks contain between 10 and 20% calcite. The other minerals present include chlorite, clay minerals, quartz and unaltered pyroxene and plagioclase. Dissolution of more and more calcite would leave the residual rocks comparatively depleted in ^{18}O and in time the ore-fluids would reflect this depletion.

(b) A gradual increase in pH with time results in dissolution of less and less calcite thus giving waters with gradually declining $\delta^{18}O$ values.

(c) Mixing of magmatic waters with increasing amounts of meteoric waters could produce a gradual change in $\delta^{18}O$ values.

Possibly all of these factors have contributed towards a decrease in $\delta^{18}O_{H_2O}$ with time.

The slight increase in $\delta^{18}O_{H_2O}$ during stage IVC may be due to the influx of heavier (magmatic?) waters concurrent with the second period igneous activity. It is also possible that the circulating solutions changed their path (possibly as a result of tectonic disturbances related to the second period of igneous activity) and equilibrated with fresh (and relatively ^{18}O-rich) rocks.

It appears that the $\delta^{18}O$ of stage IIA fluids decreased during their ascent (Fig. 9.4B) while no spatial changes are apparent (from the existing data) during the other (later) stages. This decrease is probably due to mixing with ground water as the solutions rose. It is likely that during the early stages the rocks were saturated with ^{18}O-deficient (cold) ground waters of meteoric origin. With time the $\delta^{18}O$ inhomogeneities would be smoothed out leaving channels occupied solely by introduced water of constant isotopic composition.

9.5.4 Source of the ore solutions

The δD values of the majority of samples from stages II to IV (Table 9.6; Figs. 9.6 and 9.9) are comparable to those of local meteoric waters but $\delta^{18}O$ (calculated) values are about 10‰ greater. Enrichments in $\delta^{18}O$ can either be due to mixing of meteoric and magmatic waters or due to isotopic exchange of meteoric waters with the country rocks, or it may be the result of a combination of these two processes. Extensive enrichments in ^{18}O are considered to be due to isotopic exchange of meteoric waters with the country rocks in a number of deposits and geothermal waters (Craig, 1963; Taylor, 1974; O'Neil & Silberman, 1974; Casadevall & Ohmoto, 1977).

It can be seen from Fig. 9.9 that two of the δD values are distinctly higher than either the magmatic or meteoric water. Apart from magmatic and meteoric waters, there are two other possible sources: sea water and sedimentary formation water. The δD values of formation waters tend to be higher than the meteoric waters in a number of areas (Taylor, 1974). Mixing of magmatic and/or meteoric waters with either sea water or formation waters could result in an increase in the δD values. The suggested $\delta^{34}S$ values for total sulphur (i.e. 0‰) indicate that any major involvement of sea water is unlikely but it has already been shown that carbon in the ore-fluids (stages I to III) was derived from a sedimentary source. The same rocks may have been the source of the formation waters envisaged.

Deposits formed from a predominantly magmatic source usually have higher and variable salinity values (Eastoe, 1979; Rye & Sawkins, 1974). The near constant low salinity (average 5.5 wt. % eq. NaCl) values of the Emperor mine ore-fluids, therefore, indicate that a wholly magmatic source is unlikely.

Considering the similarities in the δD values of local meteoric waters and the fluid-inclusion waters, and the previous discussion, it is suggested that the stage I to stage IV fluids at the Emperor mine were largely meteoric waters which underwent extensive isotopic exchange with the underlying rocks. The proximity of ore fluids and magmatic fluids on the $\delta^{18}O$-δD diagram (Fig. 9.9) could be due to geographical rather than genetic factors.

The δD values of fluid-inclusion waters from stage V calcite appear to be heavier than meteoric waters and have close affinity with the magmatic waters of Fig. 9.9. The $\delta^{13}C$ values of stage V calcite also indicate a magmatic parentage. It is therefore suggested that the stage V fluids could have a significant magmatic component, probably derived largely by leaching of cauldron rocks.

Chapter 10

CONDITIONS OF ORE DEPOSITION

10.1 GENERAL

Some chemical parameters prevailing at the time of ore deposition can be approximated on the basis of stability relations amongst the ore and gangue minerals, fluid-inclusion studies, stable-isotope studies and the geology. In this chapter all these factors will be used to reconstruct the physicochemical conditions of ore deposition.

To facilitate discussion the following diagrams are used:

$\text{Log } f_{O_2}/f_{S_2}$

$\text{Log } f_{O_2}/\text{pH}$

$\text{Log } f_{O_2}/T$

$\text{Log } f_{O_2}/m_{\Sigma Te}$

$\text{Log } f_{O_2}/f_{Te_2}$

The methods of construction of these diagrams have been described by Holland (1959, 1965), Garrels & Christ (1965), Barnes & Kullerud (1961), Ohmoto (1972) and Walshe (1977). The equilibrium constants and other pertinent data are given in Appendix E.

An existing computer program in the University of Tasmania has been modified to generate the various diagrams presented in this chapter.

It is important to realise that much of the thermochemical data used in this study are poorly established, and most calculations yield, at best, order-of-magnitude estimates.

The following species are assumed to be significant:

$$m_{\Sigma S} = m_{H_2S} + m_{HS^-} + m_{S^{2-}} + m_{SO_4^{2-}} + m_{KSO_4^-} + m_{NaSO_4^-} + m_{MgSO_4^o} + m_{CaSO_4^o} \quad (1)$$

$$m_{\Sigma C} = m_{H_2CO_3(ap)} + m_{HCO_3^-} + m_{CO_3^{2-}} \quad (2)$$

$$m_{\Sigma Te} = m_{H_2Te} + m_{HTe^-} + m_{Te^{2-}} + m_{H_2TeO_3} + m_{HTeO_3^-} + m_{TeO_3^{2-}} + m_{Te_2^{2-}} \quad (3)$$

The important tellurium species in aqueous solutions at about 250°C are $H_2Te_{(aq)}$, HTe^-, Te^{2-}, H_2TeO_3, $HTeO_3^-$, TeO_3^{2-} and Te_2^{2-} (D'yachkova & Khodakovskiy, 1968). The $m_{\Sigma Te}$ in the solution should therefore be equal to the sum of these species (equation 3 above). Substituting activity for molality in this equation leads to:-

$$m_{\Sigma Te} = \frac{a_{H_2Te}}{\zeta_{H_2Te}} + \frac{a_{HTe^-}}{\zeta_{HTe^-}} + \frac{a_{Te^{2-}}}{\zeta_{Te^{2-}}} + \frac{a_{H_2TeO_3}}{\zeta_{H_2TeO_3}} + \frac{a_{HTeO_3^-}}{\zeta_{HTeO_3}} + \frac{a_{TeO_3^{2-}}}{\zeta_{TeO_3^{2-}}} + \frac{a_{Te_2^{2-}}}{\zeta_{Te_2^{2-}}} \quad (4)$$

where a and ζ stand for activity and activity coefficient respectively.

Substituting the following equilibrium reactions

$$H_2Te = H^+ + HTe^- \quad (5)$$

$$HTe^- = H^+ + Te^{2-} \quad (6)$$

$$H_2Te + 3/2O_2 = H_2TeO_3 \quad (7)$$

$$H_2TeO_3 = H^+ + HTeO_3^- \quad (8)$$

$$HTeO_3^- = H^+ + TeO_3^{2-} \quad (9)$$

$$Te_2^{2-} + 2H^+ + H_2O = 2H_2Te + \tfrac{1}{2}O_2 \quad (10)$$

into equation (4) leads to

$$m_{\Sigma Te} = a_{H_2Te}(A^1+A^2+A^3+A^4+A^5+A^6) + (a_{H_2Te})^2(A^7)$$

where

$$A^1 = \frac{1}{\zeta_{H_2Te}}$$

$$A^2 = \frac{K5}{\zeta_{HTe^-}.a_{H^+}}$$

$$A^3 = \frac{K5.K6}{\zeta_{Te^{2-}}.(a_{H^+})^2}$$

$$A^4 = \frac{K7.fO_2{}^{3/2}}{\zeta_{H_2TeO_3}}$$

$$A^5 = \frac{K7.K8.fO_2{}^{3/2}}{\zeta_{HTeO_3^-}.a_{H^+}}$$

$$A^6 = \frac{K7.K8.K9.fO_2{}^{3/2}}{\zeta_{TeO_3^{2-}}.(a_{H^+})^2}$$

$$A^7 = \frac{fO_2{}^{1/2}}{\zeta_{Te_2^{2-}}.a_{H_2O}.K10.(a_{H^+})^2}$$

The data enabling calculations of the activity coefficients of the aqueous tellurium species are not known and for the present calculations they have been assumed to be equal to sulphur species of similar charge and type (Appendix E.3).

$H_2Te_{(aq)}$ is related to $f_{Te_2(g)}$ by the following equation

$$H_2O_{(l)} + \tfrac{1}{2}Te_{2(g)} = H_2Te_{(aq)} + \tfrac{1}{2}O_2 \qquad (11)$$

The distribution of the aqueous tellurium species is shown on a log f_{O_2}-pH diagram (Fig.10.1). An interesting feature of this diagram is the relatively large field of Te_2^{2-}. The field of this species is dependent on the total tellurium concentration and shrinks towards the centre with decreasing tellurium concentration, disappearing at a tellurium concentration of about 10^{-10} molal at 250°C. The behaviour of tellurium species is quite different from that of sulphur. The sulphur species corresponding to Te_2^{2-} is S_2^{2-}, which is apparently unimportant. The corresponding selenium species, Se_2^{2-}, is of some importance and its behaviour is more or less similar to Te_2^{2-} (D'yachkova & Khodakovskiy, 1968).

10.2 GEOCHEMICAL PARAMETERS

10.2.1 Temperature

This can be approximated from the homogenisation temperatures of the fluid inclusions in the quartz of stages IIA and IIIA. These temperatures range from 170 to 317°C, with modes near 215 and 235°C. For the purpose of preliminary discussion a temperature of 250°C is assumed.

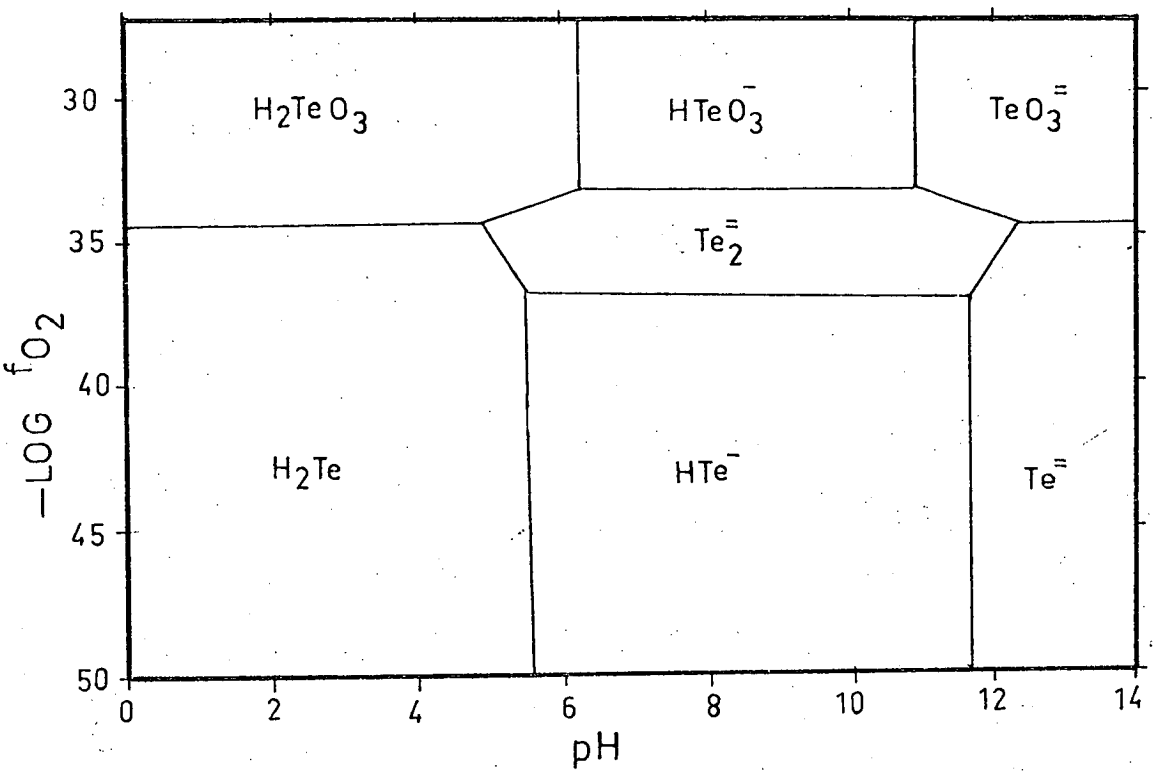

Fig. 10.1 Log f_{O_2}-pH diagram showing the distribution of aqueous tellurium species. T=250°C, activity of each species within the specified area = 10^{-8} .

10.2.2 Pressure

The majority of fluid-inclusions show evidence that the solutions were boiling when trapped. From the temperature-depth-salinity data for NaCl solutions summarised by Haas (1971) an average total pressure of about 30 bars can be approximated for the depositing environment (Chapter 7).

10.2.3 Ionic Strength

This parameter can be calculated from the salinity data and the leachate analyses. The average salinity obtained from the freezing temperatures of the fluid-inclusions is 5.5 wt.% eq. NaCl and the average Na-K-Ca-Mg molal proportions adjusted to this salinity are 0.32:0.09:0.25:0.005. Assuming all the cations are balanced by Cl^- an ionic strength (I) of about 1 can be approximated from the following formula:-

$$I = \tfrac{1}{2}\Sigma m_i z_i^2$$

where m_i and z_i stand for molality and charge of the i^{th} species respectively.

10.2.4 pH

At the Emperor mine both sericite and potassium feldspar (adularia and/or orthoclase) occur in close association and may be in equilibrium. The pH of the ore-fluids can be approximated from the following reaction:-

$$3KAlSi_3O_8 + 2H^+ = KAl_3Si_3O_{10}(OH)_2 + 2K^+ + 6SiO_2 \qquad (12)$$

Using the average molality of potassium obtained from the leachate analyses (0.1 molal), an ionic strength of 1 and the constants given in Appendix E.2 and E.3, a pH of 5.47 is obtained at 250°C. At 200 and 300°C the pH is 5.57 and 5.45 respectively. Neutral pH at 250°C is about 5.56 and at 200 and 300°C it is 5.64 and 5.70 respectively.

It is suggested that the pH of the Emperor ore-fluids was about 5.5. This pH refers to solutions in equilibrium with the K-silicate assemblage only. Solutions in equilibrium with the propylitic assemblage were probably more alkaline because there is no sericite.

10.2.5 Fugacity of sulphur (f_{S_2})

This can be approximated from the FeS content of sphalerite co-existing with pyrite. The FeS contents range from 1.3 to 6.9 mole % (Appendix D.1). These values, used in conjunction with the curves given in Barton & Skinner (1967), indicate log f_{S_2} values at 250°C between -10.5 and -12.

10.2.6 Fugacity of CO_2 (f_{CO_2})

Ankerite, dolomite and calcite are the only carbonate minerals present at the Emperor mine. Ankerite is more common in the propylitic rocks, calcite is post-mineralization (stage V) and dolomite is generally associated with the ore minerals. As shown in the paragenetic sequence (Fig. 6.5) precipitation of dolomite was repeated in several stages and was more or less intermittent, suggesting that the solutions may be close to the dolomite saturation boundary. The dolomite saturation reaction can be written as follows:-

$$2H_2O + Ca^{2+} + Mg^{2+} + 2CO_{2(g)} = CaMg(CO_3)_2 + 4H^+ \qquad (13)$$

Using the average Ca and Mg concentrations approximated from the leachate analyses (0.25 and 0.005 molal respectively; Table 7.2) and the constants given in Appendix E.2 and E.3 the f_{CO_2} can be approximated. The f_{CO_2} value calculated with the above assumptions at 250°C and at pH = 5.5 is about 2.5. Increasing the Ca and Mg concentrations to 0.5 and 0.05 molal respectively will drop the f_{CO_2} to 0.56 (at 250°C and pH = 5.5). Increasing pH by about a half unit will result in a decrease

in f_{CO_2} (at T = 250°C, m_{Ca} = 0.25 and m_{Mg} = 0.005) to 0.25. As such changes may occur both temporally and spatially, it is suggested that the f_{CO_2} at 250°C may be between 0.25 and 2.5.

At 300°C (pH = 5.5, m_{Ca} = 0.25 and m_{Mg} = 0.005) the f_{CO_2} calculated from the above reaction is 6.3.

10.2.7 Fugacity of Te_2 (f_{Te_2})

The presence of several telluride minerals and native tellurium at the Emperor mine can be used to put some limits on the f_{Te_2}. The reaction indicating the upper limit of f_{Te_2} (lower limit for native tellurium) is:-

$$2Te_{(c)} = Te_{2(g)} \qquad (14)$$

Log $K_{250°C}$ = 7.74 (Appendix E.2)

hence log f_{Te_2} = -7.74.

Both calaverite and native gold are observed at the Emperor mine. They are not closely associated and while calaverite is restricted to stage IIB, major precipitation of native gold occurred in stage IIIB. This relationship can be expressed as:-

$$Au_{(c)} + Te_{2(g)} = AuTe_2 \quad \text{(Appendix E.2)} \qquad (15)$$

Log $K_{250°C}$ = 9.44

hence log f_{Te_2} = -9.44

This reaction suggests that during stage IIB, which includes both native tellurium and calaverite, f_{Te_2} was higher than $10^{-9.44}$, while during the stage IIIB, which includes native gold and lacks native tellurium and calaverite, it was less than this value.

Several telluride and sulphide phases are plotted on a log f_{S_2}/ log f_{Te_2} diagram which has been constructed at 250°C (Fig. 10.2). The Emperor mine assemblage can now be discussed in more quantitative terms.

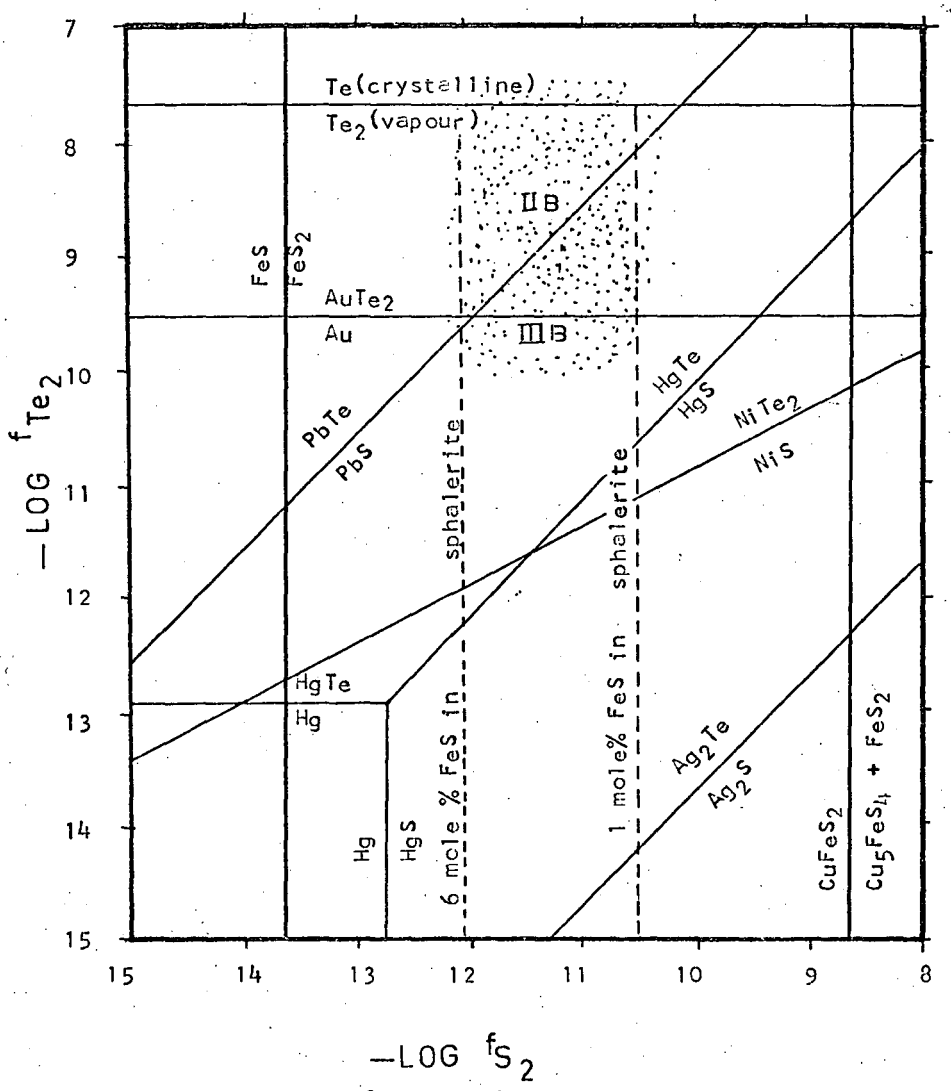

Fig. 10.2 Log f_{S_2}- log f_{Te_2} diagram showing the stability fields of tellurides and sulphides. The stippled area indicates the suggested environment at the Emperor mine. Roman numerals refer to stages in the paragenetic sequence.

Basically there are two assemblages:-

(a) Stage IIB includes native tellurium, calaverite, krennerite, sylvanite, altaite, coloradoite, melonite and galena.

(b) Stage IIIB includes native gold, petzite, hessite, empressite, altaite, coloradoite, melonite and galena.

Thermodynamic data for krennerite and sylvanite are not available, but the occurrence of these tellurides with native tellurium and calaverite indicates that their phase boundaries might lie between the calaverite-native gold and native tellurium saturation line (i.e. log f_{Te_2} between -9.44 and -7.74 at 250°C; Fig. 10.2). Thermodynamic data for petzite and empressite are also not available but the close association of these tellurides with native gold suggests that their stability fields may lie at log f_{Te_2} below -9.44 at 250°C.

In order to keep the galena-altaite boundary within the range of f_{S_2} suggested by the FeS contents of sphalerite, the f_{Te_2} must remain above about $10^{-9.5}$ (Fig. 10.2).

In summary it is suggested that f_{Te_2} (at 250°C) was between $10^{-9.5}$ and $10^{-7.5}$ during stage IIB and dropped below $10^{-9.5}$ during stage IIIB.

10.2.8 Fugacity of oxygen (f_{O_2})

The upper limit of f_{O_2} is fixed by the absence of hematite in the Emperor mine through the following reaction:-

$$3Fe_2O_3 = 2Fe_3O_4 + \tfrac{1}{2}O_2 \qquad (16)$$

Log K_{250^oC} = 17.18 (Appendix E.2)

hence log $f_{O_2} < -34.37$

The near constant value of $\delta^{13}C$ dolomite (+0.3 to -1.41‰) indicate that the solutions were well outside the reduced carbon field (Ohmoto, 1972). The lower limit of f_{O_2} can then be fixed by the following reaction:-

$$CH_{4(aq)} + 2O_{2(g)} = H_2CO_{3(ap)} + H_2O_{(l)} \quad (17)$$

Log K_{250^oC} = 77.52 (Appendix E.2)

hence log f_{O_2} > -38.76

Magnetite is widespread in the propylitic assemblage but in the mineralized rocks, most of it is replaced by pyrite. In many specimens this replacement is incomplete and in a few samples (e.g. sample 103428) single grains show alternate rings of magnetite and pyrite. This indicates that (a) magnetite was locally precipitated in the mineralized rocks and (b) the solutions probably did not stray far from the pyrite-magnetite boundary. This relationship can be explained by the following reaction:-

$$3FeS_2 + 2O_{2(g)} = Fe_3O_4 + 3S_{2(g)} \quad (18)$$

Log K_{250^oC} = 35.44 (Appendix E.2)

Using the f_{S_2} values deduced from the FeS contents of sphalerite (10^{-12} to $10^{-10.5}$) an f_{O_2} range between $10^{-35.9}$ and $10^{-33.65}$ is obtained for such an assemblage.

The fluctuations in the $\delta^{34}S$ values of pyrite (-5.5 to -15.3‰) indicate significant proportions of oxidised sulphur species. The f_{O_2} must then be close to the $\Sigma S_r = \Sigma S_o$ boundary (Σ reduced sulphur species = Σ oxidised sulphur species), which at 250°C and at pH = 5.5 lies at a log f_{O_2} value of about -35.4 (see details of calculation in the following section).

Stability fields of several sulphide and oxide minerals are plotted on a log f_{O_2}/log f_{S_2} diagram (Fig. 10.3) along with the FeS contours of sphalerite, the sulphide-sulphate boundary and total sulphur contours. The stippled area in this diagram indicates the f_{O_2}-f_{S_2} conditions at the Emperor mine. From the above discussion the f_{O_2} is likely to have varied between 10^{-35} and 10^{-37} at 250°C.

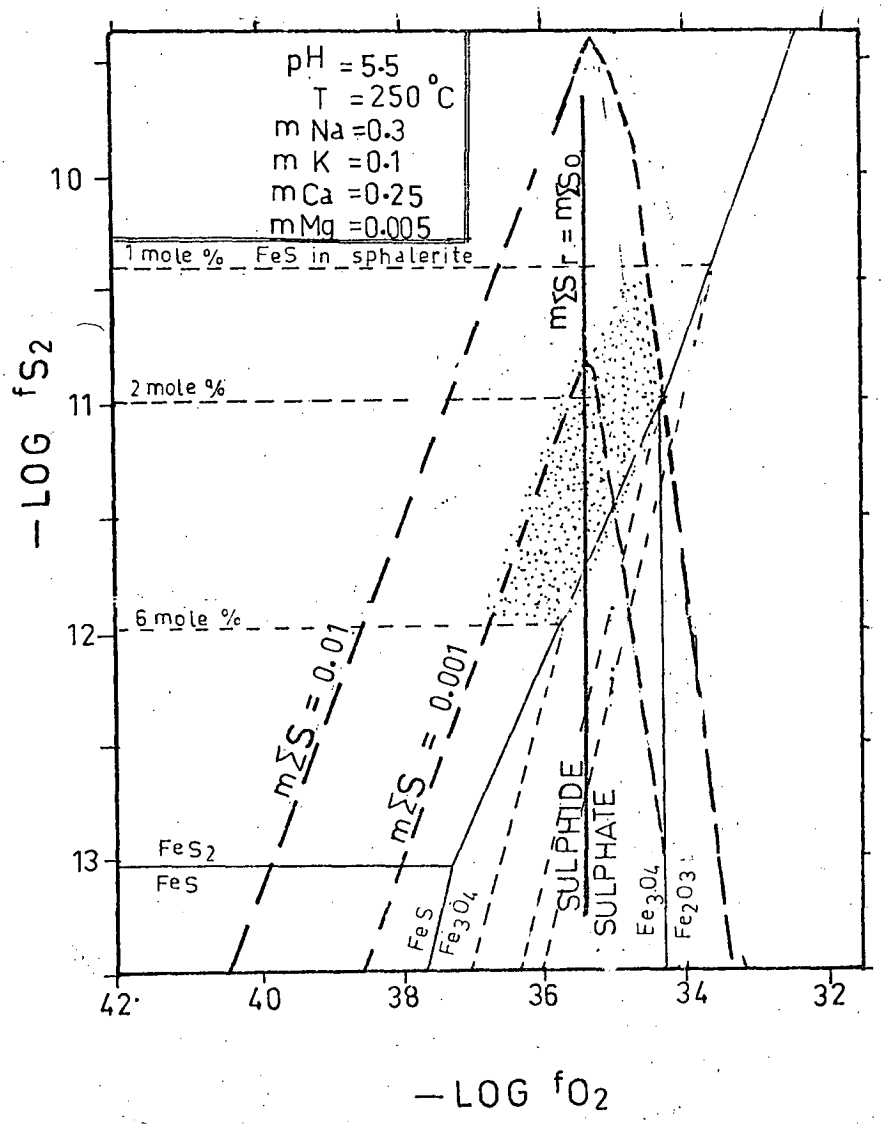

Fig. 10.3 Log fS_2-log fO_2 diagram showing the stability fields of Fe-S-O minerals and contours of mole% FeS in sphalerite. The contours of total sulphur are drawn at a pH=5.5. The stippled area indicates the suggested environment at the Emperor mine. H_2S is the dominant species in the sulphide field and $CaSO_4^\circ$ is the dominant species in the sulphate field.

10.2.9 Total sulphur ($m_{\Sigma S}$)

At the f_{O_2}-pH-T conditions of the Emperor fluids the important dissolved sulphur species were $H_2S_{(aq)}$, HS^-, HSO_4^-, SO_4^{2-}, $NaSO_4^-$, KSO_4^-, $CaSO_4^o$ and $MgSO_4^o$. The species S^{2-} is not considered here because recent data on the second dissociation constant of H_2S (Naumov *et al.*, 1979) indicate that it is not an important species at the pH range of the Emperor fluids. In the reduced sulphur field (shown in the diagrams as ΣS_r):

$$m_{\Sigma S_r} = m_{H_2S_{(aq)}} + m_{HS^-} \tag{19}$$

In the oxidised sulphur field (shown in the diagrams as ΣS_o):

$$m_{\Sigma S_o} = m_{\Sigma SO_4} = m_{HSO_4^-} + m_{SO_4^{2-}} + m_{NaSO_4^-} + m_{KSO_4^-} + m_{CaSO_4^o} + m_{MgSO_4^o} \tag{20}$$

Using the following equilibrium reactions

$$H_2S_{(aq)} + \tfrac{1}{2}O_2 = H_2O + \tfrac{1}{2}S_2 \tag{21}$$

$$HS^- + H^+ + \tfrac{1}{2}O_2 = H_2O + \tfrac{1}{2}S_2 \tag{22}$$

$$HSO_4^- + H^+ = H_2O + \tfrac{1}{2}S_2 + \tfrac{3}{2}O_2 \tag{23}$$

$$SO_4^{2-} + 2H^+ = H_2O + \tfrac{1}{2}S_2 + \tfrac{3}{2}O_2 \tag{24}$$

$$NaSO_4^- + 2H^+ = H_2O + \tfrac{1}{2}S_2 + \tfrac{3}{2}O_2 + Na^+ \tag{25}$$

$$KSO_4^- + 2H^+ = H_2O + \tfrac{1}{2}S_2 + \tfrac{3}{2}O_2 + K^+ \tag{26}$$

$$CaSO_4^o + 2H^+ = H_2O + \tfrac{1}{2}S_2 + \tfrac{3}{2}O_2 + Ca^{2+} \tag{27}$$

$$MgSo_4^o + 2H^+ = H_2O\ \tfrac{1}{2}S_2 + \tfrac{3}{2}O_2 + Mg^{2+} \tag{28}$$

the following relationship is obtained:-

$$m_{H_2S} + m_{HS^-} = \frac{a_{H_2O} \cdot f_{S_2}^{\frac{1}{2}}}{\zeta_{H_2S} \cdot f_{O_2}^{\frac{3}{2}} \cdot K21} + \frac{a_{H_2O} \cdot f_{S_2}^{\frac{1}{2}}}{\zeta_{HS^-} \cdot a_{H^+} \cdot K22} \tag{29}$$

$$m_{\Sigma SO_4} = f_{S_2}^{\frac{1}{2}} \cdot f_{O_2}^{\frac{7}{2}} \cdot a_{H_2O} \left[\frac{1}{\zeta_{HSO_4^-} \cdot a_{H^+} \cdot K23} + \frac{1}{\zeta_{SO_4^{2-}} \cdot (a_{H^+})^2 \cdot K24} \right.$$

$$+ \frac{m_{Na^+} \cdot \zeta_{Na^+}}{\zeta_{NaSO_4^-} \cdot (a_{H^+})^2 \cdot K25} + \frac{m_{K^+} \cdot \zeta_{K^+}}{\zeta_{KSO_4^-} \cdot (a_{H^+})^2 \cdot K26}$$

$$\left. + \frac{m_{Ca^{2+}} \cdot \zeta_{Ca^{2+}}}{\zeta_{CaSO_4^o} \cdot (a_{H^+})^2 \cdot K27} + \frac{m_{Mg^{2+}} \cdot \zeta_{Mg^{2+}}}{\zeta_{MgSO_4^o} \cdot (a_{H^+})^2 \cdot K28} \right] \quad (30)$$

where K21-28 are the equilibrium constants for reactions 21 to 28 above. Following Helgeson (1969) the activity coefficients of $CaSO_4^o$ and $MgSO_4^o$ are taken as unity. Other pertinent data are given in Appendices E.2 and E.3.

Using equations (29) and (30) the total sulphur contours are drawn on a log f_{O_2}/log f_{S_2} diagram (Fig. 10.3). It can be seen that at the f_{O_2}-f_{S_2} values indicated by the mineral stability data the total sulphur is close to 10^{-3} molal.

10.2.10 Total carbon ($m_{\Sigma C}$)

As $H_2CO_{3(ap)}$ is the dominant solution species of carbon at the f_{O_2}-pH-T conditions deduced so far, it can be assumed as an approximation that:-

$$m_{\Sigma C} = m_{H_2CO_{3(ap)}} \quad (31)$$

Molality of $H_2CO_{3(ap)}$ can be determined from the following reaction:-

$$CO_{2(g)} + H_2O = H_2CO_{3(ap)} \quad (32)$$

Using the constants given in Appendices E.1 and E.2 and the f_{CO_2} values deduced earlier, $m_{H_2CO_{3(ap)}}$ can be determined. At 250°C and at f_{CO_2} = 2.5, a $m_{H_2CO_{3(ap)}}$ value of about 10^{-2} is obtained. There would be some HCO_3^- so $m_{\Sigma C}$ may be slightly higher than this value.

Using a f_{CO_2} value of 0.25 gives a $m_{H_2CO_3}$ value of about 10^{-3} at 250°C, this may be the lower limit.

10.2.11 Total tellurium ($m_{\Sigma Te}$)

Using the constants given in Appendices E.2 and E.3, the stability fields of several tellurides are plotted on a log f_{O_2}/log $m_{\Sigma Te}$ diagram (Fig. 10.4A). The assumed conditions are T = 250°C, $m_{\Sigma S} = 10^{-3}$, I = 1, and pH = 5.5. The stability boundaries galena-altaite, cinnabar-coloradoite, nicolite-melonite, argentite-hessite are dependent on $m_{\Sigma S}$ and to show this dependence Fig. 10.4B is constructed at $m_{\Sigma S} = 10^{-2}$.

The probable environments at the Emperor mine are marked by the stippled area. It can be seen that at the suggested f_{O_2}-pH-T conditions, $m_{\Sigma Te}$ in the Emperor mine ore-fluids ranges from 10^{-10} to 10^{-12}, from which a value of 10^{-11} is tentatively selected for 250°C.

A compilation of data on the solubility of TeO_2 (Beas and Mesmer, 1976) shows that at T = 25°C, pH = 3 to 5, the solubility is about 10^{-5} molal and rises to about 10^{-3} molal at a pH of about 1. The tellurium concentration in sea water is about 10^{-7} molal (Chapter 2). Nabivanets & Kapantsyan (1968) obtained the solubility of freshly precipitated tellurium hydroxide in HCL and LiCl solutions at pH = 3, T = 18°C, I = 1, to be about $10^{-2.7}$ molal. This increased to about $10^{-1.67}$ molal at a pH of about 1. It thus appears that the suggested value for the Emperor mine fluids (10^{-11} molal) is several orders of magnitude too low. This may be for two reasons.

(i) Errors in the thermodynamic data.

(ii) Presence of other aqueous species.

As suggested by D'yachokova & Khodokovskiy (1968) many of the thermodynamic constants used have largely become obsolete and a revision of these constants is very much needed.

Nabivanets & Kapantsyan (1968) explained the increased solubility in their experiments in terms of $TeO(OH)Cl^{o}$, $TeOCl_2^{o}$, $TeOCl_3^{-}$ and $TeOCl_4^{2-}$.

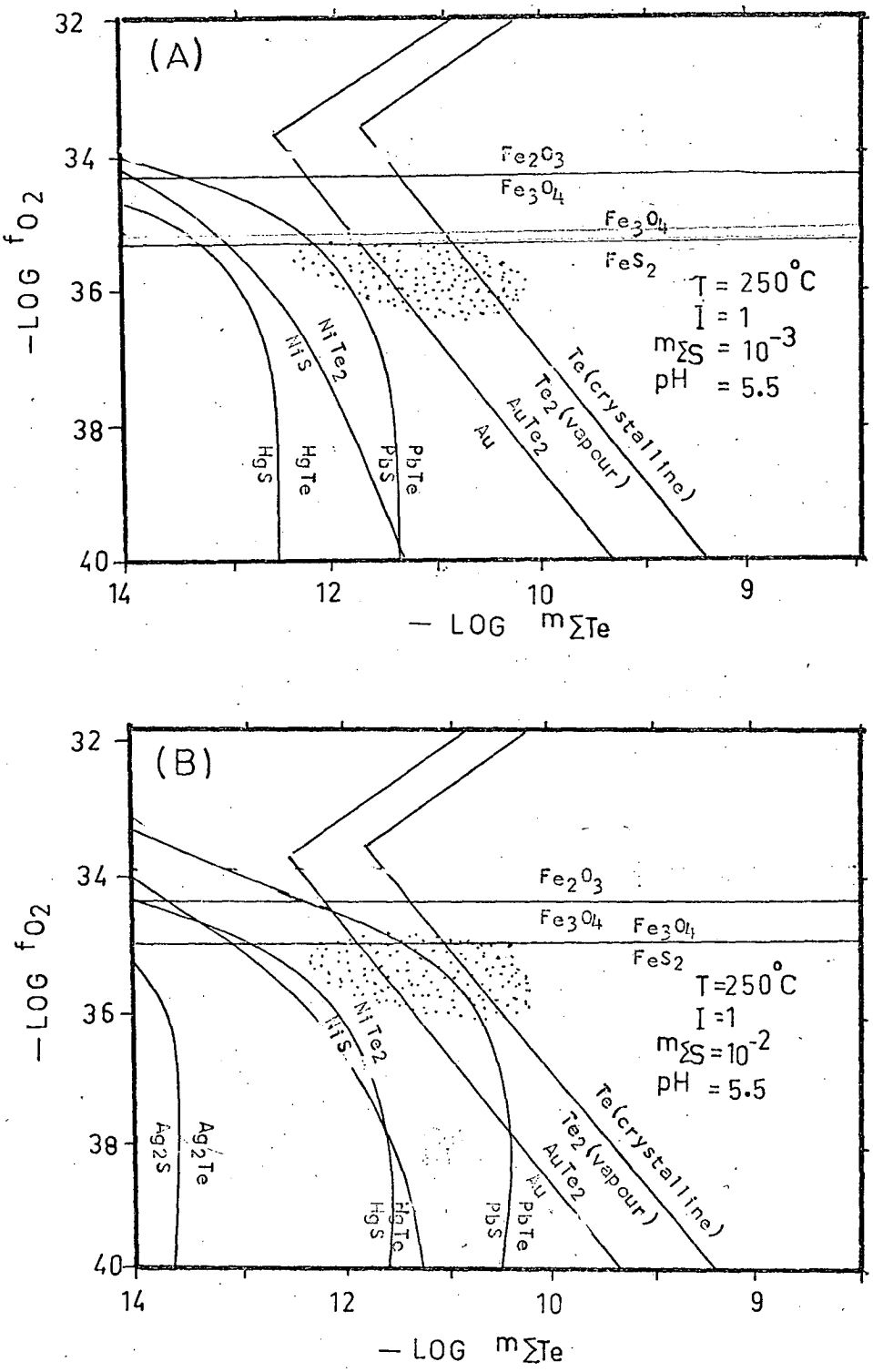

Fig. 10.4 Log fO_2- $m\Sigma Te$ diagrams showing the stability fields of sulphides, tellurides and oxides. (A) at $m\Sigma S$ =0.001 and (B) at $m\Sigma S$ =0.01. Note changes in the sulphide-telluride boundaries with increasing sulphur concentration. The stippled area indicates the suggested environments at the Emperor mine.

It is possible that some of these species may be important as carriers of tellurium in the hydrothermal solutions but the available data are insufficient to consider their probable role.

Although in the following presentation the stability boundaries of tellurides have been drawn on log f_{O_2}/T and log f_{O_2}/pH diagrams, they should be treated as tentative and may change significantly if and when the thermodynamic data on aqueous tellurium species are revised.

10.3 CHANGES IN pH AND TEMPERATURE

So far a temperature of 250°C and pH of 5.5 have been assumed in order to approximate the other geochemical parameters. In Chapter 7 it was shown that variations in temperature have occurred both temporally and spatially. In the same Chapter, evidence showing boiling of the ore-fluids was presented, and boiling of gases like CO_2, H_2S and H_2Te may result in fluctuations in pH. It therefore appears that assumptions involving constant pH and temperature are not reasonable.

10.3.1 pH changes at 250°C

Changes in mineral stability and other data due to variations in pH are depicted on log f_{O_2}/pH diagrams (Figs. 10.5, 10.6 and 10.7). These diagrams require assumptions regarding $m_{\Sigma S}$, $m_{\Sigma C}$ and $m_{\Sigma Te}$. In the following presentations, unless otherwise noted, these values are assumed to be as follows:-

$$m_{\Sigma S} = 10^{-3}$$

$$m_{\Sigma C} = 10^{-2}$$

$$m_{\Sigma Te} = 10^{-11}$$

These assumptions are themselves not strictly valid because boiling alone may reduce these values to some extent.

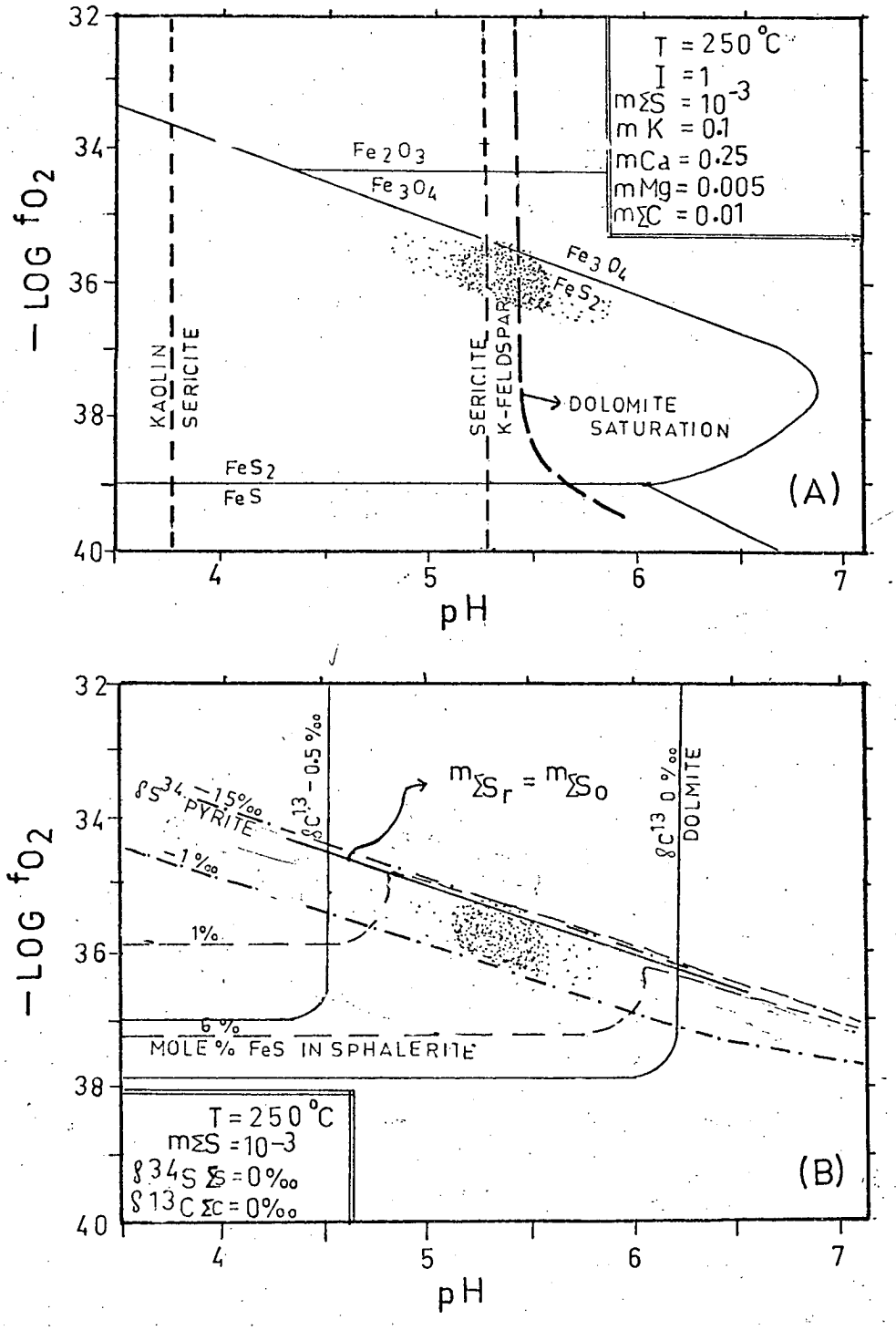

Fig. 10.5 Log f_{O_2}-pH diagram showing :(A) the stability fields of Fe-S-O minerals, silicates and dolomite; and (B) the contours of mole% FeS in sphalerite, $\delta^{13}C$ contours of dolomite , $\delta^{34}S$ contours of pyrite and $m_{S_r}=m_{S_o}$ boundary. The stippled area indicates the suggested environment at the Emperor mine. Major deposition probably occurred within the heavily stippled area.

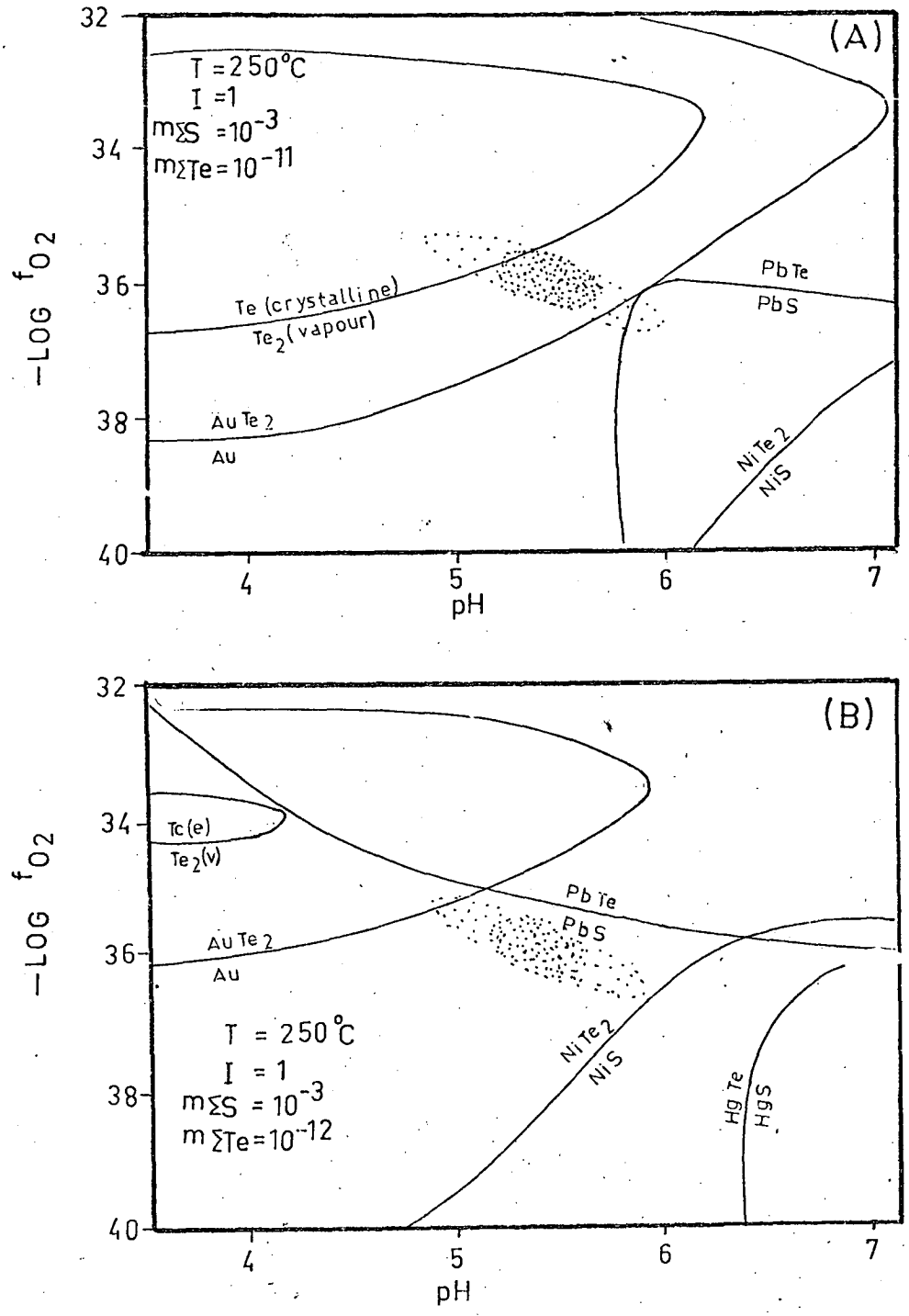

Fig. 10.6 Log f_{O_2}-pH diagram showing (A) the stability fields of tellurides and sulphides at $m_{\Sigma Te}=10^{-11}$; and (B) at $m_{\Sigma Te}=10^{-12}$. The stippled area indicates the suggested region for the Emperor mine ore-fluids. Major precipitation probably occurred within the heavily stippled area.

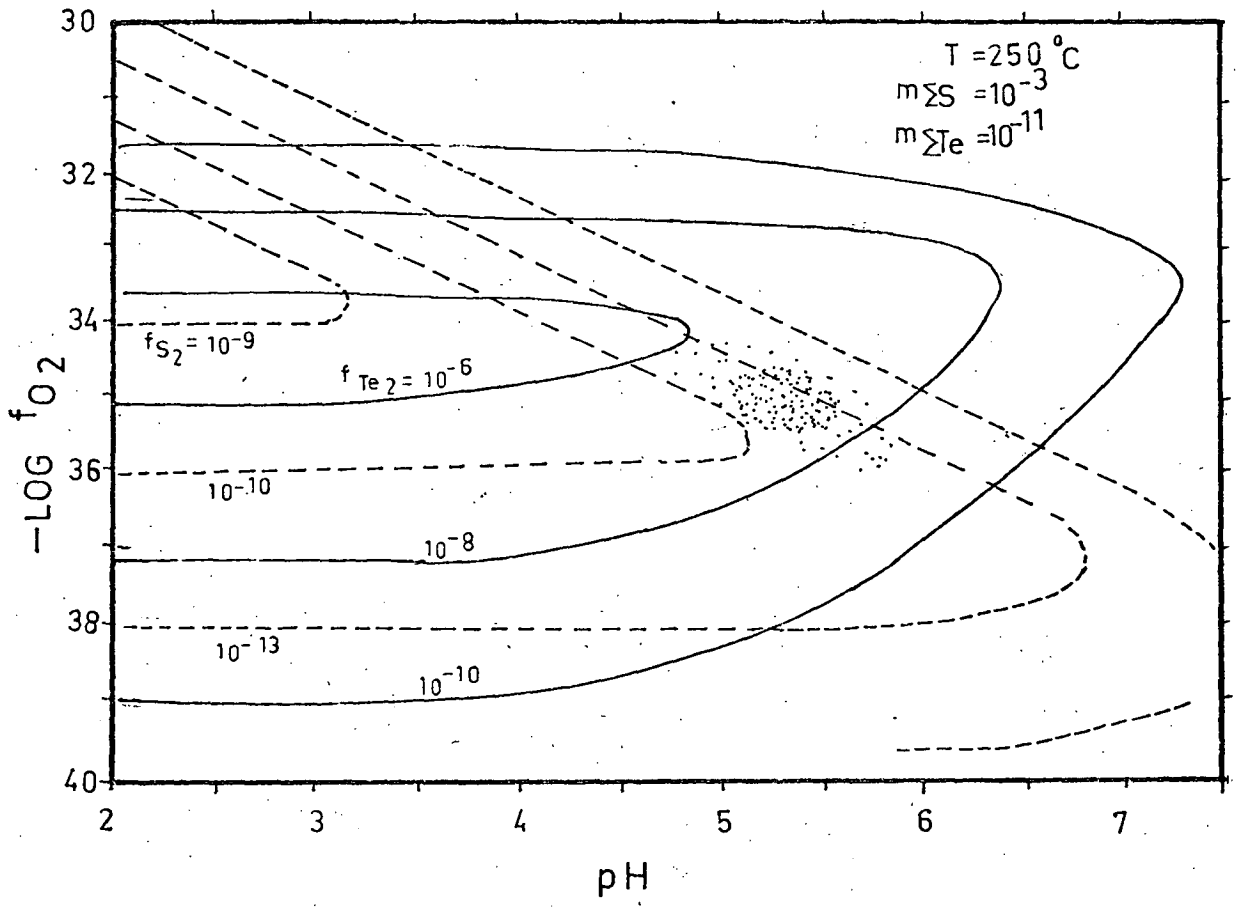

Fig. 10.7 Log f_{O_2}-pH diagram showing f_{S_2} and f_{Te_2} contours.

The silicates, carbonates and Fe-S-O mineral boundaries (Fig. 10.5A) are compatible with a pH of 5.5 and the bulk of mineralization may have occurred within ±0.25 units of this value. The intermittent precipitation of dolomite (Chapter 6) may be due to periodic boiling which could increase the pH of the ore fluids to the dolomite saturation line. The $\delta^{13}C$ values of dolomite and $\delta^{34}S$ values of pyrite at the suggested f_{O_2}-pH conditions (Fig. 10.5B) indicate a sedimentary source of carbon ($\delta^{13}C_{\Sigma C}$ = 0‰) and an igneous source of sulphur ($\delta^{34}S_{\Sigma S}$ = 0‰). The fluctuations in the $\delta^{34}S$ values of pyrite (-4.2 to -15.3‰) suggest that the fluids may be close to the $\Sigma S_r = \Sigma S_o$ boundary (Fig. 10.5B). Variations in the FeS contents of sphalerite (1.4 to 6.9 mole %) could be explained by fluctuations in the pH and/or f_{O_2} (see footnote *). The telluride mineral boundaries (Fig. 10.6A) suggest that the stage IIIB fluids may have been at a relatively higher pH. Alternatively tellurium concentration may have been dropped to 10^{-12} molal (Fig. 10.6B) during stage IIIB. In the suggested regions of the Emperor mine ore-fluids, the log f_{Te_2} could vary from -6 to -9 and the log f_{S_2} from -10 to -12 (Fig. 10.7). These values are more or less similar to the values shown in Figs. 10.2 and 10.3.

It can thus be concluded that at 250°C the mineral stability and other geochemical data suggest a pH of 5.5 ± 0.5.

---

* In diagrams showing the FeS contours of sphalerite the equilibrium constant for the reaction $FeS_2 = FeS + \frac{1}{2}O_2$ has been adjusted to make the FeS content of sphalerite at the py/po and py/bn/ccp boundaries consistent with the experimental data [see Barton *et al.* (1977) for a summary of the difficulties and implications of changing the equilibrium constant.]

10.3.2 Temperature changes

Changes in mineral stability and chemical parameters with temperature are depicted on log f_{O_2}/T diagrams (Figs. 10.8 and 10.9). Along with the other assumptions detailed in Section 10.3.1, construction of log f_{O_2}/T diagrams also require an expression relating pH and temperature. It can be seen from earlier discussions that the average pH of the Emperor fluids was probably very nearly neutral (Section 10.2.4). In the constructions of log f_{O_2}/T diagrams the dissociation constant of water is therefore used for relating pH and temperature. As the majority of fluid-inclusions temperatures on the stage IIA and IIIA quartz fall within a range of 210 to 260°C, it has been assumed that major ore mineral precipitation probably occurred within this temperature range (the heavily stippled area in Figs. 10.8 and 10.9).

The Fe-S-O mineral boundaries (Fig. 10.8A) indicate that the pyrite field terminates at about 285°C, whereas the actual fluid-inclusion temperatures range up to 320°C. This discrepancy is probably due to the assumption that $m_{\Sigma S}$ was constant at 10^{-3}. A slight increase in this value may enlarge the pyrite field to the estimated temperatures. Considering the various other uncertainties (in thermodynamic data, fluid-inclusion temperatures, and assumptions regarding pH etc.) this discrepancy is only of minor importance. The stable isotope data and FeS contents of sphalerite are more or less compatible with the suggested environment of the Emperor fluids (Fig. 10.8B).

The telluride mineral boundaries are plotted in Figs. 10.9A and 10.9B. Note that PbTe and Ag_2Te are stable phases throughout in Fig. 10.9A. The latter may react with $AuTe_2$ and Au to form mixed gold-silver tellurides (i.e. krennerite, sylvanite, petzite). Stabilization of galena and native gold in the f_{O_2}/T range of the Emperor fluids

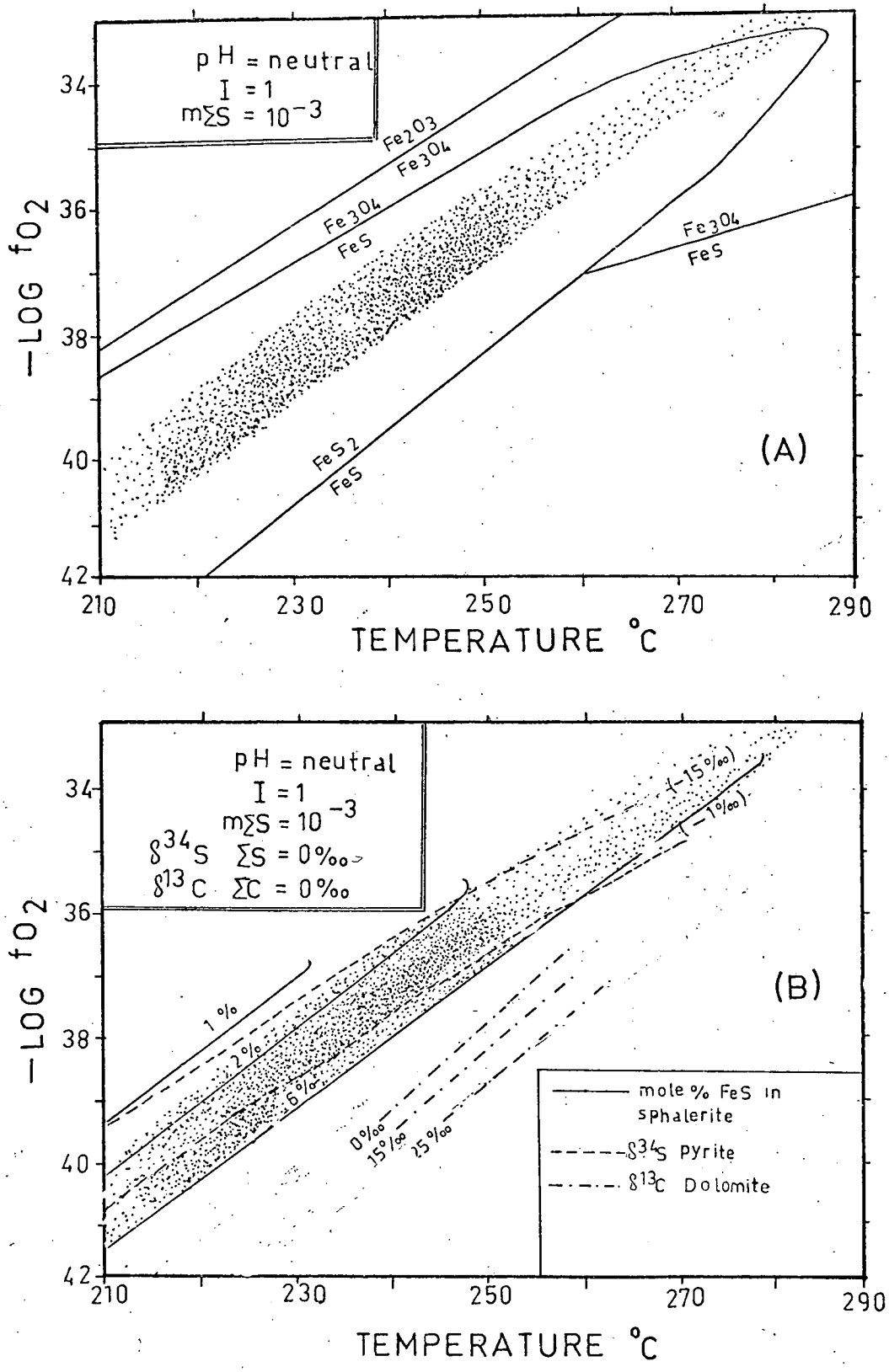

Fig. 10.8 Log fO_2- temperature diagram showing:(A) the stability fields of Fe-S-O minerals and (B) the contours of mole % FeS in sphalerite, $\delta^{13}C$ contours of dolomite and $\delta^{34}S$ contours of pyrite. The stippled area indicates the suggested environment at the Emperor mine. Major deposition probably occurred within the heavily stippled area.

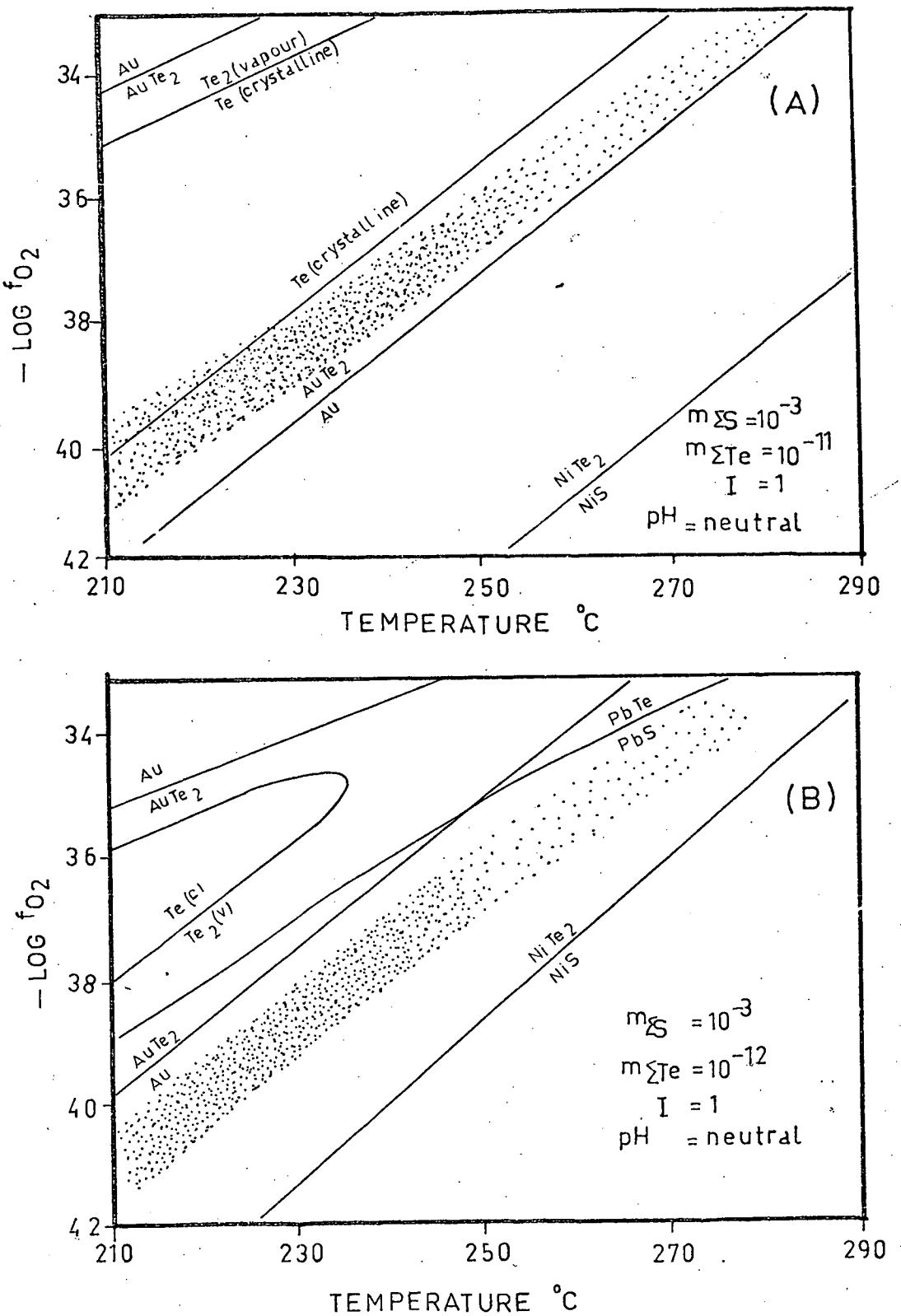

Fig. 10.9 Log f_{O_2}-temperature diagram showing the stability fields of sulphides and tellurides. (A) at $m_{\Sigma Te} = 10^{-11}$ and (B) at $m_{\Sigma Te} = 10^{-12}$.

(i.e. within the stippled area) may be possible with about a half unit increase in pH (cf. Fig. 10.6B) or a decrease in the $m_{\Sigma Te}$ by about an order-of-magnitude (Fig. 10.9B). Galena can also be stabilised in the stippled area by increasing $m_{\Sigma S}$ by about an order-of-magnitude (cf. Fig. 10.4B) but not native gold. As the available data on aqueous tellurium species are of doubtful validity it appears pointless to consider this problem any further. It can perhaps be suggested that the presence of native gold in stage IIIB is possibly due to lower tellurium concentration and/or slightly higher pH.

10.4 METAL SOLUBILITIES

The following assumptions concerning the important aqueous species are made in order to calculate the metal solubilities:

$$m_{\Sigma Zn} = m_{ZnCl^+} + m_{ZnCl_2^o} + m_{ZnCl_3^-} + m_{ZnCl_4^{2-}} + m_{Zn^{2+}},\ \text{sphalerite (ZnS) saturated} \quad (33)$$

$$m_{\Sigma Pb} = m_{PbCl^+} + m_{PbCl_2^o} + m_{PbCl_3^-} + m_{PbCl_4^{2-}} + m_{Pb^{2+}},\ \text{galena (PbS) or altaite (PbTE) saturated} \quad (34)$$

$$m_{\Sigma Ag} = m_{AgCl^o} + m_{AgCl_2^-} + m_{Ag^+},\ \text{argentite } (Ag_2S) \text{ or hessite } (Ag_2Te) \text{ saturated} \quad (35)$$

$$m_{\Sigma Cu} = m_{CuCl^o} + m_{Cu(HS)_2^-} + m_{Cu(HS)_2.H_2S^-},\ \text{chalcopyrite } (CuFeS_2) \text{ or bornite } (Cu_5FeS_4) \text{ saturated} \quad (36)$$

$$m_{\Sigma Fe} = m_{FeCl^+} + m_{Fe^{2+}},\ \text{pyrite } (FeS_2), \text{ pyrrhotite } (FeS), \text{ magnetite } (Fe_3O_4) \text{ or hematite } (Fe_2O_3) \text{ saturated} \quad (37)$$

$$m_{\Sigma Au} = m_{AuCl_2^-} + m_{Au(HS)_2^-},\ \text{native gold (Au) or calaverite } (AuTe_2) \text{ saturated} \quad (38)$$

The expression relating solubility to pH, f_{O_2}, T, m_{Cl} and $m_{\Sigma S}$ are given in Nriagu (1971a) and Anderson (1977). Following the latter the activity coefficients of doubly and singly charged complexes of lead and

zinc are assumed to be equal to $\zeta_{M^{++}}$ and ζ_{Cl^-} respectively, where M stands for metal ion. The activity coefficients of neutral species of lead, zinc and silver are assumed to be equal to the activity coefficient of CO_2 in NaCl solutions. The activity coefficients of singly charged complexes of silver and gold are assumed to be equal to ζ_{Cl^-}. Calculations of copper and iron solubility do not involve these assumptions as activity is assumed to be equal to molality in the retrieval of thermodynamic data from the experiments (Crerar & Barnes, 1976).

10.4.1 Zinc

Complexing with chlorine (Helgeson, 1969) and sulphur (Barnes, 1965; Barnes & Czamanske, 1967) has been suggested to account for the zinc solubility in the hydrothermal solutions and it appears that in near-neutral and acid environments chloride complexes will dominate while under alkaline conditions considerable zinc can be transported as sulphur complexes. Some experimental results are available on the solubility of sphalerite (Hinners & Holland, 1963; Melentyev *et al.*, 1969; Barnes, 1965; Barnes & Czamanske, 1967). These experiments indicate that sphalerite solubility decreases with increase in pH in strongly acid solutions, is near constant in the intermediate pH range and rises again in more alkaline solutions. The solubility in the near-neutral and alkaline pH range is thought to be due to $Zn(HS)_2^0$ (Hinners & Holland, 1963; Melentyev *et al.*, 1969) and $Zn(HS)_3^-$ (Barnes, 1965; Melentyev *et al.*, 1969).

In this study only chloride complexes are considered and because of the likely presence of sulphur complexes near the pH values assumed for the Emperor fluids, the solubility values at a pH greater than about 6 should be treated as minima.

The zinc solubility is contoured on log f_{O_2}/pH and log f_{O_2}/T diagrams (Figs. 10.10A and 10.10B). It can be seen that in the region of the Emperor fluids, the zinc concentrations range from about 10 to 1 ppm.

10.4.2 Lead

Complexing with chlorine (Helgeson, 1969; Nriagu & Anderson, 1971) and sulphur (Hemley, 1953; Anderson, 1962; Nriagu, 1971b) has been suggested to account for the solubility of lead in the hydrothermal solutions. As for zinc, it appears that in near-neutral and acid environments chloride complexes will dominate while under alkaline conditions considerable lead can be transported as lead-sulphur complexes. Some experimental results are available on the solubility of galena (Hemley, 1953; Anderson, 1962; Nriagu, 1971b; Barrett, 1974, in Anderson, 1977). These experiments indicate a trend similar to sphalerite (see above). The solubility in the near-neutral and alkaline pH range is considered to be due to $PbS.2H_2S$ and $Pb(HS)_3^-$ (Anderson, 1962; Nriagu, 1971b) but thermodynamic data on these complexes at elevated temperatures is not very reliable and only chloride complexes are considered in the solubility calculation.

The dissociation constants used (for the lead chloride complexes) are from Helgeson (1969). The solubility of lead has been calculated assuming that either galena or altaite is saturated (Figs. 10.11 and 10.12). Because of the uncertainty in the thermodynamic data on the aqueous tellurium species, the altaite solubility is doubtful and is not considered in the following discussions. Assuming only galena saturation, it appears that the lead solubility (Figs. 10.12A and 10.12B) in the Emperor fluids ranged from 0.1 to 0.001 ppm. These values are about two orders-of-magnitude lower than that of zinc. Though previous workers (Barton *et al.*, 1977; Casadevall, 1976; Casadevall & Ohmoto, 1977)

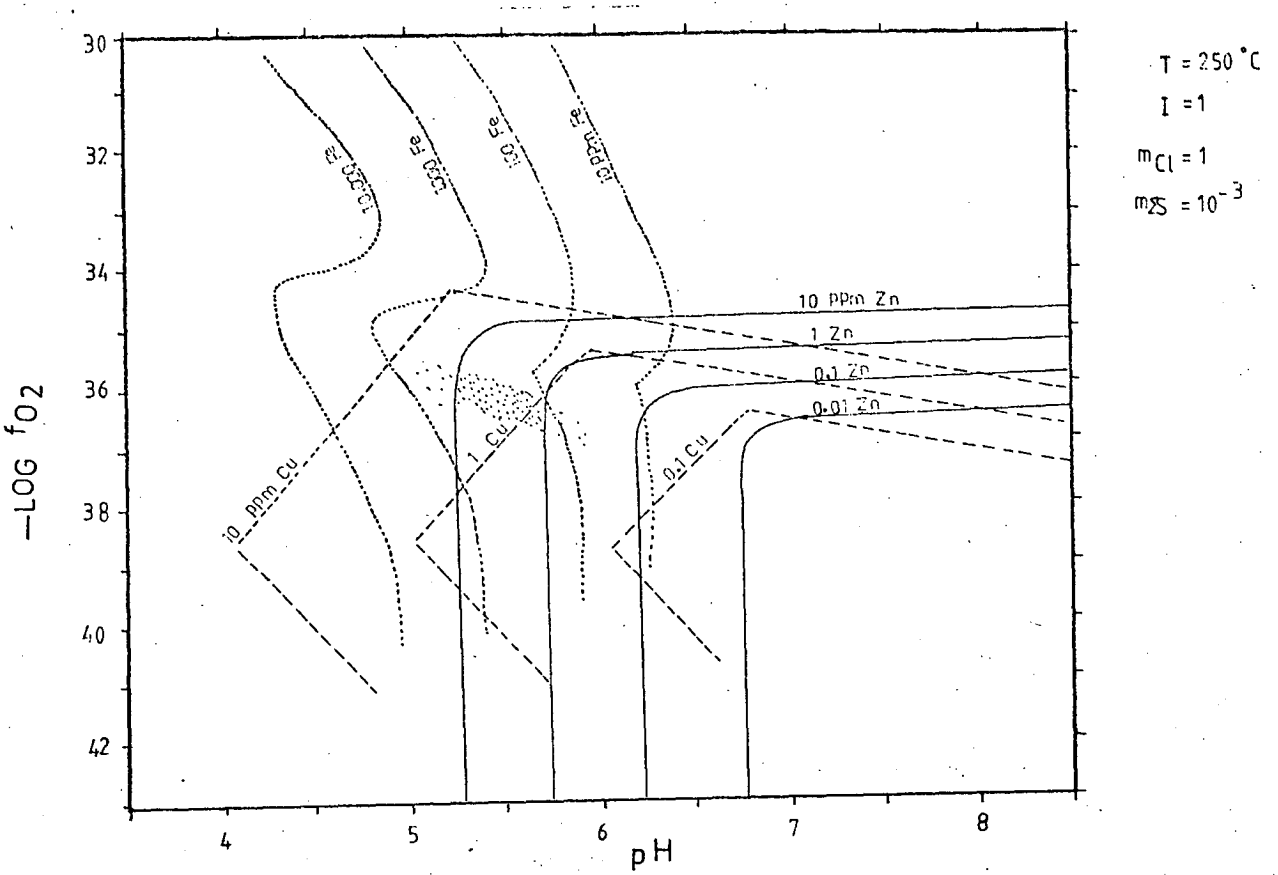

Fig. 10.10A Log f_{O_2}/pH diagram showing solubility contours (ppm) of Cu, Fe and Zn. Stippled area indicates the probable environment at the Emperor mine.

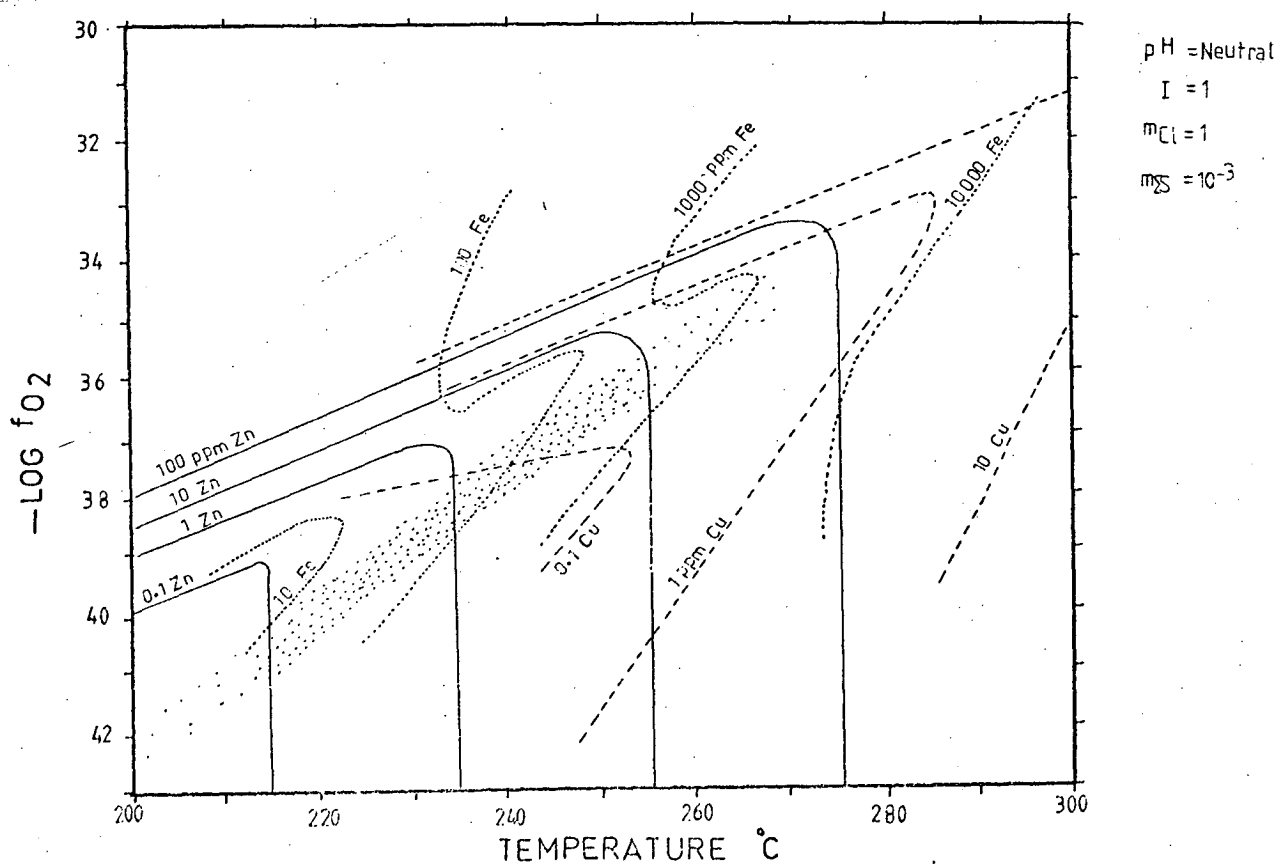

Fig. 10.10B Log f_{O_2}/temperature diagram showing solubility contours (ppm) of Cu, Fe and Zn.

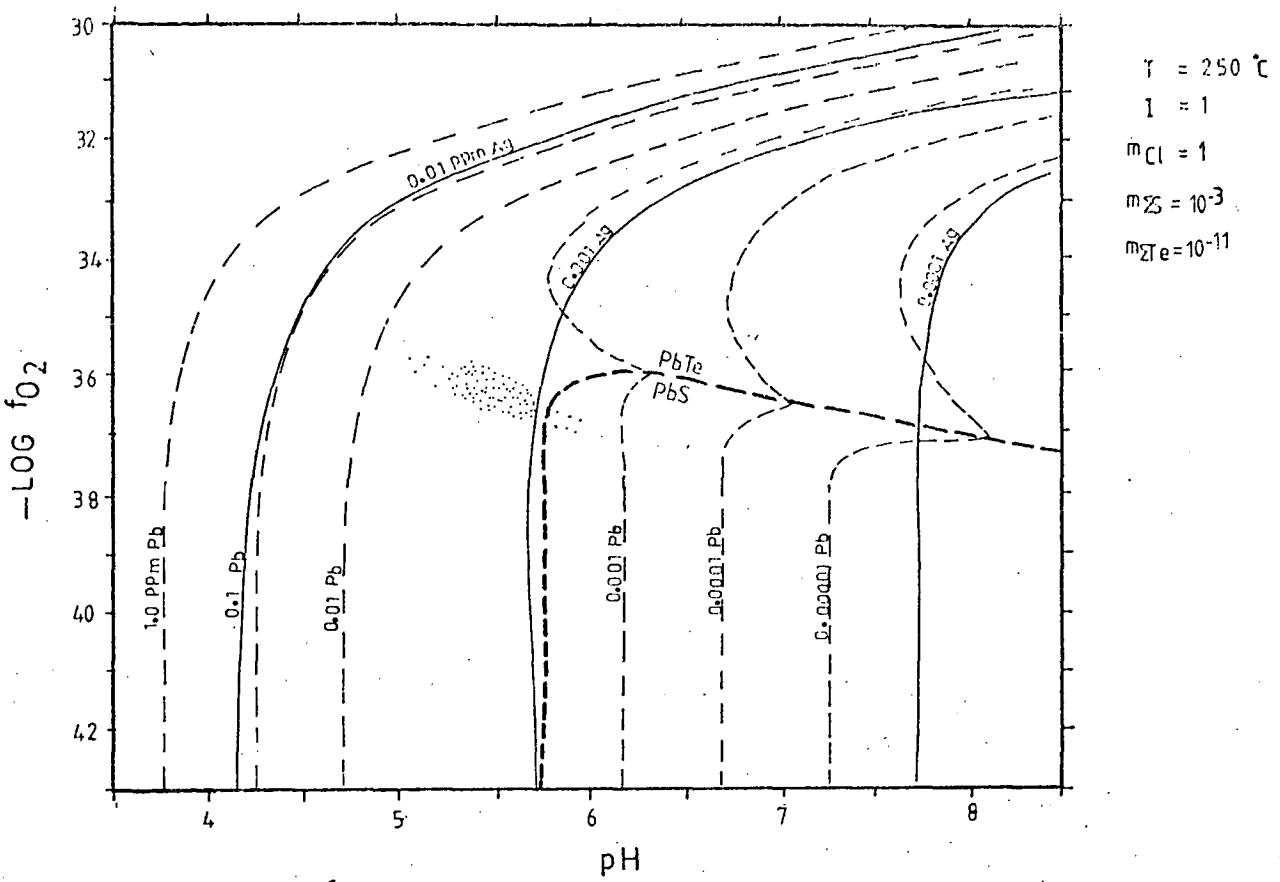

Fig. 10.11A Log f_{O_2}/pH diagram showing solubility contours (ppm) of Ag and Pb. Note that hessite is stable throughout the diagram.

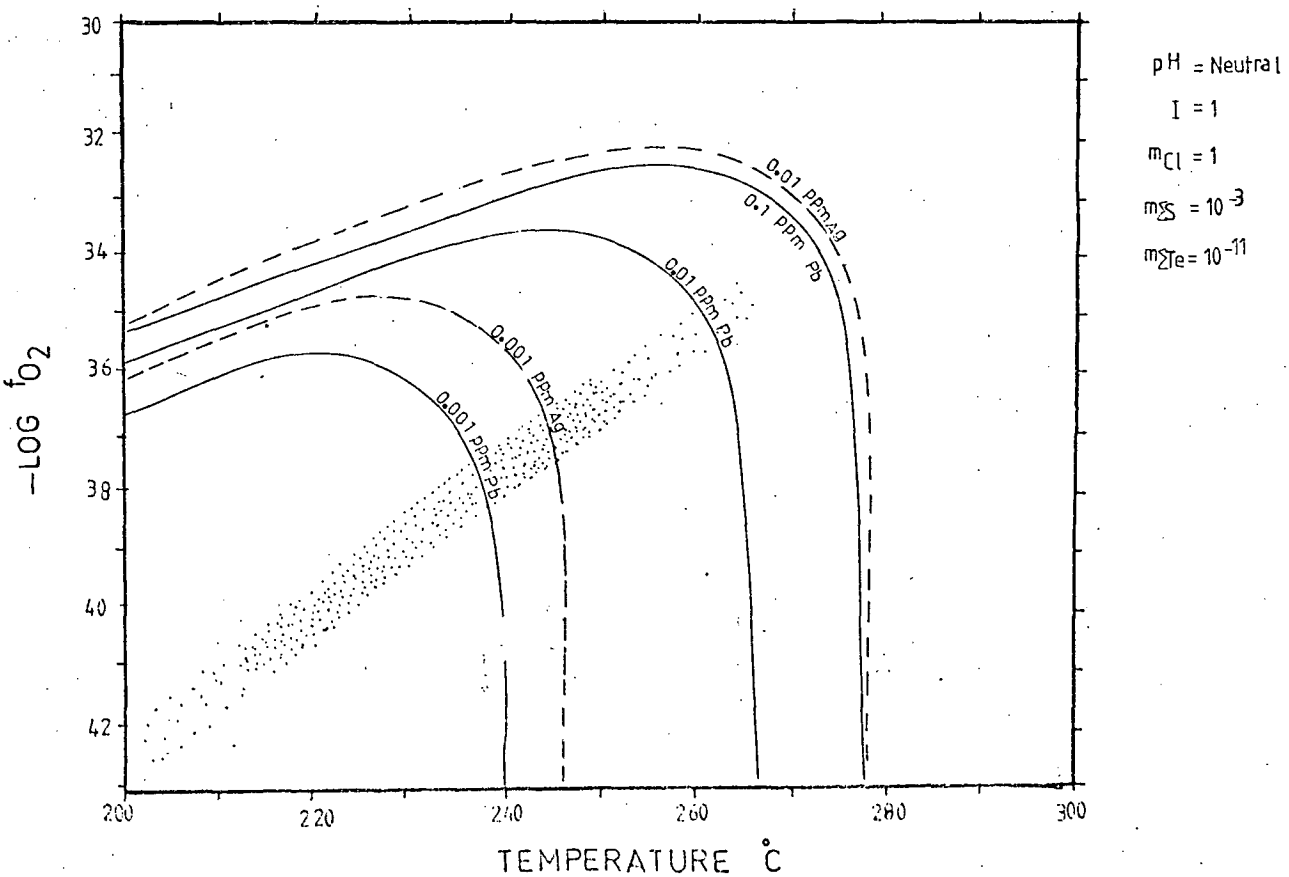

Fig. 10.11B Log f_{O_2}/temperature diagram showing solubility contours (ppm) of Ag and Pb. Note that hessite and altaite are stable throughout the diagram.

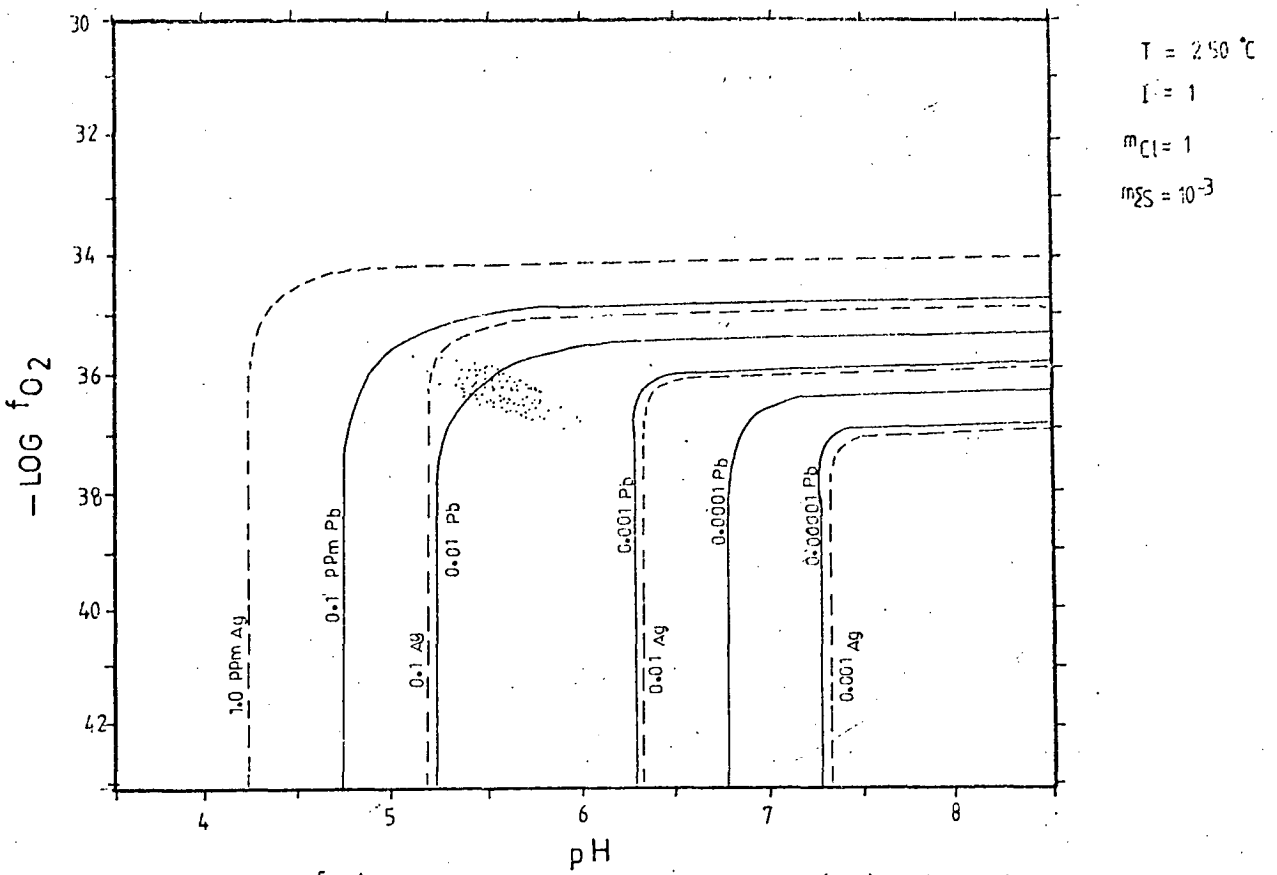

Fig. 10.12A Log f_{O_2}/pH diagram showing solubility contours (ppm) of Ag and Pb.
Note that argentite and galena are stable throughout the diagram.

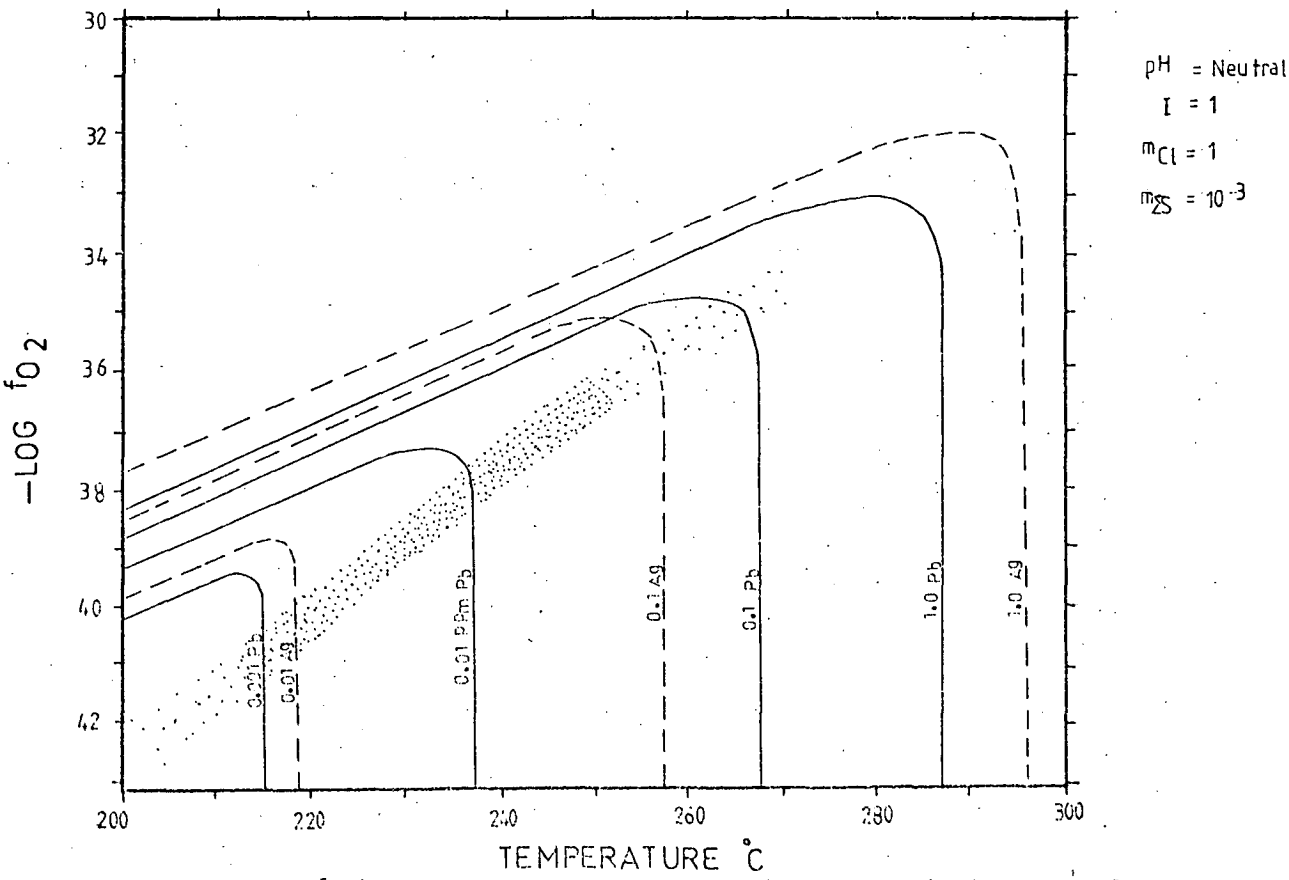

Fig. 10.12B Log f_{O_2}/temperature diagram showing solubility contours (ppm) of Ag and Pb.
Note that argentite and galena are stable throughout the diagram.

have suggested solubility of lead the same as zinc, it may well be that zinc solubility is too high. The relatively good agreement between solubilities by experiments at 80°C (Barrett, 1974 in Anderson, 1977) and Helgeson's constants for chloride complexes lends more credence to lead solubilities than given to zinc solubilities.

10.4.3 Silver

Complexing with chlorine (Helgeson, 1969; Seward, 1976) and sulphur (Anderson, 1962; Cloke, 1963) has been suggested as the mechanism for the transport of silver in the hydrothermal solutions.

Seward (1976) experimentally determined the solubility of silver chloride and suggested that it is controlled by $AgCl^{o}$ and $AgCl^{-}$ in near-neutral and acid environments at temperatures between 100 and 353°C. He compared the determined solubility with the silver concentrations in the Broadlands geothermal waters (pH = 6.1, a_{Cl^-} = .033, $m_{H_2S} = 4 \times 10^{-3}$, T = 260°C). The calculated silver solubility at these conditions was 0.25 ppb whereas the actual silver concentration in these waters was 0.6 to 0.7 ppb . He concluded that within the uncertainty inherent in the data used in the calculations, chlorosilver complexes probably account for much of the silver present. His calculations for Salton Sea brines show similar results.

Melentyev *et al.* (1969) measured the solubility of argentite in H_2S-saturated chloride solutions at temperatures between 100 and 180°C. They demonstrated that the solubility of argentite in acid solutions decreases with an increase in pH reaching a minimum at near-neutral pH. Then it remains constant for a range of pH, the length of which decreases as the temperature is increased. On further increase in pH, solubility increases with pH. Their experiments indicate the strong possibility that silver-sulphur complexes exist. Cloke (1963) suggested that in

alkaline conditions, silver solubility is primarily due to the complex $Ag(HS)S_4^{2-}$. Anderson (1962) summarised the solubility measurements on acanthite and suggested the complex $Ag_2S.nH_2S$ for pH up to 8 and $Ag_2S.nHS^-$ for the pH range above 8.

Until more data on silver-sulphur complexes is available, they can not be used to calculate the solubility of silver at hydrothermal temperatures. However, it seems likely that in near-neutral and alkaline solutions such complexes contribute significantly towards silver solubility.

Seward (1976) has suggested that complexes like $Ag(NH_3)_2^+$, $Ag(NH_3)_2Cl^o$, $AgHCO_3^o$ and the ion pair $NaAgCl_2^o$ may also contribute to silver solubility but no data is available on these complexes at elevated temperatures. Furthermore, silver-tellurium complexes also probably exist.

Silver concentrations are calculated assuming that either hessite or argentite is saturated (Figs. 10.11A, 10.11B, 10.12A and 10.12B). Several other silver-bearing phases are present in the assemblage (e.g. sylvanite, petzite, krennerite) but no thermodynamic data is available for these phases. Because of uncertainty in the thermodynamic data on the aqueous tellurium species even the silver concentrations obtained assuming hessite saturation (0.01 to 0.001 ppm, Figs. 10.11A and 10.11B) are doubtful. The nearest approximation to estimate the silver concentrations in the Emperor fluids is to assume argentite saturation. This suggests that the silver concentrations may have ranged from 0.1 to 0.01 ppm (Figs. 10.12A and 10.12B).

10.4.4 Iron

Although there have been a number of studies on the determination of iron solubility (see Crerar *et al.*, 1978 for a summary), the number of chemical variables required to define the system has not been controlled or determined. Two recent studies in which variables like f_{O_2}, pH, T etc. have been controlled are those of Crerar & Barnes (1976) and Crerar *et al.* (1978). Unfortunately these two studies gave contrasting iron solubilities under similar set of conditions. For example at pH = 4, T = 250°C, $m_{Cl} = 1$, $m_{\Sigma S} = 10^{-3}$, $f_{O_2} = 10^{-40}$ (pyrrhotite saturated), data given in Crerar *et al.* (1978) suggest iron concentrations of about 10^2 ppm while that given in Crerar & Barnes (1976) suggest iron concentrations of about 10^6 ppm. The earlier set measurements are probably in error, the most likely source of error being the graphite-CO_2 buffer used in the experiments (Crerar *et al.*, 1978).

In this study the equilibrium constants given in Crerar & Barnes (1976) are used to calculate the iron solubility in solutions saturated with magnetite, hematite, pyrite and pyrrhotite (Figs. 10.10A and 10.10B). It can be seen that in the Emperor fluids the iron concentrations may have ranged from 10^{-3} to 10 ppm. However, it must be emphasized that these values are probably too high by at least three orders-of-magnitude.

10.4.5 Copper

The solubility of copper has been calculated assuming chalcopyrite or bornite saturation. The complexes controlling the copper solubility are CuCl, $Cu(HS)_2^-$ and $Cu(HS)_2.2H_2S$ (Crerar & Barnes, 1976). In calculating the total copper solubility the sum of these complexes is used.

The uncertainty in the data on iron solubility (see above) also affects the values of copper solubility, and it is probable that the solubilities obtained from data given in Crerar & Barnes (1976) are too high. The concentrations of total copper are contoured on log f_{O_2}/pH and log f_{O_2}/T diagrams (Figs. 10.10A and 10.10B) and it can be seen that the copper concentrations in the Emperor fluids may have ranged from 0.1 to 0.01 ppm.

10.4.6 Gold

Complexing with Cl^-, HS^-, Te_2^{2-}, AsS_3^{3-} and SbS_2^{2-} has been proposed for the transport of gold in hydrothermal solutions. In a review paper, Krauskopf (1951) calculated the solubility of gold at 25°C from the thermodynamic data and found good agreement between calculated and experimental solubilities. He concluded that in acid solutions gold may be transported as $AuCl_4^-$ and in alkaline solutions as AuS^-. Helgeson & Garrels (1968) calculated the solubility of gold at elevated temperatures from thermodynamic data and found that the results compared well with geological predictions. They concluded that gold is carried in hydrothermal solutions primarily as chloride complexes.

The experimental data of Weissberg (1970) indicate that in near-neutral low-salinity solutions, the sulphide complex AuS^- is more than adequate to account for the gold concentrations observed in the present-day geothermal systems. Unfortunately Weissberg's experiments were not buffered with respect to f_{O_2}, f_{S_2}, f_{H_2} or pH and therefore cannot be used to calculate the equilibrium constants.

Henley (1973) investigated the solubility of gold in chloride solutions at temperatures between 300 and 500°C and at pressures of 1 to 2 kbars. The pH of the solutions was buffered by K-feldspar-quartz-sericite equilibria and f_{O_2} was buffered by magnetite-hematite equilibria. Henley (1973) suggested that the solubility of gold in his

experiments was due to a molecular species such as $Au_2Cl_6(HCl)_2(H_2O)_n$. Casadevall (1976) suggested that such a species implies a charge of +3 which is unlikely at the T, P, pH and f_{O_2} conditions. He suggested that the solubility of gold in Henley's experiments was due to the species $AuCl_2^-$ and gave the sollowing reaction for the formation of this complex:-

$$Au + 2Cl^- + \tfrac{1}{4}O_2 + H^+ = \tfrac{1}{2}H_2O + AuCl_2^- \qquad (39)$$

The equilibrium constants for this reaction have been calculated by Casadevall (1976) and are given in Appendix E.2. The solubility calculated using these constants is about four orders-of-magnitude greater than that calculated from the constants given in Helgeson (1969). In this study the constants used are those given by Casadevall (1976).

Seward (1973) investigated the solubility of gold in aqueous sulphide solutions at neutral pH (pH = 6 ± 3) in the presence of pyrite and pyrrhotite at temperatures of 160 to 300°C and pressure of 100 bars. He concluded that in neutral and near-neutral solutions, complex $Au(HS)_2^-$ is the dominant species, while $Au(HS)_2S^{2-}$ and $Au(HS)_2^o$ are important in alkaline and acid conditions respectively. He gave the equilibrium constants for the following reactions at temperatures from 175 to 250°C:

$$Au + 2H_2S_{(aq)} + HS^- = Au(HS)_2^- + \tfrac{1}{2}H_2 \qquad (40)$$

$$2Au + H_2S_{(aq)} + 2HS^- = Au_2(HS)_2S^{2-} + H_2 \qquad (41)$$

At pH between 5 and 8, the complex $Au(HS)^-$ is the dominating species. Using Seward's data, Casadevall (1976) calculated the equilibrium constant for the following reaction:

$$Au + 2H_2S_{(aq)} + \tfrac{1}{4}O_2 = Au(HS)_2^- + \tfrac{1}{2}H_2O + H^+ \; * \qquad (42)$$

---

* Note that the equilibrium constants for reaction 42 given in Casadevall (1976) and Casadevall & Ohmoto (1977) give $Au(HS)_2^-$ concentrations about four orders of magnitude higher than shown in their solubility diagrams.

Equations (39) and (42) have been used for calculation of the total gold solubility in those parts of the diagrams where native gold is saturated (Figs. 10.14 to 10.16). In the stability field of calaverite the following reaction can be added to these two equations

$$AuTe_2 = Au + Te_{2(g)} \quad (43)$$

to yield the equations:

$$AuTe_2 + 2Cl^- + \tfrac{1}{2}O_2 + H^+ = \tfrac{1}{2}H_2O + Te_{2(g)} + AuCl_2^- \quad (44)$$

$$AuTe_2 + 2H_2S_{(aq)} + \tfrac{1}{2}O_2 = \tfrac{1}{2}H_2O + Te_{2(g)} + Au(HS)_2^- + H^+ \quad (45)$$

As with lead and silver, the uncertainty in the thermodynamic data on aqueous tellurium species does not allow any rigorous discussion on the solubility of calaverite but some generalisations can be made.

The solubility of calaverite appears to be minimum (Figs. 10.13 and 10.14) at the likely f_{O_2} (say, near the magnetite-hematite buffer), pH (say between 4 and 6) and temperatures (below 250°C) range of most gold ore-forming fluids. The present data indicate gold concentrations as low as 0.0001 ppm within this range. It must be noted that reactions (43), (44) and (45) are not affected by the uncertainty in the thermodynamic data on the *aqueous* tellurium species and the topology of the gold solubility contours is strongly dependent on the shape of the f_{Te_2} contours (Fig. 10.7). Furthermore for calaverite and native tellurium saturation the f_{Te_2} should ne higher than $10^{-7.75}$ at 250°C (Fig. 10.2). For an assemblage containing calaverite and native tellurium with f_{O_2} buffered by magnetite-hematite equilibria, pH = 4 to 6, $m_{Cl} = 1$, gold concentration may be approximately between 0.001 and 0.00001 ppm at 250°C. Such low solubilities require some explanation. Complexing with tellurium is one possibility. Seward (1973) suggested that complexes like $Au(Te_2)_2^{3-}$, $AuTe_2^-$ and $AuTe_2^o$ probably exist. At present virtually nothing is known about gold-tellurium complexes and it is not possible to investigate this problem any further.

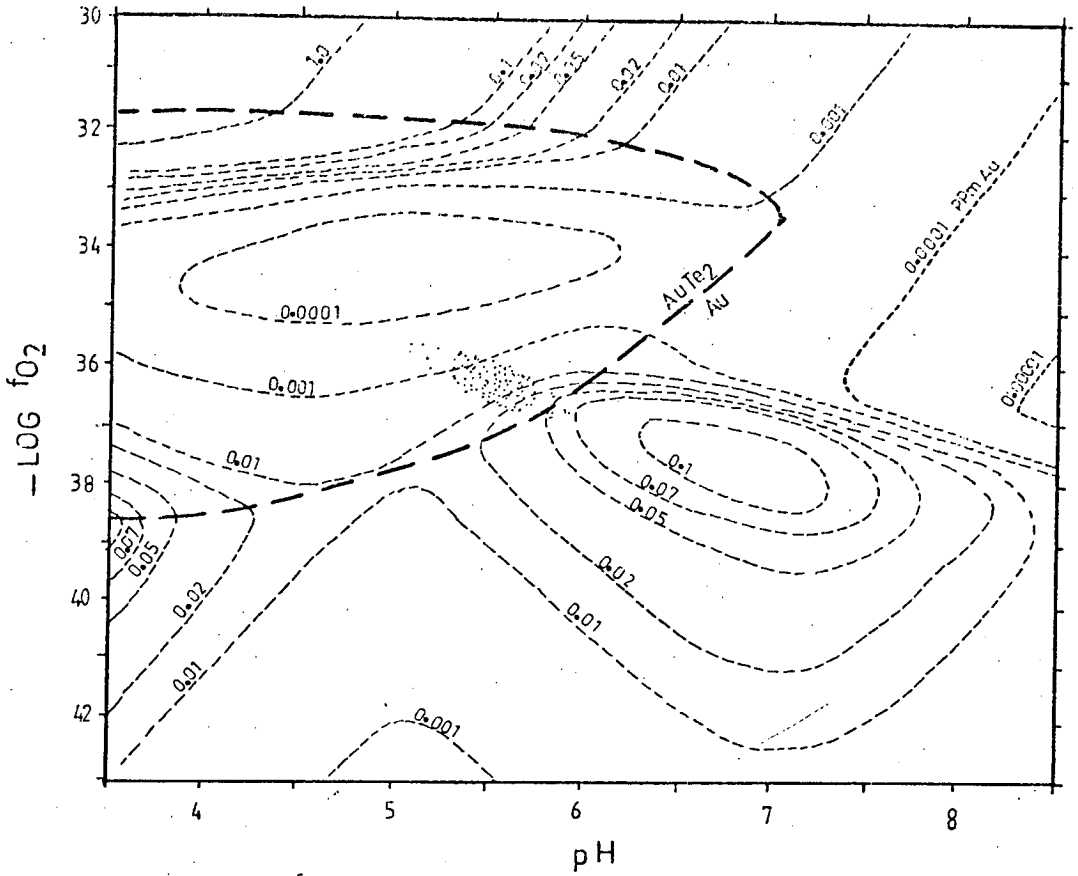

Fig. 10.13 Log f_{O_2}/pH diagram showing solubility contours (ppm) of Au. Note the solubility minimum in the area saturated with calaverite.

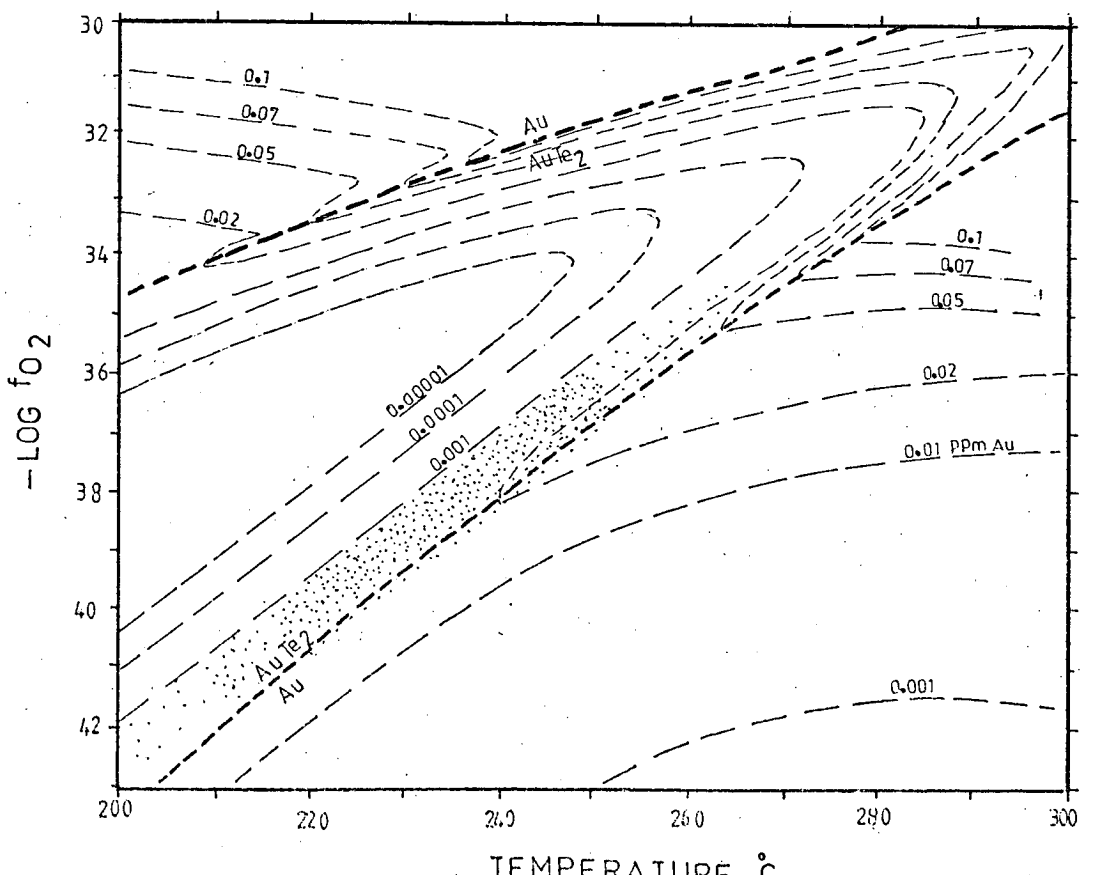

Fig. 10.14 Log f_{O_2}/temperature diagram showing solubility contours (ppm) of Au. Note the solubility minimum in the area saturated with calaverite.

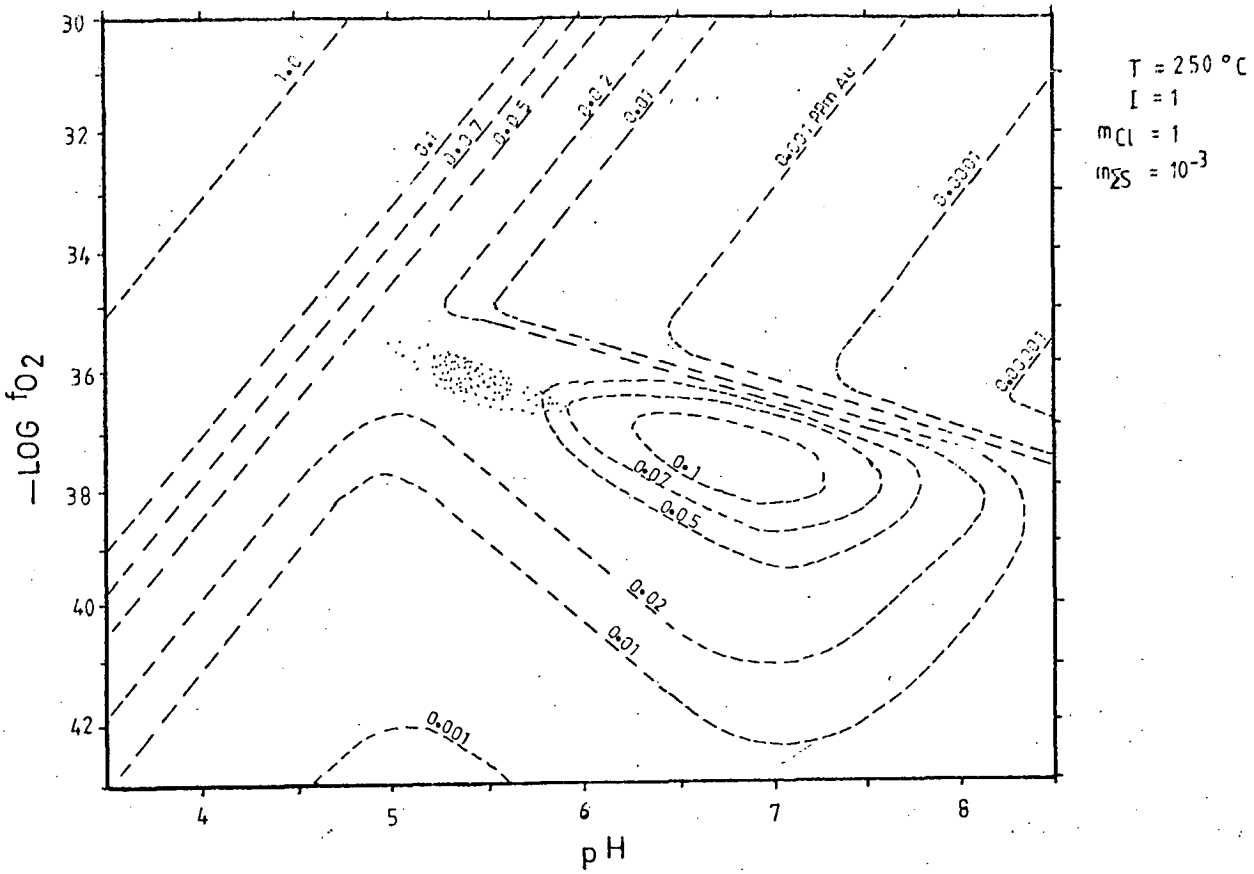

Fig. 10.15 Log f_{O_2}/pH diagram showing solubility contours (ppm) of Au. Note that native gold is saturated throughout the diagram.

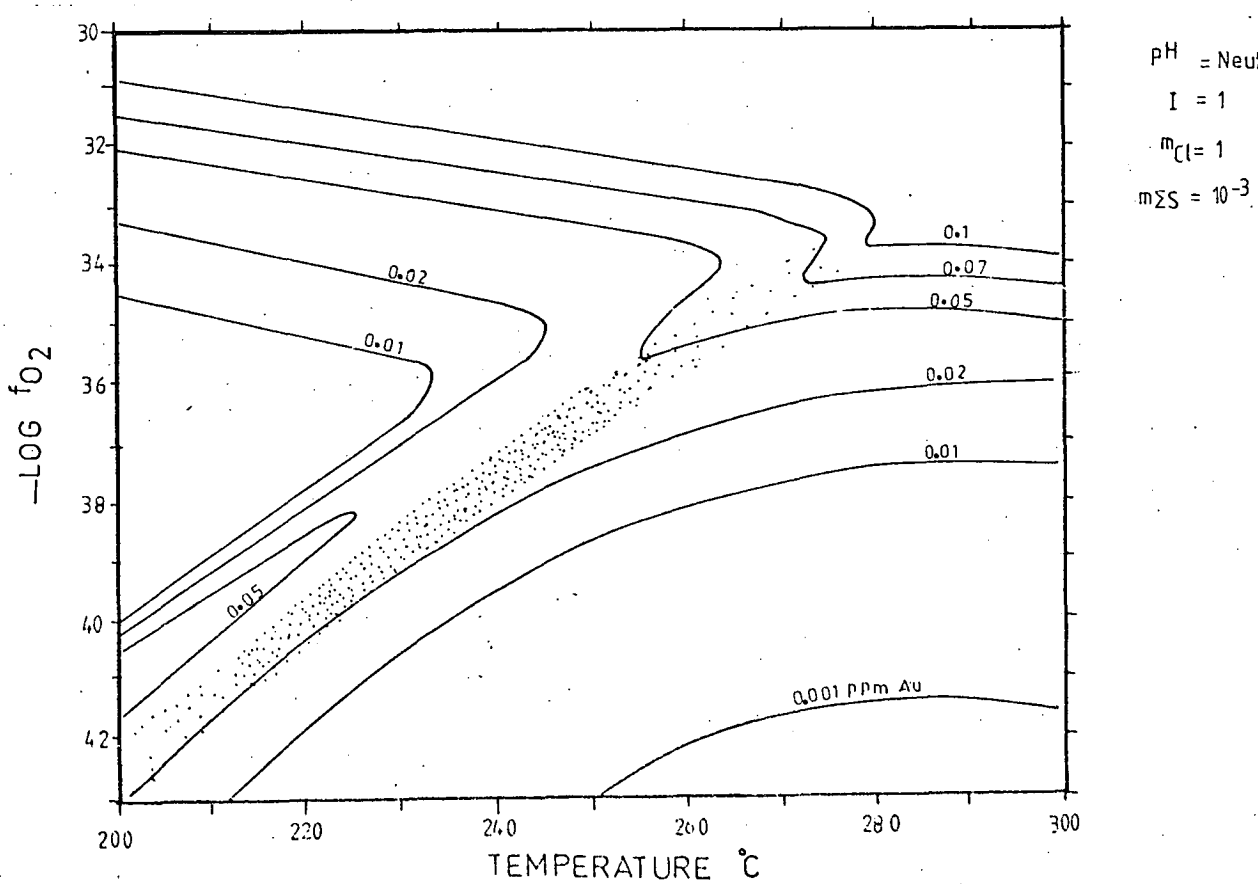

Fig. 10.16 Log f_{O_2}/temperature diagram showing solubility contours (ppm) of Au. Note that native gold is saturated throughout the diagram.

Pending further investigations there is no alternative to assuming native gold saturation. This assumption indicates that gold concentrations in the Emperor fluids may have ranged between 0.05 and 0.01 ppm (Figs. 10.15 and 10.16).

10.5 PROBABLE PHYSICO-CHEMICAL CHANGES IN THE ORE FLUIDS

In preparing phase and metal solubility diagrams a temperature = 250°C or pH = neutral and $m_{\Sigma S} = 10^{-3}$, $m_{\Sigma C} = 10^{-2}$, $m_{\Sigma Te} = 10^{-11}$, $m_{Cl} = 1$ and ionic strength = 1 has been assumed. In Chapter 7 it was shown that variations in temperature have occurred both temporally and spatially and that the solutions boiled locally. Loss of gases like H_2S, CO_2 and H_2Te is likely to result in an increase in the pH and a decrease in $m_{\Sigma S}$, $m_{\Sigma C}$, $m_{\Sigma Te}$ and metal solubilities. As a result of partitioning of H_2S into the vapour phase the oxidised to reduced sulphur ratio will increase. Loss of vapour due to boiling would cause a drop in temperature due to latent heat of vapourisation. Boiling will also result in an increase in the m_{Cl} and ionic strength and as a consequence the metal solubilities may slightly increase but the drop in metal solubilities due to other factors (like decrease in temperature and in $m_{\Sigma S}$ and increase in pH) is likely to be overwhelming. Boiling should also result in an increase in the $\delta^{18}O$ and a decrease in δD of the fluids but calculations given in Kamilli & Ohmoto (1977) indicate that these changes are negligible even if 50% of the fluid has vapourised.

Ideally one needs a mass transfer programme to work out various changes induced by boiling. A. Bush & J.L. Walshe (pers. comm., 1979) have recently formulated such a programme and although some minor details are to be worked out, their preliminary results show that 10% boiling

(of solutions having 10^{-2} molal ΣS, 10^{-1} molal ΣC, pH = 4.7, T = 250°C and $f_{O_2} = 10^{-35}$) will lower the temperature by about 50°C, increase the pH by about 1 unit and drop the f_{O_2} to about 10^{-40}.

It is suggested that a drop in temperature is probably the most significant cause of metal precipitation. Inspection of the log f_{O_2}/T diagrams at constant pH (Figs. 10.8B, 10.9A & B, 10.10B, 10.11B, 10.12B, 10.14 and 10.16) suggests that fall in temperature accounts for most of the mineralogical changes. The only unexplained events are (a) the intermittent precipitation of dolomite and ore minerals and (b) stabilisation of native gold during stage IIIB. The first effect may reflect periods of increased pH due to boiling and the second an increase in pH and/or a drop in $m_{\Sigma Te}$ due to boiling.

Chapter 11

THE EMPEROR CONVECTION SYSTEM

11.1 GENERAL

The injection of magma beneath the Tavua cauldron may have introduced an aqueous phase to the local rocks and almost certainly caused buoyancy-driven circulation of the fluids contained in the rock column. The sub-surface structure at that time was probably not unlike that envisaged for porphyry-copper and massive-sulphide deposits and the flow patterns associated with these systems have been studied (Norton & Knight, 1977; Cathles, 1977, 1978; Parmentier & Spooner, 1978). In this chapter the results of these and other studies have been adopted in a qualitative manner to the Emperor situation.

11.2 THE SUB-SURFACE STRUCTURE OF THE TAVUA CAULDRON

At some distance from the caldera, marine carbonate-bearing greywackes, siltstones, sandstones etc. may be seen underlying the Mba volcanics. The latter are about 2 km thick near the Emperor mine and are presumably underlain by similar sediments (i.e. the Vatukoro formation or one or more of the Mio-Pliocene sedimentary groups). They are probably no more than 1500 m thick. The carbon isotope data (Chapter 9, Section 9.2.3) indicate that the carbon of the Emperor fluids, stages I to III, is probably derived from the carbonate of these sediments.

The sedimentary rocks are probably underlain by the volcanics and interbedded sediments of the Wainimala Group, which is the oldest group of rocks exposed in Viti Levu.

The rock pile underlying the Emperor mine is therefore essentially volcanic with a small thickness of sedimentary rocks sandwiched between the volcanics (Fig. 11.1).

It is assumed that a pluton lay at some distance beneath the caldera with its top at least deeper than the base of the carbonate-bearing sediments i.e. at least 3500 m below surface. This seems to be a likely depth beneath a volcano (Macdonald, 1972; Steinberg & Rivoch, 1965). It is also assumed that the width of the pluton is comparable to the width of the cauldron (see also Denholm, 1967b), i.e. about 5 km (Fig. 11.1). By analogy with high-level plutons observed in the Andes (Pitcher, 1978) it is likely that the pluton has a flat top and steep sides. Though the temperature of the magma could vary between 725 and 1200°C (Macdonald, 1972) a figure of 920°C is taken to facilitate direct comparisons with the flow paths plotted by Norton & Knight (1977).

11.3 QUALITATIVE RECONSTRUCTION OF THE EMPEROR FLUID SYSTEM

The Emperor system is comparable to the situations envisaged in model P4 and P5 of Norton & Knight (1977). Basalt permeability ranges from 10^{-8} to 10^{-12} cm^2 (Norton & Knapp, 1977) and a permeability of 10^{-11} cm^2 is taken for the Mba volcanics. The permeability of the rocks belonging to the Wainimala Group could be less than the Mba volcanics as these rocks are generally metamorphosed. Data given in Norton & Knapp (1977) shows that the permeability of greenschist facies rocks ranges between 10^{-11} and 10^{-15} cm^2 and that of metabasalt is 2×10^{-8} cm^2. The permeability of the rocks belonging to the sedimentary groups in the Tavua succession may be slightly higher than the Mba volcanics as these sediments are generally coarse grained sandstones and conglomerates.

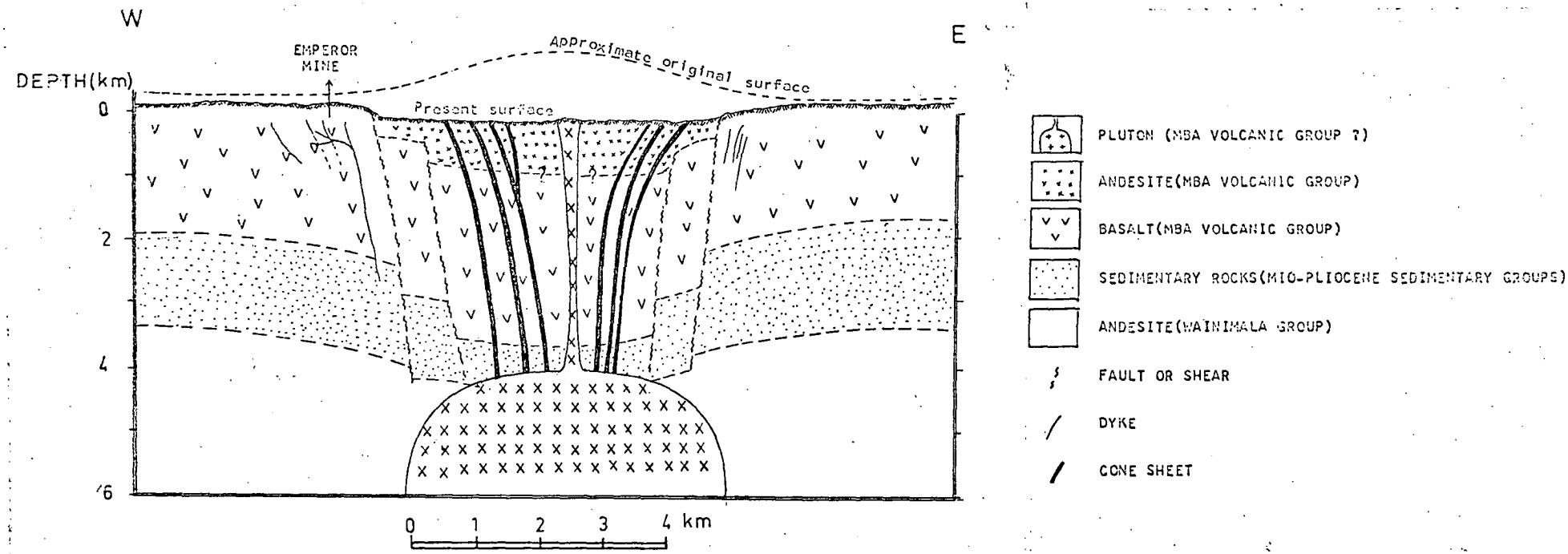

Fig. 11.1 Postulated section through the Tavua cauldron. Note that cauldron subsidence is probably post stage II mineralization, see text.

For the purpose of the present study it is convenient and reasonable to use values similar to those of models P4 and P5 (Norton & Knight, 1977) i.e. Mba basalt: 10^{-11} cm^2, sediments: 10^{-10} cm^2 and Wainimala rocks: 10^{-12} cm^2 (Fig. 11.2).

The dominant rocks exposed within the limits of the Tavua caldera are rather loosely welded tuff and breccia. The permeability of these rocks can be taken as very nearly equal to that of the sedimentary rocks, i.e. 10^{-10} cm^2. Evidence given in Chapter 4 (Section 4.7) and Chapter 5 (Section 5.4) indicates that these rocks were probably deposited later than the mineralization at the Emperor mine and are probably not pertinent to this discussion.

Numerous steep fractures surrounding the cauldron must considerably increase the permeability locally and the Emperor vein system probably represents a narrow zone of very high permeability.

The adoption of models P4 and P5 (Norton & Knight, 1972) is shown in Fig. 11.3. The principal distinction is due to the highly permeable fracture zone and it has been assumed that a much higher permeability prevailed in the Emperor region, concentrating the flow in a few fractures. The pattern of flow envisaged is supported by experimental data. Elder (1966, 1967a, b, 1968) has shown from both linear theory and experiment that at low Rayleigh numbers, and a heater-width/depth (W/D) ratio less than 2, there is only one buoyant plume centred over the heater (see for example Fig. 11.4). At a W/D value greater than 2, small cells (Rayleigh cells) develop over the heater and this has been confirmed by the three-dimensional experiments of Combarnous & Bories (1975). M. Solomon and J.L. Walshe (pers. comm., 1979), using Hele-Shaw cells, have been able to show that at the Rayleigh numbers probably prevailing in natural systems (>3000), the single central plume is the stable mode at W/D values up to 4.

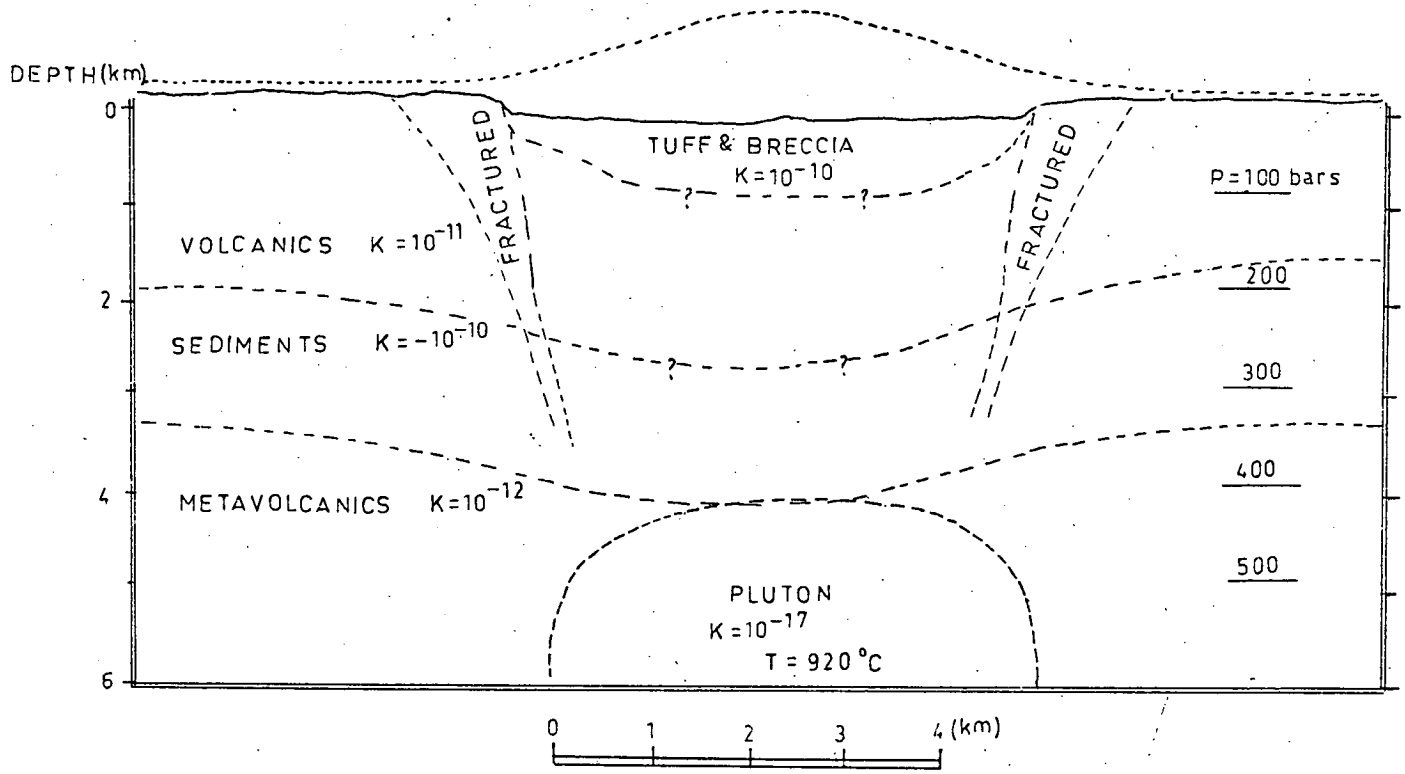

Fig. 11.2 Cross section through the Tavua cauldron showing postulated rock permeabilities (K), temperature(T) and hydrostatic pressures(P).

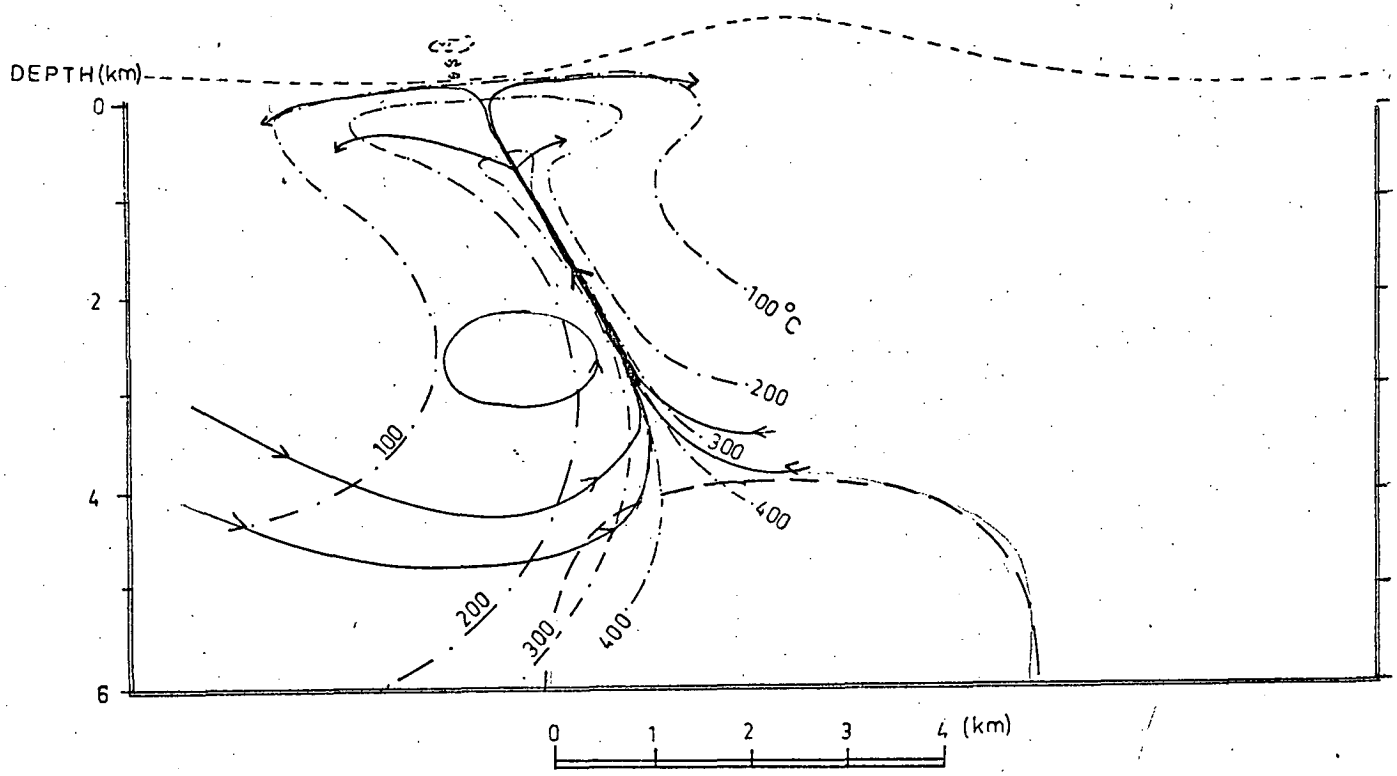

Fig. 11.3 Fluid convection model at the Emperor mine. Broken lines: isotherms °C; solid lines: fluid circulation paths.

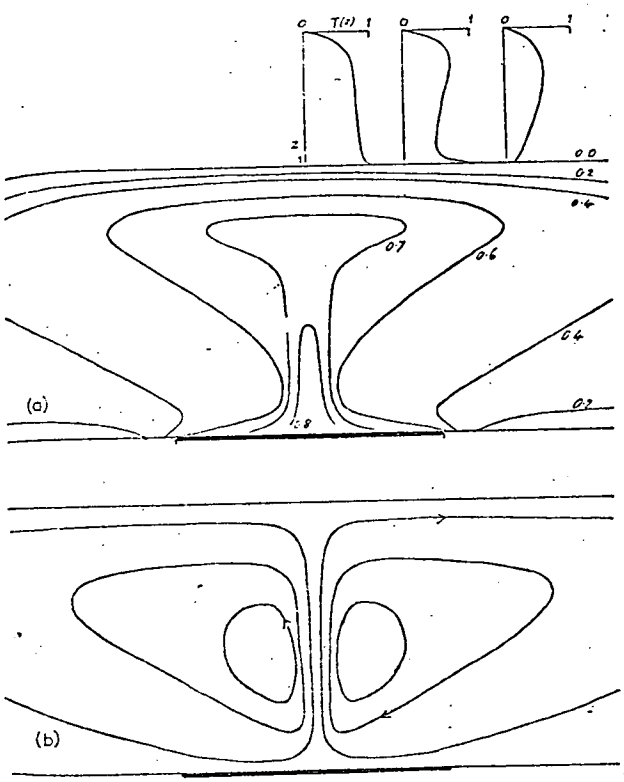

Fig. 11.4 Two-dimensional temperature, velocity distribution for free convection in a porous medium, Rayleigh number=1000:(a) isotherms and temperature distribution with depth;(b) streamlines. Heavy line indicates the width of the heater, after Elder(1966, Fig.8).

The fluid isotherms sketched in Fig. 11.3 are different from those obtained by Norton & Knight (1977). These workers have assumed that rock temperatures everywhere are the same as the fluid temperatures. This assumption may be true for the fluids flowing through the pore spaces, but fluids flowing through open channels may have considerably higher temperatures, than the enclosing rocks. The flow of hot water, even at present times, through some of these fractures in the Emperor mine workings (and also in many other Tertiary epithermal deposits) testify to the fact that in many cases fluids may have higher temperatures than the host rocks. The result is a marked concentration of isotherms in the fracture zone and relatively high temperatures close to the surface. Natural surfaces tend to be relatively impermeable and though springs may well have allowed fluid to escape, a considerable fraction was probably returned to the convection cell.

As discussed in Chapter 9, the carbon isotope data indicate that the source of carbon in the Emperor mine ore-fluids changed markedly with time. The early carbonates (stages I to III) indicate a sedimentary source while the late carbonates (stage V) indicate an igneous parentage. This evidence suggests that either the late-stage convection system somehow excluded the sedimentary rock from the convection cell or the sedimentary carbon was exhausted during the initial stages. Looking at the data given in Norton & Knight (1977) and Cathles (1977, 1978) it appears that the pattern of fluid circulation in the domain shown in Fig. 11.2 would probably not change significantly even 160,000 years after the intrusion. Also, M. Solomon and J.L. Walshe (pers. comm., 1978) have noted pronounced hysteresis effects during cooling of Hele-Shaw cells, and the cell system established at the peak of the heating tends to persist until flow ceases even though the heater is only just maintaining a temperature difference across the system.

If the depth of the pluton shown in Fig. 11.2 somehow decreased by about 2 km, it would be possible to exclude the sedimentary rocks from the convection cell. As discussed in Chapter 4, the age determinations on igneous rocks from the Tavua area indicate two major periods of igneous activity, separated by a period of relative quiescence of about 2.5 m.y. The telluride mineralization probably coincided with the first period of igneous activity (Chapter 5). It is possible that after the main convection system died down, the subsequent period of intrusion of dykes and plugs was accompanied by a rise in height of the magma chamber. The water circulating during this phase would leach carbon solely from the igneous rocks and deposit it as stage V calcite. It is also possible that the stage V carbon is of direct magmatic parentage, i.e. exsolved from igneous intrusions. Some indications of such a renewed igneous activity can be sought in the oxygen and hydrogen isotope data. The $\delta^{18}O_{H_2O}$(calculated) values during stage IVC show a slight reversal in the general trend of depletion through time (Fig. 9.3) and the δD values of fluid inclusion water from stage V calcite are identical to magmatic waters (Fig. 9.9).

The nature of gold occurrences *within* the Tavua caldera (Fig. 4.2) can now be discussed. As these prospects are located in the rocks belonging to the second period of igneous activity, they are probably younger than the bulk of the mineralization at the Emperor mine. It is suggested that these occurrences are probably formed from the relatively shallow circulation which may have developed in the tuffaceous sediments as a consequence of relatively high-level magma intrusion.

The minor gold occurrences in the volcanic rocks along the southeastern and northwestern periphery of the Tavua caldera (Fig. 4.2) may have formed from minor circulation at the time of the main Emperor mineralization.

11.4 TONNAGE AND SOLUBILITY CONSTRAINTS

Amongst the various causes of ore-mineral precipitation a drop in temperature is probably the most significant (Chapter 10, section 10.5). The fluid-inclusion temperatures on stage IIA and IIIA quartz range from 170 to 317°C (Table 7.1) with modes at 235 and 215°C respectively (Fig. 7.1). It can probably be assumed that the bulk of metal precipitation occurred between 250 and 200°C (neglecting a few inclusions which gave temperatures outside this range). It can be seen from metal-solubility diagrams (Figs. 10.10, 10.12, 10.15 and 10.16) that cooling from 250 to 200°C may cause the following changes in metal concentration in solutions saturated with native gold, sphalerite, galena, argentite and chalcopyrite (because of uncertainty in the data on the aqueous tellurium species, metal tellurides are not considered):

(a) Gold concentration will drop from about 0.05 to 0.01 ppm

(b) Zinc concentration will drop from about 10 to 1 ppm

(c) Lead concentration will drop from about 0.1 to 0.01 ppm

(d) Silver concentration will drop from about 0.1 to 0.01 ppm

(e) Copper concentration will drop from about 0.1 to 0.01 ppm.

The tonnage and grades of precious and base-metals at the Emperor mine are given in Table 11.1. The total amount of water required to precipitate $10^{2.18}$ tons of gold (a solubility drop from 0.05 to 0.01 ppm) will be about $10^{15.58}$ g or about 3.8 km^3. At the solubility changes given above, this water will also deposit $10^{4.58}$ tons Zn, and $10^{2.28}$ tons of Pb, Ag and Cu each. The values for copper and lead are about an order of magnitude lower than the estimated tonnage (Table 11.1) and those for zinc and silver are about half an order of magnitude higher. Considering the various assumptions and uncertainties involved (e.g. pH, T, $m_{\Sigma S}$, m_{Cl}, extrapolation and uncertainty of the thermodynamic and experimental data, etc.) there appears to be an overall agreement with the actual and estimated tonnage.

Table 11.1

Tonnage and grade of precious and base metals at the Emperor mine.

Metal	Total tonnage (tons)	Average grade (gm/ton)	Total metal (tons)	Source of data
Au	$10^{7.3}$	7.75	$10^{2.18}$	Average grade calculated from Blatchford (1953) and tonnage from probable total reserves of gold (mined and present).
Ag	$10^{7.3}$	3.1	$10^{1.79}$	Average grade calculated from Blatchford (1953).
Cu	$10^{7.3}$	$10^{2.27}$	$10^{3.57}$	Average grade from analyses given in Appendix C.3.
Zn	$10^{7.3}$	$10^{2.71}$	$10^{4.01}$	Average grade from analyses given in Appendix C.3.
Pb	$10^{7.3}$	$10^{1.98}$	$10^{3.28}$	Average grade from analyses given in Appendix C.3.

Table 11.2

Average diameter of pyrite grains on the growth zones (in quartz crystals) or between quartz crystals.

Specimen number	Diameter range (cm)	Number of observations	Average diameter (cm)
103298	0.003 to 0.01	53	0.006
103312	0.003 to 0.015	15	0.009
103329	0.003 to 0.015	18	0.006
103340	0.003 to 0.015	8	0.006
103343	0.003 to 0.017	88	0.008

Assuming that the average gold concentration of basalt may be about 5 ppb (Chapter 3) and about 10% of this is available for leaching, then about 10 km^3 rock is required to be leached to produce a deposit of the size of the Emperor mine. This would be equivalent to a block size of 2.5 km x 2 km x 2 km. Thus there is no problem regarding the supply of gold to the ore-fluids.

11.5 FLUID VELOCITY

Very few studies are available concerning the fluid velocities in hydrothermal vein systems. Roedder (1960) calculated fluid velocities between 0.0001 and 0.01 cm/sec using reasonable assumptions regarding change in metal concentration and likely time required to form an ore body containing 10^8 tons of 1% ore. Barton *et al.* (1971) calculated flow rates for the OH vein, Colorado, between 0.2 and 1 cm/sec, based on the settling properites of hematite needles.

It was suggested (Chapter 6, section 6.3.1) that sulphide and telluride grains have probably settled on the growth zones of vein quartz crystals under the influence of gravity from solutions which were moving upward. Size determinations on 182 pyrite grains, situated either on the growth zones in vein quartz or in between quartz crystals are given in Table 11.2, and the frequency distribution is shown in Fig. 11.5. The majority of pyrite grains occur as euhedral crystals with square, hexagonal, triangular or rectangular sections (Plates 11.1 to 11.4) and measurements consisted of determining by inspection an average diameter. If it is assumed that these grains are nearly spherical, the velocity of current required to transport them (as suspended particles) can be approximated from the Stokes law:

$$V = \frac{2ga\ (\ell 1 - \ell 2)}{9\eta}$$

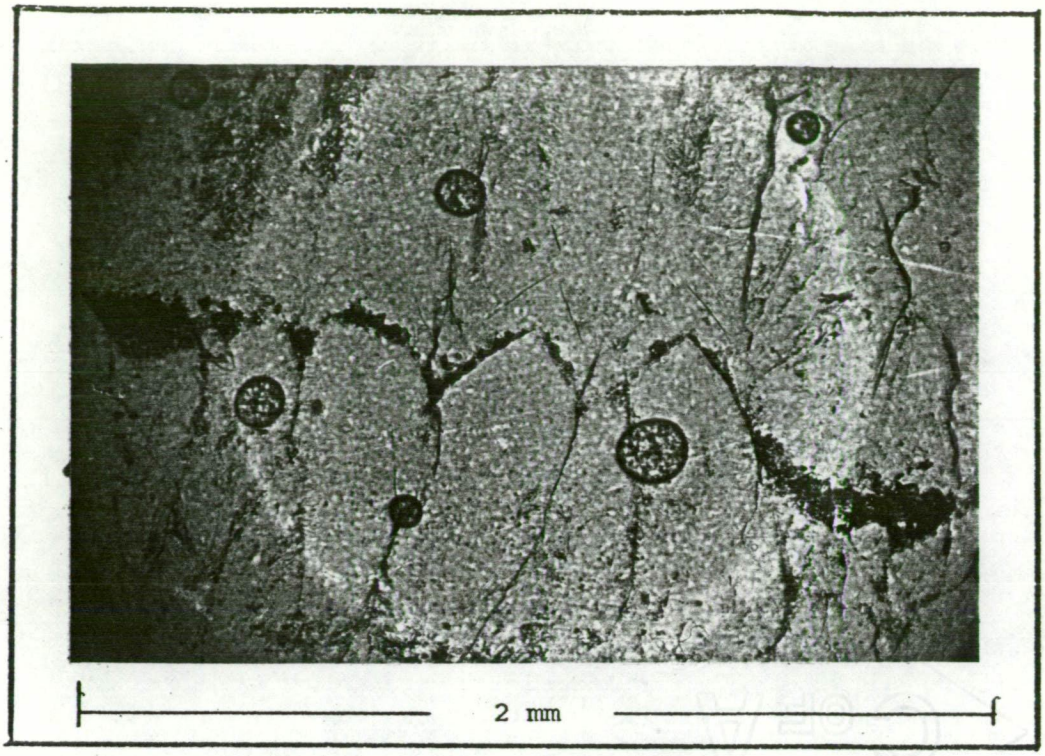

Plate 11.1 Photomicrograph showing carbonate-sulphide-telluride grains along a growth zone in vein quartz. Rounded areas are air bubbles formed during the preparation of the thin section. Sample 103292, 166 flatmake, 9 level.

Plate 11.2 Photomicrograph showing grains of pyrite along growth zones in vein quartz. This sample suggests a bimodal size distribution. It is suggested that larger particles represent periods of boiling and smaller, periods of relatively stable conditions. Sample 103292, 166 flatmake, 9 level.

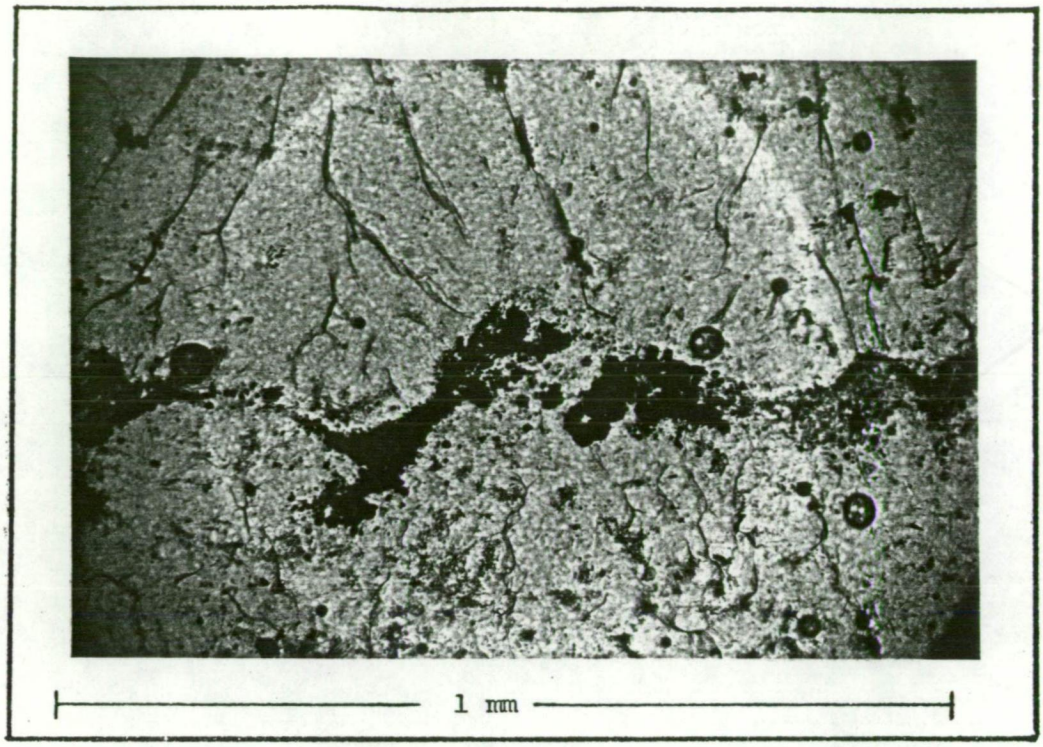

Plate 11.3 Photomicrograph showing grains of pyrite along growth zones in vein quartz. Sample 103298, 166 flatmake, 7 level.

Plate 11.4 Photomicrograph showing grains of pyrite along a growth zone in vein quartz. Note hexagonal, square or triangular outlines of pyrite grains. Sample 103298, 166 flatmake, 7 level.

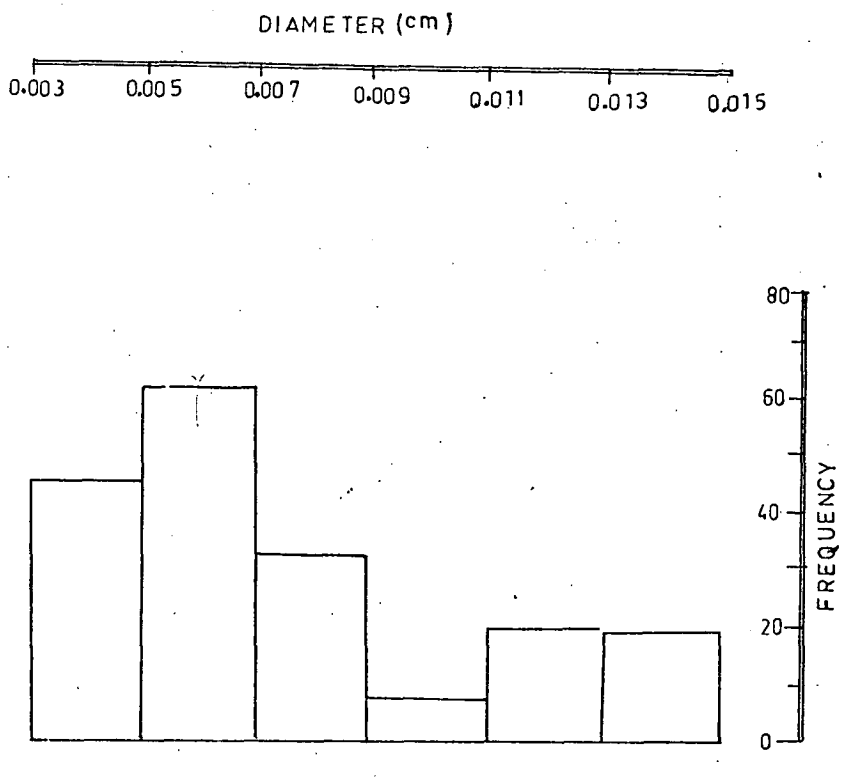

Fig.11.5 Frequency histogram of the diameters of pyrite grains along growth zones in vein quartz or in between quartz crystals.

where $\ell 1$ = density of pyrite = 5.02 gm/cm^3

$\ell 2$ = density of fluid = 0.84 gm/cm^3 (density of 5% NaCl solution at 250^{o}C, Haas, 1971)

a = radius of pyrite grain

g = acceleration due to gravity = 981 cm/sec^2

η = viscosity = 0.0011 poises at 250^{o}C (Mayinger & Grigull Barton *et al.*, 1971)

Using the modal diameter of the pyrite grains (0.006 cm) a velocity of 4 cm/sec is obtained. Calculations using the maximum and minimum diameter gave velocities of 24 cm/sec and 1 cm/sec respectively. The larger particles may have grown in size after settling, alternatively they may represent periods of local turbulance probably caused by boiling of fluids. It is suggested that the value obtained from the modal grain size is probably more representative and that the velocity of 4 cm/sec is an order-of-magnitude indication of the fluid velocity.

Amongst the various lodes mined at the Emperor mine only one, namely the Crown lode, extends down to 16 level. The other lodes are mineralized only in the upper levels. It is suggested that this fracture (i.e. the Crown lode) has probably acted as the main feeder channel. The horizontal extent of this lode is about 350 m and the average width is about 1 m. Water probably flowed freely through say 1% of this width at any one time. Assuming that all the water ($10^{15.58}$ gm, see above) passed through this channel at about 4 cm/sec, it will require say 10^3 years to form a deposit of the size of the Emperor mine.

11.6 APPLICATION TO GOLD EXPLORATION

The fluid circulation model for the Emperor system has important implications for the exploration geologist in Fiji. As suggested earlier in this chapter, the gold occurrences within the Tavua caldera are probably formed by shallow convection cells generated as a result of intrusion of small plugs and dykes during the second period of igneous activity. These occurrences are therefore unlikely to produce any significant tonnage. The main stage mineralization must have been a single plume type of system concentrated on the Emperor mine and there is little chance of there having been a coeval second plume. It is possible that the plume moved to another situation after clogging of the Emperor system but experimental data of Elder (1967b) and M. Solomon & J.L. Walshe (pers. comm., 1979) indicate that the established system is likely to remain stable throughout its history. The minor occurrences of gold around the caldera rim are therefore not alternative targets for further investigation.

Extensions of the Emperor mineralization.

It seems unlikely in the terrestrial situation of the Emperor mine that more than a small fraction of the plume fluid is discharged at the surface. The fluid is largely returned to the cell to give a mushroom shape to the circulation (Fig. 11.4). If this pattern was set up in the Emperor case (and there is no evidence for or against this suggestion) then the major mineralization (up to stage IIB, Chapter 7) may have spread eastward. If so, it was probably downfaulted by the movements on the caldera margin and should exist beneath the late stage igneous rocks to the east of the cauldron wall.

Mineralization in other volcanic centres.

Mba volcanic eruptions took place at a number of centres. Four main centres are known and several minor vents recognised (Rodda, 1967). The geology and structure of these volcanic centres (other than the Tavua cauldron) is rather imperfectly known. If the understanding of the nature of the Emperor mineralization is taken as an example, these volcanic centres may provide useful targets for future gold exploration in Viti Levu.

Chapter 12

THE GENESIS OF THE EMPEROR MINERALIZATION - A SUMMARY

12.1 GENERAL

The data presented in this study put several constraints on the origin of mineralization at the Emperor mine. Important aspects that must be considered are:

(a) Regional geology: The Mba basalt, host rock for the lodes, is approximately 2000 m thick and is probably underlain by calcareous sediments approximately 1500 m thick. These sediments in turn are probably underlain by early Tertiary andesitic rocks of the Wainimala Group.

(b) Mine geology: The mine is located at the periphery of a Pliocene cauldron in which five phases of igneous activity have been recognised. The igneous activity started with widespread eruptions of alkali olivine basalt and terminated with intrusions of minor plugs and dykes of monzonite and trachyte. Apparently, there were two major periods of cauldron activity, the first accompanying phase I volcanism and the second accompanying phase III volcanism. The present caldera boundary was probably formed during the second period. K/Ar dates indicate two major periods of igneous activity, the first period commencing at about 10 m.y. and terminating at about 7.5 m.y. The Te^{130}-Xe^{130} dating on a telluride sample gave an age of about 7.2 m.y., indicating that the bulk of the mineralization was probably related to the first period of igneous activity.

(c) Lode characteristics: The Emperor lodes are essentially fracture fillings with well developed crustification textures and vughs. Ore-mineral and carbonate precipitation appears to have been

intermittent, whereas quartz precipitation was essentially uninterrupted and continued even after the cessation of ore-mineral precipitation. The mineralized veins are fringed by a narrow zone of K-silicate alteration beyond which is a zone of fairly widespread propylitic alteration. The propylitic rocks are depleted in silica while the K-silicate rocks show extensive enrichment.

(d) Ore-mineral distribution: The bulk of the mineralization (stage IIB tellurides) is restricted to 12 level and above, while stage IIIB tellurides are distributed throughout. All steep lodes except the Crown lode are mineralized only above their intersection with the Prince-Dolphin flatmake.

(e) Temperature: Temperatures of fluid inclusions in stage IIA and IIIA quartz (i.e. the stages adjacent to the mineralized stages) range from 170° to 317°C with modes near 215° and 235°C respectively. The temperatures of later barren quartz (stage IV) are generally less than 200°C with the mode at 185°C.

(f) Salinity: Salinity of the ore-fluids ranges from 4 to 7 wt.% eq. NaCl and averages about 5.5 wt.% eq. NaCl. There are no apparent indications of either temporal or spatial variations in salinity.

(g) Boiling: Fluid-inclusion evidence indicates that in most of the lodes the fluids were on the boiling curve. There are indications that major boiling during stage IIA occurred between 11 and 14 level, while during stage IIIA the lower limit of boiling dropped by about 100 m in the area near the Crown lode.

(h) Source of carbon: Carbon-isotope values for early carbonates (dolomite and/or ankerite - stages I to III) indicates a sedimentary parentage while those for late calcite (stage V) indicate an igneous parentage.

(i) Source of sulphur: Sulphur-isotope data is compatible with an igneous source,

(j) Source of water: Oxygen- and hydrogen-isotope data indicate that the water could have been derived from a meteoric source, however a magmatic source cannot be disproved and possibly some sedimentary formation waters were also involved.

12.2 THE SYSTEM AT DEPTH

The probable sequence of events is summarised in Table 12.1 and some salient features are discussed below.

The cauldron structure probably developed over a pluton emplaced during the first period of igneous activity (10 to 7.5 m.y.). The resultant concentric fracturing was probably important in establishing convective flow of ground water resulting from magmatic heating (see Fig. 11.3). The geometry of the cauldron almost certainly requires a single plume discharge of hot fluid. Fluid temperatures immediately adjacent to the pluton were probably initially equal to, or greater than, 300-350^{o}C and gradually declined through the life of the system.

It is postulated that the bulk of ground water drawn into the discharge zone must have passed through the calcareous sediments. In so doing they acquired carbon of $\delta^{13}C \approx 0‰$ and became enriched in ^{18}O. Near the pluton it is likely that secondary silicates formed as the result of reactions like the following:

$$3CaMg(CO_3)_2 + 4SiO_2 + H_2O = Mg_3Si_4O_{10}(OH)_2 + 3CaCO_3 + 3CO_2 \quad (1)$$

dolomite quartz talc calcite

$$2Mg_3Si_4O_{10}(OH)_2 + 3CaCO_3 = Ca_2Mg_5Si_8O_{22}(OH)_2 + CaMg(CO_3)_2 + H_2O + CO_2 \quad (2)$$

talc calcite tremolite dolomite

Table 12.1

Suggested sequence of events.

	Events	Igneous Activity	Volcanic Phases	Cauldron Activity	Source of Carbon	Source of Water	Paragenetic Stages	Temperature (°C)	Gangue Minerals	Ore Minerals
				Period 1						
1.	Volcanism and pluton emplacement.									
2.	Fracturing.									
3.	Establishment of convection system.									
4.	Propylitization.	Period 1 (10 - 7.5 m.y.)	Phase I				IA	>350?	Ankerite, chlorite dolomite etc.	
5.	K-silicate alteration and mineralization.			Period 2	Sedimentary	Meteoric	IB, IIA & IIB	200-300	Quartz, sericite, K-feldspar, dolomite etc.	About 90% of the total, mainly native tellurium & gold-rich tellurides.
6.	Formation of present caldera, mineralization continues.						IIIA & IIIB	200-250		About 10% of the total mainly native gold & silver-rich tellurides.
7.	Cessation of ore mineral deposition, barren quartz precipitation continues.						IVA, IVB & IVC	<200	Mainly barren quartz	
8.	Intrusion of cone sheets and minor plugs and dykes, limited effusive activity.	Period 2 (5 - 4.3 m.y.)	Phases II-V		Igneous?	Igneous?				
9.	Establishment of shallow convection cells and barren calcite deposition.						V	<150?	Mainly calcite	

TIME

$$5CaMg(CO_3)_2 + 8SiO_2 + H_2O = Ca_2Mg_5Si_8O_{22}(OH)_2 + 3CaCO_3 + 7CO_2 \quad (3)$$

dolomite quartz tremolite calcite

$$Ca_2Mg_5Si_8O_{22}(OH)_2 + 3CaCO_3 + 2SiO_2 = 5CaMgSi_2O_6 + 3CO_2 + H_2O \quad (4)$$

tremolite calcite quartz diopside

$$CaCO_3 + SiO_2 = CaSiO_3 + CO_2 \quad (5)$$

calcite quartz wollastonite

At $p_{H_2O} = p_{CO_2} = 1$ bar, the equilibrium temperatures of reactions (1), (2), (3), (4) and (5) are 170, 180, 230, 260 and 270°C respectively, and increase sharply with increase in p_{CO_2} (Turner, 1968). Such reactions may cause the solutions to become undersaturated in silica and enriched in CO_2. From this situation the solutions probably travelled relatively rapidly in highly permeable zones of fracturing and thus may have undergone only minor chemical modification by reaction with wall rocks. As they approached the zone of boiling and spread laterally through the host basalt they leached silica and precipitated carbonates in a widespread propylitic halo. As the solutions at depth cooled they became less and less undersaturated with respect to silica and developed lower concentrations of CO_2, changes that may have heralded the initiation of K-silicate alteration at higher levels.

The pH of the system in depth would be controlled by carbonate solution, e.g.

$$CaCO_3 + 2H^+ = H_2CO_{3(ap)} + Ca^{2+} \quad (6)$$

$$\log K_{350^oC} = 5.76 \text{ (calculated from reactions given in Naumov } et\ al.\text{, 1974)}$$

For a temperature of say 350°C and using conditions inferred for the environment of deposition (Chapter 10), it can be inferred that the pH was between 5 and 6.

It can probably be assumed that the f_{O_2} of the solutions in equilibrium with a rock pile which is mainly basaltic in composition will be between quartz-magnetite-fayalite and the magnetite-hematite buffer.

Experimental data (Ellis & Mahon, 1964, 1967; Ellis, 1968; Bischoff & Dickson, 1975; Mottl, 1976; Ewers, 1975) show that hot water (sea water or distilled) can effectively leach a number of elements as a result of reaction with basalt and other rock types. The actual concentrations of these elements removed by solutions depend on the temperature, alteration mineral produced, rock composition, water/rock ratios, starting pH, chlorine concentrations and f_{O_2} of the solutions. Unfortunately no analytical data is available regarding leaching of Au, Ag and Te from rocks but it seems reasonable to assume that such a process can account for the ore and gangue mineral constituents in the Emperor solutions. Analyses summarised in Chapter 3 indicate that calcareous and other sedimentary rocks are richer in tellurium than basaltic and other igneous rocks, suggesting that the sedimentary rocks underlying the volcanics at the Emperor mine could have been the major supplier of tellurium. Gold is probably more likely to have been obtained from basalt (Chapter 3).

12.3 THE EMPEROR MINE SYSTEM

It can be seen from gold solubility contours (Figs. 10.13 to 10.16) that in the Emperor mine gold precipitation could have been caused by:

(1) Increase in f_{O_2} and decrease in pH at constant temperature (calaverite saturated, Fig. 10.13).

(2) Decrease in temperature and f_{O_2} at constant pH (calaverite saturated, Fig. 10.14).

(3) Increase in f_{O_2} in the alkaline pH range (sulphur complexes dominating, Fig. 10.15).

(4) Decrease in chlorine concentration.

(5) Decrease in sulphur concentration.

(6) Increase in pH in the acid pH range (chloride complexes dominating, Fig. 10.15).

(7) Decrease in temperature and f_{O_2} at constant pH (Fig. 10.16).

Possibilities (1) and (2) cannot be evaluated because of uncertainty in the data for aqueous tellurium species and a lack of understanding regarding the possible role of gold-tellurium complexes. As the pH of the Emperor fluids was near neutral possibility (3) is unlikely to cause any major gold precipitation. Possibility (4), precipitation due to drop in the concentration of chloride ions, may occur by fluid dilution as a result of mixing of relatively dilute fluid with a more saline ore-fluid. However there appear to be no variations in salinity either temporally or spatially suggesting that gold precipitation due to dilution in unlikely. This leaves possibilities (5), (6) and (7) and all these can be embraced in a single genetic model.

The bulk of the mineralization at the Emperor mine occurs near and above the intersection of the Prince-Dolphin flatmake and the steeply dipping fractures (Fig. 12.1). The only exception to this rule is the Crown lode in which the mineralization continues to about 100 m below its intersection with the flatmake. The mineralization in the Crown lode in the deeper levels mainly belongs to stage IIIB, a problem to be considered a little later in this discussion.

In Chapter 7 it was shown that the stage IIA solutions boiled above an altitude between 11 and 14 levels (see also Fig. 12.1). Stage IIB mineralization could thus be directly related to boiling. Removal of H_2S by boiling would drop the concentrations of total sulphur in the solutions, thereby decreasing the gold solubility (possibility 5).

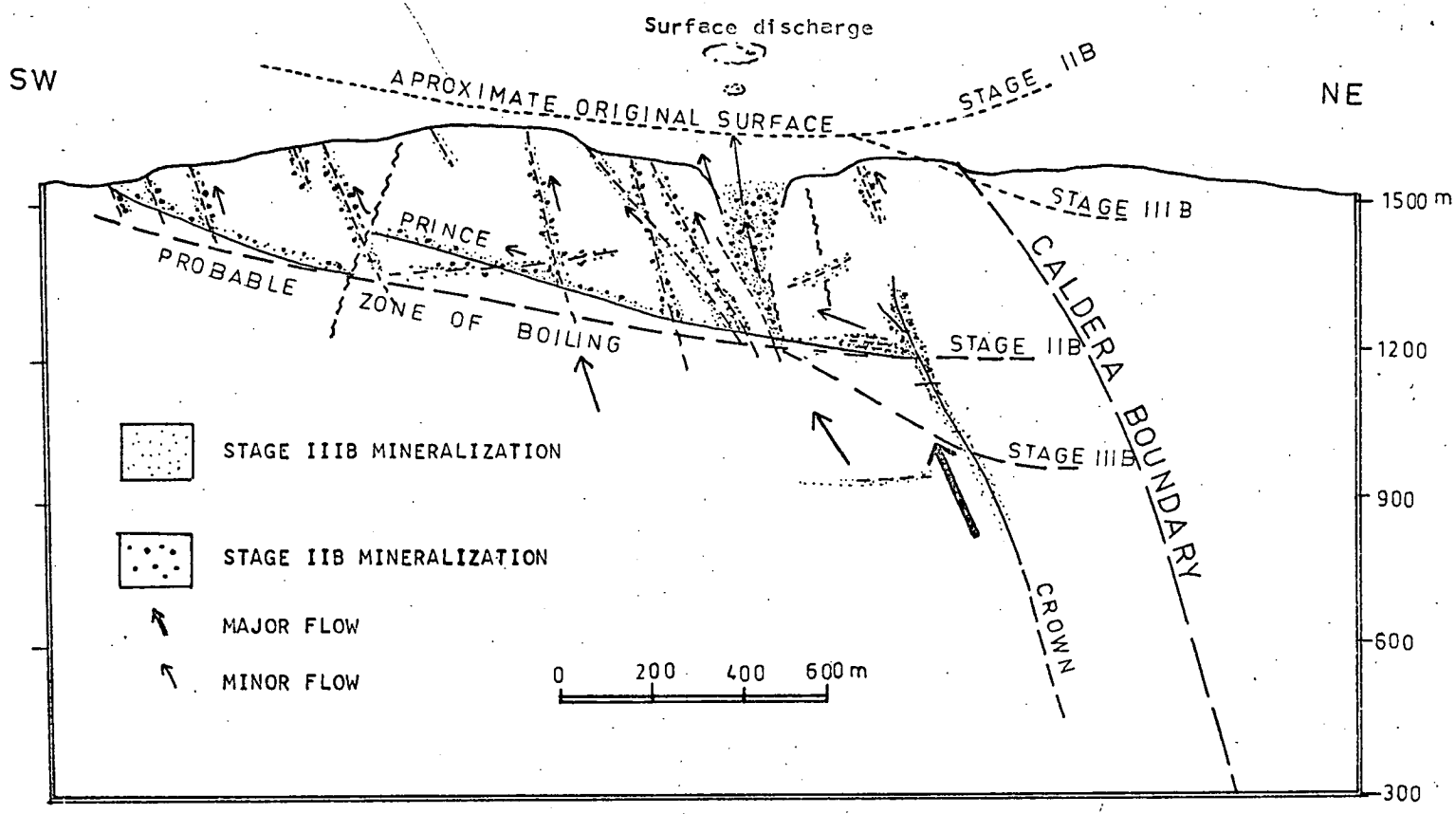

Fig. 12.1 Suggested model for mineralization at the Emperor mine. For lode names and location refer to Fig.5.1. For details regarding the depth of boiling and the position of the surface at the time of mineralization refer to Fig. 7.5, 7.6 and 7.7. The arrows indicate the flow direction of the solutions.

While some increase in the solution pH is possible due to loss of H_2S and H_2Te, more significant increases would probably occur as a result of CO_2 partition into the vapour phase. Again the solubility of gold and other metals would drop as a result of increase in pH (possibility 6). Loss of H_2O vapour would cause of drop in temperature due to latent heat of vapourization, thereby decreasing gold and other metal solubilities (possibility 7).

It thus seems reasonable to ascribe stage IIB mineralization to boiling and its attendant effects. Stage IIIB mineralization is present at deeper levels than stage IIB (Fig. 12.1) and this is probably because boiling commenced at lower levels, judging from fluid-inclusion evidence presented in Chapter 7 (Fig. 7.6A). Such a lowering might have been brought about by caldera formation, which may have resulted in the subsidence of the area previously overlying the Crown lode but may have had little or no effect in the area overlying the western lodes (Fig. 12.1).

Mineralization probably ceased when ore-fluid temperature dropped below about 200^{o}C (stage IV).

Intrusions of minor plugs and dykes during the second period of igneous activity (5 to 4.3 m.y.) probably resulted in the formation of shallow convection cells and precipitation of stage V calcite.

REFERENCES

Anderson, G.M., 1962. The solubility of PbS in H_2S-water solutions. *Econ. Geol., 57,* 809-828.

Anderson, G.M., 1977. Thermodynamics of sulphide solubilities. *In* Greenwood, H.J. editor. Application of thermodynamic to petrology and ore deposits. *Mineralogical Association of Canada,* short course, p.136-149.

Anderson, G.M. and Burnham, C.W., 1965. The solubility of quartz in supercritical water. *Am. J. Sci., 263,* 494-511.

Andrusenko, N.I., Timofeevsky, O.A., Grebenchikov, A.M. and Adrianova, S.I., 1971. Formation temperatures of gold ore deposits from inclusions in minerals. *In* Roedder, E., editor. Fluid inclusion research. *Proc. of COFFI, 4,* 96-100.

Andrusenko, N.I., Kosovets, T.N., Ushakova, L.K., Shungunova, N.A. and Bochek, L.I., 1978. Conditions of formation of gold in a complex ore field. *Internat. Geol. Rev., 20,* 916-926.

Anufriyev, Yu.N., Stupakov, G.P. and Moskabyuk, A.A., 1974. Characteristics of quartz of Kochkar gold deposit. *Internat. Geol. Rev., 16,* 405-416.

Barnes, H.L., 1965. Environmental limitations to mechanisms of ore transport. *Symposium on Problems of Postmagmatic Ore Deposition, Prague, 2,* 316-326.

Barnes, H.L. and Czamanske, G.K., 1967. Solubilities and transport of ore minerals. *In* Barnes, H.L., editor, *Geochemistry of Hydrothermal Ore Deposits.* New York, Holt, Rinehart and Winston, Inc. p.334-381.

Barnes, H.L. and Kullerud, G., 1961. Equilibria in sulphur-containing aqueous solutions in the system Fe-S-O and their correlation during ore deposition. *Econ. Geol., 56,* 648-688.

Barton, P.B. Jr., Bethke, P.M. and Toulmin, M.S., 1977. An attempt to determine the vertical component of flow rate of ore forming solutions in the OH vein, Creede, Colorado. *Soc. Mining Geologists Japan Spec. Issue 2*, 132-136. (Proc. IMA-IAGOD Meetings 70, joint symp. vol.)

Barton, P.B. Jr., Bethke, P.M. and Roedder, E., 1977. Environment of ore deposition in the Creede mining district, San Juan Mountains, Colorado. Part III: Progress towards interpretation of the chemistry of ore forming fluid for the OH vein. *Econ. Geol., 72*, 1-24.

Barton, P.B. Jr., and Skinner, B.J., 1967. Sulphide mineral stabilities. *In* Barnes, H.L. ed., *Geochemistry of Hydrothermal Ore Deposits*, 236-333. Holt, Rinehart and Winston, Inc., New York.

Barton, P.B. Jr., and Skinner, B.J., (in press). Sulphide mineral stabilities. *In* Barnes, H.L., ed. *Geochemistry of Hydrothermal Ore Deposits*, 2nd edition. John Wiley and Sons, New York.

Bartram, G.D. and McCall, G.J.H., 1971. Wall rock alteration associated with the auriferous lodes in the Golden Mine, Kalgoorlie. *Geol. Soc. Aust. Spec. Pub. 3*, 191-199.

Batchelor, J., 1977. Light stable isotope and fluid inclusion study of the porphyry copper deposit at Copper Canyon, Nevada. *Econ. Geol., 77*, 60-70.

Bateman, J.D., 1958. Uranium-bearing auriferous reefs at Jacobina, Brazil. *Econ. Geol., 53*, 417-425.

Bateman, A.M., 1959. *Economic Mineral Deposits*. John Wiley and Sons, New York. 916p.

Beas, C.F. Jr. and Mesmer, R.E., 1976. *The Hydrolysis of Cations*. John Wiley and Sons, New York. 489p.

Beaty, R.D. and Manuel, O.K., 1973. Tellurium in rocks. *Chem. Geol., 12,* 155-159.

Beyschlag, F., Vogt, J.H.L. and Kruschi, P., 1916. *The Deposits of the Useful Minerals and Rocks, Their Origin, Form and Content.* Vol.II, 515-598. Macmillan and Co. Ltd., London.

Binns, R.A., Gunthorpe, R.J. and Groves, D.I., 1976. Metamorphic patterns and development of greenstone belts in the Eastern Yilgarn Block, Western Australia. *In* Windley, B.F., editor, *The Early History of the Earth.* John Wiley and Sons, London. p.303-316.

Bischoff, J.L. and Dickson, F.W., 1975. Seawater-basalt interaction at 200°C and 500 bars: Implication for origin of sea-floor heavy metal deposits and regulation of seawater chemistry. *Earth Planet. Sci. Letters, 25,* 385-397.

Blatchford, A., 1953. Geology of the Tavua goldfield, Viti Levu. *Proc. Aust. Inst. Min. Metall., 168-169,* 13-51.

Blattner, P., 1975. Oxygen isotopic composition of fissure-grown quartz, adularia and calcite from Broadland Geothermal Field, New Zealand. *Am. J. Sci., 275,* 785-800.

Borcos, M., 1966. Some considerations on the determination of the thermodynamical conditions of formation of some hydrothermal veins and deposits in the metalliferous mountain region. *Rev. Roum. Geol. Geophys., Geogr.-serie de Geologie, 10,* 99-113.

Borcos, M. and Manilici, V., 1965. Geothermometric analysis - A criterion for the determination of thermodynamic conditions of hydrothermal mineralization. Symposium: *Problems of Postmagmatic Ore Deposition, II.* Geological Survey of Czechoslovakia, 356-363.

Bottinga, Y., 1968. Calculation of fractionation factors for carbon and oxygen isotopic exchange in the system calcite-carbon dioxide-water. *J. Phys. Chem., 72,* 800-808.

Bottinga, Y. 1969. Calculated fractionation factors for carbon and hydrogen isotope exchange in the system calcite-carbon dioxide-graphite-methane-hydrogen-water vapour. *Geochim. Cosmochim. Acta, 33,* 49-64.

Bottinga, Y. and Javoy, M., 1973. Comments on oxygen isotope geothermometry. *Earth Planet. Sci. Letters, 20,* 250-265.

Boyle, R.W., 1955. The geochemistry and origin of gold bearing quartz veins and lenses of the Yellowknife greenstone belt. *Econ. Geol., 50,* 51-66.

Boyle, R.W., 1961. The geology, geochemistry and origin of gold deposits of the Yellowknife District. *Geol. Surv. Canada Mem. 310.*

Boyle, R.W., 1968. The geochemistry of silver and its deposits. *Geol. Surv. Canada Bull., 160,* 264p.

Brock, R.W., 1924. Sketch of the geology of Viti Levu, Great Fiji. *Proc. roy. Soc. Canada, Sec.3, 18,* 63-83.

Bryner, L., 1969. Ore deposits of the Philippines - an introduction to their geology. *Econ. Geol., 64,* 644-666.

Burbank, W.S., 1960. Pre-ore propylitization, Silverton Caldera, Colorado. *U.S. Geol. Surv. Prof. Paper 400B,* 13-14.

Cabri, L.J., 1965. Phase relations in the Au-As-Te system and their mineralogical significance. *Econ. Geol., 60,* 1569-1606.

Callow, K.J. and Worley, B.W. Jr., 1965. The occurrence of telluride minerals at the Acupan gold mine, Mountain province, Philippines. *Econ. Geol., 60,* 251-268.

Casadevall, T., 1976. Sunnyside mine, Eureka mining district, San Juan County, Colorado: geochemistry of gold and base metal ore formation in the volcanic environment. Ph.D. thesis, Pennsylvania State University, 146 p.

Casadevall, T. and Ohmoto, H., 1977. Sunnyside mine, Eureka mining district, San Juan County, Colrado: geochemistry of gold and base metal ore formation in the volcanic environment. *Econ. Geol., 72,* 1285-1320.

Cathles, L.M., 1977. An analysis of the cooling of intrusives by ground-water convection which includes boiling. *Econ. Geol., 72,* 804-826.

Cathles, L.M., 1978. Hydrodynamic constraints on the formation of Kuroko deposits. *Mining Geology, 28,* 257-265.

Clayton, R.N. and Mayeda, T.K., 1963. The use of bromine pentafluoride in the extraction of oxygen from oxides and silicates for isotopic analysis. *Geochim. Cosmochim. Acta, 27,* 43-52.

Clayton, R.N., O'Neil, J.R. and Mayeda, T.K., 1972. Oxygen isotope exchange between quartz and water. *J. Geophys. Res., 77,* 3057-3067.

Cloke, P.L., 1963. The geologic role of polysulphides - Part II. The solubility of acanthite and covellite in sodium polysulphide solutions. *Geochim. Cosmochim. Acta, 27,* 1299-1319.

Cohen, E.M., 1962. Revided geology of the Tavua gold field, Fiji. *Proc. Aust. Inst. Min. Metall., 204,* 135-160.

Cohen, M., 1962. Wall-rock alteration of the Prince and Crown lodes. Unpublished report to the Emperor Gold Mining Co. Ltd., Fiji.

Cole, W.S., 1960. Upper Eocene and Oligocene larger formaminifera from Viti Levu, Fiji. *U.S. Geol. Surv. Prof. Pap. 374A,* 7p.

Combarnous, M.A. and Bories, S.A., 1975. Hydrothermal convection in saturated porous media. *In* Ven Te Chow, editor. *Advances in Hydroscience.* Academic Press, New York. p.231-307.

Cox, D.P., 1967. Regional environment of the Jacobina auriferous conglomerate, Brazil. *Econ. Geol., 62,* 773-780.

Craig, H., 1963. The isotopic chemistry of water and carbon in geothermal areas. *In* Tongiongi, E., editor. *Nuclear Geology in Geothermal Area.* Spoleto: Pisa, Consiglio Nazionale dell a Ricerche Laboratorio de Geologica Nucleare, p.17-53.

Crerar, D.A. and Barnes, H.L., 1976. Ore solution chemistry: V. Solubilities of chalcopyrite and chalcocite assemblages in hydrothermal solutions at 200° to 300°C. *Econ. Geol., 71,* 772-794.

Crerar, D.A., Susak, N.J., Boreisk, M and Shwartz, S., 1978. Solubility of the buffer assemblage pyrite + pyrrhotite + magnetite in NaCl solutions from 200 to 350°C. *Geochim. Cosmochim. Acta, 42,* 1427-1437.

Davletov, I.K. and Dzhakshibayev, Sh., 1970. The mineral balance and the behaviour of gold during the emplacement of an intrusive body. *Geochem. Internat., 7,* 997-1005.

Deer, W.A., Howie, R.A. and Zussman, J., 1971. *An Introduction to the Rock-Forming Minerals.* Longman, London. 528p.

Denholm, L.S., 1967a. Lode structures and ore shoots at Vatukoula, Fiji. *Proc. Aust. Inst. Min. Metall., 222,* 73-83.

Denholm, L.S., 1967b. Structural and economic aspects of the Vatukoula caldera. *Bull. Vulcan., 29,* 223-234.

Denholm, L.S., 1967c. Geological exploration for gold in the Tavua basin, Viti Levu. *N.Z. J. Geol. Geophys., 10,* 1185-1186.

D'yachkova, I.B. and Khodakovskiy, I.L., 1968. Thermodynamic equilibria in the system S-H_2O, Se-H_2O and Te-H_2O in the 25 to 300°C temperature range and their geochemical interpretations. *Geochem. Internat., 5,* 1108-1125.

Eastoe, C.E., 1978. A fluid inclusion study of the Panguna porphyry copper deposit, Bougainville, Papua New Guinea. *Econ. Geol., 73,* 721-748.

Eastoe, C.E., 1979. The formation of the Panguna porphyry copper deposit, Bougainville, Papua New Guinea. Ph.D. thesis, University of Tasmania. 255p.

Elder, J.W., 1966. Heat and mass transfer in the earth: hydrothermal systems. *Bull. N.Z. D.S.I.R., 169,* 115p.

Elder, J.W., 1967a. Steady free convection in a porous medium heated from below. *J. Fluid Mech., 27,* 29-48.

Elder, J.W., 1967b. Transient convection in a porous medium. *J. Fluid Mech., 27,* 609-623.

Elder, J.W., 1968. The unstable thermal interface. *J. Fluid Mech., 32,* 69-96.

Ellis, A.J. and Mahon, W.A.J., 1964. Natural hydrothermal systems and experimental hot-water/rock interactions (Part I). *Geochim. Cosmochim. Acta, 28,* 1323-1357.

Ellis, A.J. and Mahon, W.A.J., 1967. Natural hydrothermal systems and experimental hot-water/fluid interactions (Part II). *Geochim. Cosmochim. Acta, 31,* 514-538.

Ellis, A.J., 1968. Natural hydrothermal systems and experimental hot-water/rock interactions: reactions with NaCl solutions and trace metal extraction. *Geochim. Cosmochim. Acta, 32,* 1356-1363.

Emmons, W.H., 1937. *Gold Deposits of the World.* McGraw-Hill Book Co., Inc. 562p.

Epstein, S. and Mayeda, T.K., 1953. Variations of ^{18}O contents of waters from natural sources. *Geochim. Cosmochim. Acta, 4,* 213-224.

Ewers, G.R., 1975. Experimental hot water-rock interactions and their significance to natural hydrothermal systems in New Zealand. *Geochim. Cosmochim. Acta, 41,* 143-150.

Ewers G.R., and Keays, R.R., 1977. Volatile and precious metal zoning in the Broadland geothermal field, New Zealand. *Econ. Geol., 72,* 1337-1354.

Finucane, K.J., 1965. Ore deposition and lode structure in the Kalgoorlie gold field. *In* McAndrew, J. editor. *Geology of Australian Ore Deposits.* 8th Commonwealth Mining and Metallurgical Congress, Melbourne. p.80-86.

Flanagan, F.J., 1969. U.S.G.S. Standards - II. First compilation of data for the U.S.G.S. rocks. *Geochim. Cosmochim. Acta, 33,* 81-120.

Flanagan, F.J., 1973. 1972 values for international geochemical reference samples. *Geochim. Cosmochim. Acta, 37,* 1189-1200.

Ford, J.H., 1976. A geochemical and stable isotope study of the Panguna porphyry copper deposit, Bougainville. Ph.D. thesis, University of Queensland. 120p.

Forsythe, D.L., 1967. Ore mineral distribution in the Crown-Crescent lode, Emperor gold mine, Fiji. M.Sc. thesis, University of Melbourne. 221p.

Forsythe, D.L., 1971. Vertical zoning of gold-silver tellurides in the Emperor gold mine, Fiji. *Proc. Aust. Inst. Min. Metall., 240,* 25-31.

Fournier, R.O. and Truesdell, A.H., 1973. An empirical Na-K-Ca geothermometer for natural waters. *Geochim. Cosmochim. Acta, 37,* 1255-1275.

Fripp, R.E.P., 1976. Stratabound gold deposits in Archaean banded iron formations, Rhodesia. *Econ. Geol., 71,* 58-75.

Freuh, A.J., 1959. The structure of hessite, Ag_2Te - III. *Zeit. fur Krist., 112,* 44-52.

Freuh, A.J. and Vincent, E.A., 1974. Silver. *In Handbook of Geochemistry, II-4.* Springer-Verlag, Berlin.

Gain, J.E., 1962. Geology and ore deposits of Nova Lima and Rio Lima quadrangle, Minas Gerais, Brazil. *U.S. Geol. Surv. Prof. Pap. 341A,* 67p.

Ganapathy, R., Keays, R.R., Lauk, J.C. and Anders, E., 1970. Trace elements in Apollo 11 lunar rocks: Implication for meteorite influx and origin of moon. *Geochim. Cosmochim. Acta,* Proceedings of the Apollo 11 lunar science conference, part 2, Suppl.1, 34.

Garetty, M.D., 1936. Geology and ore deposits, Tavua gold field, Fiji. Unpublished report.

Garrels, R.M. and Christ, C.L., 1965. *Solutions, Minerals and Equilibria.* Harper and Row, New York. 450p.

Glynn, C., 1978. Gold. *Mining Annual Review 1978,* 27-29.

Golding, L.Y., 1978. Mineralogy, chemistry and origin of the Kalgoorlie gold deposits, Western Australia. Ph.D. thesis, University of Melbourne, 402p.

Goodwin, A.M., 1965. Mineralized volcanic complexes in the Porcupine-Kirkland Lake-Noranda region, Canada. *Econ. Geol., 60,* 955-971.

Gosling, A.W., Jenne, E.A. and Chao, T.T., 1971. Gold content of natural waters in Colorado. *Econ. Geol., 66,* 309-313.

Gottfried, D., Rowe, J.J. and Tilling, R.I., 1972. Distribution of gold in igneous rocks. *U.S. Geol. Surv. Prof. Paper 727,* 42p.

Greenland, L.P. and Fones, R., 1971. Geochemical behaviour of silver in differentiated tholeiitic dolerite sheets. *Neuhr. Jharb. Mineral. Monatsh., 9,* 393-398.

Griffin, B.J., 1979. Energy dispersive analysis system calibration and operation with TAS-SUEDS, an advanced interactive data-reduction package. *University of Tasmania, Geology Dept. Pub. No.343.* 44p.

Gross, W.H., 1968. Evidence for a modified placer origin for auriferous conglomerates, Canavieiras mine, Jacobina, Brazil. *Econ. Geol., 63,* 271-276.

Haas, J.L. Jr., 1971. The effect of salinity on the maximum thermal gradient of a hydrothermal system at hydrostatic pressure. *Econ. Geol., 66,* 940-946.

Haas, J.L. Jr. and Robie, R.A., 1973. Thermodynamic data for wustite, magnetite and hematite. *Am. Geophys. Un. Trans., 54,* 483.

Hall, H.I.E. and Bekker,C., 1965. Gold deposits of Norseman. *In* McAndrew, J. editor. *Geology of Australian Ore Deposits.* 8th Commonwealth Mining and Metallurgical Congress, 1, 101-106.

Hattori, K., 1975. Geochemistry of ore deposition at the Yatani lead-zinc and gold-silver deposit, Japan. *Econ. Geol., 70,* 677-693.

Helgeson, H.C., 1969. Thermodynamics of hydrothermal systems at elevated temperatures and pressures. *Am. J. Sci., 267,* 729-804.

Helgeson, H.C. and Garrels, R.M., 1968. Hydrothermal transport and deposition of gold. *Econ. Geol., 63,* 622-635.

Hemley, J.J., 1953. A study of lead sulphide solubility and its relation to ore deposition. *Econ. Geol., 48,* 113-138.

Henley, R.W., 1973. Solubility of gold in hydrothermal chloride solutions. *Chem. Geol., 11,* 73-87.

Hey, M.H., 1954. A new review of the chlorites. *Mining Mag., 30,* 277.

Hinners, N.W. and Holland, H.D., 1963. Solubility of sphalerite in aqueous solutions at 80°C. (Abs.) *Am. Geophys. Un. Trans., 44,* 116.

Hoefs, J., 1973. *Stable Isotope Geochemistry.* Springer-Verlag, New York. 140p.

Holland, H.D., 1959. Some applications of thermochemical data to problems of ore deposits. I. Stability relations among the oxide, sulphides, sulphates and carbonates of ore and gangue minerals. *Econ. Geol., 54,* 184-233.

Holland, H.D., 1965. Some applications of thermochemical data to problems of ore deposits. II. Mineral assemblage and the composition of ore-forming fluids. *Econ. Geol., 60,* 1101-1166.

Hulston, J.R. and Shilton, W.B., 1958. Sulphur isotopic variations in nature. Part 4 - Measurements of sulphur isotopic ratio by mass spectrometry. *N.Z. J. Sci., 1,* 91-102.

Ibbotson, P., 1960. Geology of the Suva area, Viti Levu. *Geol. Surv. Fiji Bull., 4,* 44p.

Ibbotson, P., 1967. Petrology of the Tavua caldera, Tavua gold field. *Geol. Surv. Fiji Mem. 3,* 59p.

Jahnke, F.M., 1976. Structures and vein development at the Al gold mine, Victoria, Australia. M.Sc. thesis, University of Melbourne.

Kamilli, R.J. and Ohmoto, H., 1977. Paragenesis, zoning, fluid inclusion and isotopic studies of the Finlandia vein, Colqui District, central Peru. *Econ. Geol., 72,* 950-982.

Kelly, W.C. and Goddard, E.N., 1969. Tellurid ores of Boulder County, Colorado. *Geol. Soc. Am. Mem. 109,* 237p.

Kennedy, G.C., 1950. A portion of the system silica-water. *Econ. Geol., 45,* 629-653.

Kharkar, D.P., Turekian, K.K. and Berline, K.K., 1968. Stream supply of dissolved As, Mo, Sb, Se, Cr, Co, Rb and Cs to the ocean. *Geochim. Cosmochim. Acta, 32,* 285-298.

Kitihara, S., 1960. The solubility of quartz in water at high temperatures and high pressures. *Rev. Phys. Chem. Japan, 30,* 109-140.

Kolosova, T.B. and Onishchuk, Yu.V., 1971. A new type of gold-ore mineralization in Eastern Transbaykal. *Internat. Geology Rev., 13,* 1027-1035.

Koltum, L.I., 1965. Application of mineralothermometric analysis in studies of the origin of certain gold deposits in Ural. *In* Roedder, E. editor. *Researches on the Nature of Mineral Forming Solutions*. Pergamon Press, Oxford. p.426-457.

Koppel, V.H. and Saager, R., 1973. Lead isotope evidence for the detrital origin of Witwatersrand pyrite and its bearing on the provenance of the Witwatersrand gold. *Econ. Geol. Res. Unit Inf. Circ. 79*, 1-17.

Kracek, F.C., Ksanda, C.J. and Cabri, L.J., 1966. Phase relations in the silver-tellurium system. *Am. Mineralogist, 51*, 14-28.

Krauskopf, K.B., 1951. The solubility of gold. *Econ. Geol., 46*, 858-870.

Ladd, H.S., 1934. Geology of Viti Levu, Fiji. *Bull. Bishop. Mus. Honolulu, 119*, 263p.

Leutwein, F., 1974. *Handbook of Geochemistry*. 11-3. Springer-Verlag, Berlin.

Lindgren, W., 1933. *Mineral Deposits*. McGraw-Hill, New York. 930p.

Logsdon, M.J., 1969. A fluid inclusion study of the porphyry copper deposits at Ray and San Manuel, Arizona. (Abs.) *Fluid Inclusion Research - Proc. COFFI*, 20.

Lowell, J.D. and Guilbert, J.M., 1970. Lateral and vertical alteration mineralization zoning in porphyry ore deposits. *Econ. Geol., 65*, 373-408.

Lyakhov, Yu.V. and Popivnyak, I.V., 1978. Physicochemical conditions of development of gold mineralization in northern Buryatia. *Internat. Geol. Rev., 20*, 955-967.

Lyon, G.L. and Cox, M.A., 1975. The reduction of water to hydrogen for D/H ratio analysis using zinc in a matrix of sand. *Laboratory note, Inst. Nuclear Sci. N.Z. No.50/108/GLL.*

Macdonald, G.A., 1972. *Volcanoes*. Prentice-Hall Inc., Englewood Cliffs, New Jersey. 510p.

Markham, N.L., 1960. Synthetic and natural phases in the system Au-Ag-Te. *Econ. Geol., 55,* 1148-1178.

Mason, B., 1958. *Principles of Geochemistry.* John Wiley and Sons, Inc., New York. p.310.

McCrea, J.M., 1950. On the isotopic chemistry of carbonates and a paleo-temperature scale. *J. Chem. Physics, 18,* 849-857.

McDougall, I., 1963. Potassium-argon ages of some rocks from Viti Levu, Fiji. *Nature, 198 (4881),* 677.

Melent'yev, B.N., Ivanenko, V.V. and Pamfilova, L.A., 1969. Solubility of some ore forming sulphides under hydrothermal conditions. *Geochemistry Internat., 6,* 416-460.

Meyer, C. and Hemley, J.J., 1967. Wall rock alteration. *In* Barnes, H.L., editor. *Geochemistry of Hydrothermal Ore Deposits.* Holt, Rinehart and Winston, Inc., New York. p.166-235.

Mills, K.C., 1974. *Thermodynamic Data for Inorganic Sulphides, Selenides and Tellurides.* Butterworth and Co., London. 945p.

Morey, G.W. and Hesselgessar, J.M., 1951. The solubility of some minerals in super heated steam at high pressures. *Econ. Geol., 46,* 821-835.

Morey, G.W. Fournier, R.O., and Rawe, J.J., 1962. The solubility of quartz in water in the temperature interval from 25° to 300°C. *Geochim. Cosmochim. Acta, 26,* 1029-1043.

Mottl, M.J., 1976. Chemical exchange between sea water and basalt during hydrothermal alteration of the oceanic crust. Ph.D. thesis, Harvard University. 188p.

Nabivanets, B.I. and Kapantsyan, E.E., 1968. State of tellurium (IV) in HCl and LiCl solutions. *Russian Journal of Inorganic Chemistry, 13,* 946-949.

Naryanaswami, S., Ziauddin, M. and Romachandra, A.V., 1960. Structural control and localization of gold-bearing lodes, Kolar gold field, India. *Econ. Geol., 55,* 1429-1459.

Nash, J.T., 1972. Fluid inclusion studies of some gold and silver deposits in Nevada. *U.S. Geol. Surv. Prof. Paper 800C,* C15-C19.

Nash, J.T., 1973. Geochemical studies in the Park City district: 1. Ore fluids in the Mayflower mine. *Econ. Geol., 68,* 34-51.

Nash, J.T., 1975. Fluid inclusion studies of vein, pipe and replacement deposits, northwestern San Juan Mountain, Colorado. *Econ. Geol., 70,* 1148-1162.

Nash, J.T., 1976. Fluid inclusion petrology - data from porphyry copper deposits and application to exploration. *U.S. Geol. Surv. Prof. Paper 907D,* 17p.

Nash, J.T. and Theodore, T.G., 1971. Ore fluids in the porphyry copper deposits at Copper Canyon, Nevada. *Econ. Geol., 66,* 385-399.

Naqvi, S.M., 1976. Physicochemical conditions during the Archaean as indicated by Dharwar geochemistry. *In* Windby, B.F., editor. *The Early History of the Earth.* John Wiley and Sons, New York. p.289-298.

Naumov, G.B., Ryzhenko, B.N. and Khodakovsky, I.L., 1974. *Handbook of Thermodynamic Data.* National Technical Information Service, U.S. Dept. of Commerce. 328p.

Nickel, E.H., 1977. Mineralogy of the "green leader" gold ore at Kalgoorlie, Western Australia. *Proc. Aust. Inst. Min. Metall., 283,* 9-14.

Nesterenko, G.V., Belyayev, Yu.I. and Phi, P.H., 1969. Silver in the evolution of mafic rocks. *Geochemistry Internat., 6,* 119-126.

Nickolds, C., 1976. A program for quantitative analysis of minerals. *Edax Editor, 6,* 34-41.

Norrish, K. and Chappell, B.W., 1967. X-ray fluorescence spectrography. *In* Zussman, J. editor. *Physical Methods in Determinative Mineralogy*. Academic Press.

Norrish, K. and Hutton, J.T., 1969. An accurate X-ray spectrographic method for analysis of a wide range of geological samples. *Geochim. Cosmochim. Acta, 33,* 431-453.

Northrop, D.A. and Clayton, R.N., 1966. Oxygen isotope fractionation in systems containing dolomite. *J. Geol., 74,* 174-196.

Norton, D. and Knapp, R., 1977. Transport phenomena in hydrothermal systems: the nature of porosity. *Am. J. Sci., 277,*913-936.

Norton, D. and Knight, J., 1977. Transport phenomena in hydrothermal systems: cooling plutons. *Am. J. Sci., 277,* 937-981.

Nriagu, J.O., 1971a. Expressions for calculating the solubilities of metal sulphides in hydrothermal solutions. *Can. J. Earth Sci., 8,* 813-819.

Nriagu, J.O., 1971b. Studies in the system PbS-NaCl-H_2S-H_2O: Stability of lead (II) thio complexes at 90°C. *Chem. Geology, 8,* 299-310.

Nriagu, J.O. and Anderson, G.M., 1971. Stability of lead (II) chloride complexes at elevated temperatures. *Chem. Geology, 7,* 171-183.

Ohmoto, H., 1972. Systematics of sulphur and carbon isotopes in hydrothermal ore deposits. *Econ. Geol., 67,* 551-578.

O'Neil, J.R. and Taylor, H.P. Jr., 1967. The oxygen isotope and cation exchange chemistry of feldspar. *Am. Mineralogist, 52,* 1414-1437.

O'Neil, J.R., Clayton, R.N. and Mayeda, T.K., 1969. Oxygen isotope fractionation in divalent metal carbonates. *J. Chem. Physics, 51,* 5547-5558.

O'Neil, J.R. and Silberman, M.L., 1974. Stable isotope relations in epithermal Au-Ag deposits. *Econ. Geol., 69,* 902-909.

O'Neil, J.R., Silberman, M.L., Fabi . B.P. and Chesterman, C.W., 1973. Stable isotope and chemical relations during mineralization in the Bodie mining district, Mono County, California. *Econ. Geol., 68,* 765-784.

Park, C.F. Jr., and MacDiarmid, R., 1964. *Ore Deposits.* W.H. Freeman and Co., San Francisco. 522p.

Parmentier, E.M. and Spooner, E.T.C., 1978. A theoretical study of hydrothermal convection and origin of the ophiolitic sulphide ore deposits of Cyprus. *Earth Planet. Sci. Letters, 40,* 33-44.

Phillips, K.A., 1965. Geological map of Fiji. *Geol. Surv. Fiji Ann. Rep. No.4-6.*

Pitcher, W.S., 1978. The anatomy of a batholith. *Quart. J. Geol. Soc. London, 135,* 157-182.

Potter, R.W., Clynne, M.A. and Brown, D.L., 1978. Freezing point depression of aqueous sodium chloride solutions. *Econ. Geol., 73,* 284-285.

Pretorius, D.A., 1974. The geology of the South Rand gold field. *In* Haughton, S.H., editor. *The Geology of Some Ore Deposits in S. Africa.* Geological Society of S Africa. p.219-282.

Pretorius, D.A., 1976. The nature of the Witwatersrand gold-uranium deposit. *In* Wolf, K.H., editor. *Handbook of Strata Bound and Stratiform Ore Deposits. II. Regional studies and specific deposits.* Elsevier Publishing Company. p.29-87.

Rafter, T.A., 1957a. Sulphur isotopic variations in nature. Part 2. A quantitative study of the reduction of barium sulphate by graphite for recovery of sulphide-sulphur for sulphur isotopic measurements. *N.Z. J. Sci. Technology, sect. B, 38,* 955-968.

Rafter, T.A., 1957b. Sulphur isotopic variations in nature. Part 3. A study of the combustion characteristics of silver sulphide and lead sulphide for sulphur isotopic measurements. *N.Z. J. Sci. Technology, sect. B, 38,* 969-981.

Reed, S.J.B. and Ware, N.G., 1975. Quantitative microprobe analysis of silicates using energy dispersive X-ray spectrometry. *J. Petrol., 16,* 499-519.

Rickard , M.J., 1963. The geology of the Mbalevuto area, Viti Levu. *Geol. Surv. Fiji Bull. 2,* 36p.

Roberts, R.J., Radtke, A.S. and Coats, R.R., 1971. Gold bearing deposits in the north central Nevada and southern Idaho. *Econ. Geol., 66,* 14-33.

Robie, R.A. and Waldbaum, D.R., 1968. Thermodynamic properties of minerals and related substances at 298.15^{o}K (25^{o}C) and one atmosphere (1.013 bars) pressure and at higher temperatures. *U.S. Geol. Surv. Bull. 1259,* 256p.

Robinson, B.W., 1974. The origin of mineralization at the Tui mine, Te Aroha, New Zealand, in the light of stable isotope studies. *Econ. Geol., 69,* 910-925.

Robinson, B.W. and Kusakahe, M., 1975. Quantitative preparation of sulphur dioxide for $^{34}S/^{32}S$ analysis from sulphides by combustion with cuprous oxide. *Anal. Chem., 4,* 1179-1181.

Rodda, P., 1967. Outline of the geology of Viti Levu. *N.Z. J. Geol. Geophys., 10,* 1260-1273.

Rodda, P., Snelling, N.J. and Rex, D.C., 1967. Radiometric age data on rocks from Viti Levu, Fiji. *N.Z. J. Geol. Geophys., 10,* 1248-1259.

Roedder, E., 1960a. Primary fluid inclusions in sphalerite from the OH vein, Creede, Colorado. (Abs.) *Geol. Soc. Am. Bull., 71,* 1958.

Roedder, E., 1960b. Fluid inclusions as samples of ore forming fluids. *XXI Internat. Geol. Congr. Part XVI,* 218-229.

Roedder, E., 1967. Fluid inclusions as samples of ore fluids. *In* Barnes, H.L., editor. *Geochemistry of Hydrothermal Ore Deposits.* Holt, Rinehart and Winston, Inc. p.515-574.

Roedder, E., 1971. Fluid inclusion studies on the porphyry-type ore deposits at Bingham, Utah, Butte, Montana and Climax, Colorado. *Econ. Geol., 66,* 98-120.

Rowland, J.F. and Berry, L.G., 1951. The structural lattice of hessite. *Am. Mineralogist, 36,* 471-479.

Rye, R.O. and Sawkins, F.J., 1974. Fluid inclusion and stable isotope studies at the Casapalca As-Pb-Zn-Cu deposit, Central Andes, Peru. *Econ. Geol., 69,* 181-205.

Rye, R.O., Doe, B.R. and Wells, J.D., 1974. Stable isotope and lead isotope study of the Cortez, Nevada, gold deposit and surrounding area. *J. Research U.S. Geol. Surv., 2,* 13-23.

Saager, R. and Esselaar, P., 1969. Factor analysis of geochemical data from the basal reef, Orange Free State goldfield, South Africa. *Econ. Geol., 64,* 445-451.

Sakharova, M.S., 1969. Mineralogy of Darasun goldfield in Eastern Zabaykal'ye. *Internat. Geol. Rev., 11,* 45-59.

Schneeberg, E.P., 1973. Measurement of sulphur fugacities with the electrochemical cell Ag/AgI/Ag_2S. *Econ. Geol., 68,* 507-517.

Seward, T.M., 1973. Thio complexes of gold in hydrothermal ore solutions. *Geochim. Cosmochim. Acta, 37,* 379-399.

Seward, T.M., 1976. The stability of chloride complexes of silver in hydrothermal solutions up to 350°C. *Geochim. Cosmochim. Acta, 44,* 1329-1341.

Shackleton, R.M., 1936. Geology of Viti Levu. Unpublished report and maps at Geological Survey of Fiji, Suva.

Shapiro, L., 1975. Rapid analysis of silicate, carbonate and phosphate rocks - revised edition. *U.S. Geol. Surv. Bull. 1401,* 76p.

Sheppard, S.M.F. and Schwarcz, H.P., 1970. Fractionation of carbon and oxygen isotopes and magnesium between metamorphic calcite and dolomite. *Cont. Min. Petrology, 26,* 161-198.

Sheppard, S.M.F., Nielsen, R.L. and Taylor, H.P. Jr., 1971. Hydrogen and oxygen isotope ratios in minerals from porphyry-copper deposits. *Econ. Geol., 66,* 515-542.

Sheppard, S.M.F. and Taylor, H.P. Jr, 1974. Hydrogen and oxygen isotope evidence for the origin of water in the Boulder batholith and the Butte ore deposits, Montana. *Econ. Geol., 69,* 926-946.

Sheherbakov, Yu.G., 1964. Geochemistry of gold. *Geochemistry Internat., 1,* 489-496.

Shutz, D.F. and Turekian, K.K., 1965. The investigation of geographical and vertical distribution of several trace elements in sea water using neutron activation analysis. *Geochim. Cosmochim. Acta, 29,* 259-313.

Simons, F.S. and Prinz, W.C., 1973. Gold. *U.S. Geol. Surv. Prof. Paper 820,* 263-275.

Sindeeva, N.D., 1964. *Mineralogy and Type of Deposits of Selenium and Tellurium.* English translation, ed. E. Ingerson. Interscience Publications. John Wiley and Sons, New York.

Skinner, B.J., White, D.E., Rose, H.J. and May, R.E., 1967. Sulphides associated with the Salton Sea geothermal brines. *Econ. Geol., 62,* 316-330.

Srinivasan, B., Alexander, E.C. Jr. and Manuel, O.K., 1972. Te^{130}-Xe^{130} age determinations on tellurium minerals. *Econ. Geol., 67,* 592-596.

Steinberg, G.S. and Rivosh, L.A., 1965. Geophysical study of Koonachatka volcanoes. *J. Geophys. Research, 70,* 3341-3369.

Stillwell, F.L., 1949. Occurrence of tellurides at Vatukoula, Fiji. *Proc. Aust. Inst. Min. Metall. 154-155,* 3-28.

Stillwell, F.L. and Edwards, A.B., 1946. An occurrence of sub-microscopic gold in the Dolphin East lode, Fiji. *Proc. Aust. Inst. Min. Metall. 141,* 31-46.

Stoll, W.C., 1961. Tertiary channel gold deposit at Tipuani, Bolivia. *Econ. Geol., 59,* 1258-1264.

Stumpfl, E.F., 1970. New electron probe and optical data on gold telluride. *Am. Mineralogist, 55,* 808-814.

Swain, J.S., 1956. Absorptiometric determination of low concentrations of chlorides. *Chemistry and Industry,* 418-420.

Taylor, H.P., 1974. The application of oxygen and hydrogen isotope studies to problems of hydrothermal alteration and ore deposition. *Econ. Geol., 69,* 843-883.

Taylor, S.R., 1965. The application of trace element data to problems in petrology. *Physics and Chemistry of the Earth, 6,* 133p.

Thompson, R.M., 1949. The telluride minerals and their occurrences in Canada. *Am. Mineralogist, 34,* 342-382.

Tilling, R.I., Gottfried, D. and Rowe, J.J., 1973. Gold abundances in igneous rocks: bearing on gold mineralization. *Econ. Geol., 68,* 168-186.

Turekian, K.K., 1969. *Hydrosphere Distribution of the Elements.* Year Books of Science and Technology. McGraw-Hill Co., New York.

Turekian, K.K. and Wedepohl, K.H., 1961. Distribution of the elements in some major units of the earth's crust. *Geol. Soc. Am. Bull. 72,* 175-192.

Turner, F.J., 1968. *Metamorphic Petrology.* McGraw-Hill Co., New York. 403p.

Vinogradov, A.P., 1954. *Geochemie setner und nur in Spuren Varlandence Chemisher Elemente.* In Borden, 1954. German translation (Acad. Verlag., Berlin) of the Russian original 1950.

Vinogradov, A.P., 1962. Average contents of chemical elements in the principal types of igneous rocks of the earth's crust. *Geochemistry, 7,* 641-664.

Voskresenskaya, N.T. and Zvereva, N.F., 1968. Geochemistry of gold and its distribution in the magmatic complexes of northern Kazakhstan. *Geochemistry Internat., 5,* 373-381.

Wagner, L.R. and Mitchell, R.L., 1952. The distribution of trace elements during strong fractionation of basic magma - a further study of the Skaergaard intrusion. *Geochim. Cosmochim. Acta, 1,* 129-208.

Walshe, J.L., 1977. The geochemistry of Mt. Lyell copper deposits. Ph.D. thesis, University of Tasmania. 174p.

Ward, H.J., 1965. Gold copper deposits of Paris gold mine. *In* McAndrew, J., editor. *Geology of Australian Ore Deposits.* 8th Commonwealth Mining and Metallurgical Congress, V-I.

Watanabe, M., 1952. Mode of occurrences of tellurium bearing minerals in Japan. *Sci. Rep. Tohoku Univ. Ser.III, 4,* 45-80.

Weissberg, B.G., 1969. Gold silver ore grade precipitates from New Zealand thermal waters. *Econ. Geol., 64,* 95-108.

Weissberg, B.G., 1970. Solubility of gold in hydrothermal alkaline sulphide solutions. *Econ. Geol., 65,* 551-556.

White, D.E., 1955. Thermal springs and epithermal ore deposits. *Econ. Geol., 50th Anniv. Vol.,* 99-154.

White, D.E., 1967. Mercury and base metal deposits with associated thermal and mineral waters. *In* Barnes, H.L., editor. *Geochemistry of Hydrothermal Ore Deposits.* Holt, Rinehart and Winston, Inc., New York. p.575-631.

White, D.E., 1974. Diverse origin of hydrothermal fluids. *Econ. Geol., 69,* 954-973.

Weill, D.F. and Fyfe, W.S., 1964. The solubility of quartz in H_2O in the range 1000-4000 bars and 400 to 550°C. *Geochim. Cosmochim. Acta, 28,* 1243-1255.

Wichmann, A., 1882. Ein Beitrag zur Petrographie des Viti-Archipels. *Tschermak's Miner. Petrog. Mitt., 5,* 1-60.

Williams, G.J., 1974. *Economic Geology of New Zealand.* Aust. Inst. Min. Metall. Monograph No.4, 490p.

Woodall, R., 1965. Structure of the Kalgoorlie gold field. *In* McAndrew, J., editor. *Geology of Australian Ore Deposits, V-I.* 8th Commonwealth Mining and Metallurgical Congress, Melbourne. p.71-79.

Worl, R.G., 1978a. Ore controls at the Mahd Adh Dhahab gold mine, Kingdom of Saudi Arabia. *U.S. Dept. of Interior Rept. No. 232,* 28p.

Worl, R.G., 1978b. Mineral exploration: Mahd Adh Dhahab district, Kingdom of Saudi Arabia. *U.S. Dept. of Interior Rep. NO.233,* 85p.

APPENDICES

APPENDIX A - Sample locations and descriptions.

Five- and six-digit numbers are catalogue numbers at the University of Tasmania. Field numbers (1, 2, 3 ...) refer to numbers given at the time of sample collection. Numbers prefixed with 'F' are from Forsythe's (1967) collection; portions of certain samples (from Forsythe's collection) are housed at the University of Tasmania and local catalogue numbers have been given to these. Other samples are housed in the University of Melbourne. Sample numbers suffixed with 'S' were collected by Dr. M. Solomon during his visit to the Emperor mine in 1975. Sample numbers prefixed with 'S' are surface samples from the area in and adjacent to the Emperor mine. Sample numbers prefixed with 'SS' are from the sedimentary rocks surrounding the Mba volcanics. Samples SS-8 and C-249 were kindly provided by P. Rodda, Geological Survey of Fiji. Sample numbers prefixed with 'DDH' are from diamond drill holes (bore hole numbers are also given). Samples from underground workings are referred to the Emperor mine co-ordinates with origin at the Karoere triangulation station (Fig. 5.1). For easy location, level numbers and lode names are also given. Location of surface samples are given with reference to known localities and/or geographical co-ordinates. Sample numbers prefixed with 'E' were taken from the geology office at the Emperor mine and exact locations are not known. The abbreviation adopted for cataloguing the samples at the University of Tasmania is as follows:

H	Hand specimen
T	Thin section
PT	Polished thin section
PS	Polished section
D	X-ray disc
P	X-ray pill

C Crushed specimen

PD Powdered specimen

F Chips for fluid-inclusion studies

CA Chemical analysis.

For sample description the following abbreviations are used:

ALB altered basalt

ALA altered andesite

ALM altered monzonite

ALT altered tuff

ASH ash bed

FB fresh basalt

FA fresh andesite

CALST calcareous sandstone

CALGYK calcareous greywacke

CALSLT calcareous siltstone

GYK greywacke

LST impure limestone

P vein of massive pyrite

VA vein ankerite

VC vein calcite

VD vein dolomite.

VQ vein quartz

APPENDIX B - Sample mineralogy.

Where polished thin sections or polished sections and thin sections on individual samples are available all observed minerals are listed. Where only thin sections were prepared, transparent minerals are listed. Where only polished slabs are made (mostly from Forsythe's collection) opaque minerals are listed.

APPENDICES C.1 to C.4 - Major and trace element analyses.

Major and trace element analyses were done by XRF methods using a Philips PW 1410 X-ray spectrometer, under the guidance of Mr. P. Robinson, using the techniques described by Norrish and Chappell (1967) and Norrish and Hutton (1969). Major elements were determined on fused glass discs of a mixture of rock powder, lithium tetraborate, lithium carbonate and lanthanum oxide "fusion mixture" and sodium nitrate. Matrix corrections are based on the techniques of Norrish and Hutton (1969).

Trace element and sodium analyses were made on pressed rock pills (packed in boric acid). Mass absorption coefficients for all radiation types were calculated from the major element analyses. Corrections have been made for interfering elements (e.g. titanium and vanadium) using the method of Norrish and Chappell (1967). The instrument setting precision and detection limits are given in Appendix C.7.

APPENDIX C.5 - Carbon-dioxide determinations.

The CO_2 determinations were made by techniques given in Shapiro (1975, pages 17-18). Powdered samples weighing from 0.1 to 1 g (depending on anticipated carbonate concentrations) were placed in test tubes (with side arms) with 1 g of $HgCl_2$ and 2 ml of a saturated solution of $HgCl_2$. The mixture (sample + $HgCl_2$ + HgCl solution) was then covered with paraffin oil and placed in a heating block at 145 ± 5°C. CO_2 evolved by addition of 1:1 HCl was then collected in the side arm of the test tube. The volume of CO_2 (cooled to 25°C) was compared with standards (varying amounts of pure $CaCO_3$). Analyses of the duplicate samples indicate a precision of ± 0.1% CO_2.

APPENDIX C.6 - Specific gravity determinations.

Accurately weighed samples were placed in a graduated cylinder (filled with water) and the volume of the samples was determined. Specific gravity was then obtained by dividing the sample weight by the volume.

APPENDIX D - Electron microprobe analyses.

The analyses were carried out on a JEOL JXA-50A scanning electron microprobe analyser, under the guidance of Dr. A. McKee and Mr. B. Griffin. Quantitative reduction of the X-ray data collected by an EDAX energy dispersive system were made by a computer program TAS-SUEDS (Griffin, 1979). This program was modified from that given in Nockolds (1976) and Reed & Ware (1975). Pure metals (Au, Ag, Te), silicates, oxides and sulphides were used as standards. Detection limits are ± 0.2% for elements with abundances greater than 1 wt. %. Precision is about ± 0.02% at 2 wt. %.

APPENDIX E - Thermodynamic data and equilibrium constants.

The sources of data in Appendices E.1, E.2 and E.3 are given in footnotes. For the equilibrium constants calculated in this study, data given in Appendix E.1 was used. Methods used for the calculation of equilibrium constants were those given in Naumov *et al.* (1974, pages 22-26). Where heat capacity coefficients were available, the following equation was used to obtain ΔG^{o} at higher temperatures:

$$\Delta G^{o}T = x + (\Delta a - y)T - \Delta aT\ln T - \tfrac{1}{2}\Delta bT^{2} - \tfrac{1}{2}\Delta cT^{-1}$$

where $x = \Delta H^{o}_{298.15} - \Delta a(298.15) - \tfrac{1}{2}\Delta b(298.15)^{2} + \Delta c(298.15)^{-1}$

$y = \Delta S^{o}_{298.15} - \Delta a \ln 298.15 - \Delta b(298.15) + \tfrac{1}{2}\Delta c(298.15)^{-2}$

Where heat-capacity coefficients were not available (e.g. $NiTe_2$) the following equation was used to obtain ΔG^{o} at higher temperatures:

$$\Delta G^{o}T = \Delta H^{o}_{298.15} - T\Delta S^{o} + \Delta C^{o}_{p}\left[(T - 298.15) - (T\ln\frac{T}{298.15})\right]$$

Individual ion activity coefficients (Appendix E.3) were estimated by procedures outlined in Helgeson (1969) for 1 molal NaCl solutions and correspond approximately to an ionic strength of 1. No data is available on the a^{o} values of aqueous tellurium species. In this study the activity coefficients of tellurium species are assumed to be equal to sulphur species of similar charge and type. This approximation is probably reasonable for species except Te_2^{2-} which has been equated with S^{2-}.

Appendix A.1

LOCATION OF ORE SAMPLES.

Specimen Number	Field No.	Code	Description	Lode name	Mine level	Co-ordinates
103288	1	R,PT	ALB,VC	Crown	10	1160N-1260E
103289	2	R,F	ALB,VC	Crown	10	1520N-1140E
103290	4	R,F	ALB,VC	Monarch	9	2050N- 350W
103291	6	R,F	ALB,VC	608	9	150S- 325W
103292	7	R,F	ALB,VQ,VC	166	9	50S- 275E
103293	8	R,F	ALB,VQ,VC	166	9	00 - 800E
103294	9	R,F	ALB,VQ	166	9	50N- 350E
103295	10	R,F	VQ	?	7	2070N- 80E
103296	11	R,PT,F	ALB,VQ	166	7	330N- 820E
103297	11B	R,F	VQ	166	7	?
103298	12	R,F	ALB,VC	166	7	390N- 100E
103299	13	R,F	ALA,VQ,VC	Monarch	7	130S- 650W
103300	14	R,PT,F	ASH,VQ	04S	8	130S- 190E
103301	15	R,PT	ALB,VQ,VC	Monarch	8	500S- 500W
103302	16	R,F	ALB,VQ,VC	Monarch	8	350S- 445W
103303	17	R,F	VQ,VD	Monarch	8	75S- 350W
103304	18	R,PT,F	ALB,VQ	608	8	25S- 350W
103305	19	R,PT,F	ALA,ASH,VQ	166	8	175S- 750E
103306	20	R,F	ALA,VQ	1010	8	650S-1000W
103307	23	R,F	ALA,VQ	Dolphin	10	574S-1800W
103308	24	R,F	ALB,VC	P.O.W.	10	1275S-2575W
103309	25	R,PT,F	ALB,VQ	Dolphin	10	1170S-2125W
103310	26	R,PT,F	ALB,VQ	Dolphin	10	1500S-2450W
103311	28	R,PT	ASH,VQ,ALT	04S	8	100S- 190E
103312	29	R,PT,F	ALB,VQ,ALT	1010	8	530S-1070W
103313	30	R,PT,F	ALB,VQ	P.O.W.	11	1300S-2350W
103314	31	R,PT,F	ALB,VC	Dolphin	11	1550S-2100W
103315	33	R,F	ALB,VC	Prince	11	590S- 990W
103316	34	R,F	ALA,VQ	Crown	10	1520N-1550E
103317	35	R,T,PT	ALA	Prince	10	410S- 720W
103318	36	R,F	ALA,VQ	Crown	9	1730N-1512E
103319	41	R,PT,F	ALT,VQ	?	9	1650N-1800E
103320	42	R,PT,F	ALB,VC	Prince	10	1660N-1255E
103321	43	R,PT,F	ALB,VC	Prince	10	1528N-1140E
103322	44	R,F	ALB,VQ	Prince	10	1470N-1550E
103323	45	R,F	ALB,VQ,ALT	1600	10	1600N-1665E
103324	46	R,F	ALB,VQ,P	1600	10	1600N-1665E
103325	47	R,F	ALB,VQ,VC	Crown	12	1592N-1564E
103326	50	R,F	ALB,VC	Crown	13	1751N-1544E
103327	51	R,F	ALB,VC	Prince	13	450N-1170E
103328	52	R,F	ALB,VC	Prince	14	200N-1280E
103329	53	R,F	ALB,VQ,VC,P	Crown	14	1610N-1615E
103330	55	R,PT,F	ASH,VQ	608	8	80S- 500W
103331	56	R,T,PT	ALB,ALT	608	9	150S- 210W
103332	58	R	ALT,VD	?	9	140S- 930W

Specimen Number	Field No.	Code	Description	Lode name	Mine level	Co-ordinates
103333	59	R,T	ALB	?	9	140S- 930W
103334	60	R,PT,F	ALB,VQ,VD	608	9	100N- 840W
103335	62	R,PT,F	ALT,VQ,VD	Cardigan	2	1263S-1635W
103336	63	R,T,F	ALB,VQ	State	2	1595S-1460W
103337	64	R,PT	ALB,VQ	608	2	1860S-1270W
103338	65	R,PT,F	ALB,VQ,VC	608	2	1608S-1640W
103339	66	R,F	ALB,VQ,VC	Cardigan	3	1200S-1580W
103340	67	R,F	ALB,VQ	Cardigan	3	645S-1840W
103341	68	R,PT,F	ALB,VQ,VD	Shatter	4	640S-1780W
103342	69	R,F	VQ,VD,VA	Cardigan	5	730S-1630W
103343	70	R,PT,F	ALB,VD,VQ	608	7	500S-1000W
103344	73	R,F,D,P, PD,CA	ALT,VQ	1010	9	?
103345	75	R,PT,F	ALB,T	1600	10	?
103346	78	R,PT,F	ALB,VQ,ALT	1010	9	?
103347	79	R,PT	ALA	608	2	?
103348	80	R	ALB,VQ,VD,ALT	166	7	?
103349	81	R,PT	VQ,VD,VA	9Q	?	?
103350	82	R,PT	ALT,VQ	Cardigan	2	?
103351	83	R,PT	ALB,ALA	9Q	?	?
103352	85	R,PT	ALT,P	D-28	?	?
103353	86	R,PT	ALB,P	D-106	?	?
103354	87	R,PT	VQ,VD,VA	9G	?	?
103355	89	R,PT,D,P, PD,CA	ALB	Crown	9	1705N-1480E
103356	90	R,D,P,PD, CA	ALB	Crown	9	1705N-1480E
103357	91	R,PT,D,P, PD,CA	ALB	Crown	9	1705N-1480E
103358	94	R,PT,D,P, PD,CA	ALB	?	9	1704N-1422E
103359	95	R	ALB	Crown	9	1672N-1650E
103360	96	R,F	VQ,VD	Crown	9	1740N-1485E
103361	97	R	ALA,VQ,VD,P	Crown	9	1780N-1360E
103362	105	R,PT,D,P, PD,CA	ALB	Prince	7	215N-1795W
103363	106	R,PT,D,P, PD,CA	FB	Prince	9	220N-1670W
103364	108	R,F	ALB,VQ	Wunawali	9	220S- 720E
103365	109	R,F	ALB,VQ	166	9	30N- 730E
103366	109B	R	VQ	166	9	30N- 730E
103367	110	R,F	ALB,VQ	166	9	15N- 780E
103368	111	R,F	ALB,VQ	Wunawali	9	50N- 340E
103369	119	R,F	ALB,VQ	166	10	210S- 815E
103370	120	R,F	ALB,VQ	166	10	170S- 950E
103371	121	R,F	VQ	166	10	155S-1150E
103372	123	R,D,P,PD, CA	ALB	166	11	300S- 850E
103373	126	PT,D,P,PD, CA	FB	2000	16	1850N- 860E
103374	127	PT,D,P,PD, CA	ALB	2000	16	1850N- 860E
103375	131	R,F	ALA,VQ	?	16	800N- 145W

Specimen Number	Field No.	Code	Description	Lode name	Mine level	Co-ordinates
103376	132	R,D,P,PD, CA	FB	?	16	440N- 145W
103377	3-S	R,F	ALB,VQ	Prince	9	?
103378	4-S	R,F	ALB,VQ,VC	1010	9	?
103379	5-S	R,F	ALB,VQ	Prince	9	?
103380	6-S	R,F	ALB,VQ	Prince	9	?
103381	7-S	R,F	ALB,VQ	1010	9	?
103382	8-S	R,F	ALB,VQ	Prince	9	?
103383	9-S	R,F	ALB,VQ	Prince	9	?
103384	F-1	R,PT	ALT,VC	Crown	10	2604N- 938E
103385	F-3	R,PT	ALB,VQ	Crown	10	2567N- 883E
103386	F-6	R,PT	ALB,VQ	Crown	10	2876N- 706E
103387	F-8	R	ALB,VQ	Crown	20	2800N- 770E
103388	F-41	R,PT	ALA,VQ	Crown	7	1616N-1260E
103389	F-44	R	ALA,VQ,VC	Crown	7	1616N-1234E
103390	F-46	D,P,PD,CA	ALA	Crown	7	1759N-1213E
103391	F-48	R	ALT	Crown	7	1864N-1162E
103392	F-50	R,PT,F	ALB,VQ	Crown	8	1480N-1150E
103393	F-52	D,P,PD,CA	ALB	Crown	8	1540N-1190E
103394	F-54	R,PT	ALA	Crown	8	1750N-1220E
103395	F-58	R,F	ALA,VQ	Crown	9	1863N-1326E
103396	F-60	R,D,P,PD, CA	ALT	Crown	9	1769N-1320E
103397	F-61	R,PT	ALA	Crown	9	1678N-1363E
103398	F-63	R,PT,D,P, PD,CA	ALB,VC	Crown	9	1647N-1445E
193399	F-69	PT	ALB	Crown	10	1832N-1356E
103400	F-70	R,PT	ALA,VQ	Crown	10	1726N-1450E
103401	F-71	R	ALB,VQ	Crown	10	1692N-1460E
103402	F-73B	D,P,PD,CA	ALA,VC	Crown	10	1616N-1492E
103403	F-75	R,PT	ALA	Crown	10	1467N-1557E
103404	F-109	D,P,PD,CA	ALB	Crown	11	1007N-1380E
103405	F-111	R,PS	ALA	Crown	11	1963N-1400E
103406	F-113	R,D,P,PD	ALA	Crown	11	1932N-1424E
103407	F-114	R	ALA	Crown	11	1945N-1382E
103408	F-116	R	ALA,VQ	Crown	11	1832N-1446E
103409	F-118	R,PT	ALA,VQ,VC,P	Crown	11	1771N-1482E
103410	F-120	R	ALA	Crown	11	1675N-1520E
103411	F-125	R,PT	ALA	Crown	11	1376N-1663E
103412	F-128	R,PT	ALA,VC	Crown	11	1280N-1705E
103413	F-131	R,PT	ALA,VQ	Crown	12	1804N-1480E
103414	F-133	D,P,PD,CA	ALB	Crown	12	1820N-1465E
103415	F-138	D,P,PD,CA	ALB	Crown	12	1732N-1517E
103416	F-140	R,D,P,PD, CA	ALA	Crown	12	1520N-1590E
103417	F-142	R,PT	ALA	Crown	12	1428N-1640E
103418	F-143	R	ALA	Crown	11	1820N-1425E
103419	F-144	R	ALA,VC	Crown	11	1862N-1405E
103420	F-147	R,F	ALA,VQ	Crown	15	1525N-1742E

Specimen Number	Field No.	Code	Description	Lode name	Mine level	Co-ordinates
103421	F-151	R,PT	ALA	Crown	14	?
103422	F-152	R,D,P,PD CA	ALB	Crown	14	1517N-1726E
103423	F-155	R	ALA	Crown	14	1802N-1513E
103424	F-157	R,PT	ALB	Crown	14	1871N-1560E
103425	F-159	R	ALB,VC	Crown	14	1906N-1541E
103426	F-163	R,D,P,PD	ALA,VQ	Crown	13	2001N-1483E
103427	F-167	R,D,P,PD	ALB	Crown	14	1815N-1576E
103428	F-169	R,PT	ALA,VC	Crown	14	1771N-1601E
103429	F-171	R,D,P,PD	ALA,VC	Crown	14	1740N-1610E
103430	F-173	R,F	ALA,VQ	Crown	14	1706N-1614E
103431	F-175	PT	ALA	Crown	14	1582N-1638E
103432	F-177	R	ALA,VQ	Crown	14	1560N-1646E
103433	F-179	R,F	VQ,VD,VA	Crown	14	1560N-1646E
103434	F-210	R,F	ALA,VQ	Crown	16	1447N-1786E
103435	F-213	R	ALB,VQ	Crown	16	1547N-1738E
103436	F-215	R,D,P,PD, CA	ALA,VQ	Crown	16	1604N-1707E
103437	F-217	R	ALB,VQ	Crown	16	1632N-1703E
103438	F-219	R,D,P,PD	ALB,VQ	Crown	16	1673N-1688E
103439	F-225	R,PT	ALA	Crown	16	1820N-1627E
103440	F-227	R,PT	ALA	Crown	16	1863N-1655E
103441	F-281	R,D,P,PD, CA	ALA	Crown	13	1671N-1573E
103442	F0283	PT,F	ALA	Crown	13	1855N-1487E
103443	F-285	R	ALA	Sceptre	9	1998N- 747E
103444	F-286	R	ALB	?	10	431N- 28E
103445	F-301	R	ALB	?	10	439N- 61E
103446	F-304	R,F	ALA,VQ	2000N	15	1261N-1040E
103447	F-307	R,F	ALA,VQ	608	9	414N- 798W
103448	F-312	R,PT	ASH	Basin mineral-ization	11	2630N-3270E
103449	F-313	R,F	ALA	Dolphin	6	?
103450	F-317	R	ALA	Basin mineral-ization	14	1200N-1350E
103451	E-1	R,PT	ALB,ALT	?	?	?
103452	E-2	R,PT	ALB,ALT	?	?	?
103452	E-3	R	ALA with stibnite	Cardigan	open cut	?
103453	E-4	R	ALB,ALT	?	?	?
103454	E-5	R	ALB,ALT	?	?	?
103455	133	R	Pyrite cst.	?	?	?
103456	135	R	ALA,massive pyrite vein	?	?	?
103457	136	R	Recent cal-cite growing over a blasting wire		11	?
103458	72	PD,PS	Pyrite concen-trate		?	?
103459	F-311	PD	Native tell-urium crystal	608	8	25N- 890W

Appendix A.1 cont.

Specimen Number	Field No.	Code	Description	Lode name	Mine level	Co-ordinates
103460	134	R	Pyrite	Cardigan?	?	?
103461	F-277		ALB	Crown	13	1804N-1517E
103462	27	R,F	ALB	P.O.W.	10	?
103463	77	F	VQ			½ mile NO of Emperor mine
103464	E-6	R	ALA,VQ	?	?	?
103465	E-7	R	ALB,P	?	?	?

Appendix A.2

LOCATION AND DESCRIPTION OF ROCK SAMPLES

A.2.1 Bore Hole Samples

Specimen Number	Field Number	Code	Description
DDH MA56	Coordinates 238S-1071E, R.L. 505', angle 90°		
47209	983	D,P,CA	ALB
47210	955	R,D,P,PD,CA	ALB
47211	956	R,T,PD	ALB
47212	960	R,D,P,PD,CA	ALB
47213	961	T	ALB
47214	962	R,TP	ALB
47215	965	T	ALB
47216	966	R,D,P,PD,CA	ALB
47217	968	R,PT	ALB
47218	972	R,T,D,P,PD,CA	ALB
47219	973	R,PT	ALB
47220	974	R,T	ALB
47221	975	R,T	ALB
47222	976	R,T,D,P,PD,CA	ALB
47223	980	R,D,P,PD,CA	ALB
47224	981	R,PT	ALB
47225	985	R,T,D,P,PD,CA	ALB
47226	986	R,T	ALB
47227	989	R,PT	ALB
47228	990	R,T,D,P,PD,CA	ALB
47229	992	R,PT	ALB
47230	993	R,T,D,P,PD,CA	ALB
47231	994	R,PT,D,P,PD,CA	ALB
47232	995	R,T	ALB
47233	999	R,T,D,P,PD,CA	ALB
47234	100'6"	R,D,P,PD,CA	ALB
47235	1003	R,T	ALB
47236	1004'6"	R,T	ALB
47237	1005	R,D,P,PD,CA	ALB
47238	1007	R,D,P,PD,CA	ALB
47239	1008	R,PT	ALB
47240	1009	R,D,P,PD,CA	ALB
47241	1009'6"	R,T,D,P,PD,CA	ALB
47242	1011'6"	R,T	ALB
47243	1012'6"	R,T	ALB
47244	1013'10"	R,PT	ALB
47245	1014	R,D,P,PD,CA	ALB
47246	1015	R,T	ALB
47247	1016	R,PT	ALB
47248	1016'6"	R,T,D,P,PD,CA	ALB
47249	1018	R,T	ALB

Appendix A.2.1 cont.

Specimen Number	Field Number	Code	Description
47250	1019'6"	R,T	ALM
47251	1020	R,PT,D,P,PD,CA	ALM
47252	1022	R,T	ALM
47253	1023	R,T	ALM
47254	1024	R,T,D,P,PD,CA	ALM
47255	1025	R	ALM
47256	1026	R,T	ALM
47257	1028	R,T	ALM
47258	1029'6"	R,T	ALM
47259	1031	R,D,P,PD,CA	ALB
47260	1032	R,T	FB
47261	1034	R,T	FB
47262	1036	R,T,D,P,PD,CA	FB
47263	1037	R,T,D,P,PD,CA	FB
47264	1075	R	FB
47265	1835	R,F	ALB,VQ
DDH E838	Emperor Mine		
47267	110	R,PT	ALA
47268	951	R,PT	ALA
DDH MD-4	Bore hole drilled for dam-site investigation about 50 km south of Tavua.		
47269	27 m	R,T	CALST
47270	29.5 m	R	CALSLT
47271	38 m	R	CALGYK
47272	55.19 m	R	CALGYK
DDH MP-1B	Bore hole drilled for dam-site investigation about 50 km south of Tavua.		
47273	90 m	R,T	CALSLT
DDH N-1	Bore hole drilled for damsite investigation about 50 km south of Tavua.		
47274	47.22 m	R,T	CALGYK
DDH N-2	Bore hole drilled for dam-site investigation about 50 km south of Tavua.		
47275	48.19 m	R,T	CALGYK

A.2.2 Surface Samples

Specimen Number	Field Number	Code	Description	Location/ Geographical Co-ordinates
47276	99	R	ALB	Loloma open cut, Emperor Mine area.
47277	100	R,PT,D,PD	ALB	"
47278	101	R,PT,D,PD	ALB	"
47279	102	R	ALB	"
47280	113	R,PT,P,D,PD	ALB	"
47281	114	R,PT,P,D,PD	ALB	"
47282	115	R,PT,P,D,PD	ALB	"
47283	116	R	ALB,VQ	"
47284	117	R	ALA,ALB,VQ	"
47285	118	R	FA	"
47286	S-1	R,T	FA	177°52'50"E-17°30'S
47287	S-2	R	ALT	" "
47288	S-3	R,T	FB	177°53'E-17°30'5"S
47289	S-4	R	ALT	" "
47290	S-5	R,PT	ALB	177°52'50"E-17°40'S
47291	S-6	R	ALA	" "
47292	S-7	R,D,P,PD	ALA	177°53'E-17°30'50"S
47293	S-8	R,PT,D,P,PD	ALB	177°51'50"E-17°30'S
47294	S-9	R,PT,D,P,PD	FA (augite andesite)	177°52'E-17°30'S
47295	S-10	R,PT,D,P,PD	FB	177°51'50"E-17°30'S
47296	S-11	R	FA (augite andesite)	177°53'E-17°30'50"S
47297	SS-1	R,D,P,PD	CALSLT	177°41'E-17°34'S
47298	SS-2	R,D,P,PD	CALSLT	177°41'E-17°34'S
47299	SS-3	R,T,D,P,PD	CALSLT	177°42'E-17°37'S
47300	SS-4	R,T,D,P,PD	CALSLT	178°14'E-17°37'S
47301	SS-5	R,T,D,P,PD	GYK	178°15'E-17°37'S
47302	SS-6	R	CALSLT	178°15'E-17°35'S
47303	SS-7	R,D,P,PD	CALGYK	178°15'E-17°38'S
47304	SS-8	R	LST	177°48'E-17°40'S
47305	C-249	R	LST	178°08'E-17°34'S
42306	SS-9	R		177°41'E-17°34'S

Appendix B

SAMPLE MINERALOGY

Specimen No.	103288	103290	103292	103296	103298	103300	103301	103302
Augite		x	x					
Olivine								
Plagioclase		x						
Magnetite		x		x				
Chlorite	x	x		x			x	x
Dolomite (d)	x	x	x	x	x		x	x
Quartz	x		x	x	x	x	x	x
Sericite	x		x	x	x	x	x	x
K-feldspar	x		x	x				
Adularia	x				x	x		
Roscoelite			x	x	x.	x		
Calcite	x		x	x	x		x	
Pyrite[a]	x	x	x	x	x	x	x	x
Fahlerz[b]		x	x		x			
Chalcopyrite		x			x			
Sphalerite	x		x	x	x	x		
Tellurium								
Calaverite								
Krennerite								
Sylvanite								
Petzite								
Hessite					x			
Gold								
Coloradoite								
Altaite								
Melonite								
Bournonite								
Galena								
Polybasite[c]						x		

Appendix B cont.

Specimen No.	103304	103305	103309	103310	103312	103313	103314	103317
Augite								
Olivine								
Plagioclase							x	x
Magnetite			x				x	
Chlorite							x	x
Dolomite (d)	x	x					x	x
Quartz	x	x	x	x	x	x	x	x
Sericite		x	x	x	x	x		
K-feldspar		x	x	x		x		
Adularia		x			x	x		
Roscoelite						x		
Calcite			x			x		
Pyrite[a]	x	x	x	x	x	x		x
Fahlerz[b]			x		x	x		
Chalcopyrite				x	x	x		
Sphalerite			x	x	x	x		
Tellurium								
Calaverite					x	x		
Krennerite					x	x		
Sylvanite								
Petzite								
Hessite								
Gold								
Coloradoite					x			
Altaite								
Melonite								
Bournonite								
Galena				x				
Polybasite[c]								

Appendix B cont.

Specimen No.	103319	103320	103321	103330	103331	103333	103335	103336
Augite								
Olivine								
Plagioclase								
Magnetite					x	x		
Chlorite		x				x		
Dolomite (d)	x	x	x	x	x	x		x
Quartz	x	x	x	x	x	x	x	x
Sericite	x	x	x	x	x		x	x
K-feldspar		x					x	x
Adularia	x	x	x		x		x	
Roscoelite		x		x			x	
Calcite		x		x			x	
Pyrite[a]	x	x	x	x	x		x	x
Fahlerz[b]	x				x			
Chalcopyrite	x							
Sphalerite	x			x				
Tellurium								
Calaverite								
Krennerite								
Sylvanite				x				
Petzite				x				
Hessite				x				
Gold				x				
Coloradoite								
Altaite								
Melonite								
Bournonite								
Galena								
Polybasite[c]								

Appendix B cont.

Specimen No.	103337	103338	103341	103343	103345	103346	103347	103348
Augite								
Olivine								
Plagioclase		x						
Magnetite	x	x	x					
Chlorite	x							
Dolomite (d)	x	x	x	x	x	x	x	x
Quartz	x	x	x	x	x	x	x	x
Sericite	x	x	x	x		x	x	
K-feldspar	x	x	x		x		x	
Adularia				x	x		x	
Roscoelite				x	x		x	
Calcite	x		x	x	x			
Pyrite[a]	x	x	x	x	x	x	x	x
Fahlerz[b]		x						
Chalcopyrite	x	x						
Sphalerite	x	x		x	x			
Tellurium					x			x
Calaverite					x			x
Krennerite					x			x
Sylvanite		x						
Petzite								
Hessite								
Gold								
Coloradoite					x			
Altaite					x			
Melonite								
Bournonite								
Galena								
Polybasite[c]								

Appendix B cont.

Specimen No.	103349	103350	103351	103352	103353	103354	103355	103356
Augite							x	
Olivine								
Plagioclase							x	
Magnetite						x	x	x
Chlorite							x	x
Dolomite (d)	x	x		x	x	x	x	x
Quartz	x	x	x	x	x	x	x	x
Sericite		x	x	x	x			
K-feldspar		x			x			
Adularia		x	x		x			
Roscoelite		x		x				
Calcite	x					x		
Pyrite[a]	x	x	x	x	x	x	x	x
Fahlerz[b]		x		x				
Chalcopyrite		x		x				
Sphalerite		x		x		x		
Tellurium				x				
Calaverite				x				
Krennerite				x				
Sylvanite				x				
Petzite				x				
Hessite				x				
Gold								
Coloradoite								
Altaite								
Melonite								
Bournonite								
Galena								
Polybasite[c]								

Appendix B cont.

Specimen No.	103357	103358	47277	47278	47279	103362	103363	47280
Augite	x	x	x	x	x	x	x	x
Olivine				x			x	
Plagioclase		x	x	x	x	x	x	
Magnetite	x	x	x	x	x	x	x	x
Chlorite	x	x	x	x	x	x	x	x
Dolomite (d)	x	x		x	x	x		x
Quartz	x	x						x
Sericite					x?			x
K-feldspar								
Adularia								x
Roscoelite								
Calcite								
Pyrite[a]	x					x		x
Fahlerz[b]								
Chalcopyrite								
Sphalerite								
Tellurium								
Calaverite								
Krennerite								
Sylvanite								
Petzite								
Hessite								
Gold								
Coloradoite								
Altaite								
Melonite								
Bournonite								
Galena								
Polybasite[c]								

Appendix B cont.

Specimen No.	47281	47282	103372	103373	103374	103376	47290	47292
Augite	x	x	x	x	x	x	x	x
Olivine				x	x	x	x	
Plagioclase	x		x	x	x	x	x	x
Magnetite	x	x	x	x	x	x	x	x
Chlorite	x	x	x	x				x
Dolomite (d)	x	x	x					x
Quartz		x						
Sericite	x	x						
K-feldspar								
Adularia								
Roscoelite								
Calcite								
Pyrite[a]	x	x	x		x			
Fahlerz[b]								
Chalcopyrite	x							
Sphalerite								
Tellurium								
Calaverite								
Krennerite								
Sylvanite								
Petzite								
Hessite								
Gold								
Coloradoite								
Altaite								
Melonite								
Bournonite								
Galena								
Polybasite[c]								

Appendix B cont.

Specimen No.	47293	47294	47295	103389	103385	103386	103388	103392
Augite	x	x	x					
Olivine	x		x					
Plagioclase	x	x	x					
Magnetite	x	x	x					
Chlorite	x	x	x					
Dolomite (d)				x	x	x	x	x
Quartz				x	x	x	x	x
Sericite				x	x	x	x	x
K-feldspar				x			x	
Adularia	x	x	x	x	x			
Roscoelite	x		x					
Calcite				x	x	x	x	x
Pyrite[a]				x	x	x	x	x
Fahlerz[b]				x	x	x	x	x
Chalcopyrite				x	x	x	x	x
Tellurium								
Calaverite						x		
Krennerite						x		x
Sylvanite						x		x
Petzite						x		
Hessite						x		
Gold						x		x
Coloradoite								
Altaite						x		
Melonite						x		
Bournonite						x		
Galena						x		
Polybasite[c]								

Appendix B cont.

Specimen No.	103394	103396	103397	103398	103399	103400	103402	103345
Augite								
Olivine								
Plagioclase								
Magnetite	x		x	x		x		
Chlorite	x		x	x				
Dolomite (d)	x	x	x	x	x	x		x
Quartz	x	x	x	x	x	x		x
Sericite	x	x		x	x	x		x
K-feldspar	x	x	x	x	x	x		
Adularia						x		x
Roscoelite						x		
Calcite	x				x	x	x	x
Pyrite[a]	x	x	x	x	x	x	x	x
Fahlerz[b]	x	x	x	x		x		x
Chalcopyrite		x	x	x		x	x	x
Sphalerite	x	x	x	x		x	x	x
Tellurium								
Calaverite					x		x	
Krennerite		x			x	x	x	
Sylvanite		x		x		x	x	
Petzite		x		x		x	x	x
Hessite		x				x	x	x
Gold		x		x		x	x	x
Coloradoite		x		x			x	
Altaite								
Melonite								
Bournonite		x						
Galena		x						
Polybasite[c]								

Appendix B cont.

Specimen No.	103404	103405	103408	103409	103410	103411	103412	103413
Augite								
Olivine								
Plagioclase								
Magnetite								
Chlorite								
Dolomite (d)						x		x
Quartz				x		x	x	x
Sericite				x		x	x	x
K-feldspar				x			x	
Adularia				x		x	x	x
Roscoelite				x				
Calcite				x				
Pyrite[a]	x	x	x	x	x	x	x	x
Fahlerz[b]	x			x				x
Chalcopyrite	x			x	x	x	x	x
Sphalerite	x			x	x	x	x	x
Tellurium								
Calaverite		x		x				
Krennerite				x	x			
Sylvanite	x	x		x	x		x	x
Petzite	x	x		x	x			
Hessite	x	x	x	x				
Gold	x	x	x	x				
Coloradoite	x	x		x				
Altaite	x							
Melonite	x							
Bournonite								
Galena								
Polybasite[c]								

Appendix B cont.

Specimen No.	103415	103416	103417	103419	103421	103423	103424	103426
Augite								
Olivine								
Plagioclase								
Magnetite								
Chlorite								
Dolomite (d)			x		x		x	
Quartz			x		x		x	
Sericite			x		x		x	
K-feldspar							x	
Adularia			x					
Roscoelite							x	
Calcite			x				x	
Pyrite[a]	x	x	x	x	x	x	x	x
Fahlerz[b]	x	x	x			x		x
Chalcopyrite	x	x	x		x	x	x	x
Sphalerite	x	x	x		x	x	x	x
Tellurium				x				
Calaverite								
Krennerite				x				
Sylvanite	x	x	x	x				
Petzite	x	x	x	x		x	x	
Hessite	x	x	x	x		x	x	x
Gold	x	x	x	x		x	x	x
Coloradoite			x	x				
Altaite	x		x	x				
Melonite	x							
Bournonite								
Galena			x					
Polybasite[c]						x		

Appendix B cont.

Specimen No.	103428	103429	103431	103434	103436	103439	103440	103461
Augite								
Olivine								
Plagioclase								
Magnetite								
Chlorite								
Dolomite (d)	x		x		x		x	x
Quartz	x		x		x	x	x	x
Sericite			x		x	x	x	x
K-feldspar						x		x
Adularia			x			x		x
Roscoelite			x					
Calcite			x		x	x	x	
Pyrite[a]	x	x	x	x	x	x	x	x
Fahlerz[b]	x	x	x	x				x
Chalcopyrite	x	x	x	x		x		x
Sphalerite	x			x	x		x	x
Tellurium								
Calaverite								
Krennerite								
Sylvanite								
Petzite		x	x		x			x
Hessite		x	x	x	x			x
Gold			x	x	x	x		x
Coloradoite								
Altaite								
Melonite								
Bournonite								
Galena								
Polybasite[c]								x

Appendix B cont.

Specimen No.	103441	103442	103446	103447	103459	103448	103450	47211
Augite								x
Olivine								
Plagioclase								x
Magnetite		x						x
Chlorite								x
Dolomite (d)						x		x
Quartz		x				x		
Sericite		x				x		
K-feldspar		x						
Adularia						x		
Roscoelite								
Calcite		x	x					
Pyrite[a]	x	x	x		x	x	x	
Fahlerz[b]	x	x	x					
Chalcopyrite	x	x	x		x		x	
Sphalerite		x	x				x	
Tellurium				x	x		x	
Calaverite								
Krennerite				x			x	
Sylvanite				x	x		x	
Petzite	x	x						
Hessite	x	x	x					
Gold	x	x	x					
Coloradoite		x					x	
Altaite					x		x	
Melonite					x		x	
Bournonite								
Galena			x					
Polybasite[c]		x						

Appendix B cont.

Specimen No.	47213	47214	47215	47217	47218	47220	47221	47222
Augite	x	x	x		x			x
Olivine								
Plagioclase	x	x	x		x			
Magnetite	x	x	x		x	x	x	x
Chlorite	x	x	x	x	x	x	x	x
Dolomite (d)	x	x	x	x	x	x	x	x
Quartz	x	x	x	x	x	x	x	
Sericite		x		x				
K-feldspar		x		x				
Adularia		x		x				
Roscoelite								
Calcite								
Pyrite[a]								
Fahlerz[b]								
Chalcopyrite								
Sphalerite								
Tellurium								
Calaverite								
Krennerite								
Sylvanite								
Petzite								
Hessite								
Gold								
Coloradoite								
Altaite								
Melonite								
Bournonite								
Galena								
Polybasite[c]								

Appendix B cont.

Specimen No.	47229	47209	47225	47226	47227	47228	47229	47230
Augite		x						
Olivine								
Plagioclase		x						
Magnetite		x	x	x		x		
Chlorite	x	x	x	x	x	x	x	x
Dolomite (d)	x	x	x	x	x	x	x	x
Quartz	x		x		x	x	x	x
Sericite								
K-feldspar	x							
Adularia								
Roscoelite								
Calcite	x				x			
Pyrite[a]	x				x		x	
Fahlerz[b]								
Chalcopyrite	x				x		x	
Sphalerite	x				x		x	
Tellurium								
Calaverite								
Krennerite								
Sylvanite								
Petzite								
Hessite								
Gold								
Coloradoite								
Altaite								
Melonite								
Bournonite								
Galena								
Polybasite[c]								

Appendix B cont.

Specimen No.	47232	47233	47235	47236	47237	47238	47239	47242
Augite								
Olivine								
Plagioclase						x		
Magnetite						x		
Chlorite	x	x	x	x	x	x	x	x
Dolomite (d)	x	x	x	x	x	x	x	x
Quartz	x	x	x		x	x	x	x
Sericite							x	
K-feldspar								x
Adularia								
Roscoelite								
Calcite	x					x		
Pyrite[a]	x					x	x	
Fahlerz[b]								
Chalcopyrite								
Sphalerite								
Tellurium								
Calaverite								
Krennerite								
Sylvanite								
Petzite								
Hessite								
Gold								
Coloradoite								
Altaite								
Melonite								
Bournonite								
Galena								
Polybasite[c]								

Appendix B cont.

Specimen No.	47247	47243	47246	47249	47250	47251	47252	47253
Augite				x				
Olivine								
Plagioclase				x	x	x	x	x
Magnetite								
Chlorite				x		x		
Dolomite (d)		x	x	x	x	x		x
Quartz	x	x	x			x		x
Sericite	x		x		x	x	x	x
K-feldspar	x	x	x					
Adularia		x						
Roscoelite								
Calcite								
Pyrite[a]	x	x				x		
Fahlerz[b]								
Chalcopyrite	x							
Sphalerite	x	x						
Tellurium								
Calaverite								
Krennerite								
Sylvanite								
Petzite								
Hessite								
Gold								
Coloradoite								
Altaite								
Melonite								
Bournonite								
Galena								
Polybasite[c]								

Appendix B cont.

Specimen No.	47254	47256	47257	47258	47260	47261	47262	47263
Augite					x	x	x	x
Olivine							x	x
Plagioclase	x	x	x	x	x	x	x	x
Magnetite								
Chlorite					x	x		
Dolomite (d)	x	x	x		x	x		
Quartz		x		x				
Sericite	x	x	x	x				
K-feldspar								
Adularia								
Roscoelite								
Calcite								
Pyrite[a]								
Fahlerz[b]								
Chalcopyrite								
Sphalerite								
Tellurium								
Calaverite								
Krennerite								
Sylvanite								
Petzite								
Hessite								
Gold								
Coloradoite								
Altaite								
Melonite								
Bournonite								
Galena								
Polybasite[c]								

Appendix B cont.

Specimen No.	47276	47268	47286	47288	47290	103344
Augite			x	x		
Olivine				x		
Plagioclase			x	x	x	
Magnetite						
Chlorite			x			
Dolomite (d)		x	x		x	x
Quartz	x	x				x
Sericite	x	x				x
Adularia						x
Roscoelite						x
Calcite						x
Pyrite[a]	x	x				
Fahlerz[b]	x					
Chalcopyrite	x	x				
Sphalerite	x	x				
Tellurium						
Calaverite						
Krennerite						
Sylvanite						
Petzite						
Hessite						
Gold						
Coloradoite						
Altaite						
Melonite						
Bournonite						
Galena						
Polybasite[c]						

Appendix C.1

Major and Trace Element Analyses of Fresh Rocks.

Oxide %	Specimen Number				
	103363	103373	47262	47263	47295
Fe_2O_3	10.52	11.15	11.12	11.12	10.96
MnO	0.15	0.21	0.16	0.16	0.19
TiO_2	0.55	0.52	0.57	0.57	0.52
CaO	12.06	11.97	11.97	11.91	11.63
K_2O	2.28	1.24	1.08	1.08	1.62
P_2O_5	0.39	0.39	0.39	0.39	0.35
SiO_2	48.35	48.92	46.92	49.77	46.71
Al_2O_3	12.41	10.92	11.86	11.86	11.58
MgO	9.33	12.35	10.35	10.35	10.62
Na_2O	1.13	1.37	1.71	1.71	1.14
Loss	3.62	4.49	4.57	5.16	1.94
Total	100.29	103.02	100.36	103.79	97.24
Trace elements in ppm					
Cu	35	56	44	90	109
Zn	71	91	76	73	124
Pb	8	10	3	-	-
Ni	877	394	513	436	116
V	270	250	240	263	173

Appendix C.2

Major and Trace Element Analyses of Propylitic Rocks.

Oxide %	Specimen Number									
	103355	103356	103357	103358	47277	47278	103362	47281	47282	103372
Fe_2O_3	10.66	9.24	9.11	10.54	9.83	12.01	10.28	10.32	10.47	10.37
MnO	0.13	0.13	0.22	0.17	0.22	0.24	0.25	0.21	0.22	0.19
TiO_2	0.57	0.57	0.53	0.49	0.50	0.56	0.52	0.50	0.52	0.49
CaO	11.16	10.61	10.88	11.57	12.27	9.93	11.41	9.75	9.24	12.16
K_2O	1.20	3.45	3.95	1.21	2.11	3.15	2.89	2.74	2.89	1.71
P_2O_5	0.41	0.36	0.35	0.42	0.37	0.39	0.35	0.35	0.40	0.31
SiO_2	46.54	43.29	39.75	43.56	41.05	44.82	41.78	43.29	43.61	43.54
Al_2O_3	13.01	11.32	11.37	9.85	11.22	12.07	11.14	10.78	11.42	10.55
MgO	8.47	6.55	6.84	10.25	5.84	4.99	7.20	8.04	6.03	10.45
Na_2O	1.77	0.39	0.30	0.95	0.90	1.21	1.04	0.74	1.44	0.34
Loss	4.22	13.94	14.46	10.42	14.05	10.81	12.66	11.00	12.91	11.30
Total	98.13	99.22	97.46	99.43	98.35	100.17	99.52	97.73	99.15	101.40
Trace elements in ppm										
Cu	31	106	90	27	38	38	245	109	104	39
Zn	112	72	78	72	62	131	71	68	83	63
Pb	18	4	4	3	1	6	2	8	3	3
Ni	710	236	162	390	115	229	228	226	228	198
V	297	284	250	257	202	492	262	396	236	477

Appendix C.2 cont.

Oxide %	Specimen Number									
	103374	103376	47211	47212	47216	47218	47222	47223	47209	47225
Fe_2O_3	11.75	10.51	10.17	10.57	10.44	9.98	10.00	9.81	10.62	10.02
MnO	0.17	0.18	0.15	0.15	0.15	0.16	0.16	0.16	0.16	0.18
TiO_2	0.53	0.51	0.52	0.51	0.50	0.48	0.48	0.47	0.48	0.52
CaO	10.79	11.52	11.47	10.81	10.68	9.40	11.53	10.38	10.62	7.90
K_2O	1.81	1.65	1.64	2.22	2.19	2.70	1.16	1.75	2.21	3.10
P_2O_5	0.41	0.38	0.34	0.30	0.30	0.28	0.34	0.32	0.35	0.31
SiO	43.94	47.35	44.91	44.28	43.71	44.36	47.70	43.78	45.58	46.69
Al_2O_3	11.39	11.29	11.28	11.80	11.25	11.52	10.48	10.00	10.38	11.18
MgO	9.50	12.00	11.33	10.47	10.35	9.54	10.25	9.85	10.34	9.52
Na_2O	1.14	1.08	1.07	1.06	1.06	0.58	0.99	0.29	0.66	0.23
Loss	7.79	4.49	5.99	5.40	8.12	9.67	7.55	10.14	10.25	9.83
Total	99.22	100.96	98.87	97.59	98.75	98.68	100.65	96.95	100.65	99.91
Trace elements in ppm										
Cu	60	63	71	111	81	57	74	113	142	132
Zn	86	76	81	73	75	72	83	70	75	105
Pb	3	10	4	12	5	10	7	6	3	8
Ni	331	448	601	465	321	438	244	334	348	305
V	507	267	240	205	153	226	278	286	198	198

Appendix C.2 cont.

Oxide %	Specimen Number							
	47228	47230	47231	47234	47237	47240	47292	47293
Fe_2O_3	10.04	10.30	8.58	9.65	8.84	9.53	7.97	10.15
MnO	0.15	0.19	0.17	0.21	0.20	0.14	0.19	0.18
TiO_2	0.53	0.51	0.49	0.48	0.49	0.47	0.61	0.53
CaO	7.35	9.48	9.17	13.89	10.50	7.81	6.91	11.24
K_2O	3.94	3.03	4.56	1.62	5.15	5.63	4.68	2.54
P_2O_5	0.36	0.33	0.39	0.38	0.39	0.37	0.68	0.38
SiO_2	46.87	43.51	40.31	42.31	42.17	39.97	50.91	47.09
Al_2O_3	11.77	11.05	10.53	10.38	10.51	10.63	17.98	10.72
MgO	7.83	8.78	7.35	9.07	5.63	7.05	2.44	10.05
Na_2O	0.78	0.28	0.00	0.95	0.46	0.16	2.66	0.84
Loss	9.83	12.27	13.68	10.99	13.91	12.68	4.87	5.71
Total	99.46	99.74	95.26	99.93	98.24	94.45	99.81	99.44
Trace elements in ppm								
Cu	202	215	113	88	141	110	162	97
Zn	83	74	69	67	74	86	87	66
Pb	11	7	7	3	10	6	3	11
Ni	380	241	323	282	350	386	199	502
V	255	215	201	216	395	208	254	266

Appendix C.3

Major and Trace Element Analyses of Potassium Silicate Rocks.

Oxide %	Specimen Number								
	103390	103393	103396	103398	103402	103404	103406	103414	103415
Fe_2O_3	8.53	4.94	6.75	6.29	4.66	6.87	4.13	3.38	4.62
MnO	0.25	0.19	0.10	0.24	0.25	0.20	0.31	0.06	0.21
TiO_2	0.24	0.16	0.36	0.30	0.03	0.20	0.11	0.21	0.24
CaO	11.17	7.84	2.18	11.44	14.54	9.40	14.02	3.43	12.11
K_2O	4.42	3.79	4.98	4.21	0.63	3.86	1.05	2.69	4.86
P_2O_5	0.26	0.19	0.38	0.32	-	-	-	-	-
SiO_2	44.06	64.37	67.76	54.42	63.98	61.86	63.37	78.40	60.56
Al_2O_3	7.50	7.32	7.63	7.05	0.16	4.36	1.60	5.62	6.48
MgO	7.66	0.94	1.24	1.63	0.67	1.35	0.81	0.86	0.96
Na_2O	0.04	0.12	0.24	0.39	0.12	0.03	0.25	0.06	0.08
Loss	13.44	7.82	6.59	9.23	9.58	4.62	9.48	3.97	7.81
Total	102.61	97.61	98.21	95.52	94.62	97.75	95.12	94.18	97.93
Trace elements in ppm									
Cu	57	72	139	279	260	195	35	95	56
Zn	77	1052	119	246	1132	158	302	270	97
Pb	11	65	33	26	160	61	229	17	81
Ni	25	22	26	50	755	564	983	696	751
V	1820	981	3173	876	1056	3905	4515	997	-

Appendix C.3 cont.

Oxide %	Specimen Number						
	103416	103422	103426	103427	103429	103438	103441
Fe_2O_3	8.89	3.89	5.61	6.54	5.18	7.71	2.75
MnO	0.06	0.01	0.26	0.12	0.27	0.05	0.31
TiO_2	0.15	0.21	0.28	0.28	0.26	0.12	0.12
CaO	2.08	0.55	13.70	5.63	10.64	2.19	17.15
K_2O	2.14	5.06	4.00	4.64	8.27	2.33	1.68
P_2O_5	-	0.34	-	-	-	0.19	0.01
SiO_2	76.16	77.77	54.24	66.66	54.13	71.43	58.31
Al_2O_3	2.98	7.87	5.48	5.32	10.13	4.01	4.40
MgO	0.75	0.16	1.66	1.93	0.54	0.30	0.71
Na_2O	0.03	0.09	0.05	0.02	0.06	0.01	0.05
Loss	6.88	5.67	9.59	5.45	6.44	6.17	14.16
Total	98.13	101.56	94.88	96.58	95.94	94.53	99.64
Trace elements in ppm							
Cu	280	644	73	142	278	269	90
Zn	1956	1052	271	79	175	1268	128
Pb	352	132	77	12	32	198	35
Ni	827	7	609	941	612	676	20
V	3924	117	3020	3924	908	2058	2647

Appendix C.4

Major and trace element analyses of sedimentary rocks surrounding the Mba Volcanics.

	Specimen Number								
Oxide %	47297	47298	47299	47300	47301	47303	47269	47271	47274
Fe_2O_3	7.54	8.15	8.36	5.65	8.25	6.43	6.35	8.41	8.90
MnO	0.20	0.18	0.16	0.18	0.16	0.54	0.14	0.18	0.14
TiO_2	0.58	0.62	0.61	0.53	0.56	0.54	0.55	0.66	0.58
CaO	6.97	5.87	6.89	17.23	11.09	11.36	19.69	10.45	9.74
K_2O	3.07	4.70	3.25	0.72	1.90	2.82	1.46	1.40	2.22
P_2O_5	0.44	0.51	0.46	0.11	0.38	0.37	0.24	0.28	0.35
SiO_2	45.47	46.97	48.06	44.52	44.62	41.81	36.09	43.80	44.17
Al_2O_3	17.08	17.79	16.42	9.34	14.42	14.49	11.67	14.83	13.25
MgO	3.08	2.98	3.38	1.73	5.88	3.11	2.75	4.39	5.98
Na_2O	0.71	0.68	2.22	1.57	2.29	0.33	2.30	1.60	1.48
loss	15.04	11.96	11.05	17.87	12.02	19.03	19.36	12.07	12.01
Total	100.20	100.41	100.86	99.44	101.58	100.48	100.61	98.08	98.67
Trace elements in ppm									
Cu	168.3	112.8	151.7	103.0	95.6	130.2	120.9	98.9	113.2
Zn	95.3	93.7	98.6	73.5	65.5	79.3	68.7	57.9	79.6
Pb	20.2	17.7	14.7	1.3	0.4	4.1	6.5	2.6	2.2
Ni	26.0	316.3	35.2	11.4	203.5	31.1	29.0	108.3	142.9
V	182.5	202.8	187.8	130.7	322.7	173.4	483.9	517.2	24.2

Appendix C.5

Carbon Dioxide Determinations.

Specimen Number	wt. % CO_2	Specimen Number	wt. % CO_2
(A) FRESH ROCKS		(C) K-SILICATE ASSEMBLAGE	
47295	0.11	103393	5.96
103363	0.17	103398	9.78
(B) PROPYLITIC ASSEMBLAGE		103402	11.22
47212	8.11	103404	6.88
47216	4.54	103406	10.02
47209	9.74	103415	7.64
47225	7.64	103426	15.28
47228	5.13	103427	3.58
47231	14.56	103441	14.22
47237	17.19		
47292	3.34		
47294	1.19		
103357	13.61		
47278	7.40		
47281	3.10		
103372	5.73		
103374	2.39		

Appendix C.6

Specific Gravity Determination.

Specimen Number	Specific Gravity	Specimen Number	Specific Gravity
(A) FRESH BASALT		(C) K-SILICATE ASSEMBLAGE	
103363	2.59	103398	2.64
103373	2.84	103439	2.58
47262	2.83	103438	2.65
47263	2.85	103412	2.69
(B) PROPYLITIC ASSEMBLAGE		103415	2.48
103357	2.89	103416	2.81
47277	2.69	103426	2.66
47278	2.69	103427	2.88
103362	2.60	103414	2.58
103372	2.81		
47293	2.37		

Appendix C.7

Instrument Settings for XRF Analysis.

Oxide/ element	Tube	KV	mA	Crystal	Vacuum	Coll.	Counting time, sec	Counting precision	Detection limit
Fe_2O_3	Cr	50	30	LiF_{200}	yes	coarse	30	13.00±0.04%	0.01%
TiO_2	Cr	50	30	LiF_{200}	yes	fine	20	2.50±0.01%	0.002%
CaO	Cr	50	30	LiF_{200}	yes	fine	20	6.50±0.02%	0.01%
K_2O	Cr	50	30	PE	yes	fine	20	1.8±0.01%	0.003%
SiO_2	Cr	50	30	PE	yes	coarse	100	55.0±0.30%	0.02%
Al_2O_3	Cr	50	30	PE	yes	coarse	100	13.30±0.05%	0.02%
P_2O_5	Cr	50	50	GE	yes	coarse	50	1.04±0.01%	0.01%
MgO	Cr	50	50	TLAP	yes	coarse	100	10.00±0.07%	0.04%
Na_2O	Cr	50	50	TLAP	yes	coarse	100	3.00±0.05%	0.02%
MnO	Au	50	50	LiF_{200}	yes	fine	50	0.15±0.01%	0.003%
Cu	Au	50	40	LiF_{200}	no	fine	20,20,20	50±1, 300±2 ppm	1 ppm
Zn	Au	50	30	LiF_{200}	no	fine	20,20,20	50±1, 1200±5 ppm	1 ppm
Pb ($L\beta_1$)	Mo	60	40	LiF_{200}	no	fine	50,50	10±1, 200±4 ppm	3 ppm
Ni	Au	50	30	LiF_{200}	no	fine	50,50	50±1, 500±3 ppm	1 ppm
V	Cr	50	50	LiF_{200}	yes	fine	100,100	200±5, 3000±10 ppm	3 ppm

Appendix D.1

Electron Microprobe Analyses of Sphalerite

Specimen Number	Stage	S	Zn	Cu	Fe	Cd	St. Formula	Mole % FeS
103340	IB	33.21	62.71	0.87	3.21	-	$(Zn_{.92}Cu_{.013}Fe_{.055})_{.99}S_1$	5.5
103340	IB	33.52	61.49	0.98	4.00	-	$(Zn_{.90}Cu_{.014}Fe_{.069})_{.98}S_1$	6.9
103340	IB	32.98	62.55	0.48	3.98	-	$(Zn_{.93}Cu_{.008}Fe_{.069})_{1.0}S_1$	6.9
103340	IB	32.98	65.24	0.59	1.20	-	$(Zn_{.97}Cu_{.009}Fe_{.020})_{1.0}S_1$	2.0
103340	IB	32.80	61.26	5.01	0.91	-	$(Zn_{.91}Cu_{.077}Fe_{.016})_{1.0}S_1$	1.6
103411	IB	33.04	63.71	1.41	1.22	0.61	$(Zn_{.95}Cu_{.021}Fe_{.021}Cd_{.005})_1S_1$	2.1
103411	IB	32.32	64.33	1.74	0.99	0.60	$(Zn_{.97}Cu_{.036}Fe_{.018}Cd_{.005})_1S_1$	1.8
103411	IB	32.85	62.28	1.95	2.01	0.91	$(Zn_{.92}Cu_{.030}Fe_{.035}Cd_{.008})_1S_1$	3.5
103411	IB	32.45	63.01	3.74	0.78	-	$(Zn_{.95}Cu_{.058}Fe_{.014})_{1.02}S_1$	1.4
103436	IIB	32.00	60.28	3.40	3.88	0.44	$(Zn_{.92}Cu_{.053}Fe_{.069}Cd_{.004})_{1.05}S_1$	6.9
103436	IIB	31.81	61.46	2.89	3.31	0.51	$(Zn_{.95}Cu_{.045}Fe_{.059}Cd_{.005})_{1.06}S_1$	5.9
103436	IIB	32.60	61.75	2.38	2.75	0.50	$(Zn_{.93}Cu_{.037}Fe_{.049}Cd_{.004})_{1.02}S_1$	4.9
103310	IIIB	32.79	66.34	0.14	0.72	-	$(Zn_{.99}Cu_{.002}Fe_{.013})_{1.01}S_1$	1.3
103310	IIIB	32.70	66.46	0.33	0.51	-	$(Zn_{1.0}Cu_{.005}Fe_{.009})_{1.01}S_1$	0.9
103312	IIIB	32.49	64.01	0.70	2.79	-	$(Zn_{.97}Cu_{.011}Fe_{.050})_{1.03}S_1$	5.0
103312	IIIB	31.93	63.08	1.31	2.30	1.35	$(Zn_{.96}Cu_{.021}Fe_{.042}Cd_{.012})_{1.04}S_1$	4.2
103312	IIIB	33.89	63.96	1.09	1.05	-	$(Zn_{.92}Cu_{.016}Fe_{.018})_{.954}S_1$	1.8
103312	IIIB	31.90	60.84	3.38	1.46	2.40	$(Zn_{.93}Cu_{.053}Fe_{.027}Cd_{.021})_{1.03}S_1$	2.7
103312	IIIB	32.11	62.66	1.53	2.31	1.37	$(Zn_{.96}Cu_{.024}Fe_{.042}Cd_{.012})_{1.04}S_1$	4.2
103298	IIIB	33.11	63.55	0.43	2.87	-	$(Zn_{.94}Cu_{.007}Fe_{.051})_{1.00}S_1$	5.1
103298	IIIB	33.20	63.90	0.35	2.56	-	$(Zn_{.94}Cu_{.005}Fe_{.045})_{0.99}S_1$	4.5
103298	IIIB	32.62	64.93	1.32	1.13	-	$(Zn_{.92}Cu_{.021}Fe_{.021})_{0.96}S_1$	2.1

Appendix D.2

Electron Microprobe Analyses of Tellurides.

Specimen Number	Field Number	Weight %			
		Au	Ag	Te	Ni
(A) PETZITE					
103404	F-109	23.41	42.72	33.86	
103404	F-109	23.35	42.77	33.87	
103404	F-109	23.40	42.62	34.03	
103405	F-111	23.54	42.22	34.24	
103405	F-111	23.73	42.62	33.66	
(B) SYLVANITE					
103404	F-109	31.14	6.68	62.17	
103404	F-109	30.63	6.94	62.42	
103404	F-109	29.29	8.13	62.52	
103405	F-111	31.03	6.67	62.30	
103405	F-111	32.43	6.02	61.55	
103405	F-111	33.20	5.85	60.95	
103405	F-111	30.65	7.30	61.06	
103405	F-111	30.81	7.61	62.02	
	F-311*	27.76	8.50	63.74	
	F-311	27.78	8.92	63.30	
(C) KRENNERITE					
103345	75	30.78	6.58	62.63	
103345	75	33.59	4.83	61.58	
103345	75	33.68	4.80	61.52	
103409	F-118	37.05	3.55	59.38	
103409	F-118	37.20	3.51	59.29	
(D) MELONITE					
	F-311*	1.63	-	82.39	15.29
	F-311	-	-	81.57	18.43
(E) NATIVE TELLURIUM					
103345	75	-	0.24	99.76	
	F-311*	-	-	100.00	

* Samples analysed are from Forsythe's (1967) collection and no record is kept at the University of Tasmania.

All analyses normalised to a total of 100.

Appendix D.3

Electron Microprobe Analyses of Carbonates.

Specimen Number	Mineral	Stage	Ca %	Mg %	Fe %	Mn %	Total
103302	ankerite	IA	21.45	6.23	10.92	0.76	39.36
103329	ankerite	IA	18.24	9.51	9.28	0.83	37.86
103392	ankerite	IB	18.43	9.80	8.55	0.85	37.63
103392	ankerite	IB	18.38	9.30	9.78	0.52	37.98
103392	ankerite	IB	17.88	8.03	10.55	0.64	37.10
103392	ankerite	IIB	20.62	11.70	3.59	-	35.82
103392	ankerite	IIB	21.02	11.67	3.16	-	35.85
103392	dolomite	IIB	21.47	11.91	2.22	-	35.60
103337	ankerite	IIIB	19.99	11.60	4.10	0.41	36.10
103337	ankerite	IIIB	18.96	10.92	6.41	0.48	36.77
103337	ankerite	IIIB	19.62	10.61	6.35	0.27	36.85
103337	ankerite	IIIB	18.88	11.12	6.42	0.23	36.65
103337	ankerite	IIIB	18.98	11.39	5.00	1.08	36.45
103337	ankerite	IIIB	18.62	10.61	5.46	2.34	37.03
103337	dolomite	IIIB	18.24	10.48	2.62	5.84	37.18
103337	dolomite	IIIB	20.66	9.80	1.97	4.75	37.18
103337	dolomite	IIIB	19.78	11.47	1.53	3.51	36.29
103337	dolomite	IIIB	19.67	10.61	6.35	0.27	36.90
103342	dolomite	IIIB	20.19	12.89	1.19	0.93	35.20
103342	dolomite	IIIB	20.98	12.28	1.82	0.38	35.46
103342	dolomite	IIIB	23.66	11.16	-	0.85	35.67
103343	dolomite	IIIB	20.85	11.63	3.12	0.32	35.92
103343	dolomite	IIIB	20.61	11.86	3.05	0.29	35.81
103360	ankerite	V?	0.18	13.63	23.40	1.43	38.64
103296	calcite	V	38.6		1.00	0.67	38.27
103329	calcite	V	38.48	-	0.87	0.95	40.40
103329	calcite	V	38.72	-	0.67	0.84	40.23
103409	calcite	V	37.74	-	1.35	0.44	39.53
103409	calcite	V	38.00	-	1.25	0.77	40.02
103409	calcite	V	33.12	-	1.99	1.40	36.51
103409	calcite	V	37.88	-	1.53	0.91	40.32
103457	calcite	super-gene	38.72	0.76	0.08	0.17	39.73

Appendix D.4

Electron Microprobe Analyses of Silicates.

Specimen Number	Oxide Percentages							Number of Ions					
	MgO	Al_2O_3	SiO_2	K_2O	CaO	FeO	Total	Mg^{2+}	Al^{3+}	Si^{4+}	K^{+}	Ca^{2+}	Fe^{2+}
(A) CHLORITE													
103290	25.42	14.21	34.01	0.23	2.00	23.98	99.85	6.91	3.05	6.20	0.05	0.39	3.66
103290	26.23	17.14	39.17	0.16	0.83	16.33	99.86	6.74	3.48	6.75	0.03	0.15	2.35
103290	27.03	17.33	38.40	0.12	0.29	16.65	99.82	6.95	3.53	6.63	0.02	0.05	2.40
103290	27.36	17.45	38.10	0.08	0.48	16.30	98.77	7.03	3.55	6.57	0.02	0.08	2.35
103302	24.82	22.49	31.32	0.48	0.28	20.25	99.64	6.58	4.72	5.57	0.10	0.05	3.01
103302	23.86	22.64	31.64	0.57	0.35	20.56	99.62	6.33	4.75	5.63	0.13	0.07	3.06
103302	23.18	20.82	34.23	0.12	0.25	21.10	99.70	6.12	4.34	6.06	0.03	0.05	3.12
103302	21.52	22.24	34.65	0.76	0.22	20.36	99.75	5.66	4.62	6.11	0.17	0.04	3.00
103333	19.00	21.82	33.63	0.40	0.39	24.04	99.28	5.09	4.64	6.04	0.09	0.07	3.62
103333	19.32	22.09	33.65	0.34	0.20	23.95	99.55	5.17	4.67	6.04	0.07	0.04	3.60
103333	19.35	22.20	33.16	0.39	0.29	23.99	99.38	5.19	4.71	5.96	0.09	0.06	3.61
103356	26.35	18.90	34.91	0.17	0.21	18.95	99.49	6.88	3.92	6.14	0.03	0.04	2.78
103356	24.38	19.67	37.41	0.61	0.34	17.37	99.78	6.30	4.02	6.49	0.14	0106	2.52
103372	27.29	17.36	37.71	0.20	0.45	16.57	99.58	7.04	3.54	6.53	0.05	0.08	2.40
103372	29.48	16.96	35.87	0.00	0.22	17.19	99.72	7.66	3.48	6.25	0.00	0.04	2.51
103376	28.57	13.15	41.93	0.47	1.12	12.88	98.12	7.28	2.65	7.17	0.10	0.21	1.84
103376	28.82	14.32	41.93	0.20	0.83	13.30	99.40	7.29	2.87	7.12	0.04	0.15	1.89

Appendix D.4 cont.

Specimen Number	Oxide Percentages								Number of Ions							
	SiO_2	Al_2O_3	FeO	MgO	Na_2O	K_2O	CaO	Total	Si^{4+}	Al^{3+}	Fe^{2+}	Mg^{2+}	K^+	Na^+	Ca^{2+}	Total
(B) SERICITE																
103319	55.92	31.05	1.78	1.26	-	8.14	1.85	99.96	6.94	4.57	0.18	0.23	1.29	-	0.25	13.43
103319	53.91	31.67	1.61	1.31	-	8.37	3.15	100.02	6.75	4.67	0.16	0.25	1.34	-	0.42	13.59
103319	54.61	32.82	1.81	1.18	-	8.60	0.98	100.00	6.78	4.80	0.19	0.22	1.37	-	0.13	13.49
103459	55.75	28.74	1.58	-	-	11.19	2.74	100.00	7.06	4.29	0.16	-	1.81	-	0.38	13.70
47251	55.75	32.90	1.36	0.55	-	8.13	1.30	99.99	6.88	4.78	0.14	0.10	1.28	-	0.17	13.35
47251	57.01	29.87	2.21	1.06	1.21	7.53	1.09	99.98	7.07	4.36	0.23	0.19	1.26	0.29	0.15	13.55
47251	55.23	31.91	2.11	0.81	-	8.83	1.09	99.98	6.87	4.68	0.22	0.15	1.40	-	0.15	13.47
47251	50.08	30.21	3.80	2.07	-	2.44	6.35	99.95	6.42	4.57	0.40	0.39	1.22	-	0.87	13.87
47267	59.03	29.33	1.47	1.36	-	8.16	0.83	100.18	6.77	4.78	0.16	0.28	1.44	-	0.12	13.55
47267	54.42	32.52	1.76	1.36	-	8.87	1.08	100.01	6.77	4.78	0.18	0.26	1.40	-	0.15	13.54
47267	54.99	33.67	1.35	1.16	-	8.43	0.90	100.50	6.75	4.91	0.14	0.21	1.33	-	0.12	13.47

Appendix D.4 cont.

Specimen Number	Oxide Percentages							Number of Ions						
	SiO_2	Al_2O_3	K_2O	CaO	Na_2O	FeO	Total	Si^{4+}	Al^{3+}	K^+	Ca^{2+}	Na^+	Fe^{2+}	Total
(C) ORTHOCLASE ?														
103343	65.46	18.33	15.07	1.13	-	-	99.99	12.03	3.97	3.53	0.22	-	-	19.75
103343	65.40	18.46	14.99	1.16	-	-	100.01	12.01	3.40	3.51	0.23	-	-	19.15
103459	63.83	20.33	13.44	1.97	0.42	-	99.99	11.69	4.39	3.14	0.39	0.15	-	19.76
103459	64.28	20.24	13.58	1.97	-	-	100.07	11.75	4.36	3.17	0.38	-	-	19.66
47267	64.30	20.67	13.18	1.05	0.81	-	100.01	11.73	4.44	3.07	0.21	0.27	-	19.72
47267	65.29	19.76	12.59	1.12	1.25	-	100.01	11.87	4.24	2.92	0.22	0.44	-	19.69
(D) ADULARIA ?														
103343	66.58	17.80	14.66	1.02			100.06	12.16	3.84	3.42	0.20			19.63
103343	66.74	17.48	14.70	1.06			99.98	12.21	3.77	3.43	0.21			19.62
103343	66.51	17.61	14.71	1.18			100.01	12.18	3.80	3.44	0.23			19.64
103343	66.55	17.82	14.54	1.09			100.00	12.16	3.84	3.34	0.21			19.61
103343	65.89	18.05	14.94	1.13			100.01	12.09	3.90	3.50	0.22			19.71
103384	69.01	16.80	12.89	1.30			100.00	12.45	3.57	2.97	0.25			19.24
103405	64.77	18.52	15.37	1.34			100.00	11.95	4.03	3.62	0.27			19.85
103409	65.05	18.59	15.07	1.27			99.98	11.97	4.03	3.54	0.25			19.78
103409	64.43	18.06	15.77	1.75			100.01	11.94	3.95	3.73	0.34			19.96
103409	65.35	18.31	15.11	1.25			100.02	12.01	3.97	3.54	0.25			19.78

Appendix D.4 cont.

Specimen Number	Oxide Percentages									Number of Ions								
	Na_2O	Al_2O_3	SiO_2	K_2O	CaO	TiO_2	FeO	Cr_2O_3	Total	Na^+	Al^{3+}	Si^{4+}	K^+	Ca^{2+}	Ti^{4+}	Fe^{2+}	Cr^{3+}	Total
(E) OTHER SILICATES - PLAGIOCLASE																		
103376	1.86	31.31	50.08	0.75	14.50	0.17	0.23	1.04	100.00	0.66	6.76	9.16	0.17	2.84	0.02	0.16	0.03	19.44
103459	3.34	21.01	63.08	9.42	3.15	-	-	-	100.00	1.18	4.50	11.47	2.19	0.61	-	-	-	19.95
47278	4.74	21.62	62.61	5.60	4.49	-	0.94	-	100.00	1.66	4.60	11.31	1.29	0.87	-	0.14	-	19.87
47278	5.47	27.37	55.13	0.84	9.96	-	1.24		100.00	1.93	5.86	10.01	0.20	1.94	-	0.19	-	20.13
47279	4.76	27.19	55.45	2.34	8.94	-	1.31	-	99.99	1.68	5.84	1010	0.54	1.74	-	0.20	-	20.10

(E) OTHER SILICATES - AUGITE

	MgO	Al_2O_3	SiO_2	CaO	TiO_2	FeO	Cr_2O_3	Total	Mg^{2+}	Al^{3+}	Si^{4+}	Ca^{2+}	Ti^{4+}	Fe^{2+}	Cr^{3+}	Total
103290	14.63	4.89	49.44	22.42	0.52	7.70	0.28	99.88	0.81	0.21	1.84	0.89	0.01	0.24	0.02	4.02
103376	15.50	3.61	50.55	21.91	0.48	7.65	0.29	99.99	0.86	0.16	1.88	0.87	0.01	0.24	0.02	4.04

(E) OTHER SILICATES - ROSCOELITE

	MgO	Al_2O_3	SiO_2	K_2O	V_2O_5	Na_2O	NiO	Total	Mg^{2+}	Al^{3+}	Si^{4+}	K^+	V^{5+}	Na^+	Ni^{2+}	Total
103345	4.20	8.92	52.15	9.85	23.75	0.70	0.42	100.00	0.75	3.04	6.66	0.81	1.96	0.16	0.17	13.55

Appendix E.1

Thermodynamic data used in calculation of equilibrium constants in this study.

Substance	$\Delta H^{\circ}_{f(298.15)}$ cal/mole	$S^{\circ}_{(298.15)}$ cal/mole/deg	$C^{\circ}_{p(298.15)}$ cal/mole/deg	C_p a	C_p $bx10^{-3}$	C_p $-cx10^{5}$	Source
$Te_{2(g)}$	38,330	61.87	8.68	8.28	1.58	0.06	1
$Te_{(crystalline)}$	0.0	11.83	6.14	4.57	5.28	-	1
$H_2Te_{(aq)}$	18,600	33.7	28.4	-	95.2	-	2
$H_2TeO_{3(aq)}$	-132,600	52.2	45.2	-	151.6	-	2
Te_2^{2-}	27,200	15.4	-76.3	-	-256.2	-	3
$H_2O_{(l)}$	-68,315	16.71	17.995	12.65	11.38	1.73	2
H^+	0	0	0	-	-	-	2
Ag_2Te	-8,600	36.7	12.31	11.75	26.2	0.66	1, 2
$AuTe_2$	-4,450	33.87	18.06	15.20	8.93	0.41	1
$NiTe_2$	-21,000	28.76	18.15	-	-	-	1
PbTe	-16,400	26.3	12.08	11.28	2.69	-	1
NiS	-19,600	12.66	11.26	9.30	6.40	-	2
PbS	-23.500	21.8	11.83	11.17	2.20	-	1
Ag_2S	-7,550	34.3	18.19	15.63	8.60	-	1
Au	0.0	11.37	6.06	5.66	1.24	-	2
$S_{2(g)}$	30,680	54.51	7.76	8.72	0.16	0.90	1
$O_{2(g)}$	0.0	49.003	7.02	7.16	1.0	0.40	2

1. Mills (1974). 2. Naumov *et al.* (1974). 3. D'yachkova & Khodakovskiy (1968).

Appendix E.2

EQUILIBRIUM CONSTANTS FOR THE REACTIONS USED IN THIS STUDY.

	Reaction	Log K (T)					Source
		100	150	200	250	300°C	
1.	$H_2O_{(l)} = H^+ + OH^-$	-12.26	-11.64	-11.27	-11.13	-11.39	a
2.	$H_2S_{(aq)} = H^+ + HS^-$	-6.49	-6.63	-7.00	-7.55	-8.22	b
3.	$HS^- = H^+ + S^{2-}$	-11.45	-11.15	-11.10	-11.30	-11.70	b
4.	$2H_2S_{(aq)} + O_{2(g)} = 2H_2O_{(l)} + S_{2(g)}$	46.26	39.99	35.05	30.60	27.21	a
5.	$2H^+ + SO_4^{2-} = H_2S_{(aq)} + 2O_{2(g)}$	-94.31	-79.31	-67.13	-57.10	-48.55	a
6.	$HSO_4^- = H^+ + SO_4^{2-}$	-2.99	-3.74	-4.49	-5.41	-7.06	a
7.	$NaSO_4^- = Na^+ + SO_4^{2-}$	-1.30	-1.60	-1.94	-2.40	-3.0	a
8.	$KSO_4^- = K^+ + SO_4^{2-}$	-1.30	-1.60	-1.94	-2.40	-3.0	a,d
9.	$CaSO^o_{4(aq)} = Ca^{2+} + SO_4^{2-}$	-2.7	-3.1	-3.6	-4.3*	-4.90*	a
10.	$MgSO^o_{4(aq)} = Mg^{2+} + SO_4^{2-}$	-3.2	-3.9	-4.8	-4.8*	-5.4*	a
11.	$H_2CO_{3(ap)} = H^+ + HCO_3^-$	-6.41	-6.71	-7.13	-7.66	-8.26	b
12.	$HCO_3^- = H^+ + CO_3^{2-}$	-10.14	-10.34	-10.71	-11.20	-11.78	b
13.	$CH_{4(aq)} + 2O_{2(g)} = H_2CO_{3(ap)} + H_2O_{(l)}$		98.34	86.87	77.52	69.74	d
14.	$CO_{2(g)} + H_2O_{(l)} = H_2CO_{3(ap)}$	-1.99	-2.13	-2.14	-2.05	-1.90	b
15.	$CaCO_3 = Ca^{2+} + CO_3^{2-}$	-9.33	-10.28	-11.37	-12.60	-13.90	b
16.	$CaMg(CO_3)_2 = Ca^{2+} + Mg^{2+} + 2CO_3^{2-}$	-17.88	-19.91	-22.10	-24.10*	-25.80*	b
17.	$Ca^{2+} + Mg^{2+} + 2CO_{2(g)} + 2H_2O = CaMg(CO_3)_2 + 4H^+$	-19.20	-18.45	-17.86	-17.82	-18.07	l
18.	$FeS_2 = FeS + \frac{1}{2}S_{2(g)}$	-12.50 (-12.09)	-10.25 (-9.91)	-8.48 (-8.19)	-7.02 (-6.80)	-5.81 (-5.65)	a k

Appendix E.2 cont.

	Reaction	Log K (T)					Source
		100	150	200	250	300°C	
19.	$3FeS_2+2O_{2(g)} = Fe_3O_4+3S_{2(g)}$	44.10	40.51	37.70	35.44	33.93	e,f
20.	$2FeS+3/2O_{2(g)} = Fe_2O_3+2S_{2(g)}$	38.89	35.23	32.29	29.87	27.85	e,f
21.	$2FeS+2O_{2(g)} = Fe_3O_4+3/2S_{2(g)}$	82.06	71.60	63.32	56.61	51.05	e,f
22.	$Cu_5FeS_4+4FeS_2 = CuFeS_2+S_{2(g)}$	17.2	13.6	10.83	8.59	6.75	g
23.	$FeS_2+2H^++\frac{1}{2}O_{2(g)} = Fe^{2+}+S_{2(g)}+H_2O_{(1)}$			14.32	14.52	16.33	e
24.	$CuFeS_2+3H^++3/4O_{2(g)} = Cu^++Fe^{2+}+S_{2(g)}+3/2H_2O_{(1)}$			22.12	21.82	23.93	e
25.	$6Fe_2O_3 = 4Fe_3O_4+O_{2(g)}$	53.84	45.83	39.50	34.37	30.13	e
26.	$Au+2Cl^-+\frac{1}{4}O_{2(g)}+H^+ = \frac{1}{2}H_2O+AuCl_2^-$		7	7.4	7.7	7.9	h
27.	$Au+2H_2S+\frac{1}{4}O_{2(g)} = Au(HS)_2^-+\frac{1}{2}H_2O_{(1)}+H^+$		5.8	3.8	2.1	0.6	h
28.	$HS^-+H_2S+Cu^+ = Cu(HS)_2^-+H^+$			2.4	1.7	1.5	e
29.	$HS^-+2H_2S+Cu^+ = Cu(HS)_2.H_2S^-+H^+$			-	-1.32	-2.4	c
30.	$ZnS = Zn^{2+}+S^{2-}$	-22.18	-21.48	-21.31	-21.32*	21.45*	b
31.	$PbS = Pb^{2+}+S^{2-}$	-23.89	-22.63	-22.13	-21.83*	-21.76*	b
32.	$Ag_2S = 2Ag^++S^{2-}$	-39.70	-35.57	-32.9	-31.2	-30.2	b
33.	$Ag^++Cl^- = AgCl^o_{(aq)}$	2.88	2.88	2.87	3	3.5	i
34.	$Ag+2Cl^- = AgCl_2^-$	4.46	4.45	4.57	4.8	5.4	i
35.	$Pb^{2+}+Cl^- = PbCl^+$	1.73	1.88	2.1	2.4	3.0	a
36.	$Pb^{2+}+2Cl^- = PbCl^o_{2(aq)}$	2.04	2.29	2.6	3.1	3.9	a
37.	$Pb^{2+}+3Cl^- = PbCl_3^-$	2.13	2.50	3.0	3.6	4.6	a
38.	$Pb^{2+}+4Cl^- = PbCl_4^{2-}$	2.05	2.57	3.2	4.0	5.3	a

Appendix E.2 cont.

	Reaction	Log K (T)					Source
		100	150	200	250	300°C	
39.	$Zn^{2+}+Cl^{-} = ZnCl^{+}$	1.82	2.78	3.9	4.8	6.0	a
40.	$Zn^{2+}+2Cl^{-} = ZnCl^{o}_{(aq)}$	2.13	3.19	4.4	5.5	6.9	a
41.	$Zn^{2+}+3Cl^{-} = ZnCl_3^{-}$	2.23	3.34	4.8	6.0	7.7	a
42.	$Zn^{2+}+4Cl^{-} = ZnCl_4^{2-}$	2.14	3.55	5.0	6.4	8.3	a
43.	$FeCl^{+} = Fe^{2+}+Cl^{-}$			-0.67	-1.0	-1.2	e
44.	$CuCl^{o} = Cu^{+}+Cl^{-}$			-2.2	-2.4	-2.2	e
45.	$3KAlS_3O_8+2H^{+} = KAl_3Si_3O_{10}(OH)_2+2K^{+}+6SiO_2$	9.55	8.91	8.49	8.12	7.82	a
46.	$\frac{1}{2}KAl_3Si_3O_{10}(OH)_2+CaMg(CO_3)_2+K^{+}+3SiO_2+3H^{+} =$ $3/2KAlSi_3O_8+2H_2O+Ca^{2+}+Mg^{2+}+2CO_2$	14.42	13.99	13.61	13.76	14.16	m
47.	$H_2Te_{(ag)} = H^{+}+HTe^{-}$	-3.30	-3.90	-4.65	-5.50	-6.40	b
48.	$HTe^{-} = H^{+}+Te^{2-}$	-11.4	-11.3	-11.4	-11.7	-12.1	b
49.	$H_2TeO_3 = H^{+}+HTeO_3^{-}$	-4.25	-4.70	-5.40	-6.2	-7.0	b
50.	$HTeO_3^{-} = H^{+}+TeO_3^{2-}$	-10.15	-10.20	-10.50	-10.9	-11.4	b
51.	$H_2Te_{(ag)}+3/2O_2 = H_2TeO_3$	76.45	66.06	57.92	51.35	45.96	o
52.	$H_2O_{(l)}+\frac{1}{2}Te_{2(g)} = H_2Te_{(ag)}+\frac{1}{2}O_{2(g)}$	-37.26	-32.47	-28.61	-25.44	-22.77	o
53.	$Te_2^{2-}+2H^{+}+H_2O_{(l)} = 2H_2Te_{(ag)}+\frac{1}{2}O_2$	-32.13	-25.71	-20.18	-15.27	-10.83	o
54.	$Au^{o}+Te_{2(g)} = AuTe_2$	16.54	13.60	11.29	9.44	7.91	o
55.	$Te_{2(g)} = 2Te(s)$	14.08	11.45	9.40	7.75	6.40	o
56.	$NiS+Te_{2(g)} = NiTe_2+\frac{1}{2}S_{2(g)}$	10.08	8.34	6.98	5.88	4.96	o
57.	$Ag_2S+\frac{1}{2}Te_{(g)} = Ag_2Te+\frac{1}{2}S_{2(g)}$	2.55	2.23	1.97	1.78	1.63	o

Appendix E.2 cont.

	Reaction	Log K (T)					Source
		100	150	200	250	300°C	
58.	$PbS+\frac{1}{2}Te_{2(g)} = PbTe+\frac{1}{2}S_{2(g)}$	-1.73	-1.50	-1.33	-1.18	-1.06	o
59.	$2Hg+Te_{2(g)} = 2HgTe$	21.70	18.07	15.21	12.89	10.98	o
60.	$2Hg+S_{2(g)} = 2HgS_{(cinnabar)}$	22.34	18.39	15.27	12.75	10.67	j
61.	$2HgS+Te_{2(g)} = 2HgTe+S_{2(g)}$	-0.64	-0.32	-0.06	0.14	0.31	n
62.	$Ag_2Te = 2Ag^+ + Te^{2-}$	-52.03*	-47.20	-43.20*	-43.73*	-39.20	p
63.	$PbTe = Pb^{2+} + Te^{2-}$	-32.9 *	-31.1	-30.67*	-29.5 *	-29.2	p

a Helgeson (1969)
b Naumov *et al.* (1974)
c Crerar and Barnes (1976)
d Ohmoto (1972)
e Haas and Robie (1973)
f Robie and Waldbaum (1968)
g Schneeberg (1973)
h Casadevall (1976), Casadevall & Ohmoto (1977)
i Seward (1973)
j Barton and Skinner (in press)
k Adjusted to plot the FeS contours in sphalerite.
l Calculated from reactions 11, 12, 14 and 16
m Calculated from reactions 17 and 45.
n Calculated from reactions 59 and 60.
o Calculated from data given in Appendix E.1.
* Extrapolated.
p D'yachkova & Khodakovskiy (1968)

Appendix E.3

Individual ion activity coefficients† (expressed as logarithms to base 10). Total NaCl = 1 molal. Ionic strength ≃ 1.

Species	Temperature (°C)				
	100	150	200	250	300
K^+, Cl^-	-0.25	-0.29	-0.34	-0.42	-0.59
HS^-, OH, HTe*	-0.23	-0.26	-0.31	-0.38	-0.51
S^{2-}, Te^{2-}*, Te_2^{2-}*	-0.85	-0.99	-1.08	-1.30	-1.63
SO^{4-}, TeO_3*	-0.98	-1.19	-1.25	-1.50	-1.87
HSO_4^-, HCO_3^-, $NaSO_4^-$, KSO_4^-, Na^+	-0.21	-0.24	-0.28	-0.35	-0.47
Ca^{2+}	-0.75	-0.83	-0.96	-1.15	-1.45
Mg^{2+}	-0.60	-0.67	-0.77	-0.93	-1.18
CH_4, H_2S, H_2CO_3, H_2Te*, H_2TeO_3*	0.08	0.08	0.09	0.12	0.20
CO_3^{2-}, Pb^{2+}	-0.91	-1.01	-1.16	-1.39	-1.74
Zn^{2+}	-0.75	-0.83	-0.96	-1.15	-1.45
Ag^+	-0.30	-0.34	-0.40	-0.50	-0.65

† Calculated following procedures given in Helgeson (1969).

* For these species no a° values are available. It has been assumed that the activity coefficients are as for other species of similar charge and type.

Appendix F

ISOTOPE FRACTIONATION FACTORS

Oxygen isotopes

1000 $ln\ \alpha$	calcite-H_2O	$2.78(10^6/T^2)-3.39$	O'Neil *et al.*, 1969
1000 $ln\ \alpha$	dolomite-H_2O	$3.20(10^6/T^2)-1.50$	Northrop & Clayton, 1966
1000 $ln\ \alpha$	plag. An_{30}-H_2O	$2.68(10^6/T^2)-3.53$	O'Neil & Taylor, 1967
1000 $ln\ \alpha$	qtz-H_2O	$1.63(10^6/T^2)-2.59$	Blattner, 1976

Carbon isotopes

1000 $ln\ \alpha$	CO_2-cal	$-2.988(10^6T^{-1})+7.6663(10^3T^{-1})-2.4612$	Bottinga, 1968
1000 $ln\ \alpha$	Dol-cal	$0.18(10^6T^{-2}) + 0.17$	Sheppard & Schwarcz, 1970

Sulphur and carbon aqueous species

All data from Ohmoto (1972).